1-1-1984

Morphology and energetics of narrow angle tail radio sources.

Christopher P. O'Dea
University of Massachusetts Amherst

MORPHOLOGY AND ENERGETICS
OF NARROW ANGLE TAIL RADIO SOURCES

A Dissertation Presented

by

CHRISTOPHER PETER O'DEA

Submitted to the Graduate School of the
University of Massachusetts in partial fulfillment
of the requirements for the degree of

Five College
DOCTOR OF PHILOSOPHY

September 1984

Astronomy

MORPHOLOGY AND ENERGETICS AT NARROW ANGLE TAIL RADIO SOURCES

A Dissertation Presented

By

Christopher Peter O'Dea

Approved as to style and content by:

William A. Dent, Chairperson of Committee

Frazer M. Owen, Member

Eugene Tademaru, Member

David Van Blerkom, Member

James Walker, Member

LeRoy F. Cook, Department Head
Physics and Astronomy Department

ACKNOWLEDGEMENTS

Carrying out the research described in this thesis was a very exciting and enriching experience for me, and I am tremendously grateful to all who helped make this endeavor possible. First, I would like to thank the NRAO* for giving me an office at the VLA, a generous salary, lots of observing time, and in general for allowing me to carry out this work.

Many people have contributed generously to this project. Jack Burns helped with the 6 cm, B configuration observations of NGC 1265. Kevin Edgar calibrated some of the NAT survey data. Ken Mitchell and Don Wells produced the Optfit program used in the optical identifications of the radio sources. Arnold Rots wrote some of the software used in producing the figures. Pat Smiley and George Kessler did some excellent drafting. Tim Cornwell helped me to make the programming changes in CORMS and was a great help in understanding some of the finer points in image construction. Jean Eilek instructed me in the folklore of turbulence and particle acceleration and much of the discussion in Chapter VI on this topic is based on discussions with her. Saundra Mason and Phyllis Jackson did an excellent job of typing and proofreading the final version of this thesis.

*The National Radio Astornomy Observatory is operated by Associated Universities, Inc., under contract with the National Science Foundation.

I have benefited from stimulating discussions on many topics with Willem Baan, Jack Burns, Tom Balonek, Rick Perley, Alan Bridle, Larry Rudnick, Jean Eilek, Tom Jones, Tim Cornwell, Ron Ekers, and Robert Laing. Ron Ekers commented on Chapter IV, Jean Eilek commented on Chapters VI and VII, Tom Jones commented on Chapter VII, and Tom Balonek commented on Chapters I, III, and IV.

I am grateful to Bill Dent for much good advice over the duration of my career as a graduate student, for giving me my first job as a graduate student, for many good comments on the thesis, and for going to the Black Flag concert with me.

I am especially pleased to thank my advisor, Frazer Owen, for suggesting this topic, for giving me lots of great advice and encouragement, and for helping me to develop as a scientist. Because of him, this thesis has been a richly rewarding experience.

My friends in Socorro and Albuquerque helped maintain my emotional stability during the long months in Socorro. I am grateful to Ellen Hefner and her dance class for keeping me in touch with the other important things in life.

Special thanks are due to Gaila Gulack, Steve Zeitzew, Jamie Primm, Bill Mckinnon, Tom Balonek, and Stefi Baum for sharing in their own personal and wonderful ways. For cosmic inspiration and diversion I am indebted to Dave Brock and the Hawklords and also to Richard Thompson. My brothers Greg, Mark, and Brian and my many aunts, uncles, and cousins gave me lots of love and encouragement.

A B S T R A C T

MORPHOLOGY AND ENERGETICS

OF NARROW ANGLE TAIL RADIO SOURCES

(September 1984)

Christopher P. O'Dea, B.S., M.I.T.,

Ph.D., University of Massachusetts

Directed by: Frazer N. Owen

Fifty-seven radio sources in the directions of clusters of galaxies were observed with the VLA with resolutions of ~1-4". Thirty-eight Narrow Angle Tail (NAT) sources from these observations were combined with 13 from the literature to produce a representative sample of 51 NATs in the directions of Abell clusters. The global properties of this sample were investigated. Correlations between various parameters (i.e., optical rank, core and total power, width, length, galaxy velocity, distance from the cluster center, cluster richness, Bautz-Morgan type and Rood-Sastry type) were examined and discussed within the context of our current understanding of rich clusters of galaxies. The statistical results are in agreement with the hypothesis that the tailed morphology of these objects is due to the interaction of the radio plasma ejected by the moving galaxy with the intracluster medium.

The physics which may be relevant to the bending of beams in NATs is discussed in great detail and constraints on the momentum and kinetic energy flux are examined. Expressions for the bulk velocity, particle

density, Mach number, and efficiency of conversion of bulk kinetic energy into radio luminosity are given. Within the context of models for NATs, constraints are placed on these parameters for 19 sources.

Multifrequency VLA observations of the total intensity, spectral index, and polarization structure of the prototypical NAT (3C 83.1B), associated with the galaxy NGC 1265, were presented and the astrophysical implications were discussed. The collimation structure, foreground rotation measure variations, and existence of a diffuse cocoon support the hypothesis that there is an ISM in the galaxy NGC 1265.

Finally, an overview of the thesis results is given, and directions for future research are discussed.

TABLE OF CONTENTS

LIST OF TABLES

LIST OF FIGURES

CHAPTER I

INTRODUCTION

The interaction of radio sources in clusters of galaxies with the intracluster medium appears to be very important in determining many of the observed properties of these sources (e.g., De Young 1976; Burns 1979; Miley 1980). Radio sources with bent or otherwise distorted structure are preferentially found in clusters of galaxies. The most extreme example of this interaction is the class of Narrow Angle Tail (NAT) sources, which is a type of head-tail source (e.g., Rudnick and Owen 1976; RO). These sources have an unresolved radio core associated with a galaxy (the "head") and one or two diffuse streams of emission (the "tail") trailing away from the galaxy on one side. Until recently in most of these sources only a single stream of emission was seen (single tailed NATs). When observed with higher resolution, these sources tend to have a "U" shaped structure (Fig. 1.1) with two thin streams of emission bending back away from the radio core, and eventually expanding to form the diffuse tails (i.e., twin tail or twin jet NATs). This morphology is attributed predominantly to the interaction of the intracluster medium with beams of radio luminous plasma ejected by a moving galaxy. The bending of the radio jets in NATs provides important constraints on the physics of the radio beams not available in straight jets. The observed bending and radio luminosity give independent constraints on the momentum flux and kinetic energy flux in the beam. In principle, the study of Narrow Angle Tail

Figure 1.1

A comparison of the structure of the Narrow Angle Tail source NGC 1265 (3C 83.1B) on three different size scales. (Taken from Jones and Owen 1979.)

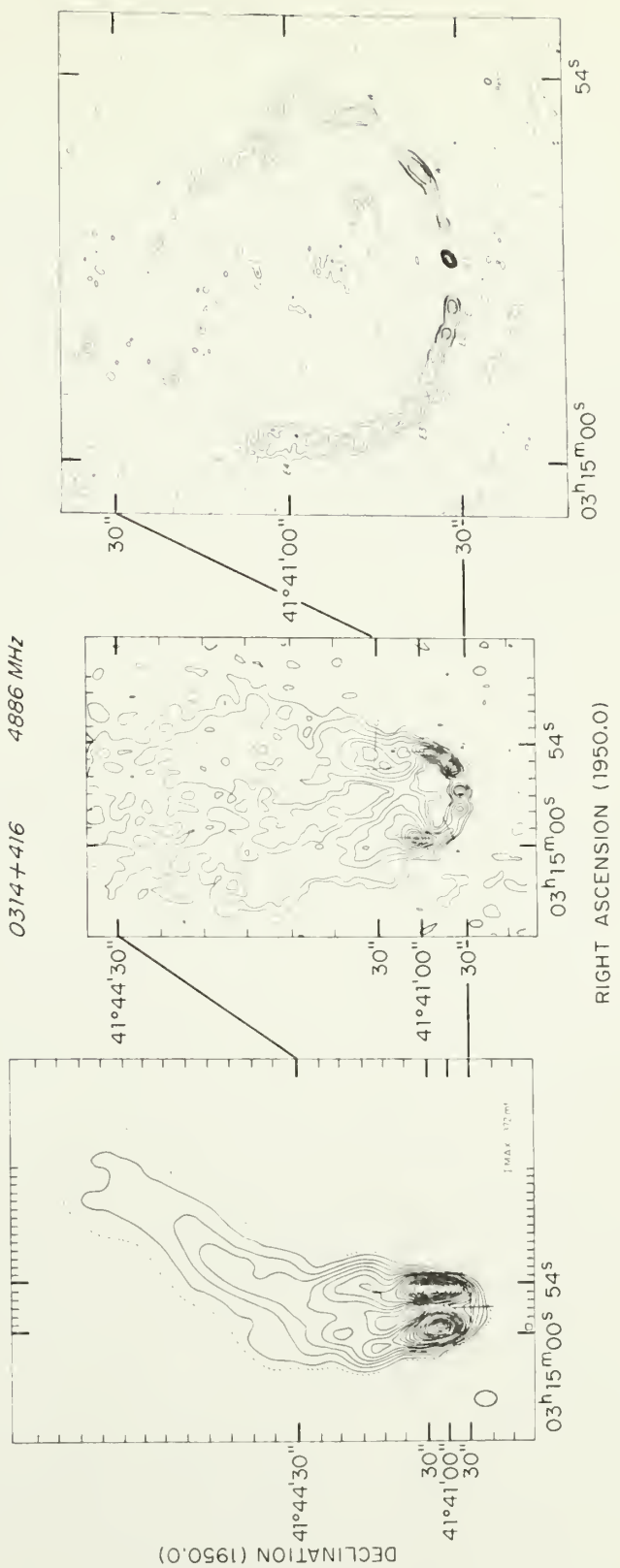
0314+416
4886 MHz
41°44'30"
30"
41°41'00"
30"
03h15m00s
54s
RIGHT ASCENSION (1950.0)
DECLINATION (1950.0)

sources can improve our understanding of the physical conditions within the beams and of their immediate environment within the galaxy and the intergalactic medium.

This introduction first reviews some basic material on the optical and X-ray properties of clusters of galaxies in which tailed radio galaxies are found. The current status of the observational data on tailed radio sources will be summarized. The various models for tailed radio sources are then discussed. Finally, the goals of the thesis and the proposed observations are presented.

1.1 Clusters of Galaxies

Reviews of the early history of the study of clusters of galaxies can be found in Abell (1975) and Shane (1975). Ever since it was recognized by Hubble in 1924 that the "nebulae" were in fact other "island universes," astronomers have been cataloging and classifying galaxies and clusters of galaxies. It was soon discovered that galaxies tended to be found in groups or clusters (e.g., Shapley 1933; Hubble 1934; Zwicky 1938). Evidence was found even for clusters of clusters or superclusters (e.g., Shapley 1957; Abell 1958). Currently it is thought that clustering is a fundamental property of the mass in the universe (e.g., Peebles 1980; Oort 1983).

The Abell catalog

Abell (1958) cataloged 2712 rich clusters of galaxies identified on the Palomar Sky Survey (PSS) photographs. One thousand six hundred and

eighty-three of these 2172 clusters which comprise a homogeneous sample were studied by Abell (1958) and Leir and Van den Bergh (1977). The clusters cataloged by Abell contain greater than 50 member galaxies which are less than two magnitudes fainter than the third brightest cluster galaxy. Abell counted the number of galaxies in this magnitude range within a circle of fixed linear distance, the Abell cluster radius, A_c, centered on the cluster center and subtracted the number within a similar circle in the nearby field. The radius of the circle in millimeters on the sky survey plate was $A_c = 4.6 \times 10^5/cz$, where c is the velocity of light in kilometers per second and z is the redshift of the cluster. Taking into account second order cosmological effects gives the following expression for A_c:

$$A_c = \frac{103\ q_o^2\ (1 + z)^2}{q_o\ z + \left[(1 + 2q_o z)^{1/2} - 1\right]\ (q_o - 1)} \text{ arcsec} \qquad (1.1)$$

(e.g., Rudnick and Owen 1977), where q_o is the deceleration parameter. Throughout the thesis a Hubble constant of $H_o = 75$ km sec^{-1} Mpc^{-1} and a deceleration parameter of $q_o = 0.1$ are assumed. This results in a linear size for A_c of 2 Mpc. All clusters north of declination $\delta = 27°$, with galactic latitudes $b > 30°$ and estimated redshifts $0.02 \leq z \leq 0.2$, were included in the complete sample. The clusters were classified according to their distance (seven distance classes) and their population (five richness classes) shown in Table 1.1.

Table 1.1

Abell Cluster Parameters

Distance Class	Magnitude Interval	Redshift Interval
1	$13.3 \leq m_{10} \leq 14.0$	$0.02 < z \leq 0.03$
2	$14.1 \leq m_{10} \leq 14.8$	$0.03 < z \leq 0.04$
3	$14.9 \leq m_{10} \leq 15.6$	$0.04 < z \leq 0.06$
4	$15.7 \leq m_{10} \leq 16.4$	$0.06 < z \leq 0.10$
5	$16.5 \leq m_{10} \leq 17.2$	$0.10 < z \leq 0.14$
6	$17.3 \leq m_{10} \leq 18.0$	$0.14 < z \leq 0.22$
7	$m_{10} > 18$	$z > 0.22$

Richness Class	Galaxy Population[b]
0	30 - 49
1	50 - 79
2	80 - 129
3	130 - 199
4	200 - 299
5	$\geq$ 300

Notes to Table 1.1

a. m_{10} is the photo-red magnitude of the tenth brightest galaxy in the cluster.

b. The population includes galaxies less than two magnitudes fainter than the third brightest galaxy.

Classification schemes for clusters of galaxies

Several attempts have been made to classify clusters of galaxies according to various properties, which are hopefully astrophysically significant. Abell (1965) divided clusters into two groups (regular and irregular) according to their degree of central condensation, radial symmetry, and galaxy type (e.g., percentage of spiral galaxies). The regular clusters, of which the Coma cluster is the prototype, are very spherically symmetric and have a high central condensation. These clusters contain at least 1000 members brighter than $M_{pv} = -15$ and tend to have a smaller percentage of spiral galaxies. The irregular clusters, of which the Virgo cluster is the prototype, have less spherical symmetry and have small subcondensations rather than a strong central condensation.

Rood and Sastry (1971; RS) classified clusters according to both the relative dominance of the brightest member and the spatial distribution of the 10 brightest member galaxies. This classification scheme was revised by Struble and Rood (1982) and several new subclasses were added. cD clusters (e.g., A 2199) contain a cD galaxy (which they defined to be a galaxy with a semi-major axis at least three times as large as any other galaxy in the cluster). The subclasses cD_p, cD_n, and cD_s designate clusters where the cD is "peculiar" or asymmetric, is composed of a "nest" of three or four nuclei within a common envelope, or contains a fainter "satellite" nucleus within its envelope. Binary clusters (B, e.g., Coma) contain two similar supergiant galaxies, which together are at least three times larger than any other galaxy, separated by less than ten galaxy diameters. The subclass B_b designates

binary pairs connected by a bridge of luminous material, e.g., stars. Line clusters (L, e.g., Perseus) contain three or more of the ten brightest galaxies arranged in a line. The subclass La designates clusters where the bright galaxies are arranged in an arc. Core-halo clusters (C, e.g., A 2065) contain at least four of the brightest ten galaxies grouped near the cluster center surrounded by many fainter galaxies. In flat clusters (F, e.g., A 397) several of the brightest ten and many of the fainter galaxies are arranged in a flattened distribution. In irregular clusters (I, e.g., Hercules) the galaxies are arranged in an irregular pattern without a clear center. Clusters with a smooth or clumpy distribution of galaxies are designated by I_s and I_c, respectively. Struble and Rood (1982) suggested that the RS types represent different stages of cluster evolution, e.g., with the I and F clusters being the youngest, and the B and cD clusters being the more evolved.

Krupp (1972) studied the 30-100 brightest members of 43 clusters from Abell's (1958) complete sample. He finds that the cluster classification can change as the number of galaxies included is increased. Some clusters which Rood and Sastry (1971) classify as flattened or irregular, Krupp classifies as radially symmetric.

Bautz and Morgan (1970; BM) classified clusters according to the relative dominance of the brightest member galaxy. Type I clusters (e.g., A 2199) contain a centrally located cD galaxy. In type II clusters (e.g., Coma) the dominant galaxy is comparable, but not as

large or as bright as a cD galaxy. Type III clusters (e.g., Virgo) contain no dominant galaxies. There are also two intermediate classes, I-II and II-III.

X-ray observations of clusters

Early observations with the Uhuru satellite (Giacconi et al. 1971) firmly established that clusters of galaxies are strong, extended sources of X-rays (Gursky et al. 1971, 1972; Forman et al. 1972). The Einstein X-ray telescope (Giacconi et al. 1979) has provided an enormous amount of data on the X-ray properties of clusters of galaxies. X-ray luminosities ranging from 10^{42} to 10^{45} ergs/sec (in the energy band 0.5 - 3.0 keV) have been detected in over 100 clusters (Forman and Jones 1982).

The interpretation of the X-ray observations is very model dependent. It is possible that there is some contribution to the cluster emission from three separate radiation processes. Inverse Compton radiation produced by the scattering of relativistic electrons off of the microwave background was first suggested by Felton and Morrison (1966). Additionally, there may also be a non-thermal (possibly synchrotron or synchrotron-self Compton) contribution from compact sources (e.g., active galactic nuclei). This is the case in the Perseus cluster where 3C 84 contributes a variable, hard spectral component to the cluster X-ray emission (Primini et al. 1981, Rothschild et al. 1981). However, the dominant emission mechanism below 10 keV is thought to be thermal bremsstrahlung from a hot intracluster gas. This

is supported by the detection of emission lines from highly ionized iron in 18 clusters, including the Perseus cluster (e.g., Mushotzky and Smith 1980).

The temperature and density distributions of this intracluster medium have been modeled in several ways. Lea et al. (1973) assumed that the gas distribution is that of a self-gravitating, isothermal sphere. The radial gas density profile, $\rho(r)$, is then given by (King 1972)

$$\rho(r) = \rho_o \left(1 + \frac{r^2}{r_c^2} \right)^{-3/2} \qquad (1.2)$$

where ρ_o is the central density and r_c is the core radius. Alternately, the gas can be modeled by a polytrope, which is in hydrostatic equilibrium with a given cluster gravitational potential, usually taken to be an isothermal sphere (e.g., Lea 1975; Cavaliere and Fusco-Femiano 1976; Gull and Northover 1975; Bahcall and Sarazin 1977; Nulsen and Fabian 1980; and Fabian et al. 1981). In these more general models, the details of the radial temperature profile depend on the assumed boundary conditions. If it is assumed that the gas temperature and density go to zero at infinity and that the cluster mass distribution is given by equation 1.2, the radial gas density profile is given by

$$\rho(r) = \rho_o \left[\ln 1y + (1 + y^2)^{1/2} y^{-1} \right]^{1/\gamma - 1} \qquad (1.3)$$

where γ is the polytropic index, and $y = r/r_c$. In these models the fits to the data give a central temperature and density of $T \sim 10^7 - 10^8$ K and $n \sim 10^{-3}$ cm^{-3}, respectively.

Cowie and Binney (1977) and Fabian and Nulsen (1977) found that the bremsstrahlung cooling time can be much less than the Hubble time for high central densities and low central temperatures. They suggested that the free-free emission could cool the gas sufficiently to cause it to contract in towards the cluster center. Their prediction of a radiatively regulated cooling flow onto the cluster center was confirmed (for the Perseus cluster) by the detection of a lower temperature gas in the center of the cluster (Mushotzky et al. 1981). Cooling cores have been found in several other clusters as well (Mushotzky and Smith 1980).

Two other dynamic models are the primordial gas infall model of Gunn and Gott (1972) and the cluster wind model of Yahil and Ostriker (1973). Although the velocities in these flows can be quite high ($\sim 10^3$ km/sec in the wind model), no correlation of the orientation of tailed radio sources with respect to the direction to the cluster center has been found (RO, Guindon 1978).

The morphology of the gas distribution can be related to current ideas of cluster dynamical evolution. White (1976) modeled the dynamics of a rich cluster of galaxies by integrating numerically the equations of motion for a 700 body system. He found that from an initially random mass distribution clustering began with small subcondensations which continually merged into a symmetric, centrally condensed cluster. The clustering is initially very asymmetric and may go through a binary stage where the mass is concentrated in two nearly equal condensations.

Forman and Jones (1982) suggest that the X-ray data are consistent with an evolutionary model of this type. Smooth, symmetrical gas distributions are associated with dynamically older, relaxed, regular clusters. And clumped gas is found in younger, irregular clusters. There is also evidence for clusters in the intermediate or binary stage (Forman et al. 1981).

The Perseus cluster. The Perseus cluster is the home of NGC 1265 (3C 83.1B), the prototypical Narrow Angle Tail radio source which is discussed in great detail in this thesis. At least two (perhaps three) other tailed sources IC 310, CR 15, (and 0309+411?) are also found in this cluster. Perseus is at a distance of ~72 Mpc (where 1 arcsec corresponds to a linear distance of 0.35 kpc; using a redshift of $z = 0.0183$ [Noonan 1981, Tifft 1978], and Hubble constant of $H_o = 75$ km sec^{-1} Mpc^{-1}). It is the prototype of the L (line classification of Rood and Sastry (1971)). Because of its large velocity dispersion, low spiral fraction, and high central density of galaxies, the cluster is considered highly evolved (Forman and Jones 1982 and references therein). The cluster has a dominant and active galaxy (NGC 1275, 3C 84) at its center. The extended cluster X-ray emission can be described by a two temperature gas (Mushotzky et al. 1981; Mushotzky and Smith 1980): a hot ($T \sim 8 \times 10^7$ K) isothermal sphere with a core radius of 8' (170 kpc), and a cooler ($T \sim 10^7$ K) gas of radius ~10 kpc centered on NGC 1275. The cool component is thought to represent a cooling accretion flow which dumps ~300 solar masses per year onto NGC 1275 (Mushotzky et al. 1981). NGC 1265 is at a projected distance of 30 arcminutes (630 kpc) from the cluster center, and is well

outside the cooling core. Based on the hydrostatic polytrope model (e.g., Bahcall and Sarazin 1977), equation 1.3, the gas density at the position of NGC 1265 is about $n \sim 5 \times 10^{-4}$ cm^{-3}.

1.2 Head-Tail Radio Galaxies

Observational characteristics

The study of head-tail (HT) radio sources began in 1968 with the first low resolution mapping of the structure of NGC 1265 (3C 83.1B) and IC 310 in the Perseus cluster by Ryle and Windram (1968) and of 3C 129 by Macdonald, Kenderdine, and Neville (1968). The striking feature of these sources was that the optical identification was located at one end of the source rather than at the center. The sources had a tadpole-like structure with a bright "head" at the position of the identification and a narrow diffuse "tail" which grew fainter with increasing distance from the head. This prompted the name head-tail radio galaxy for this class of radio source.

Head-tail sources can be divided into two classes. The Narrow Angle tails (NATs) are generally "U" shaped, (though sometimes only a single stream of emission is seen), and the angle at the core subtended by the ends of the tails is generally less than 45° (e.g., Rudnick and Owen 1976; Valentijn 1979a). The Wide Angle Tails (WATs) are generally "V" shaped, and the angle at the core subtended by the ends of the tails is greater than 90° (e.g., Owen and Rudnick 1976; Valentijn 1979a). It was originally thought that these two types of sources were part of a continuous spectrum of shapes produced by the motion of the parent

galaxy through the intracluster medium (see discussion below). However, recent work (Burns 1981, Eilek et al. 1984) suggests that at least some of the WATs are bent by a mechanism other than ram pressure from an ICM. This thesis will be concerned with the NATs.

Rudnick and Owen (1976) presented radio observations of six NATs and discussed some of the properties of 14 sources. One of them, 3C 129.1, is probably not a NAT (Downes 1980). They introduced a simple classification scheme for the relative dominance of the optical galaxies: rank 1 denotes the dominant galaxy in the cluster, rank 2 denotes a galaxy whose brightness is comparable to that of the brightest cluster galaxy; and rank 3 denotes a galaxy which is much fainter than the dominant galaxy. Rudnick and Owen found that the NATs tended to be associated with the less dominant galaxies in the cluster (i.e., rank 2 and 3). They examined the direction of the tails with respect to the cluster center. RO found that there was no tendency for the tails to point either towards or away from the cluster center. Guindon (1978) reexamined this question in more detail and came to the same conclusion. RO found that the pressures in these sources due to the relativistic particles and magnetic fields (assuming equipartition, i.e., equal energies in the particles and fields) were comparable to the pressure of the thermal gas in the intracluster medium (ICM) implied by X-ray observations of clusters of galaxies (see also Miley, Wellington, and Van der Laan 1975). Also, the estimated velocities of the sources (from the synchrotron lifetimes and the source brightness structure) were comparable to the typical velocity dispersions in rich clusters. Based

on these findings, they suggested that the data were consistent with the suggestion of Miley et al. (1972) that the tails were produced by the motion of the galaxies through the ICM.

Owen and Rudnick (1976; OR) presented observations of six WATs and compared the properties of the WATs with the NATs studied by RO. OR found that the WATs were intrinsically more powerful radio sources than the NATs and were associated with more dominant galaxies (rank 1).

Simon (1978) compared the properties of cluster radio sources with complex morphologies. Her sample consisted of 8 twin tail sources, 16 single tail sources, 11 3C 31-type sources (i.e., twin jet sources with some distortion of the structure away from linear morphology but without a head-tail structure; see Burch 1979, Fomalont et al. 1980), and 13 bent-double (WAT; i.e., "V" shaped) sources. Simon's results were in agreement with, and extended the results of, OR and RO. Simon found that the bent-double and 3C 31-type sources were more powerful radio sources and were associated with brighter optical galaxies than the twin and single tail sources. She also examined the distribution of these sources as a function of the Bautz-Morgan class, optical rank, and the cluster richness. The single and twin tail sources were associated with the lower ranking galaxies in BM class I clusters and with relatively brighter galaxies in BM class II through III. All the 3C 31-type and nearly all the bent double sources were associated with dominant galaxies. Simon found that the bent double and 3C 31-type sources were about equally likely to be found in clusters of any richness, but that the NAT sources were found preferentially in richer clusters. She noted that the properties of the twin and single tail sources were very

similar and differed from those of the 3C 31-type sources. Based on this evidence she argued that the single tail sources were probably not 3C 31-type sources; instead they were more likely to be twin tail sources in which the two tails could not be distinguished due to limited resolution or sensitivity.

Valentijn (1979a) studied the properties of a slightly larger collection of 44 tailed sources. His sample included 16 WATs and 28 (at least possible) NATs (one of which was 3C 129.1), of which only 7 (25%) showed twin tail structure. He introduced a new parameter, the opening angle, which was defined to be the angle subtended at the core by the two ends of the tails. The opening angle was defined to be 0.0 for single tail sources. Valentijn found that there was a discontinuity in the distribution of opening angles which served to sharply distinguish the WATs from the NATs. There were no sources with opening angles between 45° and 90°.

McHardy (1979) studied a complete sample of 4C and 4CT radio sources (including 13 NATs) in Abell clusters. He was not directly concerned with the properties of NATs but did examine the morphology of the sources as a function of BM class. He found no NATs in BM class I and I-II clusters, and concluded that these sources were never found in clusters of these BM types. However, four of the NATs studied by Simon (1978), and several more of the ones presented in this thesis, are located in BM class I and I-II clusters.

Other general properties are among the following:

(1) As a class, NAT sources are among the least luminous extended radio sources in elliptical galaxies (e.g., Hill and Longair 1971, RO, Simon 1978) with typical powers at 408 MHz of $P_{408} < 10^{25}$ W Hz^{-1} sr^{-1}.

(2) The spectral indices in the tails tend to steepen with increasing distance away from the head (Willson 1970; Riley 1973; Miley 1973; Miley et al. 1975; Wilson and Vallee 1977; Van Breugel 1982).

(3) The percentage polarization at centimeter wavelengths in the tails tends to increase with distance away from the head (Miley 1973; Miley et al. 1975).

(4) In some sources there is evidence that in situ particle acceleration is required in the tails (e.g., Ekers et al. 1978; Wilson and Vallee 1977; Baggio, Perola, and Tarenghi 1978; Simon 1979; and Downes 1980).

NGC 1265: Previous observations. Because of its early discovery, closeness, brightness, and the symmetry of its twin-tail structure, NGC 1265 (0314+416; 3C 83.1B) is the best studied NAT source. It is considered the prototype for the class, and is the source most often compared with theoretical models for tailed sources. The large scale structure has been studied by Ryle and Windram (1968); Miley et al. (1972); Riley (1973); Miley (1973); Wellington et al. (1973); Miley, Wellington, and Van der Laan (1975); and Gisler and Miley (1979). High resolution maps of the inner structure have been presented by Riley and Pooley (1975) and Owen, Burns, and Rudnick (1978; OBR).

The source structure on three different size scales is shown in Figure 1.1 taken from Jones and Owen (1979; JO). The 5 GHz map of Wellington et al. (1973), at ~6" resolution, shows two unresolved ridges of emission which emerge initially along the minor axis of the 14^m elliptical galaxy. The ridges are bent back (roughly 70°) into a nearly parabolic shape to the north of the galaxy. About 30" (~11 kpc) behind the galaxy, the ridges expand into two diffuse tails which maintain separate identities over an additional 3'. In the 1.4 GHz map of Miley (1973), at 23" x 30" resolution, the tails seem to merge about 4' behind the galaxy and change direction to the northwest (pointing away from the cluster center). The total length of the tails is about 10' or 200 kpc. The highest resolution map (1" x 1."4) at 4.9 GHz from OBR shows that the strongest feature is an unresolved core component. The thin ridges (~0.25 to ~2 arcseconds in width) have a knotty appearance. The radio luminosity of the tails is $L_t = 2 \times 10^{41}$ ergs/sec (Miley et al. 1975), while that of the jets was estimated to be $L_j = 5 \times 10^{39}$ ergs/sec by OBR.

Miley et al. (1975) find that the spectral index, α (defined here such that $S \propto \nu^{\alpha}$) between 0.4 and 1.4 GHz steepens from about -0.4 near the nucleus to about -0.6 at 6' from the nucleus. The spectral index between 1.4 and 5.0 GHz steepens from about -0.6 to -1.1 over the same distance. The steepening is not constant with distance but flattens out near the end of the tail.

The fractional polarization at 1.4 GHz (at 23" x 30" resolution) increases from about 10% near the nucleus to about 40% at 6' from the nucleus (with somewhat higher values at 5 GHz). Miley et al. (1975)

derived a foreground rotation measure of 44 or -36 rad m^{-2} (depending on whether the $n\pi$ ambiguity is taken to be 0 or $-\pi$) and suggest that the projected magnetic field is oriented along the tails. The magnetic fields (estimated assuming equipartition) and the model dependent estimate of the internal thermal particle densities in the tails are $B \sim 3\text{-}7$ μG and $n \sim 10^{-3} - 10^{-4}$ cm^{-3}, respectively.

Theoretical models for NAT radio sources

Through an unusual coincidence, the tails of the first four discovered NATs pointed away from a compact radio source in a nearby galaxy. These sources were NGC 1275 (3C 84) in the case of NGC 1265 and IC 310, 3C 129.1 in the case of 3C 129, and 5C 4.85 in the case of 5C 4.81 in the Coma cluster (Willson 1970). Hill and Longair (1971) developed a model based on the suggestion of Ryle and Windram that these galaxies were somehow interacting. Hill and Longair suggested that a supersonic flow of particles and magnetic fields ejected by NGC 1275, 3C 129.1 and 5C 4.85 was responsible for the radio emission of the corresponding NAT sources. The idea was that the turbulent flow past the galaxies would accelerate particles, amplify the magnetic field, and create the observed radio structure.

Miley et al. (1972) suggested an alternate explanation, based on their own higher resolution observations of the Perseus cluster and 3C 129. They detected an additional galaxy in the Perseus cluster associated with Chincarini and Rood's (1971; CR) galaxy 15. The tail of this source pointed towards NGC 1275, and thus contradicted the initial pattern. Furthermore, the observations of NGC 1265 and 3C 129 showed a

double structure in the head which was suggestive of a distortion of the symmetric structure more commonly seen in more luminous radio sources. Chincarini and Rood (1971) had shown that NGC 1265 has a large radial velocity (~2200 km/sec) with respect to the cluster mean. This led Miley et al. to suggest that tailed sources are radio sources in their own right. They suggested that these galaxies have a fairly high velocity through the ICM and that ram pressure from the ICM created the observed radio tails. Wellington et al. (1973) presented a model for NGC 1265 in which "blobs" or clouds of radio wave emitting plasma were ejected from the galaxy with a velocity twice that of the galaxy. The blobs were decelerated by ram pressure and came to rest after following a trajectory that reproduced the tail structure quite well. The more sophisticated theories discussed below are all based to some extent on this pioneering work.

Independent plasmons. The first detailed model of the morphology and spectral index and polarization distributions in NAT sources was the independent plasmon model of Jaffe and Perola (1973; JP). They supposed that identical blobs or clouds of relativistic particles, thermal particles, and magnetic fields (called plasmons by Pacholczyk and Scott 1976; PS) were ejected at supersonic velocities from the galactic nucleus. They assumed that the intracluster gas streamed freely through the galaxy (i.e., the parent galaxy did not possess a significant interstellar medium). The plasmons were decelerated by ram pressure at a rate

$$\frac{dv_p}{dt} = -(3/4)\left(\frac{\rho_{icm}}{\rho_p}\right)\frac{v_p^2}{r_p}, \qquad (1.4)$$

where ρ_{icm} is the density of the intracluster medium, and ρ_p, v_p, and r_p are the plasmon mass density, velocity, and radius, respectively. The plasmon will travel out to a stopping distance given by

$$D = (2/3)\left(\frac{\rho_{icm}}{\rho_p}\right) r_p \quad . \qquad (1.5)$$

The trajectory of the plasmons is given by

$$x = -y\cot(\theta) - D\cos(\theta)\ln(1-y/D\sin(\theta)), \qquad (1.6)$$

where v_e is the plasmon ejection velocity, v_g is the galaxy velocity, $\theta = \arctan(v_e/v_g)$, x is the distance behind the galaxy along its direction of motion, and y is perpendicular to x. JP obtained a trajectory for the plasmons which fit the existing low resolution observations of the structure of 3C 129 quite well.

The plasmons were initially confined by the external ram pressure $\rho_{icm}\ v_p^2$. As the plasmons slowed, the ram pressure decreased and the plasmons expanded until they came into pressure equilibrium with the thermal gas. In this model, the radius of the plasmons increases by the factor $\gamma^{1/4}\ M^{1/2}$, where γ is the ratio of specific heats (or adiabatic index), and M is the plasmon Mach number. For their fit to 3C 129, this factor is about 3, and adiabatic losses are substantial. The adiabatic losses shift the frequency of the break in the spectrum (due to radiative losses) to lower frequency. The predicted spectral index

steepened (with distance from the nucleus) much faster than is observed in 3C 129. JP recognized that this problem could be solved in one of two ways. They could invoke *in situ* particle acceleration or they could refuse to allow the radiating particles to experience adiabatic losses. In their second model, they attempted to prevent adiabatic losses by injecting the plasmons into a strong magnetic field tied to the nucleus of the galaxy.

They envisioned a dipole magnetic field stretched out behind the galaxy similar to the earth's magnetic tail. JP argued that the particles would be tied to a rigid magnetic field, thus eliminating adiabatic losses. They also suggested that scattering of the particles by plasma waves would reduce the plasmon expansion velocity to the Alfvén speed. Then, considering only synchrotron and inverse Compton losses, they were able to obtain a reasonable fit to the observed flux density and spectral index variations along the tails in 3C 129. They also predicted that because the magnetic field in the two tails came from opposite poles of the dipole field, the internal Faraday rotation in the two tails would have opposite signs. Miley *et al.* (1975) suggested that there was some evidence for this in NGC 1265. However, Pacholczyk and Scott (1976) pointed out that contrary to the assumption of JP the particles would still experience adiabatic losses due to the particle-wave interactions. Thus, the magnetospheric tail model of JP could not reproduce the observed spectral index structure in 3C 129. The idea of a magnetospheric tail was discarded in subsequent theoretical work.

Cowie and McKee (1975; CM) presented a modification of the first model of JP. They suggested that the plasmons were ejected with a Mach number of order one. The external thermal pressure would be comparable to the ram pressure and the plasmons would expand only slightly as they are slowed, minimizing adiabatic losses. CM noted that the time scale for the growth of Raleigh-Taylor and Kelvin-Helmholtz instabilities was comparable to the plasmon stopping time ($T = D/v_p$). However, this was discussed only in the context of connecting the plasmon and external magnetic fields, thus allowing particles to diffuse from the plasmon. Another important contribution of CM was their discussion of buoyancy and the bending of the tails in 3C 129 and NGC 1265. They suggested that heating of the material behind the galaxy either by a bow shock or by the plasmons themselves would produce a hot, low density tail. The buoyant acceleration (which produces a parabolic shape) is

$$a = (G\, M_{cl}\,(R)/R^2)\,(\rho_{icm} - \rho_t)/\rho_t \qquad (1.7)$$

where R is the distance to the cluster center, $M_{cl}\,(R)$ is the mass interior to R, and ρ_t is the density of the tail. The tail is accelerated until the ram pressure balances the buoyancy force and a terminal velocity is reached

$$v_t = \frac{[G\, M_{cl}\,(R)\, \pi\, r_t\, (\rho_{icm} - \rho_t)]^{1/2}}{[R^2\, 2\, \sin\phi\, \rho_{icm}]^{1/2}} \qquad (1.8)$$

where r_t is the radius of the tail and ϕ is the angle between the initial path and the radial direction.

Pacholczyk and Scott (1976) considered a model in which the plasmons became turbulent due to the development of Raleigh-Taylor and Kelvin-Helmholtz instabilities. PS suggested that both in situ betatron and second order Fermi acceleration would occur. Based on their interpretation of the low resolution data available at the time, they proposed a model consisting of essentially four regimes in which differing processes dominated. Synchrotron losses were assumed to exist in all four regimes. In the first regime (roughly the first 20 kpc behind the nucleus), the plasmons would expand and lose energy adiabatically. However, they expected the betatron mechanism to dominate here, causing the flux density to increase and the spectral index to flatten. In the second regime (20 to 60 kpc from the nucleus), the second order Fermi mechanism would operate instead of the betatron mechanism, but would not be sufficient to compensate for the adiabatic losses. The flux density would decrease and the spectral index would steepen in this region. Between ~60 and 170 kpc the expansion losses would be negligible and the Fermi acceleration would just balance the synchrotron losses, keeping both the flux density and spectral index constant. The turbulence died out by 170 kpc, stopping the Fermi acceleration and allowing the spectral index to steepen in the fourth regime (beyond ~170 kpc). As the turbulence died out, the magnetic field in the tail became more ordered (through shearing by the external medium) and the fractional polarization increased. PS were able to obtain reasonable fits of their model to the gross features of the data beyond the first regime. However, this is not too surprising given the number of free parameters.

Quasi-continuous flows. The following models are discussed in Chapter VII in great detail and are only summarized below.

Begelman, Rees, and Blandford (1979; BRB) presented a simple dynamical model for the ram pressure bending of a continuous beam. They suggested that a nonrelativistic twin beam is ejected from the galactic nucleus and interacts with the intracluster medium (ICM) which streams freely through the galaxy. The ram pressure from the ICM, $\rho_{icm}\, v_g^2$, creates a transverse pressure gradient of scale height, h, across the beam (in this model $h \sim r_b$, the beam radius). BRB assume that the beam velocity is constant, but allow the jet cross-section to increase with distance from the core. Ram pressure bending due only to the galaxy's forward motion is considered. The bending scale of the beam, R, is given by Euler's equation, i.e., in the nonrelativistic limit

$$R \approx h\, (\rho_b/\rho_{icm})\, (v_b/v_g)^2 \qquad (1.9)$$

if all quantities are roughly constant; where the subscripts b means beam, icm means intracluster medium, and g means galaxy. The geometry is sketched in Figure 1.2, adapted from BRB. BRB obtain a good fit of their model trajectory to the inner portion of the jets in NGC 1265, but find that the outer portions of the jets bend faster than their model predicts.

Baan and McKee (1983) have reconsidered the model of BRB and have applied it to NGC 1265, IC 708, and 1638+538. They kept the beam momentum flux and cross-section constant. They obtained good fits to the structure of IC 708 and 1638+538, but found that this simple model (i.e., keeping all parameters constant) does not quite work for

Figure 1.2

A sketch of the geometry (and definition of terms) in the Begelman, Rees, and Blandford (1979) model for the bending of continuous beams.

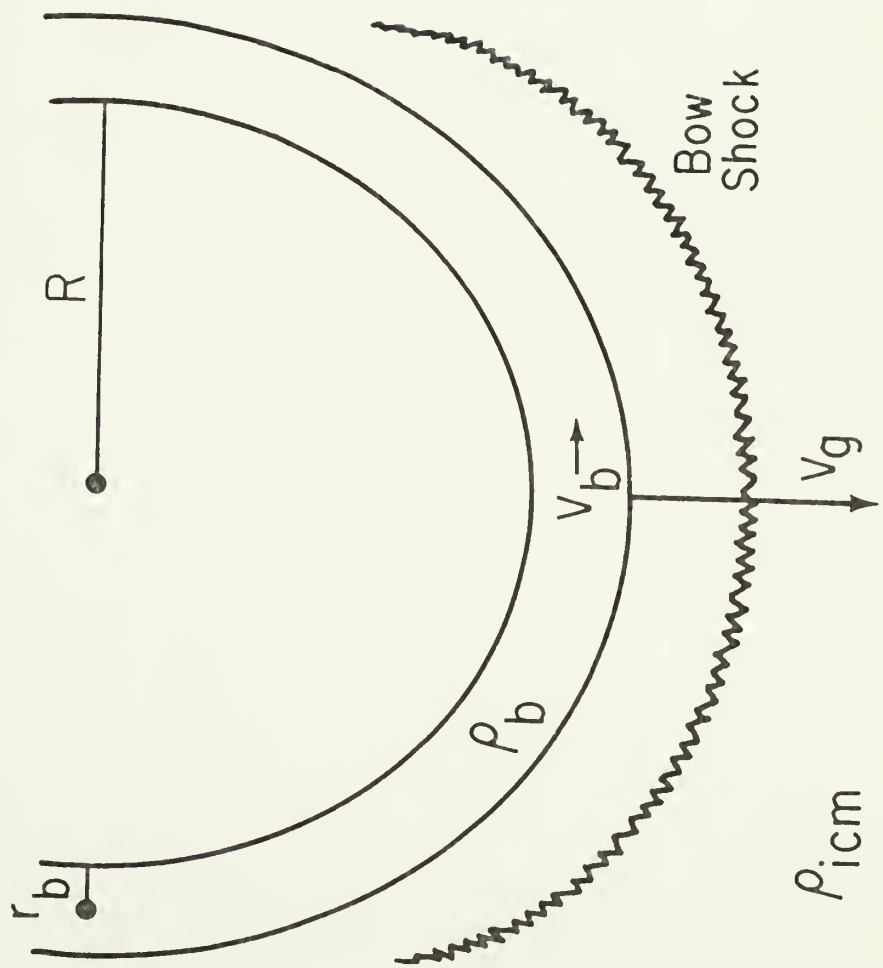
R
r_b
ρ_b
v_b
Bow
Shock
v_g
ρ_{icm}

NGC 1265. In order to fit the much faster bending in the outer portion of the jets, they introduced an increase in the ram pressure against the beam. They speculated that this is due to the jet moving from the interstellar medium of the galaxy (which shields the jets) to the intracluster medium (see discussion of the Jones and Owen model below).

An additional constraint on the BRB model is that the luminosity in the radio tails must ultimately come from the kinetic energy in the beams. If the bulk kinetic energy of the beam can be converted into radio emission with an efficiency, ε, the luminosity of the tails is given by

$$L_k \approx (1/2)\ \pi\ \rho_b\ r_b^2\ v_b^3\ \varepsilon \quad . \tag{1.10}$$

Thus, not only must the beam be bendable, but it must also power the radio emission. In the case of NGC 1265, both of these criteria can be met in the BRB model for a beam Mach number $M \sim 5$, velocity $v_b \simeq 2\times10^3\ \varepsilon^{-1}$ km/sec, and particle number density $n_b \sim 9\times10^{-2}\ \varepsilon^2\ cm^{-3}$.

Jones and Owen (1979) presented a somewhat different model for the bending of the jets in NGC 1265, based on the probable existence of an interstellar medium (ISM) within the galaxy. The fate of the ISM in an elliptical galaxy, which moves through the intracluster medium at transsonic velocity ($M \sim 1$), was investigated by Gisler (1976), Lea and De Young (1976), and Shaviv and Salpeter (1982) among others. They find that 80-90% of the ISM is swept out of the galaxy on a time scale of $\sim10^9$ yrs. However, JO point out that in the inner portion of the galaxy a significant ISM may still remain. They estimate that the radius of this region is about $r_s \sim$4-50 kpc ($r_s \sim$ 10 kpc for NGC 1265).

Since this is comparable to the size scale over which the jets are bent in many NAT sources, JO suggest that the ISM may be important in the formation of these sources.

In their model the beams are bent by a transverse pressure gradient in the ISM which is weaker than in the case of the "naked" beam of BRB by the factor r_b/r_s. The bending scale length is now given by

$$R \simeq r_s \, (\rho_b/\rho_{icm}) \, v_b/v_g)^2 \quad . \tag{1.11}$$

In the context of the JO model, $R \simeq r_s$ and thus $\rho_b \, v_b^2 \simeq \rho_{icm} \, v_g^2$. In this model the beam is expected to have a Mach number $M \simeq 1$. The beams need only power the observed radio emission in the beams themselves and not the radio emission from the tails. For NGC 1265 this requires a beam velocity of $v_b \simeq 600 \, \varepsilon^{-1}$ km/sec and $n_b \simeq 10^{-2} \, \varepsilon^2$ cm^{-3}.

JO suggest that the energy to power the radio tails is provided by the turbulent wake behind the galaxy. The available power is

$$L_g \simeq \pi \, \rho_{icm} \, v_g^3 \, r_s^2 \simeq 5 \times 10^{43} \text{ ergs/sec} \quad . \tag{1.12}$$

At 1% efficiency, this is sufficient to provide the observed radio emission.

Jones and Owen pointed out that the high resolution observations of NGC 1265 by OBR pose severe problems for the independent plasmon model (Wellington et al. 1973, JP, PS). Because the initial sizes of the plasmons near the nucleus were so small (as seen on the VLA maps) the adiabatic losses incurred during the expansion necessary to reach the sizes observed in the tails would be enormous. In order to power the observed radio emission, the plasmons would have to be ejected so

frequently that the distance between plasmons would be comparable to their size. The plasmons would merge together, approximating a continuous flow.

Christiansen, Pacholczyk and Scott (1981; CPS) suggested that this difficulty could be overcome in the case of NGC 1265 by a modification of the "multiple plasmon in a channel" model (Christiansen 1973; Christiansen, Pacholczyk, and Scott 1977). In the CPS model the energetic requirements of the plasmons are considerably reduced, if they are allowed to move through an evacuated channel in the ISM. The channel will be maintained if the time scale between plasmon ejections $t_p \approx d/v_p$ is less than the relaxation time of the channel $t_c \approx r_c\, c_{s,icm}$, where d is the distance between plasmons, r_c is the channel radius and $c_{s,icm}$ is the sound speed in the ISM. The same restrictions on the time averaged momentum flux through the channel exist as in the JO model. As in the JO model the power for the tail luminosity is provided by turbulence in the galactic wake. For NGC 1265 the required parameters are $v_p \approx 3\times10^4$ km/sec and $n_p \sim 10^4\ \varepsilon^2$ cm^{-3}.

1.3 The Project

The interpretation of the observations of the structure of NAT sources is strongly affected by projection effects (e.g., Reynolds 1980) as well as by the available sensitivity and resolution. For example, in the most recent detailed statistical study of tailed sources, Valentijn (1979a) found that given an assumed random distribution of opening angles between the tails, approximately five times as many single tail

sources are observed as would be expected from simple projection effects. However, of the 27 NATs in his study, about 20 were observed with resolutions of $\geq$ 23", which were insufficient to resolve the twin jet structure. The number of high resolution, high sensitivity maps presently available is too small to allow a determination of which of the observed properties are due to projection, resolution effects or quirks in the individual objects, and which are physical characteristics of this class of object. One goal of this thesis is to produce a high resolution, high sensitivity maps of a reasonable large sample of NAT sources. This sample, although not complete, is hopefully representative of NAT sources in rich clusters and is used to answer some of the interesting questions about these objects.

A large part of the sample of NATs studied in this thesis came from a survey of radio sources in a complete sample of Abell clusters currently in progress by Owen and collaborators. All radio sources stronger than 100 mJy at 1.4 GHz within 0.5 Abell radii A_c of the cluster center which were discovered in a survey with the 300-foot (91-m) telescope (Owen 1974 and Owen et al. 1982a) are being mapped with the VLA. Approximately 200 extended sources have been observed so far in the "snapshot" (i.e., ~5-10 minute observation) mode at 1.4 GHz with about 5 arcsec resolution. Of these 200 sources 21 appear to have a NAT morphology. Optical identifications of these sources were obtained using the Palomar Sky Survey prints in order to confirm the NAT nature of the source. This procedure for identifying NAT sources is somewhat subjective and introduces some selection effects (to be discussed in more detail in Chap. IV).

The 21 potential NAT sources found in the survey plus 25 additional sources from the literature provide the sample of NAT sources observed wtih the VLA for this thesis. Most sources were observed for about one hour at 21 cm in the A array (1."2 resolution). Some sources were observed in the B (4") and C (12") arrays because of sensitivity and resolution considerations. Additionally, a few were observed at 6 cm to reduce confusion from nearby strong sources or to achieve higher resolution. The basic observation and reduction techniques used on the data are given in Chapter II. The data from the VLA observations are presented in Chapter III. The global and statistical properties of NATs in Abell clusters are discussed in Chapter IV.

The second goal of this thesis is to study one NAT source in as much detail as possible. NGC 1265 is perhaps the NAT source best suited to such a study. Its symmetry suggests that projection effects are minimal and that the physics of the bending of beams can be applied in a straightforward manner. It's relative closeness (~72 Mpc, assuming H_o = 75 km sec^{-1} Mpc^{-1} allows the best linear resolution (0.16 kpc at 6 cm in the A array) of any NAT source. It is clear that detailed, multi-frequency, high resolution observations of the total intensity and polarization structure are needed in order to test the various theoretical models that have been applied to NGC 1265. The source was observed at 21 cm in the A (~21 hrs) and C (~2 hrs) arrays, at 6 cm in the A (~5 hrs), B (~6 hrs) and D (~2 hrs) arrays, and at 2 cm (~10 hrs) in the C array. The observations are presented in Chapter V and discussed in Chapter VI. The thesis concludes with a detailed discussion of the physics of bent beams, a comparison of the continuous

beam and multiple plasmon in a channel models, and finally an overview in which the fundamental questions of Life, the Universe and Everything are discussed (Chap. VII).

CHAPTER II

OBSERVATIONAL TECHNIQUES

In this chapter a brief description of the NRAO Very Large Array (VLA) is given. The basic principles of interferometer calibration and image construction and their implementation at the VLA are discussed and some of the terminology which will be used in this thesis is introduced. Additional details of the data reduction are given in Chapters III and V for the NAT survey and NGC 1265, respectively.

2.1 The VLA

The VLA has been described by Thompson et al. (1980) and Hjellming et al. (1982). The following discussion draws heavily on these references.

The Very Large Array is located on the Plains of San Augustin in West-central New Mexico. It is an aperture synthesis radio telescope capable of mapping the sky down to a declination of -45°, with a resolution better than that of optical telescopes. The array consists of 27 fully steerable alt-azimuth telescopes 25 meters in diameter. The feed system is Cassegrain with an asymmetric subreflector with a hyperbolic surface. There are four feeds (18-21 cm, 6 cm, 2 cm, and 1.3 cm) which lie in a ring of radius 98 cm (with respect to the main reflector axis) at the Cassegrain focus. Two orthogonal polarizations, either linear or circular, are available. The 18-21 cm feed is a corrugated horn illuminating a hybrid lens of dielectric and waveguide elements. The 6-cm feed is also a corrugated horn with a dielectric

lens. The 2 and 1.3-cm feeds are multimode horns. The subreflector can be rotated under computer control to focus the incoming radiation to any of the four feeds. The antenna efficiencies are 50%, 65%, 54%, and 46% at 18-21 cm, 6 cm, 2 cm, and 1.3 cm, respectively.

The antennas are distributed along three radial arms forming an equiangular "Y". The northern arm is at an angle of 5 degrees to the north-south direction and is 19 km long. The southeast and southwest arms are 21 km long. The four standard antenna configurations are called the A, B, C, and D arrays, with the antennas having the widest spacings in the A array. In order to optimize the coverage in the Fourier transform (i.e., u,v) plane of the array, the distance of the n^{th} antenna on each arm from the center was chosen to be proportional to $n^{1.716}$.

The 27 antennas form 351 antenna pairs, each of which measures the fringe visibility at two points in the spatial frequency (u,v) plane. As the earth rotates, the data loci sweep out 702 elliptical tracks. The sensitivity, resolution, and confusion limits of the 27-antenna array are given in Table 2.1 from Hjellming et al. (1982).

At each antenna, the RF signals are first fed into low-noise front ends. The signals are then converted into 50 MHz bandwidth intermediate frequencies (IF's A and B in one polarization and C and D for the other) at 1325, 1425, 1575, and 1675 MHz, respectively. (Not to be confused with the array configurations A, B, C, and D.) The data in this thesis were taken at the time when only the A and C IF's were implemented. The data are communicated through a buried 6-cm diameter, circular waveguide with a 52-ms cycle. During 1 ms of this cycle, control and timing data

Notes to Table 2.1

*RMS sensitivity in brightness temperature for an untapered map is given approximately by

$$\Delta T \simeq (1.46\ \lambda^2/\theta_1\theta_2)\ \Delta S,$$

where θ_1 and θ_2 are the half-power synthesized beam widths in arcseconds, λ is the wavelength in centimeters, and ΔS is the root-mean-square sensitivity per beam area in milli-janskys.

**Dynamic range is extremely dependent on declination, time of day, season, and frequency of calibration.

Table 2.1

Sensitivity, Resolution and Confusion Limits with 27 Antennas

Frequency	1.34 - 1.73	4.5 - 5.0	14.4 - 15.4	22.0 - 24.0	GHz
Wavelength	22.4 - 17.3	6.67 - 6.00	2.08 - 1.95	1.36 - 1.25	cm
Band Designation	L	C	U	K	
System Temperature	60	60	300	400	K
RMS Sensitivity in 10 Minutes (50 MHz bandwidth)	0.13	0.10	0.60	1.0	mJy
RMS Sensitivity in 12 Hours (50 MHz bandwidth)	0.015	0.012	0.07	0.12	mJy
Untapered Brightness* Temperature (A configuration)	6.9	5.5	34	54	K
Dynamic Range without Self-calibration**	100	50	10-20?	10?	
Antenna Beam Size (FWHM)	30'	9'	3.7'	2'	
Brightest Source Expected in Antenna Beam	100	2.3	<0.1	<0.01	mJy

are sent from the control building to the antenna. During the remaining 51 ms, monitor data, LO information, and the IF output signals are sent from each antenna to the control building. A 600-MHz signal is transmitted from the master local oscillator in the control building to the phase-locked local oscillator at each antenna and back again. Phase corrections to each antenna IF are determined by measuring the round-trip phase difference.

Once in the shielded room of the control building, the IFs are digitized and delayed (in 10 nanosecond increments), putting the data from each antenna onto a common time system. The digital signals are cross-correlated and self-multiplied. These correlated signals (visibilities) are then normalized and vector averaged over 10-second intervals. Some on-line corrections are applied and the data are sent to the off-line computer system for additional calibration and editing.

2.2 Calibration

In this section the techniques used in the calibration of the VLA data in this thesis are described. Some of the discussion is taken from Hjellming (1982) and Bignell (1982a).

Total intensity calibration

Let the uncalibrated data measured by two antennas, i and j, be represented by the complex number with amplitude, A, and phase, ϕ,

$$V''_{ijp} = A''_{ijp} \exp(i\phi_{ijp}), \tag{2.1}$$

where p refers to the polarization (e.g., RR, LL, RL, and LR; where R and L refer to right- and left-circular polarization, respectively). We will denote the fully calibrated data using unprimed quantities. Then

$$V_{ijp}(t) = G_{ijp}(t)\, V''_{ijp}(t), \tag{2.2}$$

where

$$G_{ijp} = a_{ip}\, a_{jp} \exp\left[i(\phi_{ip} + \phi_{jp})\right] + E_{ijp}. \tag{2.3}$$

The G's are antenna-based complex gains which are empirically determined, the a's and ϕ's are the amplitudes and phases of the individual antenna gains, and E_{ijp} are closure errors (Hjellming 1982). Given n antennas, at any time there are n(n-1)/2 measurements of the visibility function in each polarization, but only n amplitude and n-1 phase calibration functions to be determined (one antenna, the reference antenna, is assumed to have zero phase). Thus, observations of a strong point source can be used to determine the antenna based complex gains, i.e.,

$$G_{ijp}(t) = V_{ijp}(\text{calibrator})/V''_{ijp}(t). \tag{2.4}$$

The program ANTSOL solves equation 2.4 for the complex gains using the point source calibrator data. A list of the flux densities, accurate positions, and remarks on the structure of about 700 compact radio sources has been compiled by the VLA staff (see e.g., Perley 1982). An unresolved calibrator, located within 10 degrees of the source (or much closer, if possible) was chosen from this list. For nearly all the observations of NGC 1265, the nearby calibrator (1/2 degree away!) 3C 84 was used. The calibrator was observed every 10-25

minutes (with the shorter times at 2 cm and the longer times at 20 cm). The assumption was made that the antenna amplitudes and phases are fairly stable during that time. Using the program GTBCAL, the complex gains were averaged over some time interval (typically 1 to 2 hours), or, if there were noticeable gradients in the phase, linearly interpolated and applied to the visibility data of the program source.

The flux-density scale. The data were tied to the flux-density scale of Baars et al. (1977) through observations of either 3C 286 (1328+307), or 3C 48 (0134+329). These sources are partially resolved by the VLA at all frequencies and the (u,v) range used in scaling the flux densities must be restricted. Because it can also be used to calibrate the polarization position angle (see next section), 3C 286 was used preferentially. However, during some observing runs, neither 3C 286 or 3C 48 were above the horizon. In that case, one of the secondary calibrators (0212+735, 0836+710, or 1803+784), whose flux densities are frequently monitored by VLA staff, was used. The flux densities of 3C 286 and 3C 48 at the observing frequencies used in this thesis are given in Table 2.2.

Table 2.2

Calibrator Flux Densities

Frequency (MHz)	3C 286 (Jy)	3C 48 (Jy)
1413	14.77	15.82
1452	14.57	15.48
4873	7.42	5.37
4885	7.41	5.36
14915	3.46	1.73

Polarization calibration

The simplified equations for the interferometer response, R, to a point source of polarized radiation are:

$$R_{RiRj} = 1/2\ G_{Ri}\ G^*_{Rj}\ (I+V) \tag{2.5}$$

$$R_{LiLj} = 1/2\ G_{Li}\ G^*_{Lj}\ (I-V) \tag{2.6}$$

$$R_{RiLi} = 1/2\ G_{Ri}\ G^*_{Lj}\ [(D_{Ri} + D^*_{Lj})\ I + (Q + iU)\ \exp(-2i\psi)] \tag{2.7}$$

$$R_{LiRj} = 1/2\ G_{Li}\ G^*_{Ri}\ [(D_{Li} + D^*_{Rj})\ I + (Q - iU)\ \exp(2i\Psi)]\ , \tag{2.8}$$

where the subscripts R and L refer to right- and left-hand circular polarization, i and j are two antennas, * signifies complex conjugation, the G's are the complex gains, the D's are the instrumental polarizations, I, Q, U, and V are the Stokes parameters, and ψ is the parallactic angle (Bignell 1982a). It is assumed that the bandpasses of the antennas are identical, the point source is at the phase center of the interferometer and is located on the principal electrical axis of the antenna, the D's are constant over the duration of the observations, and the second order terms in Q, U, V, D_R, and D_L are negligible.

The task of polarization calibration is to determine the instrumental polarizations, D_R and D_L, the phase difference between the complex gains G_R and G_L, and to correct for the effects of ionospheric Faraday rotation (at 20 cm). A weakly polarized point source was tracked over a sufficiently long time that there was a large variation

in the parallactic angle. Then a least squares algorithm (POCAL) was used to solve for both the source polarization and the instrumental terms. The calibration of the absolute polarization position angle is achieved by observing either of the calibrators 3C 286 or 3C 138, whose position angle is known (33° and -12°, respectively, at 6 and 20 cm). 3C 138 is also partially unsolved by the VLA and a limited (u,v) range must be used in its calibration. One of these calibrators was usually observed twice (two 5-minute scans several hours apart) during the longer observing runs. Having more than one observation of the polarization calibrator is useful for a couple of reasons:

(1) To insure that calibration is obtained in the event of a power or instrument failure which wipes out part of the observing run;

(2) To check the consistency of the ionospheric Faraday rotation corrections (e.g., during the 20-cm, A configuration observations of NGC 1265 both 3C 286 and 3C 138 were observed).

The correction to the right-left (or AC) phase difference was determined and added to the phase of the complex gains and complex antenna polarizations. It is necessary that the AC phase difference of the reference antenna remains constant with time.

Ionospheric Faraday rotation can effect polarization measurements at long wavelengths (e.g., a rotation of ~10°-20° at 20 cm). The position angle of the polarization will be rotated by an amount proportional to $\int N_e B_L dl \lambda^2$, where N_e is the free electron density, B_L is the magnetic field component along the path of propagation, dl is the differential path length, and λ is the wavelength. The program FARAD (Bignell 1982b) at the VLA calculates a correction for Faraday rotation

using measurements of the ionospheric electron density made available by the World Data Center in Boulder, Colorado. A model for the earth's magnetic field consisting of a dipole plus multipole expansion terms is used. For some of the observations in this thesis, the error in the calculated corrections was estimated by comparing several corrected measurements of a polarization angle calibrator. This error was found to be ~4°.

2.3 Image Construction

In this section, the basic principles and techniques through which maps of the sky are made from the calibrated (u,v) data are discussed. These techniques, as implemented in the NRAO Astronomical Image Processing System (AIPS) software, were used in the construction of the radio source maps presented in this thesis.

Mapping

Once the data have been calibrated an image of the sky within the antenna primary beam can be constructed. The previously used notation has been appropriate to the discussion of antenna-based quantities. In the discussion of mapping (based on Sramek 1982), use will be made of the elegant Fourier transform relationships between the data (u,v) plane and the map (x,y) plane. Equation 2.1 (for calibrated data now) can be rewritten in the following notation:

$$V(u,v) = A(u,v) \exp (i2\pi (ux + vy)), \qquad (2.9)$$

where u and v are coordinates which represent the projection onto the sky of the antenna pair spacing.

The fundamental relationship upon which interferometry is based is that the sky brightness distribution (multiplied by the antenna primary beam), I'(x,y), is the Fourier transform of the visibility, V(u,v), observed by the interferometer (e.g., Fomalont and Wright 1974):

$$I'(x,y) = \iint V(u,v) \exp (i2\pi (ux + vy)) \, dudv. \qquad (2.10)$$

The most straightforward procedure is to evaluate 2.10 at the individually sampled points. However, the number of data points in a long synthesis observation can approach $N \sim 10^6$. The computational time would be much too long, so in general a Fast Fourier Transform (FFT) algorithm is used. This reduces the number of multiplications from $\sim N^4$ to $N^2 \log (N^2)$. However, the FFT requires regularly spaced data on a rectangular grid with sides which are some power of 2 (i.e., 1024).

At the VLA the calibrated visibility data points are convolved with a continuous function, C(u,v). A sinc times exponential was used for all the data presented in this thesis. The data is then resampled at regular grid points. Following Sramek (1982), the gridded visibility data can now be represented by

$$V(u,v) = III(u,v) \left[C(u,v)**(S(u,v)V'(u,v))\right], \qquad (2.11)$$

where III(u,v) is the shah function, S(u,v) is the sampling function, C(u,v) is the convolving function, ** represents convolution, and V'(u,v) is a continuous visibility function. The following Fourier transform pairs (e.g., Sramek 1982) will be used:

$$V(u,v) \quad \longleftrightarrow \quad I(x,y)$$

$$S(u,v) \quad \longleftrightarrow \quad s(x,y)$$

$$C(u,v) \quad \longleftrightarrow \quad c(x,y)$$

$$III(u,v) \quad \longleftrightarrow \quad III(x,y).$$

Then applying the convolution theorem (Bracewell 1978) to equation 2.11 gives the "dirty map," I(x,y), of the sky brightness structure:

$$I(x,y) = III(x,y)**\left[c(x,y)(s(x,y)**I'(x,y))\right]. \qquad (2.12)$$

Making the approximation that c(x,y) = 0 outside the primary map field (i.e., ignoring the convolution with III(x,y)) and dividing by c(x,y) (to correct for the effects of the convolution) gives

$$I(x,y) = B(x,y)**I'(x,y), \qquad (2.13)$$

where B(x,y) = s(x,y) is the point source response or synthesized beam, and I'(x,y) is the continuous sky brightness distribution (eq. 2.10). The process of deconvolving the beam from the dirty map or "CLEANing" is described below.

Weighting and tapering in the (u,v) plane. The sampling function in equation 2.11 can be written

$$S(u,v) = \Sigma \; W_i T_i \quad \delta(u-u_i, v-v_i), \qquad (2.14)$$

where W_i is a weight and T_i is a taper of the i^{th} visibility point. The (u,v) coverage of the VLA is, of course, not uniform; the shorter spacings are filled preferentially. Giving each visibility point equal weight (natural weighting) makes optimum use of the data in terms of

signal-to-noise. However, because of the larger amount of data per grid cell at the shorter spacings, the longer spacings are weighted lower with respect to the shorter spacings, and the full resolution available in the data is not attained. For this reason, an alternate weighting scheme (uniform weighting) was used. In uniform weighting, each grid point (see eq. 2.11) rather than each visibility point is given equal weight. In this case, each visibility point is weighted by the inverse of the total number of points (within some area of the (u,v) plane) which contributes to a given grid point. This results in a map with a slightly higher noise level, and with a higher resolution than a map produced using natural weighting.

Occasionally it is desirable to taper the (u,v) data. This is done by multiplying the visibility data with a gaussian of unity amplitude centered at (u,v) = (0,0). In the AIPS software the distance (in thousands of wavelengths, $k\lambda$) out to weight of 0.3 is specified by the user. This has the effect of decreasing the resolution and increasing the sensitivity to larger scale, lower surface brightness structure.

CLEAN

The task of image restoration is concerned with the solution of the convolution equation 2.13. This is usually done by assuming a model for the true brightness distribution and then solving for the parameters of the model. The main problem is that the solutions to equation 2.13 are not unique. There is a class of homogeneous solutions called "invisible distributions" (Bracewell and Roberts 1954). These "ghosts" contain only the unmeasured spatial frequencies so that if Z is a ghost then

B**Z=0. If I is a solution to 2.13, and α is a constant, then I+αZ is also a solution.

One solution to the convolution equation can be obtained by making the assumption that the radio source can be represented by a number of point sources in an otherwise blank field. The CLEAN algorithm (Hogbom 1974, Schwarz 1978) is an iterative procedure which determines the position and strength of the point sources. At the VLA a version of CLEAN developed by Clark (1980) is used. The algorithm consists of two cycles, the major and the minor cycles. In each minor cycle, the inner portion of the beam containing the highest sidelobes is chosen. The highest point in the map within some "CLEAN window" is found, multiplied by the beam patch times some scale factor (called the loop gain, typically ~0.1 for the observations in this thesis) and subtracted from the map. This continues until there are no points remaining greater than the highest sidelobe outside the beam patch times the peak in the map at the start of the current major cycle. During the major cycle the point sources (called CLEAN components) are convolved with the full beam and subtracted from the map. This convolution is more efficiently performed through the use of FFTs. The FFT of the CLEAN components is multiplied by the FFT of the beam and then transformed back again. The procedure alternates between the minor and major cycles until the desired level of CLEANing has been achieved. This can be chosen to be at the point where all the flux density in the map is represented in the CLEAN components or when the sidelobes of the remaining points in the map are less than the root-mean-square noise in the map. The CLEAN components are then convolved with a "CLEAN beam" which is usually

chosen by fitting an elliptical gaussian to the central region of the dirty beam. This has the effect of suppressing the higher spatial frequencies which are not present in the data and are not well estimated by the CLEAN algorithm. As the final step, the residual map is then added to the convolved CLEAN components.

Though there are some theoretical problems with CLEAN and its choice of solution to the convolution equation (Cornwell 1982a), in practice it seems to work rather well (cf., Schwarz 1978, Cornwell 1983a). CLEAN was used on all the maps presented in this thesis.

Self-calibration

Earlier it was noted that because there are only n complex gain errors (one for each antenna), but n(n-1)/2 complex visibility measurements, it is possible to solve for the antenna gains as a function of time using measurements of a point source calibrator. However, if there is a good model for the visibility function of the program source, then the same principle can be used to solve for the complex gains on a much shorter time scale (limited only by the signal-to-noise ratio of the observations). This process is called self-calibration and is useful mainly for correcting phase errors due to short time-scale fluctuations in the atmosphere. Maps with a dynamic range (the ratio of the peak in the map to the root-mean-square noise) in excess of 1000 can be produced using this technique. The procedure used at the VLA (developed by Schwab 1980) minimizes the sum of the squares of the residuals:

$$S = \Sigma_{time} \Sigma_{baseline} W_{ij} |V_{ij}\ (model)|^2\ |X_{ij} - G_i G_j|^2 , \qquad (2.15)$$

where $X_{ij} = V_{ij}(obs)/V_{ij}(model)$, the G's are again the complex antenna gains, and W_{ij} is a weight (Cornwell 1982b). First, a model of the source is made. Generally, the choice of the CLEAN components up to the first negative one is a good model. This should allow a good approximation of the source without including any spurious features in the model. The complex gains are then solved for. It is possible to restrict the solution to the antenna phases, and this is generally done for the first few iterations of self-calibration. The corrected visibility function is used to produce a new map, which is CLEANed to produce a new model for the source which is input into the next iteration of self-calibration. This can be continued until the self-calibration converges (i.e., the corrections become negligible and the map stops improving).

One problem with allowing the antenna phases to become free parameters is that the absolute positional information is lost. Thus, care must be taken in comparing self-calibrated maps.

Special problems and techniques

Many of the instrumental and data problems which can effect a map are discussed by Clark (1981, 1982), Fomalont (1982), and Ekers (1982). In this section a few problems which are relevant to the data presented in this thesis are discussed.

"Bandwidth smearing." The differential time delay, τ, at frequency, ν, for a source at position (x,y) with respect to the phase center, measured by a two-element interferometer with baseline coordinates (u,v) is given by (e.g., Fomalont and Wright 1974)

$\tau = (ux+vy)/\nu$. Thus, the different frequencies within the interferometer bandwidth, $\Delta\nu$, will have slightly different delays. If $\Delta\nu > 1/\tau$, the loss of correlation can cause problems in the map. The true visibilities of the source are multiplied by the Fourier transform of the interferometer bandpass shape which varies radially in the (u,v) plane (e.g., Perley 1981, Thompson 1982). This corresponds to a distortion of the synthesized beam. The convolution of the source with this distorted beam produces a smearing of the source structure along the line joining the source and the phase center (which is usually also the map center), and a decrease in the peak intensity. The total flux density of the source is unchanged. Figure 2.1 shows an extreme case of bandwidth smearing from the 21-cm A array observations of NGC 1265 (the source is 3C 84, with frequency ν = 1418 MHz, bandwidth $\Delta\nu$ = 25 MHz, beamwidth (FWHM) b = 1."2, and offset from the phase center θ = 30'). At present there is no software to correct for this effect, so the "cure" is prevention by using a small bandwidth. A "small" bandwidth (typically 25 MHz) was used for the observations presented in this thesis. The smearing and loss of peak intensity will then be only a few percent over a field of view of about an arcminute. The effect of bandwidth smearing on the observations of NGC 1265 is discussed in Chapter V.

Aliasing. Earlier the approximation was used that c(x,y), the Fourier transform of the convolving function, was zero outside of the primary map field. However, this requires that the convolving function be a sinc function evaluated over the entire (u,v) plane. This is never true. Because a FFT has been used on gridded visibility data, the map

Figure 2.1

A total intensity map of the point source 3C 84 showing the effect of "bandwidth smearing." The data are from the A configuration observations of NGC 1265 with an observing frequency of 1418 MHz, 25 MHz bandwidth, and a 1."2 FWHM beamwidth. 3C 84 lies ~30' to the southwest of NGC 1265, and its flux density has been reduced by the attenuation of the primary beam. The contour levels are -2.0, 2.0, 10.0, and 30 mJy/beam.

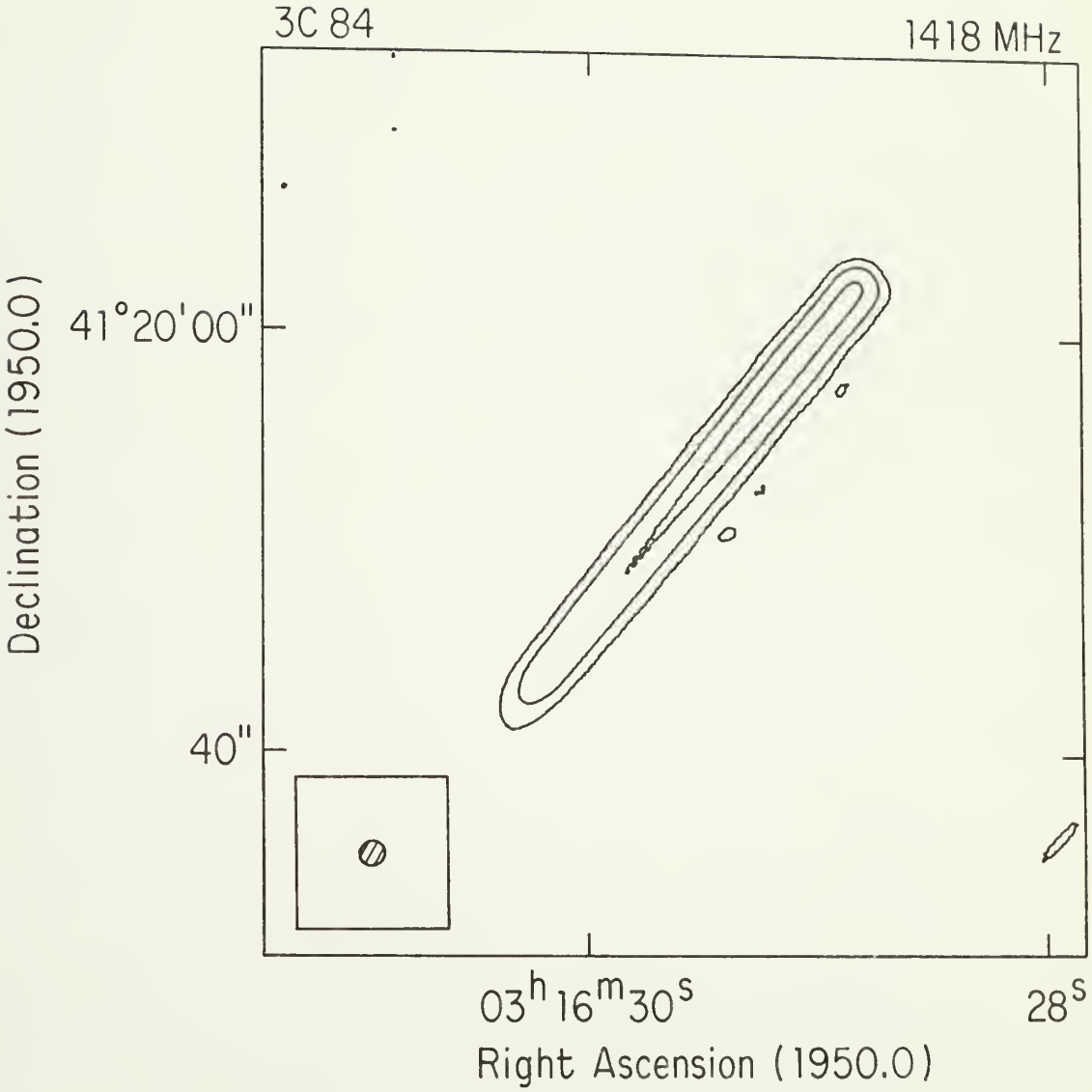
3C 84
1418 MHz
Declination (1950.0)
41°20'00"
40"
03h16m30s
28s
Right Ascension (1950.0)

includes a convolution with a shah function, III(u,v), which introduces aliasing. A source and/or its sidelobes present outside the map field will be reflected into the map. The convolution function used in the mapping program (a sinc multiplied by an exponential) suppresses aliasing quite well. A reduction of the intensity of an aliased source of a factor of 100 to 1000 at 2 to 3 map radii is achieved (Sramek 1982 and references therein). An additional procedure for dealing with an aliased source is simply to remove it from the visibility data. This procedure was also used to remove sources outside the map field whose sidelobes degraded the map. This was done by making a map shifted to the position of the aliased or confusing source. The source was CLEANed and its CLEAN components Fourier transformed and subtracted from the visibility data. This technique was especially useful in the data reduction of the NAT sample since at 20 cm the larger beam size and lower frequency result in typically a ~100 mJy confusing source within the primary beam. This procedure works well, except when the source is far from the phase center where the effects of unequal bandpasses on each baseline become important.

Correlator problems. One of the correlator problems that was encountered in this work was the problem of DC offsets. The effect of a constant DC offset to a correlator amplitude is to add a number of sine waves to the map. The sine waves will increase the noise level in the map, and will add in phase at the phase center to produce a spurious point-line feature. This feature can be several milli-jansky in strength. An example of this problem from the 2-cm observations of NGC 1265 is shown in Figure 2.2a.

This problem was solved in this work by subtracting a model of the source (2000 CLEAN components) from the visibility data. The residual visibility data contained high points due to the DC offsets. These points were edited out by clipping all the points above an amplitude of 0.3 Jy. The source data was then added back in. The map produced after this procedure is shown in Figure 2.2b.

Figure 2.2a

(a) A total intensity map of NGC 1265 at a wavelength of 2 cm showing a spurious source at the phase center produced by DC offsets in the correlator amplitudes. Contour levels are -0.5, 0.5, 1.0, 1.5, 2.0, 3.0, 5.0, and 7.0 mJy/beam. The peak in the map is 35 mJy/beam.

Figure 2.2b

(b) The total intensity map of NGC 1265 produced after editing the high amplitude (u,v) points (see text). The spurious source at the phase center has disappeared and the noise level in the map has been reduced. Contour levels are the same as for (a).

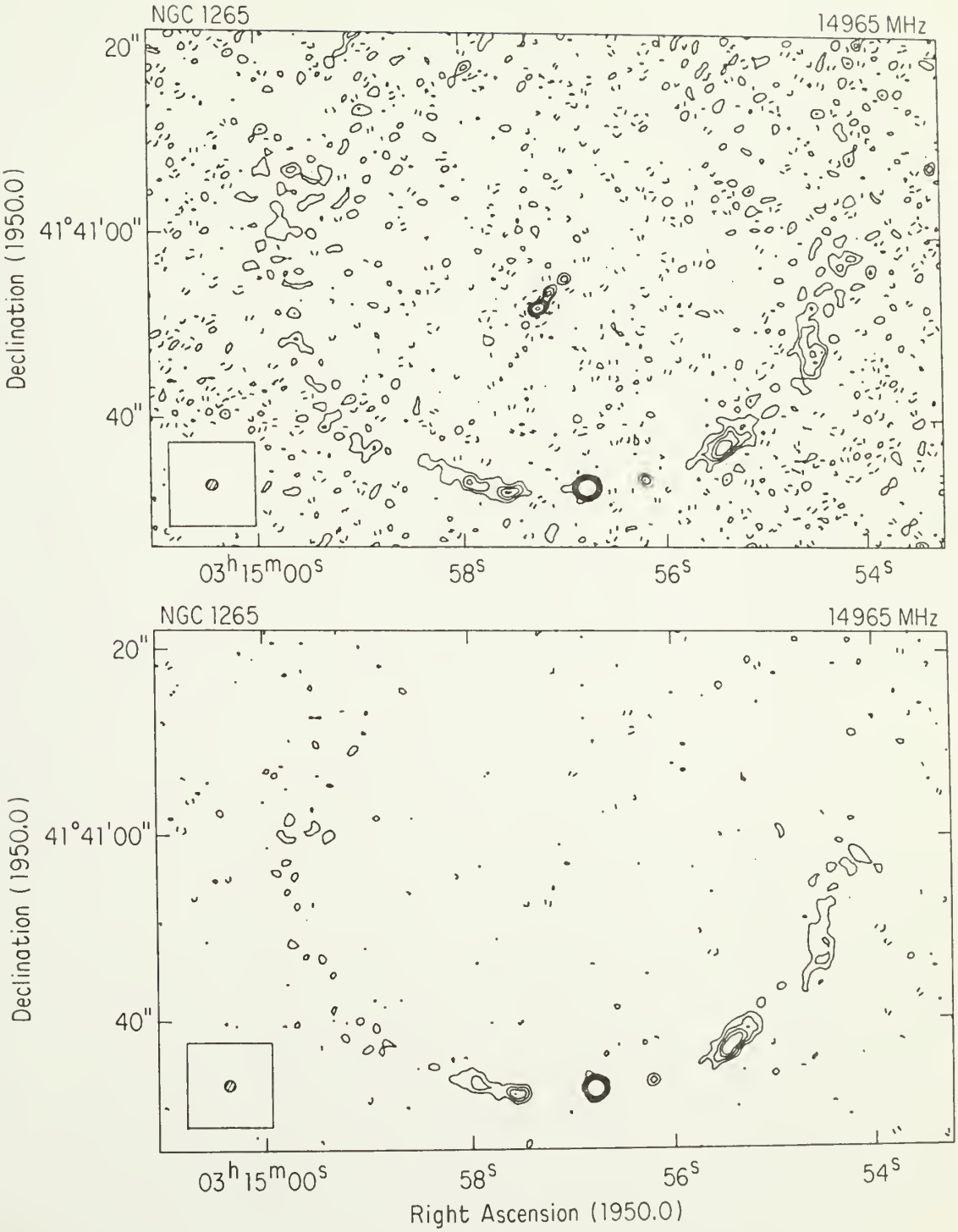
NGC 1265
14965 MHz
20"
41°41'00"
40"
Declination (1950.0)
03h15m00s
58s
56s
54s
NGC 1265
14965 MHz
20"
41°41'00"
40"
Declination (1950.0)
03h15m00s
58s
56s
54s
Right Ascension (1950.0)

C H A P T E R I I I

RADIO OBSERVATIONS OF THE ROGUES' GALLERY

VLA observations of 57 radio sources in the directions of clusters of galaxies are presented. The data include observations of 41 Narrow Angle Tail (NAT) sources, 9 Wide Angle Tail (WAT) sources, and 7 sources with complex morphology. Twin jet structure is found in ~75% of the NATs.

These observations increase the number of NATs for which there are high sensitivity (root-mean-square noise ~0.1 mJy/beam) high resolution (~1") maps by about a factor of 10. Contour plots and B/W pictures of the sources are presented. Optical finding charts for 25 previously unidentified sources are given. Brief comments on the properties of the individual radio sources are made. Finally, the general characteristics and interesting features of the different subgroups of sources are summarized. The global and statistical properties of a sample of 51 NATs in Abell clusters are discussed in Chapter IV.

3.1 The Observing Strategy

The goal of this part of the thesis is to provide high resolution maps of a large enough number of NATs that a representative statistical sample can be constructed. The literature was searched for maps of definite and possible NAT sources. The sources were chosen on the basis of their exhibiting a "tadpole-like" morphology (i.e., a bright head located at the position of the optical identification, with a lower surface brightness tail on one side). In a few sources, twin tail

structure was already evident from the available observations. Twenty-five sources were found which deserved high resolution VLA observations. The VLA snapshot survey of Abell clusters by Owen and collaborators was examined for promising sources. Optical identifications on the Palomar Sky Survey were obtained for all the likely candidates. Twenty-one additional sources were found in this manner.

It was known that these sources had relatively steep spectra (α ~-0.7 to -1), so the lowest possible observing frequency (1.4 GHz) was chosen. The VLA configuration used was based on a compromise between obtaining the highest possible resolution in order to see clearly the details of the structure, while still having a beam size large enough to detect low surface brightness features. Based on the previous maps, either the A or B array was chosen. This gave a resolution at 20 cm of about 1."2 and 4."0, respectively. A few sources seemed to have large scale structure to which the high resolution observations would not be sensitive. So observations were obtained of a few sources in the C configuration (~12" resolution). Three sources (0154+319, 0431-134, and 0647+693) were observed at 6 cm in the C array (at ~4" resolution) instead of at 20 cm in the B array because of scheduling problems. Most sources were observed for about one hour. In a few cases, only snapshots (5-10 minute observations) could be scheduled. In many cases observing time was scheduled in short blocks, making it impossible to calibrate the instrumental polarization. Full

polarization information was available for only a few sources and was therefore neglected. As discussed in Chapter II, the flux density scale of Baars et al. (1977) was used.

The parameters of the observations are given in Table 3.1. The source name is given in column 1. The Abell cluster number (Abell 1958) is given in column 2. Zw denotes a Zwicky cluster (see Zwicky et al. 1961). The date of the observations is given in column 3. An asterisk marks observations taken from the Abell cluster survey (Owen et al. 1982b). The VLA configuration is given in column 4. The observing frequency and bandwidth in megahertz are given in columns 5 and 6, respectively. The integration time (in minutes) is given in column 7. The angular resolutions are given in the captions to Figure 3.1 and in the text. The linear/angular scale in kiloparsecs per arcsecond is given in column 8. The distances were obtained from the redshifts in Table 4.1 and its references and assuming a Hubble constant of H_o = 75 km sec^{-1} Mpc^{-1} and a deceleration parameter of q_o = 0.1.

3.2 The Data Reduction

The data were edited and calibrated on the DEC-10 computer at the VLA using the procedures described in Chapter II. The calibrated data were transferred to a VAX 11/780 at the VLA, where the data were mapped and CLEANed using the NRAO Astronomical Image Processing System (AIPS) software. In most cases it was possible to add together data sets obtained in different VLA configurations. This was desirable since it improved the (u,v) coverage considerably and permitted a map to be made

Table 3.1 The Parameters of The Observations

Source	Cluster	Date	Array	Frequency (MHz)	Bandwidth (MHz)	Time (Min)	Scale (kpc/")
0039+211	0084	03-19-82	A	1452	25	50	2.1
0039-095	0085	05-08-81*	B	1413	25	10	1.0
		03-19-82	A	1452	25	50	
0039-097	0085	05-08-81*	B	1413	25	10	1.0
		12-26-81*	C	1452	25	10	
		08-26-82	B	1452	25	50	
0053-016	0119	12-26-81*	C	1452	25	10	0.86
		08-26-82	B	1452	25	50	
0053-015	0119	12-26-81*	C	1452	25	10	0.86
		08-26-82	B	1452	25	50	
0123-016	0194	12-26-81*	C	1452	25	10	0.36
		08-26-82	B	1411	12.5	50	
0154+319	0278	01-23-82	C	4885	50	50	1.8
		05-30-82	A	4885	50	50	
0256+132	0401	05-08-81*	B	1413	25	10	1.5
		01-23-82	C	1452	25	50	
		06-25-82	A	1452	25	50	
0258+356	0407	05-08-81*	B	1413	25	10	0.93
		12-26-81*	C	1452	25	10	
		06-25-82	A	1452	25	50	
0304-123	0415	12-26-81*	B	1452	25	10	1.8
		01-23-82	C	1452	25	10	
		03-19-82	A	1452	25	50	
0309+411	0426	05-28-82	A	1452	25	50	0.35
0327+246	0439	03-19-82	A	1452	25	50	2.2
		01-23-82	C	1452	25	10	
0335+096	Zw	01-23-82	C	1452	25	10	0.70
		03-19-82	A	1452	25	50	
0431-134	0496	01-23-82	C	4885	50	50	0.62

Table 3.1 - Continued

Source	Cluster	Date	Array	Frequency (MHz)	Bandwidth (MHz)	Time (Min)	Scale (kpc/")
0457+054	0526	09-20-80*	C	1465	25	10	1.1
		05-08-81*	B	1413	25	10	
		08-26-82	B	1452	25	50	
0647+693	0562	01-23-82	C	4885	50	50	2.2
0658+330	0567	09-25-82*	B	1452	25	10	2.6
0704+351	0568	05-08-81*	B	1413	25	10	1.6
		12-26-81*	C	1452	25	10	
		03-19-82	A	1452	25	20	
		05-28-82	A	1452	25	50	
0905-098	0754	09-25-82*	B	1452	25	10	1.0
		08-26-82	B	1452	25	20	
0907-091	0754	12-26-81*	C	1452	25	10	1.0
		08-26-82	B	1452	25	10	
1055+570	1132	03-19-82	A	1452	25	50	2.8
1108+411	1190	09-25-82*	B	1452	25	10	1.5
		03-25-82	A	1452	25	50	
1132+492	1314	08-06-82	B	1452	25	50	0.67
1244+699	1614	08-06-82	B	1452	25	50	3.3
1250-150	1631	05-08-81*	B	1413	25	10	1.1
		12-26-81*	C	1452	25	10	
		06-14-82	A	1446	12.5	50	
1256+282	1656	03-19-82	A	1452	25	50	0.46
1257+282		" 4					
1330+507	1758	03-19-82	A	1452	25	50	6.1
		09-25-82	B	1452	25	10	
1339+266	1775	05-08-81*	B	1413	25	10	1.4
		03-19-82	A	1452	25	50	
		06-14-82	A	4885	50	50	

Table 3.1 - Continued

Source	Cluster	Date	Array	Frequency (MHz)	Bandwidth (MHz)	Time (Min)	Scale (kpc/")
1519+488	2064	03-19-82	A	1452	25	50	2.2
1556+274	2142	08-06-82	B	1452	25	50	1.8
1615+351	Zw	04-05-82	A	1452	25	50	0.60
1615+425	2172	03-19-82	A	1452	25	50	2.8
1619+428	2183	01-23-82	C	1452	25	50	2.7
		03-19-82	A	1452	25	50	
1621+380	Zw	05-10-82	A	1452	25	50	0.63
1624+406	2197	08-06-82	B	1452	25	50	0.60
1658+326	2241	01-23-82	C	1452	25	10	2.1
		03-19-82	A	1452	25	50	
1709+397	2250	05-10-82	A	1452	25	50	1.3
		08-06-82	B	1452	25	50	
1712+638	2255	08-06-82	B	1452	25	10	1.7
1705+786	2256	06-14-82	A	1446	12.5	50	1.2
1706+786 1706+787 1707+787		09-25-82*	B	1452	25	10	
1753+580	2289	03-19-82	A	1452	25	50	3.3
1850+702	2311	05-01-82	A	1452	25	10	1.6
		08-06-82	B	1452	25	15	
		08-07-82	B	1452	25	50	
1918+439	2319	08-07-82	B	1452	25	10	1.1

Table 3.1 - Continued

Source	Cluster	Date	Array	Frequency (MHz)	Bandwidth (MHz)	Time (Min)	Scale (kpc/")
2316+184	2572	05-08-81*	B	1413	25	10	0.78
		05-30-82	A	1452	25	50	
		08-07-82	B	1452	25	50	
2322+143	2593	01-23-82	C	1452	25	10	0.87
		03-19-82	A	1452	25	50	

Notes to Table 3.1

*denotes observations taken from the VLA snapshot survey of Abell clusters by Owen et al. (1982b).

of the relatively large scale structure with high resolution. All maps were 1024x1024 pixels in size with ~3.5 pixels per CLEAN beam FWHM. The maps were inspected for signs of confusion or problems with the data. In about two-thirds of the maps it was necessary to subtract out confusing sources (i.e., strong sources outside the map field but within the primary beam whose sidelobes increased the noise in the map). For a few sources it was necessary to self-calibrate in order to reach a reasonable sensitivity. Self-calibration was used for only a few sources because of the large amount of time involved. All maps were CLEANed. A correction for attenuation by the primary beam was applied to all maps where the source was larger than ~2' in size. The final root-mean-square noise level in the maps was typically ~0.15 mJy beam^{-1} for the one hour observations and ~1 mJy beam^{-1} for the snapshots (~10 minute observations). The much larger noise in the snapshot maps is due mainly to the poorer (u,v) coverage, which makes it more difficult to remove confusing sources properly.

The positions of the optical identifications were measured on the PSS prints. The two-axis Mann measuring engine at the VLA was used to determine the positions of the objects relative to reference stars in the SAO catalog, using software written by Ken Mighell and Don Wells. Typically, eight reference stars were used giving a root-mean-square error in the derived position of ~1". For a few fields fewer stars were available, resulting in higher errors. There is an additional error of perhaps a few arcseconds in the positions of the brightest objects due to the difficulty in determining the position of the centroid of brightness. Thus, the occasional few arcsecond offset of the position of the identification from the cores seen in Figure 3.1 are probably not significant.

3.3 The Maps

Contour plots of all the sources are presented in Figure 3.1. The positions of the optical identifications are shown as crosses. The CLEAN beam Full Width to Half Maximum (FWHM) and position angle and the contour levels are given in the figure captions. Black and white radiophotographs of the sources are shown in Figure 3.2. The source parameters measured on the VLA 1.4 and 4.9 GHz maps are given in Table 3.2. The source name is given in column 1. Where two sources are close enough that the IAU coordinate designation is the same, the westernmost source (i.e., lower right ascension) is designated by A and the easternmost source (i.e., higher right ascension) is designated by B. The integrated flux density, in jansky, (obtained using IMEAN) is

given in column 2. The core flux density (in jansky) is given in column 3. In those cases where it was thought that the measured core flux density included a significant contribution from nearby emission, or the structure was uncertain, the number is given as an upper limit. Additional parameters are also given for the twin jet NATs. The average jet flux density (in jansky) for the twin jet sources is given in column 4. The deconvolved jet radius, r_j, (in kiloparsecs), obtained by fitting a gaussian to a transverse profile (or slice) across the jet, is given in column 5 for the twin jet NATs. For an unresolved cylinder, $r_j < \phi_b = 0.849\ \sigma_b$, where ϕ_b and σ_b are the second moment and half width to half maximum (HWHM), respectively, of the gaussian CLEAN beam and for a resolved cylinder, $r_j = 1.7[\sigma_{obs}^2 - \sigma_b^2]^{1/2}$, where σ_{obs} is the HWHM of the gaussian fit to the jet (e.g., Burns 1979, Burns, Owen, and Rudnick 1979). The minimum pressure due to relativistic particles and magnetic fields in the radio jets (see Chap. VI; Burns, Owen, and Rudnick 1979, Pacholczyk 1970) is given in column 6.

Table 3.2 Source Parameters

Source	Integrated Flux Density (Jy)	Core Flux Density (Jy)	Twin Jet NAT Parameters: Jet Flux Density (Jy)	Jet Radius (kpc)	Minimum Pressure 10^{-11} dynes/cm^2
0039+211	0.18	0.034	0.021	<1.0	3
0039-095A	0.07	0.0035			
0039-095B	0.05	0.0156			
0039-097	0.12	0.007	0.021	<2.1	0.3
0053-015	1.50	0.042			
0053-016	1.13	0.008	0.018	<1.9	0.3
0123-016A	0.91	0.017			
0123-016B	4.27	0.060			
0154+319	0.16[a]	0.0014[a]			
0256+132	0.19	0.0032	0.025	<0.8	1

Table 3.2 - Continued

Source	Integrated Flux Density (Jy)	Core Flux Density (Jy)	Twin Jet NAT Parameters Jet Flux Density (Jy)	Jet Radius (kpc)	Minimum Pressure 10^{-11} dynes/cm^2
0258+356	0.75	0.0067			
0304-123A	0.88	0.0047			
0304-123B	0.74	<0.065			
0309+411	0.30	0.294			
0314+416	>4.93	0.012	0.226	~0.4	3
0327+246A	0.32	0.0074			
0327+246B	0.04	0.004			
0335+096	0.37	0.017	0.023	<0.3	5
0431-134	0.52[a]	0.024[a]	0.024[a]	<1.2	2
0457+054	0.16	<0.002	0.026	<2.0	0.3
0647+693	0.80[a]	0.005[a]			
0658+330	0.36	0.052		<5.0	
0704+351A	0.28	0.001			
0754+351B	0.61	0.022			
0905-098	0.37	0.119			
0907-091	0.39	0.031	0.024	<2.2	0.2
1055+570A	0.02	<0.0025			
1055+570B	0.11	<0.0004			
1108+411	0.88	0.0135	0.123	<0.7	3
1132+492	0.16	0.034	0.009	<1.0	0.3
1244+699	0.22	0.0063	0.006	<5.7	0.1
1250-150	0.50	<0.002			
1256+280	0.13	0.002	0.016	<0.2	3
1257+282	0.17	<0.002			
1330+507	0.11	0.005			
1339+266A	0.04	<0.0007			
1339+266B	0.29	<0.007			
1519+488A	0.05	<0.005			
1519+488B	0.06	<0.0006			
1556+274	0.09	0.021			
1615+351	0.20	0.032			
1615+425	0.08	0.008		<3.0	
1619+428	0.13	0.0008	0.006	<1.6	0.6
1621+380	0.18	0.021			
1624+406	0.04	0.033			
1658+328	0.28	0.0035			
1709+397	0.27	<0.010			
1712+638	0.24	0.006	0.015	<2.8	0.3
1705+786	0.06	0.002	0.006	<1.9	0.3
1706+786	0.16	0.015			
1706+787	0.04	0.0016			
1707+787	0.01	0.0016			

Table 3.2 - Continued

Source	Integrated Flux Density (Jy)	Core Flux Density (Jy)	Twin Jet NAT Parameters: Jet Flux Density (Jy)	Jet Radius (kpc)	Minimum Pressure 10^{-11} dynes/cm^2
1753+580	0.14	<0.007	0.013	<2.0	2
1850+702	0.19	0.013	0.017	<1.5	0.4
1918+439	0.08	<0.008			
2316+184	0.29	0.015	0.085	<0.4	4
2322+143A	0.78	0.0083			
2322+143B	0.15	0.006			

Notes to Table 3.2

a. flux density measured at 4.9 GHz.

Table 3.3 The Optical Identifications

Source	Right Ascension (1950.0) h m s	Declination (1950.0) ° ' "	Ref.	Ref.	Rank	Notes
0039+211	00 39 03.09	21 07 43.0	1	14,15	2	
0039-095A	00 39 16.38	-09 33 29.7			3	
0039-095B	00 39 18.55	-09 34 37.6			1	
0039-097	00 39 18.44	-09 42 16.7			3	
0053-015	00 53 52.08	-01 31 57.1			2	ID
	00 53 52.49	-01 32 31.6			3	
	00 53 52.41	-01 32 42.0			3	
	00 53 51.23	-01 32 56.0			3	
0053-016	00 53 29.31	-01 36 16.9			3	ID
	00 53 28.36	-01 36 49.1			3	
0123-016A	01 23 11.53	-01 38 24.5	2		2	
0123-016B	01 23 26.07	-01 35 59.9	2		1	
	01 23 27.55	-01 36 18.9	2		1	ID

Table 3.3 - Continued

Source	Right Ascension (1950.0) h m s	Declination (1950.0) ° ' "	Ref.	Ref.	Rank	Notes
0154+319	01 54 22.45	32 00 34.8	3	3	2	
	01 54 21.75	32 00 24.3	3		3	
	01 54 22.08	32 00 09.5	3		1	ID?
	01 54 23.46	32 00 02.0	3		3	
	01 54 23.35	31 59 42.8	3		3	
	01 54 21.51	31 59 41.2	3		3	
	01 54 23.07	32 00 17.8	3		3	
0256+132	02 56 30.0	13 15 17	4,5	4,16	3	
0258+356	02 58 44.56	35 38 41.8	1	6	1	
	02 58 43.72	35 38 41.5	1			
	02 58 43.30	35 38 35.7	1			
	02 58 44.08	35 38 32.5	1			ID?
	02 58 43.92	35 38 24.6	1			
	02 58 45.08	35 38 24.6	1			
	02 58 45.38	35 38 38.8	1			
	02 58 46.68	35 38 30.8	1			
0304-123A	03 04 29.38	-12 17 53.7			1	ID
	03 04 29.80	-12 17 52.4			1	
	03 04 32.25	-12 18 25.1			3	
0304-123B	03 04 40.33	-12 17 18.2			3	
	03 04 39.10	-12 16 59.3			2	
0309+411	03 09 44.72	41 08 54.6			3	
	03 09 44.93	41 08 47.9			3	ID
	03 09 45.75	41 08 47.5			3	
	03 09 46.00	41 08 42.6			3	
0327+246A	03 27 31.05	24 37 36.3	3	3	2	
0327+246B	03 27 44.72	24 37 36.0	3	3	1	
0335+096	03 35 30.70	09 55 19.2			2	
0431-134	04 31 51.42	-13 28 24.6			3	ID
	04 31 52.03	-13 28 06.3			3	

Table 3.3 - Continued

Source	Right Ascension (1950.0) h m s	Declination (1950.0) ° ' "	Ref.	Ref.	Rank	Notes
0457+054	04 57 22.07	05 24 44.7			3	ID
	04 57 20.77	05 25 25.7			3	
	04 57 23.89	05 25 36.5			3	
0647+693	06 47 54.58	69 23 31.5			2	
0658+330	06 58 52.97	33 01 46.8		17	1	
0704+351	07 04 24.34	35 08 22.8	6	6	2	
	07 04 21.95	35 08 23.9	6		2	
	07 04 22.74	35 08 14.0	6		2	
0905-098	09 05 36.4	-09 47 31	7	18	3	
0907-091	09 06 59.96	-09 10 32.0			3	
1055+570A	10 55 22.14	57 03 43.5			2(1?)	
1055+570B	10 55 31.04	57 04 03.3			3	
1108+411	11 08 53.49	41 06 43.1	6	6	2	
1132+492	11 32 03.95	49 13 56.5	8	24	3	
1244+699	12 43 55.46	69 55 50.4			2	ID
	12 43 57.87	69 56 00.9			3	
	12 44 01.15	69 55 47.2			3	
1250-150	12 50 18.19	-15 04 14.6			3	ID
	12 50 20.08	-15 04 11.8			3	
	12 50 20.28	-15 03 49.3			3	
	12 50 15.84	-15 03 56.3			3	
1256+282	12 56 58.3	28 10 52.3	3	19	3	
1257+282	12 57 10.7	28 13 45.5	3	19	2	
1330+507	13 30 50.92	50 47 09.5			3	ID
	13 30 51.14	50 46 58.8			3	
1339+266A	13 39 29.49	26 37 31.6	3	3	2	
1339+266B	13 39 30.84	26 37 19.7	3	3	2	

Table 3.3 - Continued

Source	Right Ascension (1950.0) h m s	Declination (1950.0) ° ' "	Ref.	Ref.	Rank	Notes
1519+488A	15 19 09.63	48 50 08.4			3	
1519+488B	15 19 16.96	48 50 23.8			1	
1556+274	15 56 09.9	27 24 54	9		3	
1615+351	16 15 49.0	35 07 32	13	20	2	
1615+425	16 14 59.05	42 34 15.2			2	ID
	16 14 59.60	42 34 13.9			2	
1619+428	16 19 53.57	42 52 26.8			3	ID
	16 19 53.42	42 52 11.0			3	
	16 19 53.13	42 52 01.5			3	
	16 19 52.02	42 52 17.9			3	
	16 19 49.20	42 52 41.4			1	
1621+380	16 21 16.9	38 02 17	13	20	3	
1624+406	16 24 08.86	40 35 56.9		21	2	
1658+328	16 58 18.75	32 39 36.7	10	10	3	
1709+397	17 09 16.69	39 45 07.9	1	15,20	2	
1712+638	17 12 55.67	63 50 59	5	22	3	
1705+786	17 05 51.70	78 39 55.6	11	23	3	
1706+786	17 06 19.34	78 41 53.4	11	23,15	3	
1706+787	17 06 21.02	78 43 52.6	11	23	3	
1707+787	17 07 38.81	78 42 22.7	11	23	3	
1753+580	17 53 12.18	58 05 33.7			3	ID
	17 53 12.35	58 05 40.7			3	
	17 53 10.74	58 05 28.5			3	
	17 53 14.01	58 05 36.5			3	
1850+702	18 49 47.24	70 17 33.6			3	

Table 3.3 - Continued

Source	Right Ascension (1950.0) h m s	Declination (1950.0) ° ' "	Ref.	Ref. Rank	Notes
1918+439	19 18 45.3	43 57 03.7	12	3	
2316+184	23 16 09.56	18 24 58.2		3	
2322+143A	23 22 01.13	14 21 54.9		3	ID
	23 22 03.26	14 21 35.3		3	
2322+143B	23 22 04.92	14 21 56.8		3	
	23 22 04.79	14 22 03.9		3	
	23 22 06.25	14 22 05.1		3	ID

References to Table 3.3

1. Simon (1979)
2. Schilizzi (1975)
3. Owen, Rudnick, and Peterson (1977)
4. Hintzen, Scott, and Tarenghi (1977)
5. Harris, Kapahi, and Ekers (1980)
6. Rudnick and Owen (1977)
7. Harris et al. (1980b)
8. Vallee and Wilson (1976)
9. Harris et al. (1980a)
10. Bijleveld and Valentijn (1982)
11. Bridle et al. (1979)
12. Birkinshaw (1978)
13. Ekers et al. (1978)
14. Riley (1975)

15. Rudnick and Owen (1976)

16. Burns and Ulmer (1980)

17. Valentijn (1979b)

18. Melnick and Quintana (1981)

19. Willson (1970)

20. Ulrich (1978)

21. Gavazzi and Perola (1980)

22. Hintzen and Scott (1980)

23. Bridle and Fomalont (1976)

24. Webber (1974)

The coordinates of the optical identifications are given in Table 3.3. For completeness, the positions of the previously identified sources are also given. The source name is given in column 1. The right ascension and declination (epoch 1950.0) are given in columns 2 and 3, respectively. Where appropriate, a reference for the position is given in column 4. A reference to a previously published finding chart is given in column 5. The rank of the galaxy is given in column 6. The nomenclature is that given by Rudnick and Owen (1976): rank 1 denotes the dominant galaxy in the cluster, rank 2 denotes a galaxy whose brightness is comparable to the dominant galaxy, and rank 3 denotes a galaxy which is much fainter than the dominant galaxy. Notes on the identification are given in column 7. Finding charts for those sources previously unidentified, or without published finding charts are given in Figure 3.3.

Brief comments on the individual sources are given below.

A 84: 0039+211 was first shown to be a twin tail source by Rudnick and Owen (1976). It has also been mapped by Riley (1975) and Simon (1979). The jets appear to become diffuse very quickly and only bits and pieces of the tails are seen in the 1."2x1."1 resolution map.

A 85: 0039-095A and 0039-097 are two NAT sources located on roughly opposite sides of the central cD galaxy (0039-095B), which is also a radio source (Owen et al. 1982b). 0039-095A is a single tail source (at 1."6x1."2 resolution) reminiscent in appearance to IC 310 (Miley et al. 1972; Gower 1983, private communication). 0039-097 is a twin tail source (at 5."4x4."2 resolution) whose tails merge into a diffuse tail about 30" (~30 kpc) behind the nucleus.

A 119: A 119 is another cluster with two twin tail NATs, 0053-016 and 0053-015. This cluster has been mapped by Schilizzi and McAdam (1975) and Andernach, Waldthausen and Wielebinski (1980), though only the observations by Owen, Burns and White (1984) were of sufficient resolution to show the NAT nature of the two sources. 0053-015 (shown at 6."6x4."9 resolution) is very asymmetric and exhibits gaps in the jets and tails. Higher resolution observations of the region near the core are needed in order to examine the possibility that the structure in this source is due to alternating one-sided ejection (e.g., Rudnick 1982; Rudnick and Edgar 1984). In contrast, 0053-016 (shown at 5."5x4."9 resolution) is very symmetric. The wiggles in the jets (due to precession of the central collimator?) continue into the diffuse

Figure 3.1a

Total intensity contour maps. The crosses mark the positions of the optical objects in the field. The positions of the optical objects are given in Table 3.3. The FWHM of the CLEAN beam is shown as a shaded ellipse. Negative contours are dashed. Starting at the top left and going clockwise, the contour levels in multiples of 1 mJy/beam and the FWHM and position angle of the CLEAN beam are as follows: 0039+211: -0.3, 0.3, 1, 2, 5, 9, 16, (1.17"x1.13" @13.9°; 0039-095A: -0.5, 0.5, 1, 2.5, (1.6"x1.2" @-1.6°); 0039-097: -0.6, 0.6, 1, 2, 4, (5.3"x4.2" @0°); 0039-095B: -0.5, 0.5, 1, 2, 4, 7, 11, (1.6"x1.2" @-1.6°).

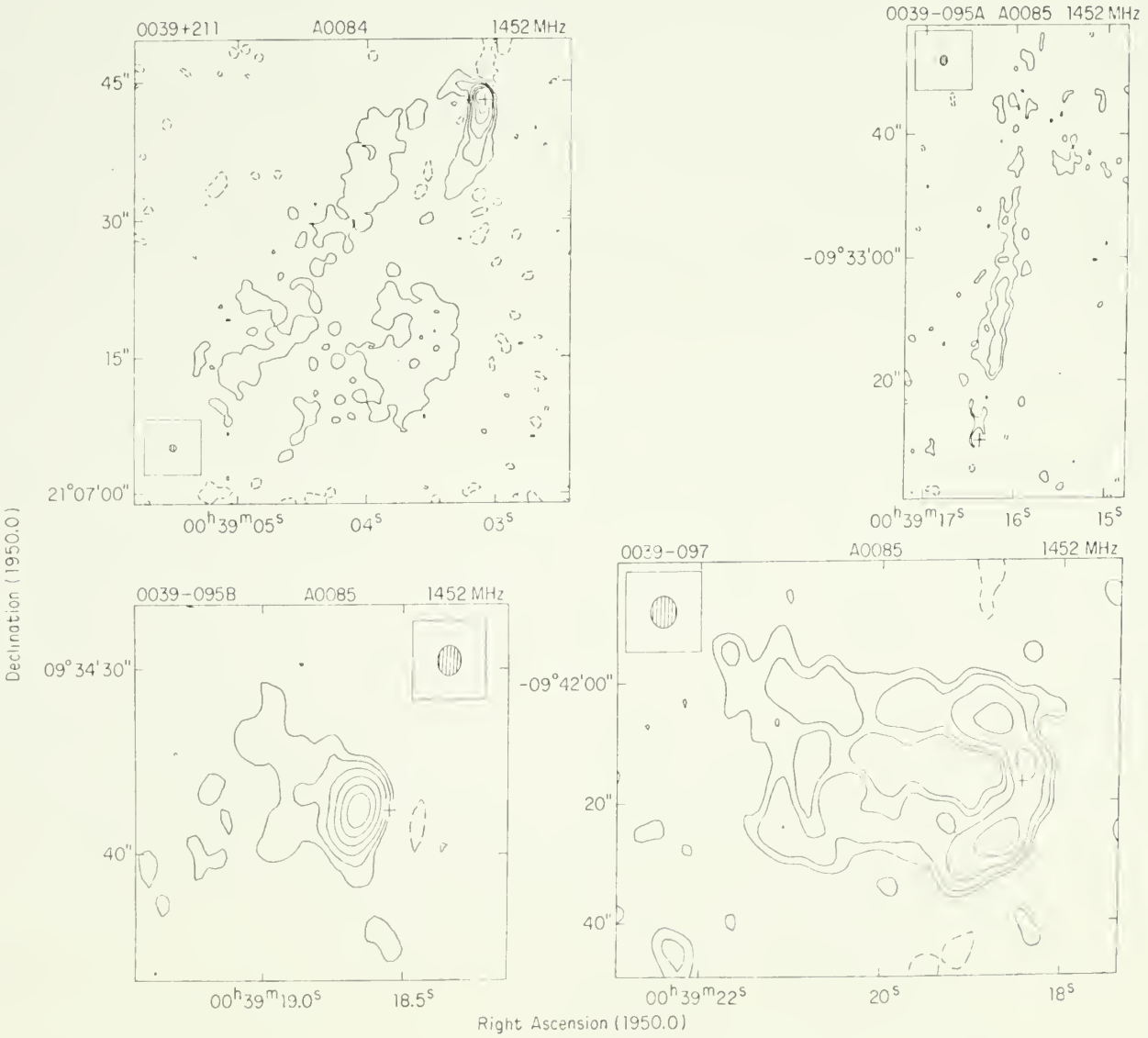
0039+211 A0084 1452 MHz
45"
30"
15"
21°07'00"
00h39m05s
04s
03s
0039-095A A0085 1452 MHz
40"
-09°33'00"
20"
00h39m17s
16s
15s
0039-095B A0085 1452 MHz
09°34'30"
40"
00h39m19.0s
18.5s
0039-097 A0085 1452 MHz
-09°42'00"
20"
40"
00h39m22s
20s
18s
Declination (1950.0)
Right Ascension (1950.0)

Figure 3.2a

B/W radiophotographs of the sources in Figure 3.1a.

0039+211 1452 MHz

0039-095A 1452 MHz

0039-095B 1452 MHz

0039-097 1452 MHz

Figure 3.3a

Optical fields of cluster radio sources, reproduced from the E prints of the Palomar Sky Survey (copyright 1960, National Geographic Society - Palomar Sky Survey. Reproduced by permission of the California Institute of Technology). The positions of the objects denoted by the bars are given in Table 3.3. The scale in arcminutes and the orientation of the charts are shown in the top left corner.

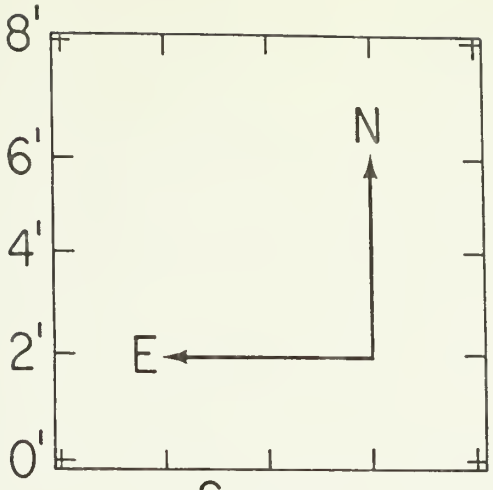

Source
(Cluster)

0039−095
A0085

0039−097
A0085

0053−015
A0119

0053−016
A0119

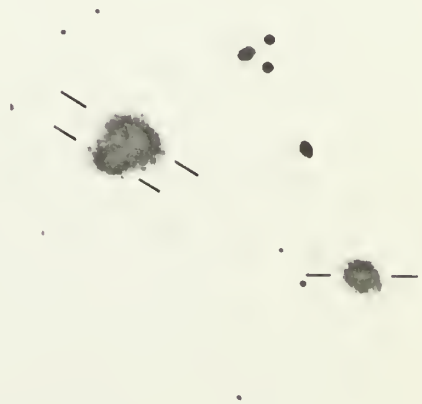

0123−016A,B
A0194

tails. These two sources have tails which point in the same direction in the sky (SW), but at very different angles to the direction to the cluster center.

A 194: Low resolution observations of 0123-016A,B (3C40) have been discussed by Schilizzi, Lockhart, and Wall (1972); Schilizzi and McAdam (1975); and Andernach, Waldthausen, and Wielebinski (1980). Both a tapered map (10."7x8."4) of both sources and a higher resolution map (5."8x5."5) of the NAT (0123-016A) are shown. The distorted double source (0123-016B) is associated with the southeasternmost galaxy of a dB (i.e., binary) galaxy pair (NGC 545-547). Note the four roughly 90° bends in the northern lobe of this source. The twin tail source is associated with NGC 541, which is also an X-ray source of luminosity $L_X \sim 10^{41}$ ergs/sec (Forman and Jones 1982).

A 278: 0154+319 was previously mapped by Owen, Rudnick, and Peterson (1977), who identified it with the dominant galaxy in the center of the cluster. The source has also been mapped at low resolution by Fanti et al. (1983). It was reobserved because it appeared to be an example of an unresolved twin tail source. However, higher resolution observations (~2"; 3.6 kpc) showed no structure above ~0.6 mJy/beam. The 4."4x4" resolution 6 cm map shown suggests a one-sided jet with a slight edge brightening at the end of the jet. The lower resolution 20 cm map of Owen et al. (1982b) reveals that the jet continues south for an additional ~1."5 (160 kpc).

Figure 3.1b

See Figure 3.1a. 0053-016: -1, 1, 2, 5, 9, 16, (5.54"x4.95" @-55.3°); 0053-015: -2.5, 2.5, 5, 9, 15, 28, (6.6"x4.9" @-59°).

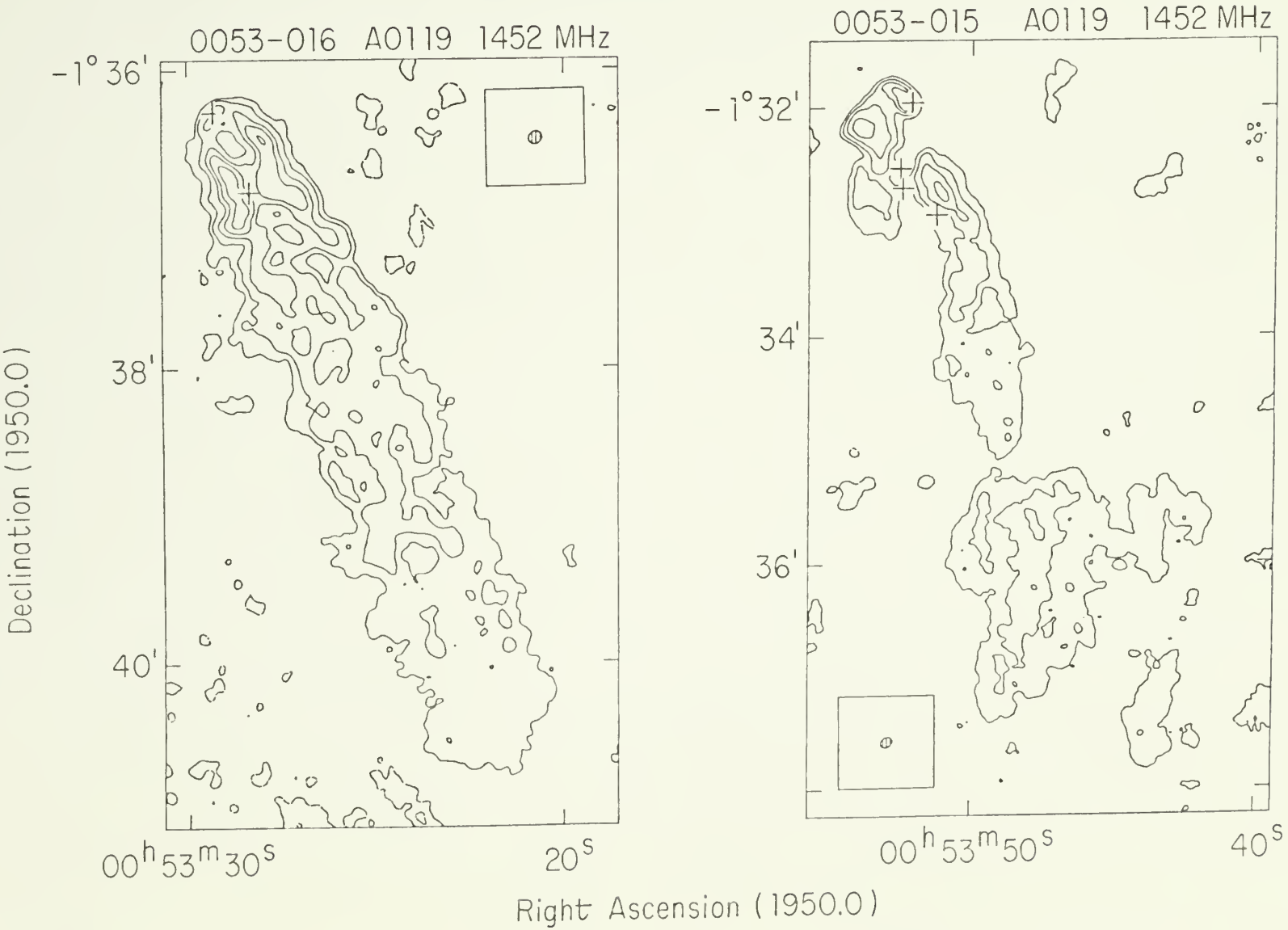
0053-016 A0119 1452 MHz
-1° 36'
38'
40'
00h53m30s
20s
0053-015 A0119 1452 MHz
-1° 32'
34'
36'
00h53m50s
40s
Declination (1950.0)
Right Ascension (1950.0)

Figure 3.2b

B/W radiophotographs of the sources in Figure 3.1b.

0053-016 1452 MHz

0053-015 1452 MHz

Figure 3.1c

See Figure 3.1a. 0123-016A,B: -1.5, 1.5, 4, 8, 20, 40, (10.7"x8.4" @-62°); 0123-016A: -1, 1, 2, 4, 8, 14, (5.8"x5.5" @-53°).

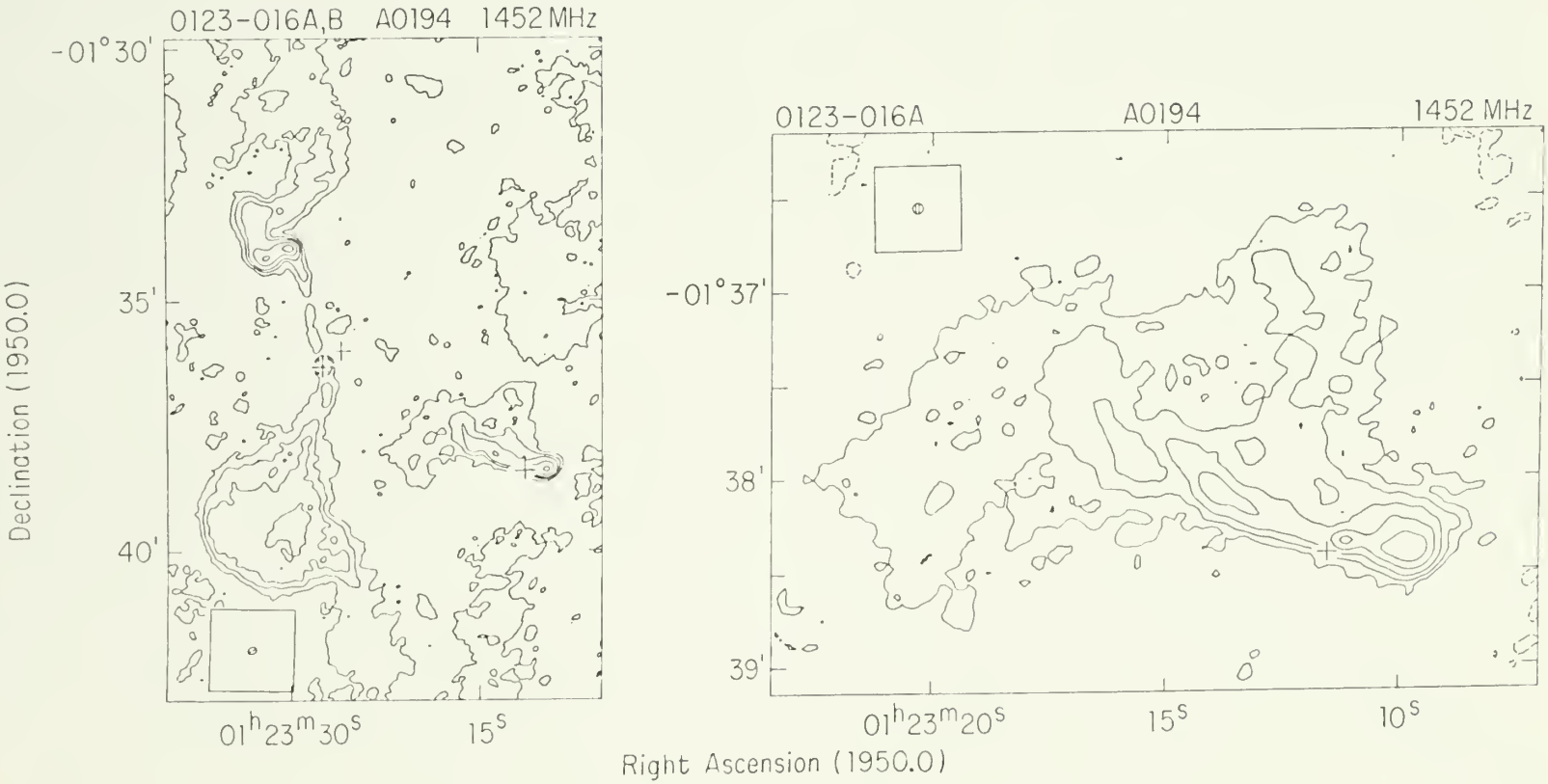
0123-016A,B A0194 1452 MHz
-01°30'
35'
40'
01h23m30s
15s
0123-016A A0194 1452 MHz
-01°37'
38'
39'
01h23m20s
15s
10s
Declination (1950.0)
Right Ascension (1950.0)

Figure 3.2c

B/W radiophotographs of the sources in Figure 3.1c.

0123−016A,B 1452 MHz

0123−016A 1452 MHz

A 401: Two NATs, 0255+133 (4C13.17A) and 0256+132 (4C13.17B), are found in this cluster. 0255+133 is well known and has been mapped by Slingo (1974b); McHardy (1978); Simon (1979); Burns and Ulmer (1980); and Harris, Kapahi, and Ekers (1980), and so was not reobserved here. 0256+132 has been observed by Harris, Kapahi, and Ekers (1980), and Burns and Ulmer (1980) who showed twin tail structure in this source. This source was reobserved in order to obtain a better map. Both a tapered map (7."1x5."7) and a higher resolution map (1."2) are shown. The twin jets merge into a low surface brightness tail (seen here for the first time) at about 30" (45 kpc) behind the nucleus. The general structure is similar to that seen in NGC 1265, however, the tail is much weaker (with respect to the jets) than in NGC 1265 (Chap. V).

A 407: 0258+356 (4C 35.06A) has been mapped by Riley (1975); Rudnick and Owen (1977); Harris and Miley (1978); and Simon (1979). These previous observations suggested that the source was associated with the nine nucleus cD galaxy (Schneider and Gunn 1982) in the center of the cluster. However, because of its apparent HT morphology and the possibility that it might simply be seen in projection against the cD, it was reobserved with the VLA. The 1."3x1."2 resolution map shows that the source is complex, featuring:

(1) an unresolved core coincident with one of the cD nuclei (at a position $\alpha = 02^h\ 58^m\ 44^s08$, $\delta = 35°\ 38'\ 32"5$; Simon 1979);

(2) twin jets; and

(3) very diffuse structure with an overall "Z" shape.

Figure 3.1d

See Figure 3.1a. 0154+139: -0.3, 0.3, 1, 2, 4, 7, (4.4"x4.0" @57.5°); 0256+132: -0.3, 0.3, 0.8, 1.5, 2.5, (1.3"x1.2" @-32°); 0256+132: -0.8, 0.8, 1.5, 3, 6, (7.1"x5.7" @-85°); 0258+356: -0.7, 0.7, 2, 3, 5, (1.3"x1.2" @26.5°).

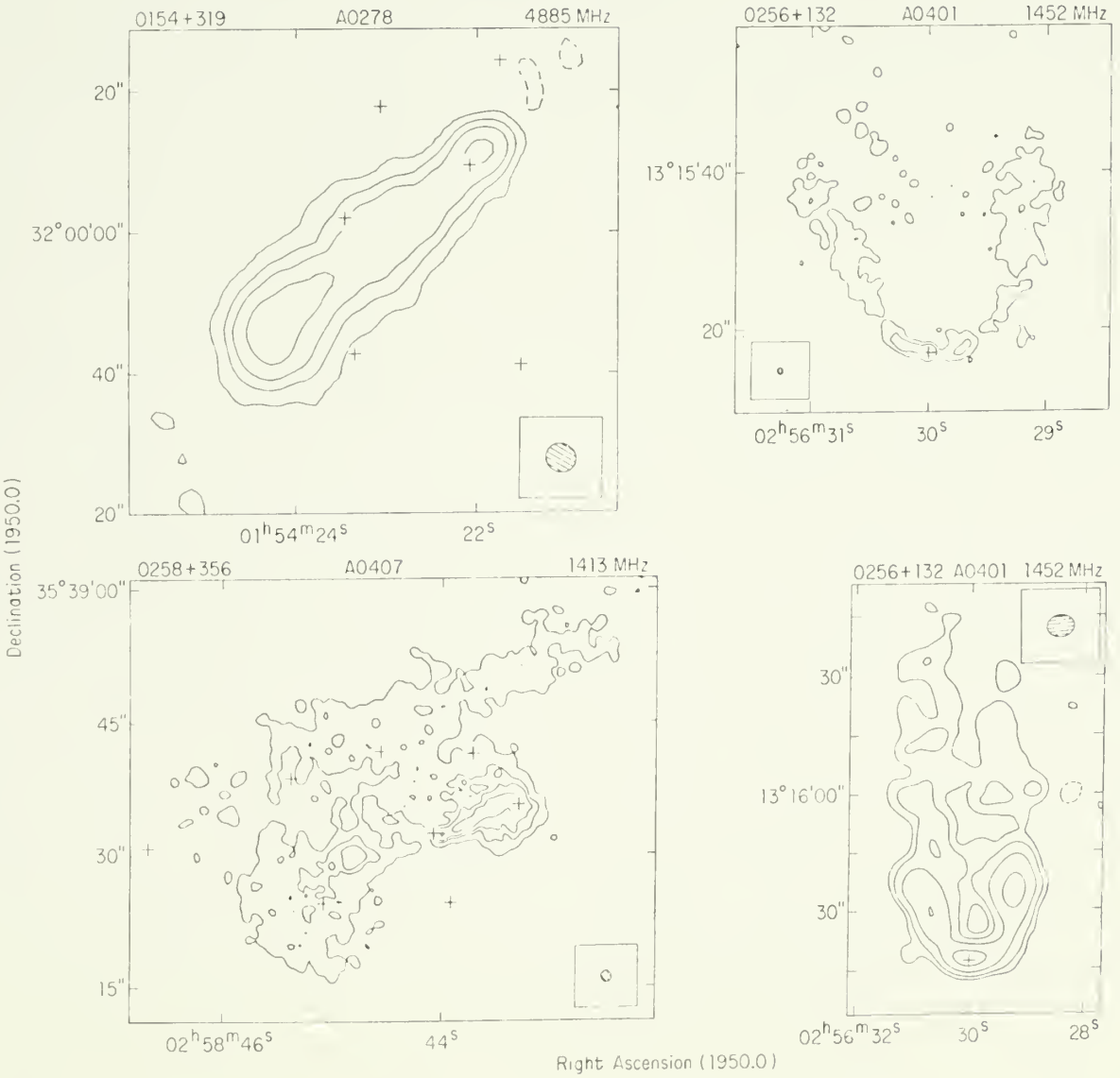
0154+319 A0278 4885 MHz
20"
32°00'00"
40"
20"
01h54m24s
22s
0256+132 A0401 1452 MHz
13°15'40"
20"
02h56m31s
30s
29s
0258+356 A0407 1413 MHz
35°39'00"
45"
30"
15"
02h58m46s
44s
0256+132 A0401 1452 MHz
30"
13°16'00"
30"
02h56m32s
30s
28s
Declination (1950.0)
Right Ascension (1950.0)

Figure 3.2d

B/W radiophotographs of the sources in Figure 3.1d.

0154+319 4885 MHz

0256+132 1452 MHz

0258+356 1413 MHz

0256+132 1452 MHz

0258+356 could be an example of a jet being "torqued" through the interaction of the cD nuclei (Wirth, Smarr, and Gallagher 1982).

A 415: 0304-123A appears to be a WAT (Owen et al. 1982b) associated with one nucleus of a possible binary system (see Fig. 3b). Optical spectroscopy is needed in order to determine whether the two optical images are indeed associated. The WAT and a ~5" double source (0304-123B) are shown at a resolution of 1."7x1."3. The tapered map (19."8x16."1) reveals that the tail of the WAT stretches ~2.'5 (260 kpc) and curves back towards the position of the double. No identification for the double was found on the PSS, suggesting that it is a background source.

A 426 (Perseus): The Perseus cluster contains three definite NAT sources, NGC 1265 (Miley 1973, Owen, Burns, and Rudnick 1978; Chap. V) IC 310 (Ryle and Wyndram 1968), and CR 15 (Miley et al. 1972). Based on their low resolution observations at 610 MHz, Gisler and Miley (1979) suggested that 0309+411 was a possible HT source. The A array observations appear to have resolved out most of the structure. A tapered map (~3") shows only a northeastern extension to the core in the direction of a blob at ~30" (11 kpc) from the core.

A 439: 0327+246A,B have been observed by Kapahi et al. (1973); Owen, Rudnick, and Peterson (1977); Menon (1980); and Harris et al. (1980a). The 1."2 resolution observations presented here are the first to show that there are actually two twin jet tailed sources. The associated galaxies are separated by ~15" (~30 kpc) and are located near

Figure 3.1e

See Figure 3.1a. 0304-123A,B: -3, 3, 8, 20, 50, 125, 300, 500, (19.85"x16.14" @6.6°); 0304-123B: -3, 3, 10, 40, 100, 200, (1.6"x1.1" @-10.6°); 0309+411: -1, 1, 2, 4, 20, 50, 125, (3.1"x3.0" @-38°); 0304-123A: -0.6, 0.6, 1.5, 4, 9, (1.75"x1.26" @-9.3°).

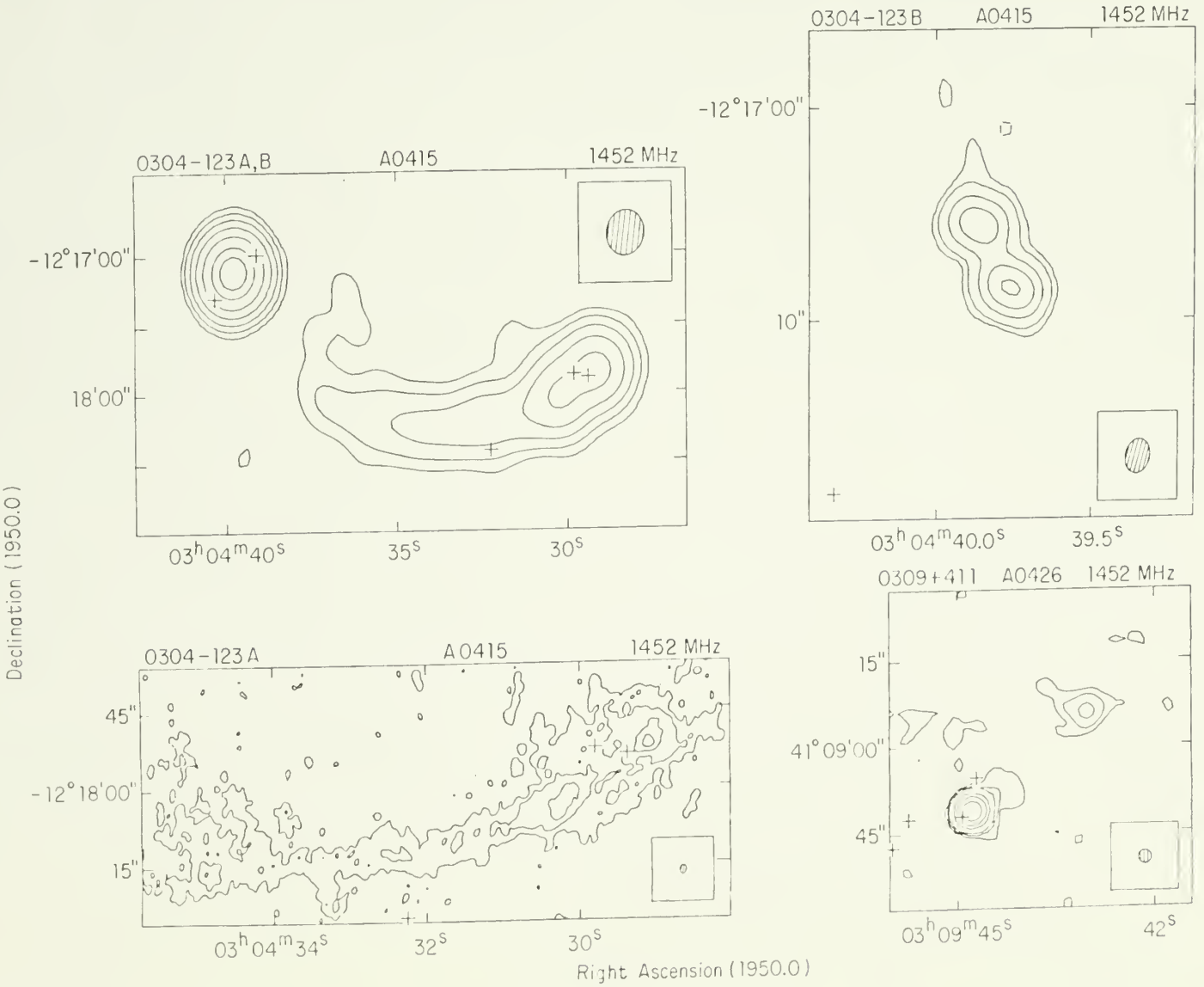
0304-123A,B
A0415
1452 MHz
-12°17'00"
18'00"
03h04m40s
35s
30s
0304-123B
A0415
1452 MHz
-12°17'00"
10"
03h04m40.0s
39.5s
0304-123A
A0415
1452 MHz
45"
-12°18'00"
15"
03h04m34s
32s
30s
0309+411
A0426
1452 MHz
15"
41°09'00"
45"
03h09m45s
42s
Declination (1950.0)
Right Ascension (1950.0)

Figure 3.2e

B/W radiophotographs of the sources in Figure 3.1e.


0304-123A,B 1452 MHz


0304-123B 1452 MHz


0304-123A
1452 MHz

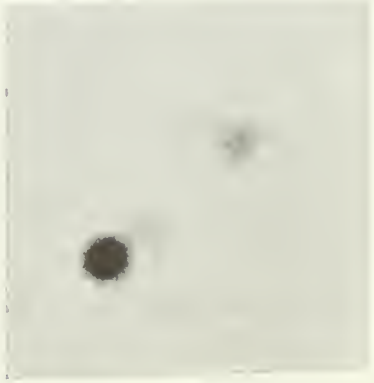
0309+411 1452 MHz

the center of the cluster. Some of the details of the structure (including the bending of the jets in the WAT) may be due to orbital motions of the two galaxies. It would be interesting to know whether the two galaxies share a common envelope, as is the case in 3C 75 (Owen, Inoue, and O'Dea 1982).

Zw 0335.1+0956: 0335+096 was shown to be a NAT by Owen et al. (1982b). It is identified with a prominent member of a medium distant Zwicky cluster (Zwicky, Karpowicz, and Kowal 1965) which is also an X-ray source (Schwartz, Schwarz, and Tucker 1980). The 1."2 resolution map of the region near the core shows twin jets which are swept back into a diffuse tail over a projected distance of ~5" (4 kpc). The tapered map (12."4x9."8) shows that the diffuse tail bends by about 40° at 1.'5 (60 kpc) behind the core and continues south for at least another 1.'5.

A 496: Observations of 0431-134 by Owen et al. (1982b) suggested that this sources was a NAT. The 6 cm, 5."0x4."1 resolution map reveals that 0431-134 is a twin tail source. There is a suggestion of curvature in the diffuse tails.

A 526: 0457+054 (discovered by Owen et al. 1982b) is a strange twin jet source. The 4."4x4."3 resolution map shows that one jet fades suddenly after bending through about 70° while the other jet breaks up into diffuse emission over a much shorter projected distance.

Figure 3.1f

See Figure 3.1a. 0327+246A,B: -0.3, 0.3, 1, 2, 3, 7, (1.2"); 0335+096: -0.7, 0.7, 2, 5, 10, 17, 25, 50, (12.4"x9.8" @58°); 0431-134: -0.4, 0.4, 1, 3, 7, 13, 21, (5.0"x4.1" @-28.4°); 0335+096: -0.3, 0.3, 1, 3, 7, 12, (1.2").

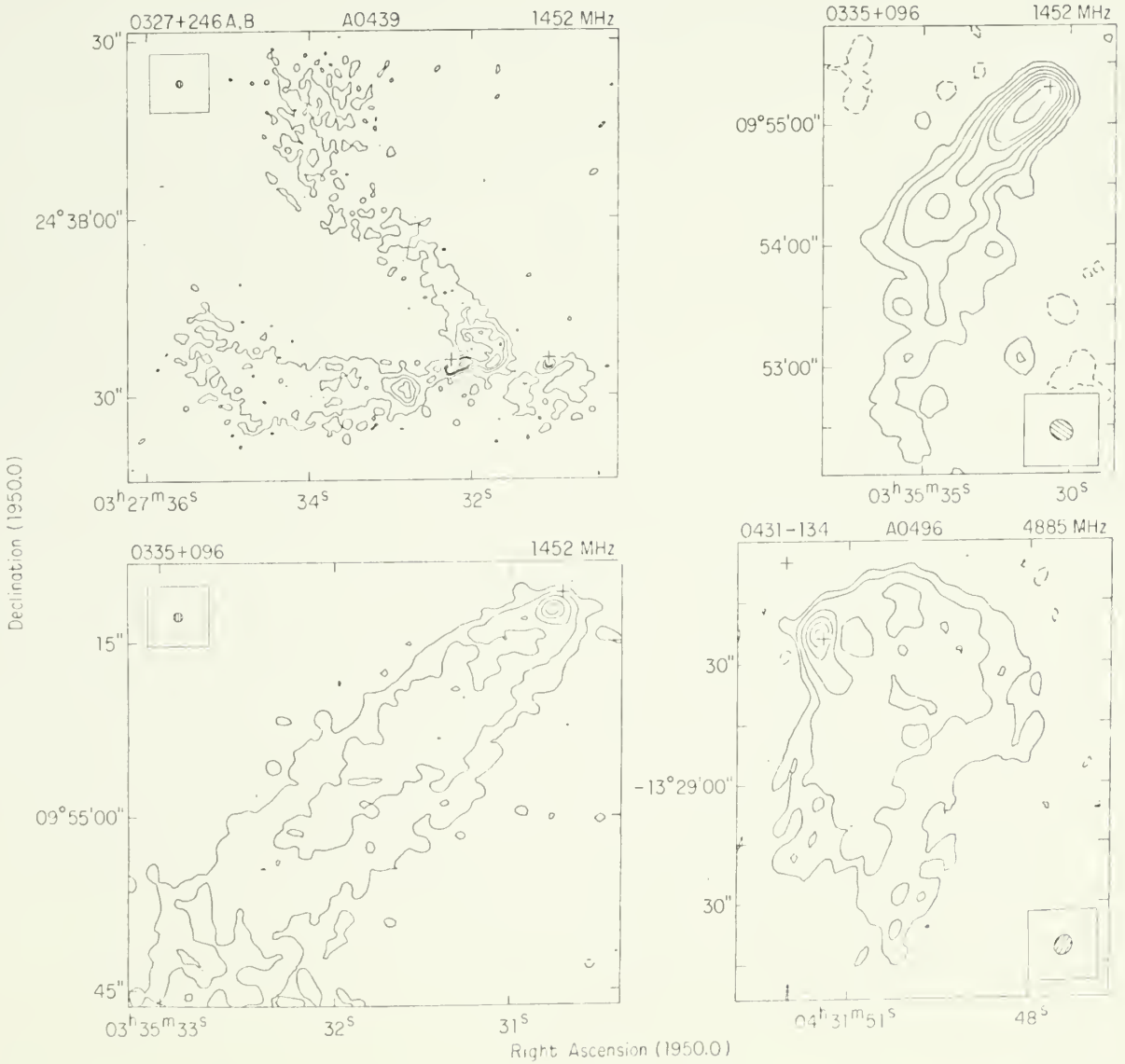
0327+246 A,B
A0439
1452 MHz
30"
24°38'00"
30"
03h27m36s
34s
32s
0335+096
1452 MHz
09°55'00"
54'00"
53'00"
03h35m35s
30s
0335+096
1452 MHz
15"
09°55'00"
45"
03h35m33s
32s
31s
0431-134
A0496
4885 MHz
30"
-13°29'00"
30"
04h31m51s
48s
Declination (1950.0)
Right Ascension (1950.0)

Figure 3.2f

B/W radiophotographs of the sources in Figure 3.1f.

0327+246A,B 1452 MHz

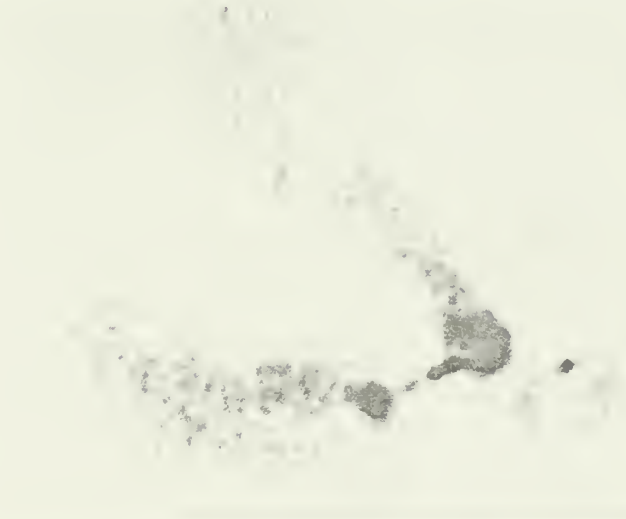

0335+096 1452 MHz

0335+096 1452 MHz

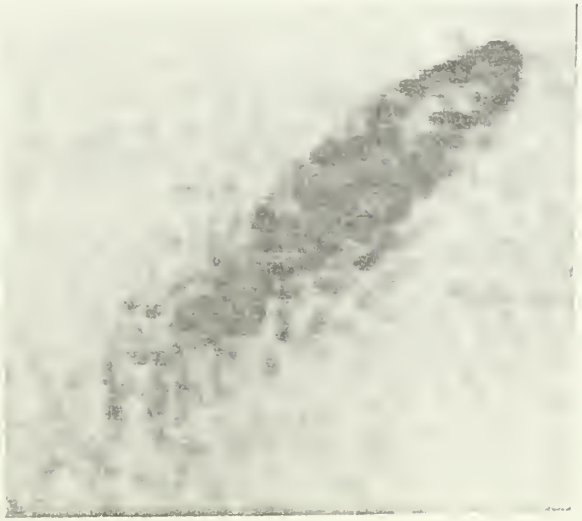

0431-134 4885 MHz

Figure 3.3b

Optical fields of cluster radio sources, reproduced from the E prints of the Palomar Sky Survey (copyright 1960, National Geographic Society - Palomar Sky Survey. Reproduced by permission of the California Institute of Technology). The positions of the objects denoted by the bars are given in Table 3.3. The scale in arcminutes and the orientation of the charts are shown in the top left corner.

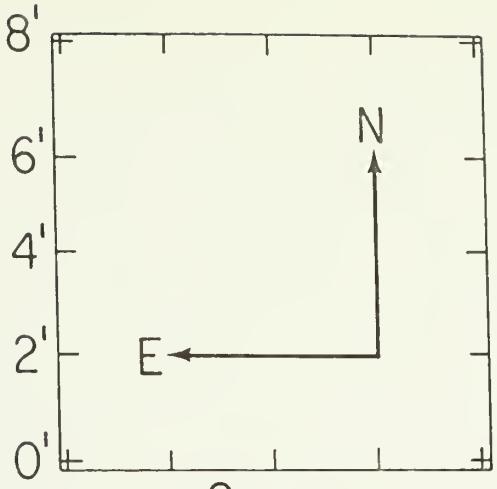

Source
(Cluster)

0304−123A,B
A0415

0309+411
A0426

0335+096

0431−134
A0496

0457+054
A0526

A 562: 0647+693 was first mapped by Owen et al. (1982b). The source is associated with one of the more dominant members of A 562. The 5."7x3."8 resolution map at 6 cm shows two tails which exit from hot spots on either side of the core. The general morphology is intermediate between NATs and WATs (see discussion in Chap. IV). The opening angle (defined as the angle at the core subtended by the ends of the tails) is 80°, which falls in the gap between NATs and WATs noted by Valentijn (1979a).

A 567: 0658+330 has been mapped by Valentijn (1979b) and Harris et al. (1980a). The source is associated with one of the more dominant galaxies in the cluster and appears to be a WAT source. The 5."0x4."0 resolution map shows twin jets which bend gradually before making a transition to diffuse lobes. Note the regularly spaced knots in the east jet.

A 568: 0704+351 has been mapped by Riley (1975), Rudnick and Owen (1977); Harris et al. (1980a); and Fanti et al. (1983). The 1."2 resolution map shown here reveals complex structure surprisingly different from that seen in the earlier low resolution, low sensitivity maps. The identification of the various regions of radio emission with the optical galaxies is uncertain. One possible interpretation is the following. The emission to the east and to the south of the bright point source form part of a WAT source. The object to the northeast is a distorted twin jet source whose southeast jet appears to bend away from the WAT. This may be a unique example of physically interacting radio sources.

Figure 3.1g

See Figure 3.1a. 0457+054: -0.5, 0.5, 1, 2, 4, (4.4"x4.3" @41.3°); 0658+330: -1.5, 1.5, 2, 3, 5, 12, 30, (5.0"x4.0" @20.4°); 0754+351: -0.4, 0.4, 1, 2, 7, (1.2"); 0647+693: -0.3, 0.3, 1, 3, 7, 13, (5.7"x3.8" @63.4°).

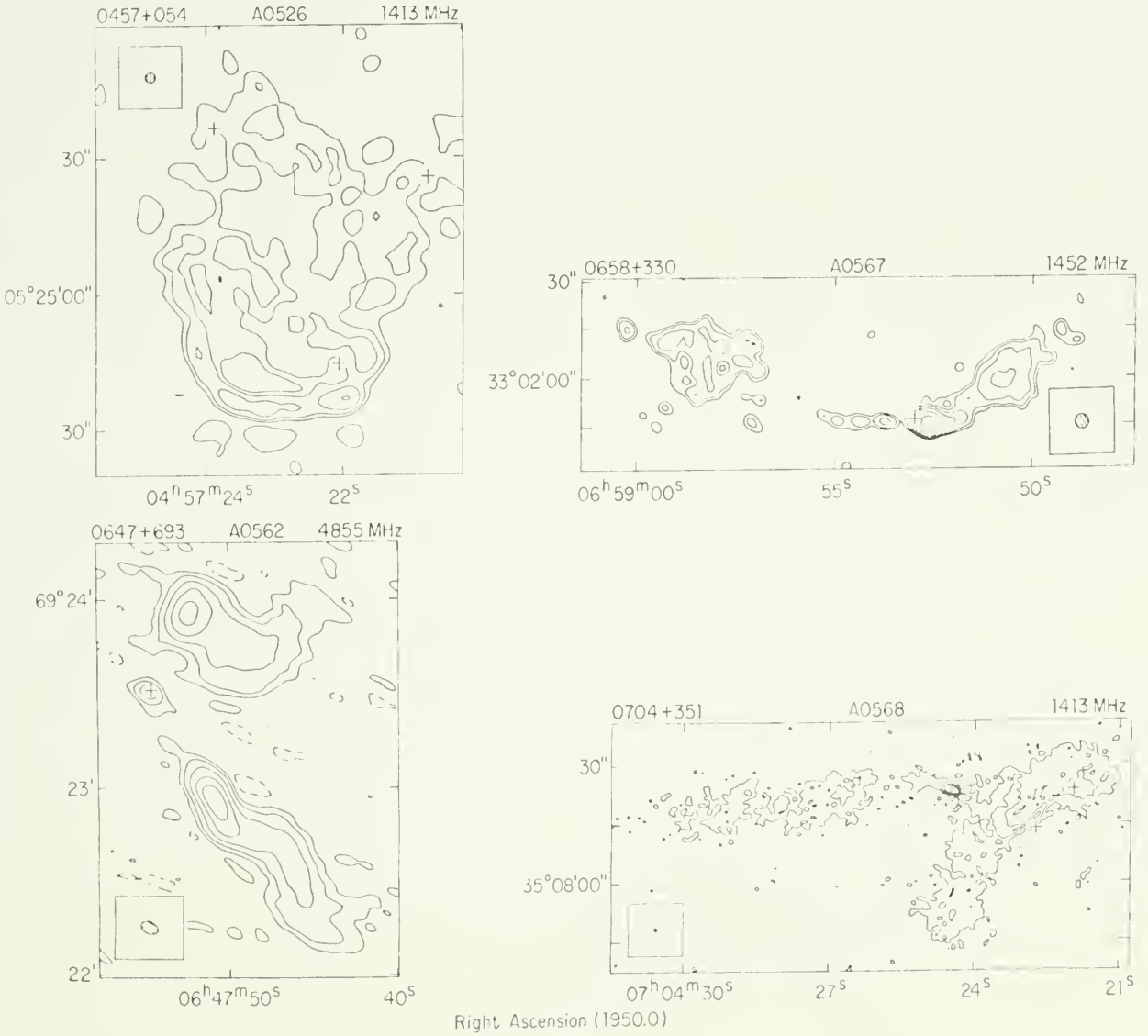
0457+054
A0526
1413 MHz
30"
05°25'00"
30"
04h57m24s
22s
0658+330
A0567
1452 MHz
30"
33°02'00"
06h59m00s
55s
50s
0647+693
A0562
4855 MHz
69°24'
23'
22'
06h47m50s
40s
0704+351
A0568
1413 MHz
30"
35°08'00"
07h04m30s
27s
24s
21s
Right Ascension (1950.0)

Figure 3.2g

B/W radiophotographs of the sources in Figure 3.1g.

0457+054 1413 MHz

0658+330 1452 MHz

0647+693 4855 MHz

0704+351 1413 MHz

A 754: A 754 has been studied by Harris et al. (1980b) at both radio and X-ray wavelengths. High resolution observations of two of the NATs in this cluster are presented here. The observations of Owen et al. (1982b) suggest that there is at least one other NAT in the cluster. The 4."5x4."2 resolution map of 0905-098 shows a single trail of emission which bends by almost 90° at ~2' (~130 kpc) from the core. Harris, Costain, and Dewdney (1984) present optical, X-ray and radio observations of this source and confirm its membership in the cluster. They find that there is weak X-ray emission ($L_X \sim 10^{42}$ ergs/sec) coincident with the tail at the position where it exits the optical galaxy. Their observations are consistent with 0905-098 being either a single jet or a tailed source. 0907-091 has been mapped at low resolution by Mills, Hunstead, and Skellern (1978). The 5."3x4."5 resolution map shows twin tail structure, though the two jets differ in brightness by a factor of ~4, and the surface brightness of the southern jet falls below the 0.6 mJy/beam level on the map. The jets expand by more than an order of magnitude into diffuse tails.

A 1132: 1055+570A,B are two NATs (Owen et al. 1982b) shown here at 1."2x1."0 resolution. The 1055+570B is a twin tail source with no visible compact core. 1055+570A appears to be a weak (~17 mJy) twin tailed source.

Figure 3.1h

See Figure 3.1a. 0907-091: -0.6, 0.6, 2, 4, 7, 20, (5.3"x4.5" @-30°); 0905-098: -0.7, 0.7, 2, 4, 15, 50, (4.5"x4.2" @-40.6°); 1055+570B: -0.4, 0.4, 1, 2, 3.5, (1.25"x1.0" @-16.5°); 1055+570A: -0.4, 0.4, 0.8, 1.2, 2, (1.25"x1.0" @-16.5°).

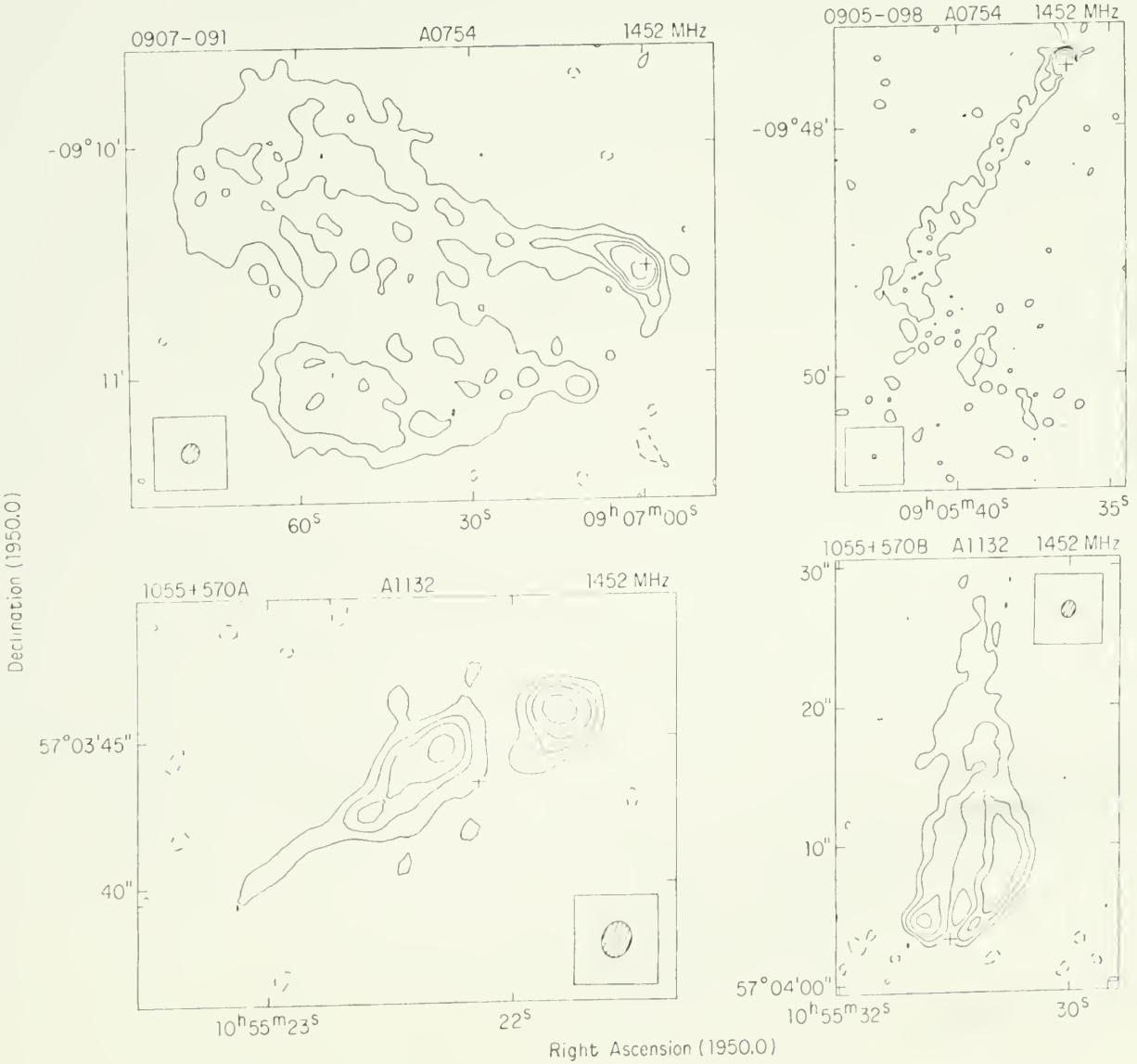
0907-091
A0754
1452 MHz
-09°10'
11'
60^s
30^s
09^h07^m00^s
0905-098
A0754
1452 MHz
-09°48'
50'
09^h05^m40^s
35^s
1055+570A
A1132
1452 MHz
57°03'45"
40"
10^h55^m23^s
22^s
1055+570B
A1132
1452 MHz
30"
20"
10"
57°04'00"
10^h55^m32^s
30^s
Declination (1950.0)
Right Ascension (1950.0)

Figure 3.2h

B/W radiophotographs of the sources in Figure 3.1h.


0907−091
1452 MHz


0905−098
1452 MHz

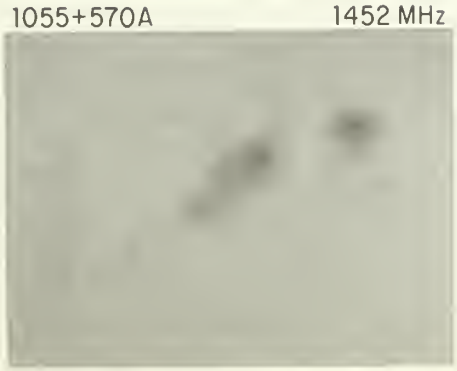
1055+570A
1452 MHz


1055+570B
1452 MHz

A 1190: 1108+411 has been mapped by Rudnick and Owen (1977), Valentijn (1979b), and Harris et al. (1980a). The 1."2x1."1 resolution map shows twin tail structure similar to that seen in 0431-134. The jets expand into very diffuse tails which appear to curve through about 90°.

A 1314: 1132+492 (IC711) is one of the two well known NATs in A 1314. Both IC 711 and 1131+493 (IC 708) have been mapped by Vallee and Wilson (1976) and Wilson and Vallee (1977). Possible explanations for the structure of IC 708 are discussed by Vallee, Wilson, and Van der Laan (1979) and Vallee, Bridle, and Wilson (1981). The 3."9x3."5 resolution map of the region near the core in IC 711 confirms the suggestion of twin tail structure seen in the data of Vallee and Wilson (1976). There is a hint that the twin jets extend continuously from the core to the diffuse tails. However, this structure is just at the noise level and is not seen in the contour plot.

A 1614: Observations of 1244+699 by Owen et al. (1982b) suggested that this source was a NAT. The source is shown to be a twin tail source by the 4."8x3."5 resolution map. The jet-tail transition occurs at the position of the hotspots located at a projected distance of ~15" (50 kpc) on either side of the core. Note the sudden change in direction of the tails to the east.

A 1631: 1250-150 has a complex morphology (Owen et al. 1982b). The 1."9x1."3 resolution map shows very diffuse structure and a ridge of brightness which may be a jet. The location of the core is not obvious. The tapered map (10."0x6."9) shows two tails of emission which (in

Figure 3.1i

See Figure 3.1a. 1108+411: -0.5, 0.5, 2, 4, 8, 14, (1.2"x1.1" @-33°); 1244+699: -0.5, 0.5, 1, 2, 4, 6, 9, (4.8"x3.5" @2.6°); 1250-150: -0.5, 0.5, 1, 2, (1.9"x1.3" @-21°); 1132+492: -0.4, 0.4, 1, 3, 9, 25, (3.9"x3.5" @16.4°).

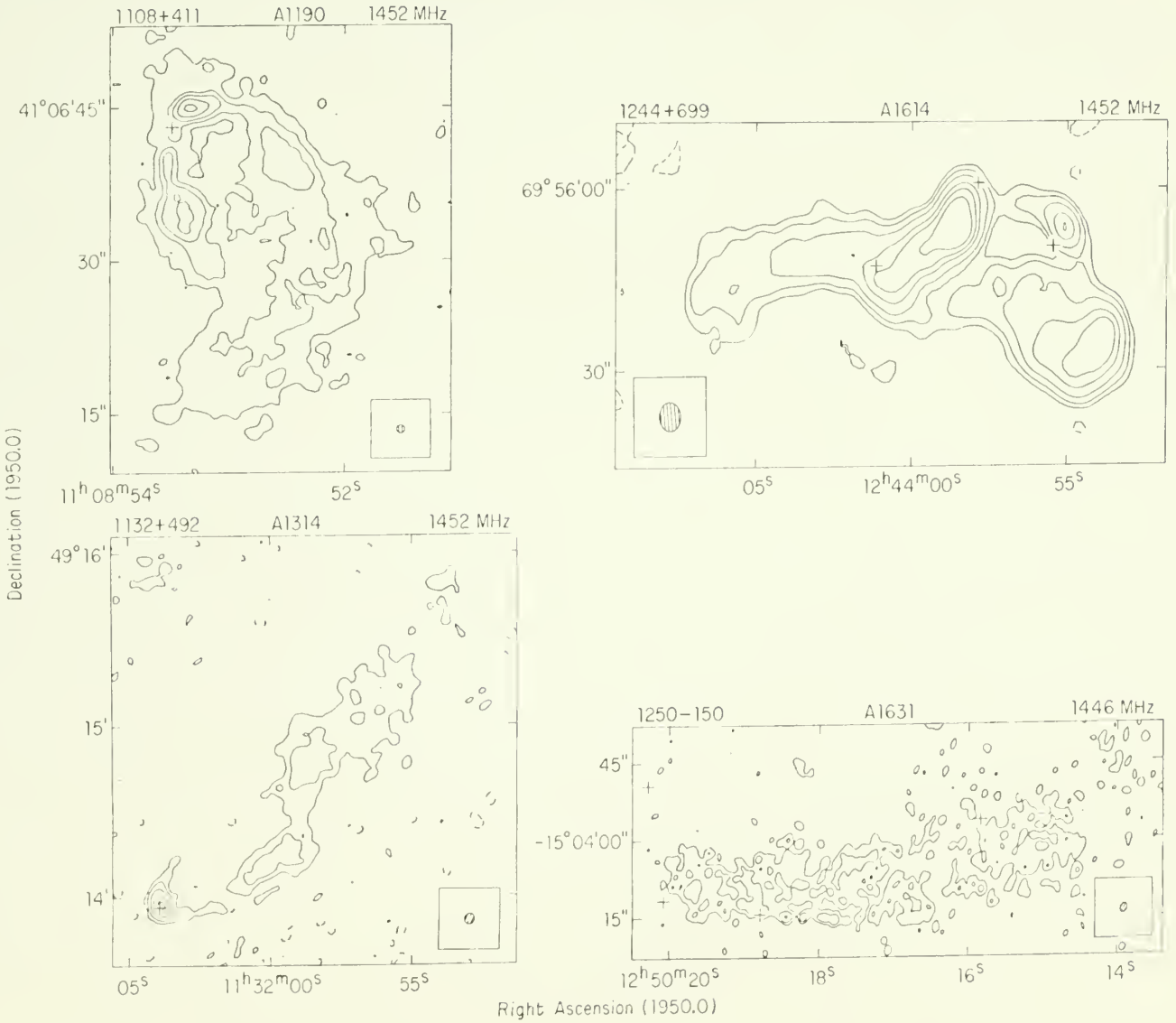
1108+411
A1190
1452 MHz
41°06'45"
30"
15"
11h08m54s
52s
1244+699
A1614
1452 MHz
69°56'00"
30"
05s
12h44m00s
55s
1132+492
A1314
1452 MHz
49°16'
15'
14'
05s
11h32m00s
55s
1250-150
A1631
1446 MHz
45"
-15°04'00"
15"
12h50m20s
18s
16s
14s
Declination (1950.0)
Right Ascension (1950.0)

Figure 3.2i

B/W radiophotographs of the sources in Figure 3.1i.

1108+411 1452 MHz

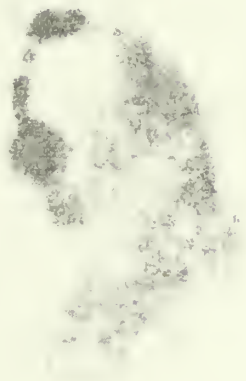

1244+699 1452 MHz

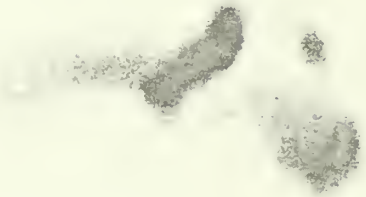

1132+492 1452 MHz

1250-150 1446 MHz

Figure 3.3c

Optical fields of cluster radio sources, reproduced from the E prints of the Palomar Sky Survey (copyright 1960, National Geographic Society - Palomar Sky Survey. Reproduced by permission of the California Institute of Technology). The positions of the objects denoted by the bars are given in Table 3.3. The scale in arcminutes and the orientation of the charts are shown in the top left corner.

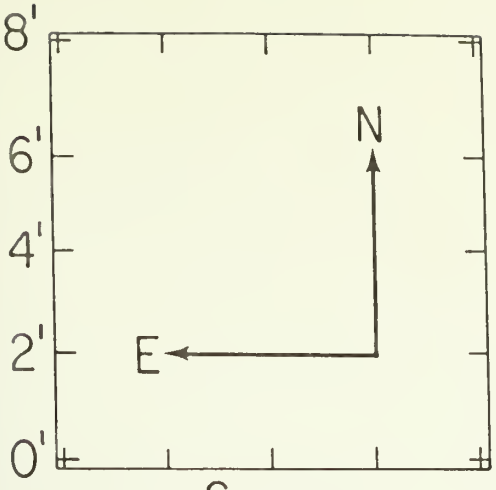

Source
(Cluster)

0647+693
A0562

0907−091
A0754

1055+570A,B
A1132

1244+699
A1614

1250−150
A1631

projection) curve through almost 90°. This may be another example of a NAT following a curved trajectory. Another possibility is that the tail is influenced by buoyancy (e.g., Cowie and McKee 1975; Gisler and Miley 1979; Harris 1982).

A 1656 (Coma): 1256+282 (5C 4.81) is a NAT associated with NGC 4869. The source has been mapped by Willson (1970); Jaffe and Perola (1974); Jaffe, Perola, and Valentijn (1976); and Owen, Rudnick and Peterson (1977). Roland (1982) has estimated various physical parameters for this source. The 1."1 resolution map presented here is the first to show the twin tail structure. The initially straight jets are bent and make a sudden transition to diffuse tails at the position of the two hot spots. It appears (at least in projection) that the beams are ejected at an angle of ~35° to the galaxy's direction of motion. Also shown is a slightly tapered map (3."3) of the small (~20", 9 kpc) bent double 1257+282 (5C 4.85). This source is associated with NGC 4874, one of the two dominant galaxies in the Coma cluster (e.g., Willson 1970, Jaffe and Perola 1974).

A 1758: 1330+507 (shown to be a NAT by Owen et al. 1982b) is located in the direction of the distance class 6 cluster A 1758. If the source is at the distance of the cluster ($z = 0.280$; Sandage, Kristian, and Westphal 1976), it would be one of the most powerful NATs known ($P_{1.4} \approx 3 \times 10^{25}$ W/Hz). The 1."2x1."1 resolution map shows that the single tail structure near the core appears to split into two tails at ~10" (~60 kpc) from the core. The blob of emission ~10" south of the core appears to be associated with another galaxy.

Figure 3.1j

See Figure 3.1a. 1250-150: -1, 1, 3, 5, 10, 15, (10.0"x6.9" @7.2°); 1257+282: -0.6, 0.6, 2, 5, 10, 17, (3.32"x3.26" @-50.4°); 1330+507: -0.3, 0.3, 0.8, 1.6, 4, (1.2"x1.1" @-29° 1256+282: -0.3, 0.3, 0.7, 1.3, 1.9, (1.14"x1.07" @-27°).

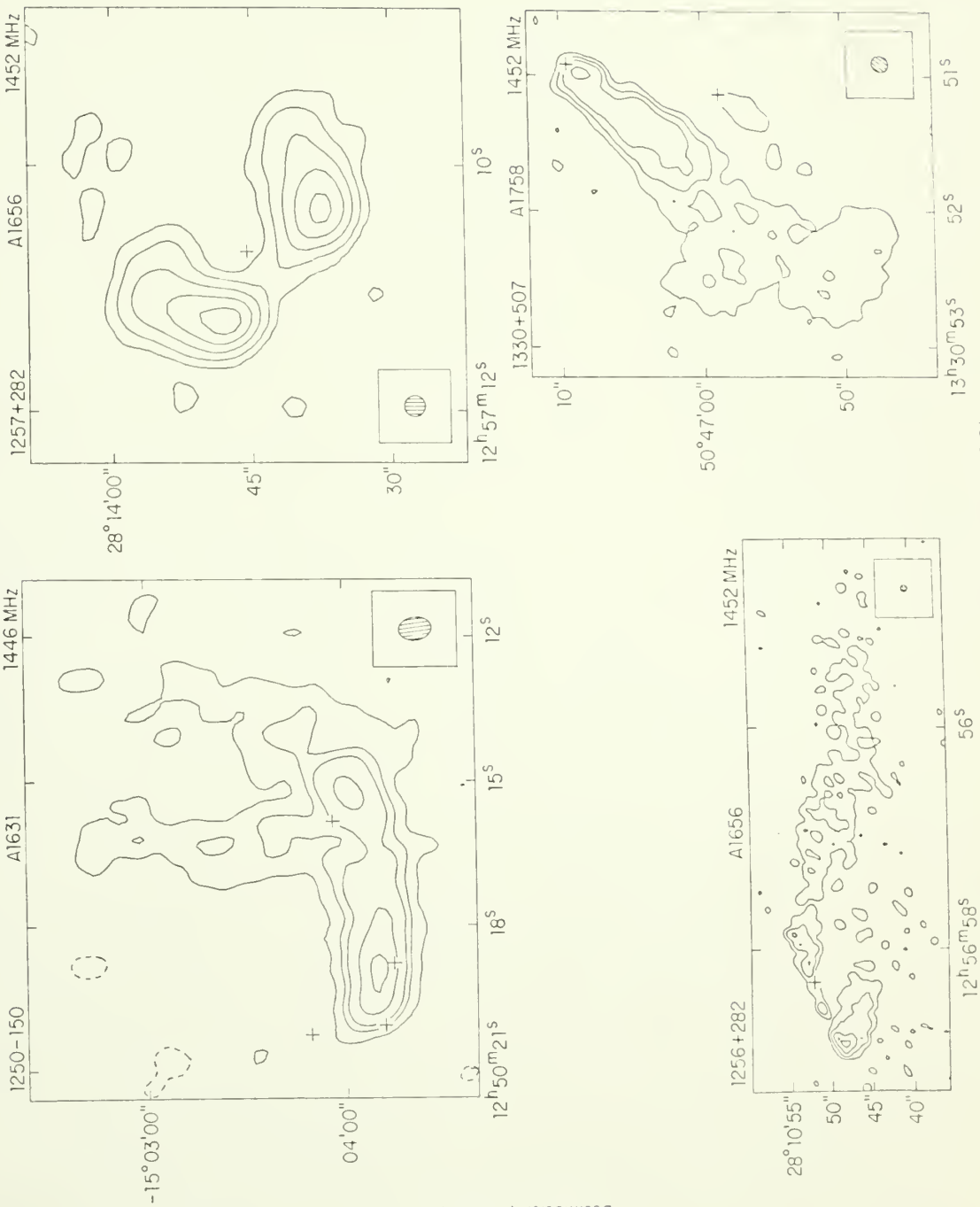
1250−150
A1631
1446 MHz
−15°03'00"
04'00"
12h50m21s
18s
15s
12s
1257+282
A1656
1452 MHz
28°14'00"
45"
30"
12h57m12s
10s
1330+507
A1758
1452 MHz
10"
50°47'00"
50"
13h30m53s
52s
51s
1256+282
A1656
1452 MHz
28°10'55"
50"
45"
40"
12h56m58s
56s
Declination (1950.0)
Right Ascension (1950.0)

Figure 3.2j

B/W radiophotographs of the sources in Figure 3.1j.

1250−150 1446 MHz

1257+282 1452 MHz

1256+282 1452 MHz

1330+507 1452 MHz

A 1775: The radio source in the center of A 1775 has been mapped by Slingo (1974a,b); Owen, Rudnick, and Peterson (1977); Miley and Harris (1977); Simon (1979); and Harris, Kapahi, and Ekers (1980). The 1."3 resolution maps of 1339+266 are the first to show clearly that there are actually two separate sources. Each radio source is associated with one of the bright galaxies in the center of the cluster. In addition to the previously known NAT (1339+266B), there is a small (~10"; 14 kpc) bent double (1339+266A) similar to 1257+282. The highest resolution map (~0.4" at 6 cm) shows only three knots in the front of the NAT. (The WAT is completely resolved by these observations.) If the suggestion of double structure in the first knot is real, then the jets are swept back with a projected radius of curvature of ~0.8 kpc. Chincarini et al. (1971) suggested that the two galaxies formed a bound system with a radial velocity difference of 1650 km/sec. However, both Miley and Harris (1977) and Hintzen (1979) have argued against that interpretation. The observations presented here are consistent with a scenario in which the east galaxy (the NAT) is moving rapidly through the ICM, while the west galaxy (the WAT) is nearly at rest with respect to the ICM.

A 2064: Observations of 1519+488A,B by Owen et al. (1982b) suggested that 1519+488A was a NAT. Both sources are shown here at 1."1x1."0 resolution. 1519+488B is a ~10" (22 kpc) bent double similar to 1257+282 associated with the dominant galaxy in A 2064. 1519+488A appears to be a NAT with an "hour glass" shape to the head. This may be due to ejection along the direction of motion. This might

Figure 3.1k

See Figure 3.1a. 1339+266A,B: -0.3, 0.3, 0.8, 1.5, 3, 7 12, (1.3"); 1519+488A: -0.4, 0.4, 0.8, 1.2, 2, 4, (1.1" x1.0" @-35.2°); 1519+488B: -0.4, 0.4, 1, 2, 4, 7, (1.1"x1.0" @-35.2°); 1339+266B: -0.3, 0.3, 0.4, 0.6, (0.38"x0.37" @52°).

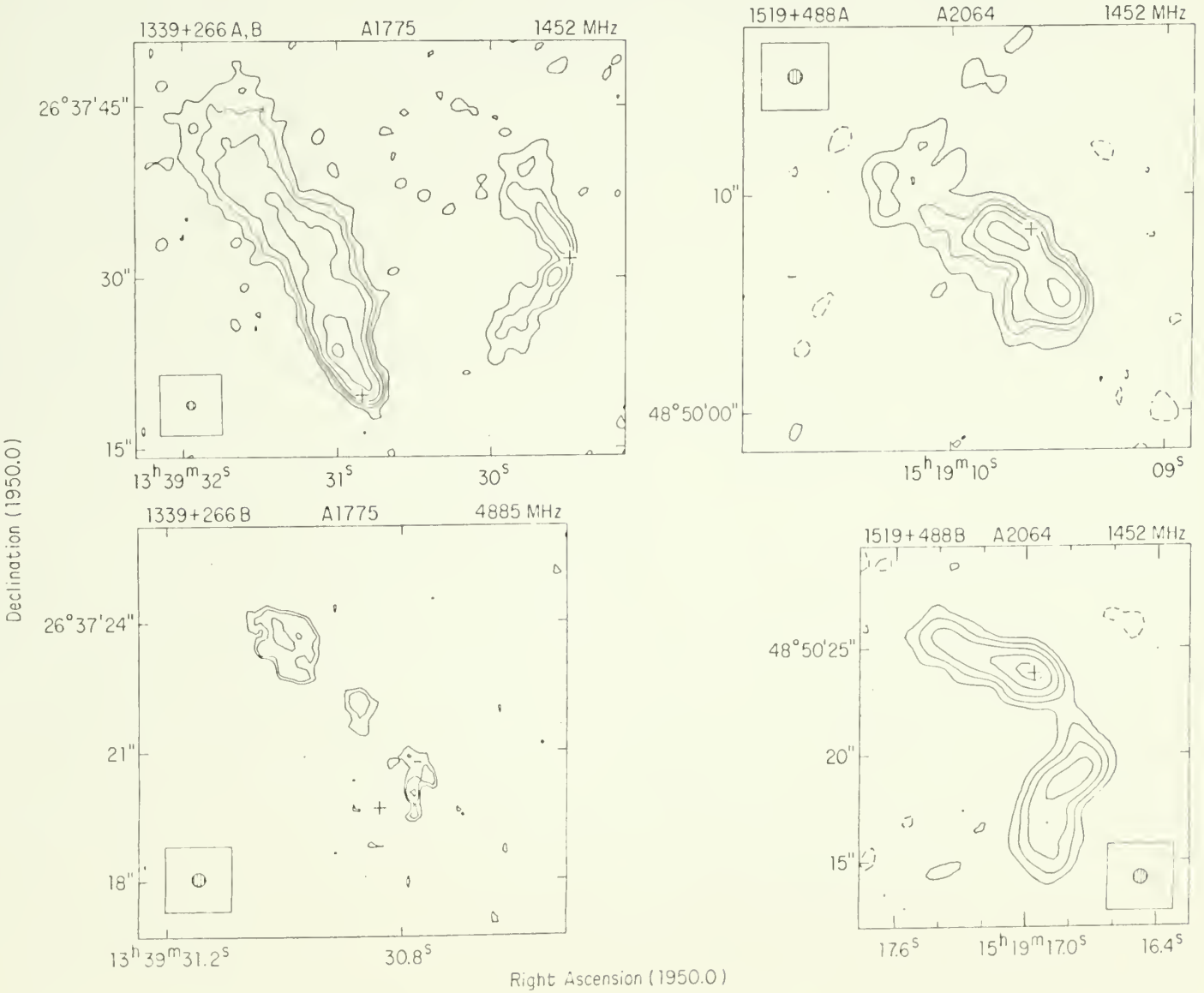
1339+266 A, B
A1775
1452 MHz
26°37'45"
30"
15"
13h39m32s
31s
30s
1519+488A
A2064
1452 MHz
10"
48°50'00"
15h19m10s
09s
1339+266 B
A1775
4885 MHz
26°37'24"
21"
18"
13h39m31.2s
30.8s
1519+488B
A2064
1452 MHz
48°50'25"
20"
15"
17.6s
15h19m17.0s
16.4s
Declination (1950.0)
Right Ascension (1950.0)

Figure 3.2k

B/W radiophotographs of the sources in Figure 3.1k.


1339+266A,B
1452 MHz

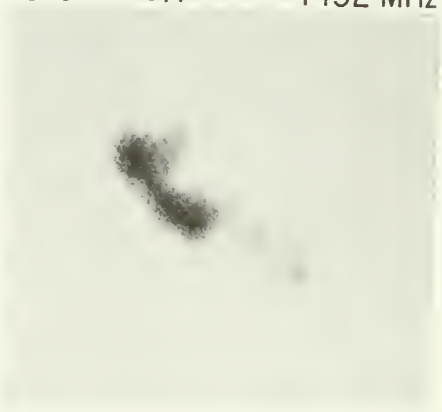
1519+488A
1452 MHz


1339+266 B
4885 MHz


1519+488B
1452 MHz

produce a leading blob similar to that seen in 2247+11 (Hardee, Eilek, and Owen 1980) and 1615+351. Higher resolution observations are needed in order to test this hypothesis.

A 2142: Previous low resolution (>23") observations of 1556+274 suggested that this source was a NAT (Harris et al. 1977, Harris et al. 1980a). The 4."2x4."0 resolution map presented here shows only a single trail of emission, consistent with the earlier maps.

Zw 1615.8+3505: The NAT 1615+351 has been studied by Ekers et al. (1978); Burns (1979); Owen et al. (1979); Fanti et al. (1981); and Burns and Gregory (1982). The 1."0 resolution map shows an edge brightened blob to the east (in front?) of the unresolved core. There is a hint of a faint jet (~0.2 mJy/beam; not seen in the contour map) connecting the blob with the core. This structure might be produced if the beams were ejected parallel and anti-parallel to the direction of motion of the galaxy (as suggested for 2247+11 by Hardee, Eilek, and Owen 1980). In this model, the beam ejected into the direction of motion would interact with the ICM in a manner more typical of double radio sources and might form the observed edge-brightened lobe.

A 2172: Observations of 1615+425 by Owen et al. (1982b) suggested that the source was a NAT. The 1."1x1."0 resolution map presented here shows twin (initially fairly straight) jets which expand and change direction in hot spots located ~10" (26 kpc) from the core. This

Figure 3.11

See Figure 3.1a. 1556+274: -0.4, 0.4, 1, 3, 7, 12, 18, (4.2"x4.0" @-79.5°); 1615+425: -0.4, 0.4, 0.8, 1.2, 1.8, (1.1" 1.0" @-38.2°); 1619+428: -0.3, 0.3, 0.7, 1.2, 2.5, (1.5"x1.3" @-54°); 1615+351: -0.4, 0.4, 1, 2, 6, 15, (1.0").

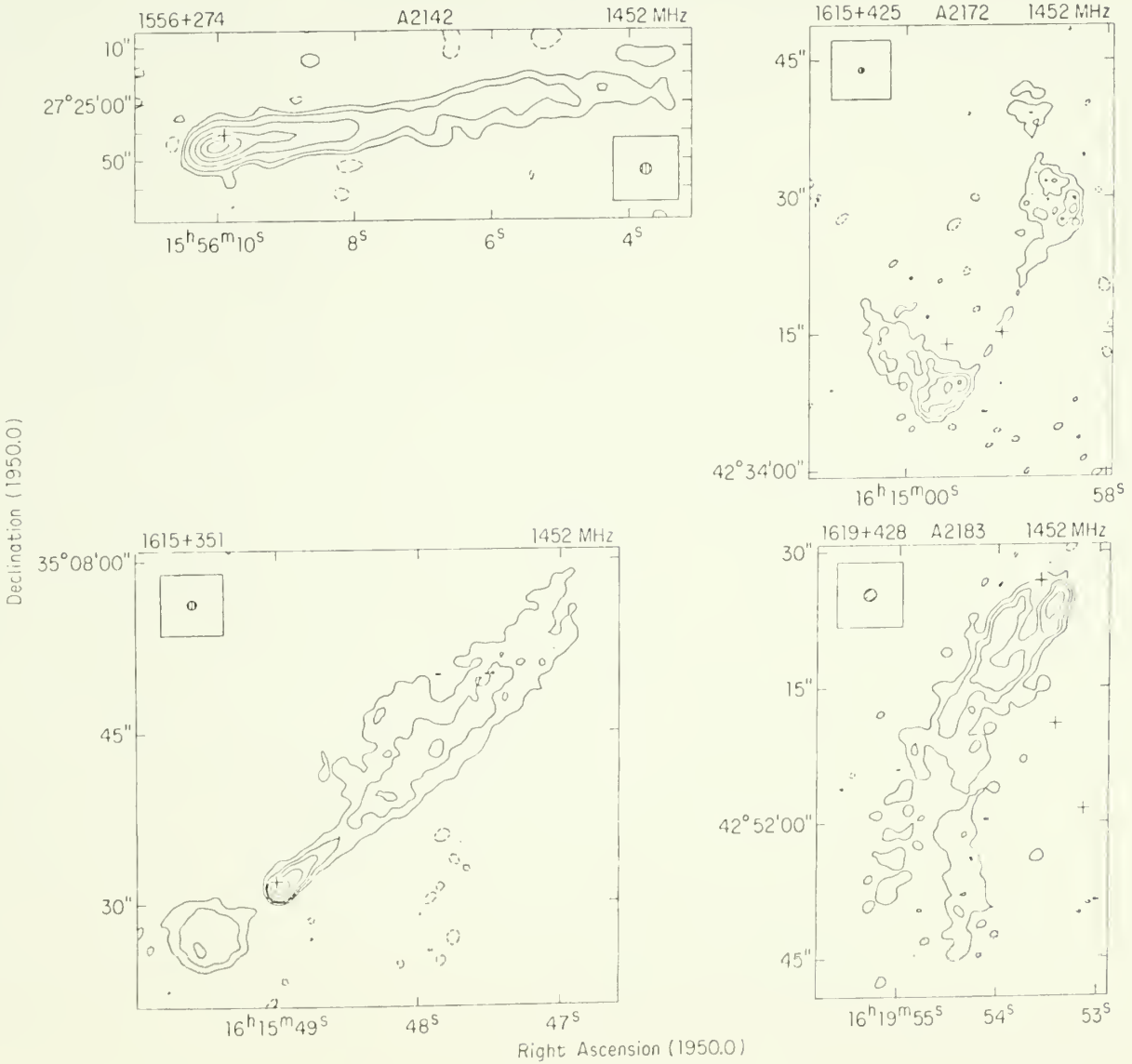
1556+274
A2142
1452 MHz
10"
27°25'00"
50"
15h56m10s
8s
6s
4s
1615+425
A2172
1452 MHz
45"
30"
15"
42°34'00"
16h15m00s
58s
1615+351
1452 MHz
35°08'00"
45"
30"
16h15m49s
48s
47s
1619+428
A2183
1452 MHz
30"
15"
42°52'00"
45"
16h19m55s
54s
53s
Declination (1950.0)
Right Ascension (1950.0)

Figure 3.21

B/W radiophotographs of the sources in Figure 3.11.


1556+274
1452 MHz


1615+425
1452 MHz

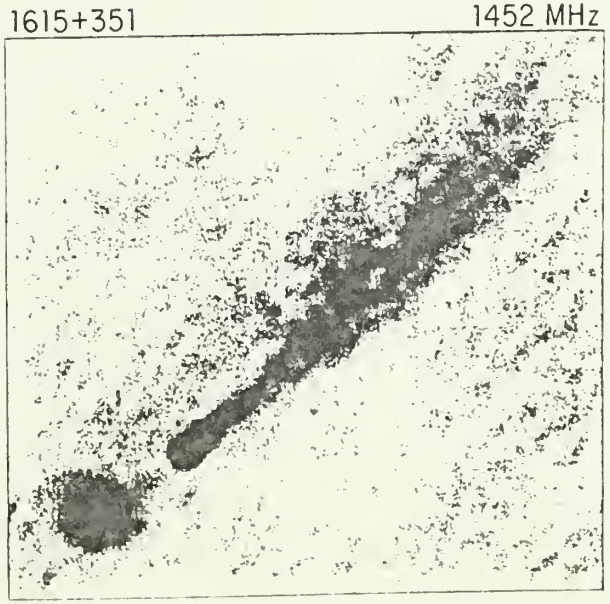
1615+351
1452 MHz


1619+428
1452 MHz

structure is similar to that observed in WATs (e.g., Owen and Rudnick 1976, Eilek et al. 1984) leading to the classification of this source as a WAT.

A 2183: 1619+428 was shown to be a NAT by Owen et al. (1982b). The source is shown to be a twin tail source by the 1."5x1."3 resolution map presented here. The tapered map (22."7x13."4) reveals a detached low surface brightness blob about 25" (68 kpc) beyond the main body of the NAT. If this blob is part of the source, it would increase the source length to ~256 kpc and would imply a projected curvature in the tail of about 50°.

Zw 1611.6+3717: The NAT 1621+380 has been studied by Ekers et al. (1978). The 1."4x1."2 resolution map shows a rather sudden transition between the two collimated jets to the diffuse tail. Because of this, and its short projected length (~16 kpc), it seems likely that this source is seen at a small angle to its direction of motion. The two jets appear to be oriented parallel to the major axis of the optical galaxy (see Ulrich 1978 for an optical picture).

A 2197: 1624+406 has been mapped at 610 MHz (with a resolution of 53"x81") by Gavazzi and Perola (1980) who suggest the source is a NAT associated with NGC 6150. The 1452 MHz (3."7 resolution) map shows only a slight extension to the core in the direction of the single tail seen by Gavazzi and Perola.

Figure 3.1m

See Figure 3.1a. 1619+428: -0.5, 0.5, 2, 4, 6, 10, 15, 30, 50, (29.6"x16.6" @67.7°); 1624+406: -0.6, 0.6, 2, 5, 9, 15, (3.7"); 1658+326: -0.5, 0.5, 1, 2, 3, (2.2"); 1621+380: -0.4, 0.4, 1, 2.5, 5, 8, (1.4"x1.2" @-71°).

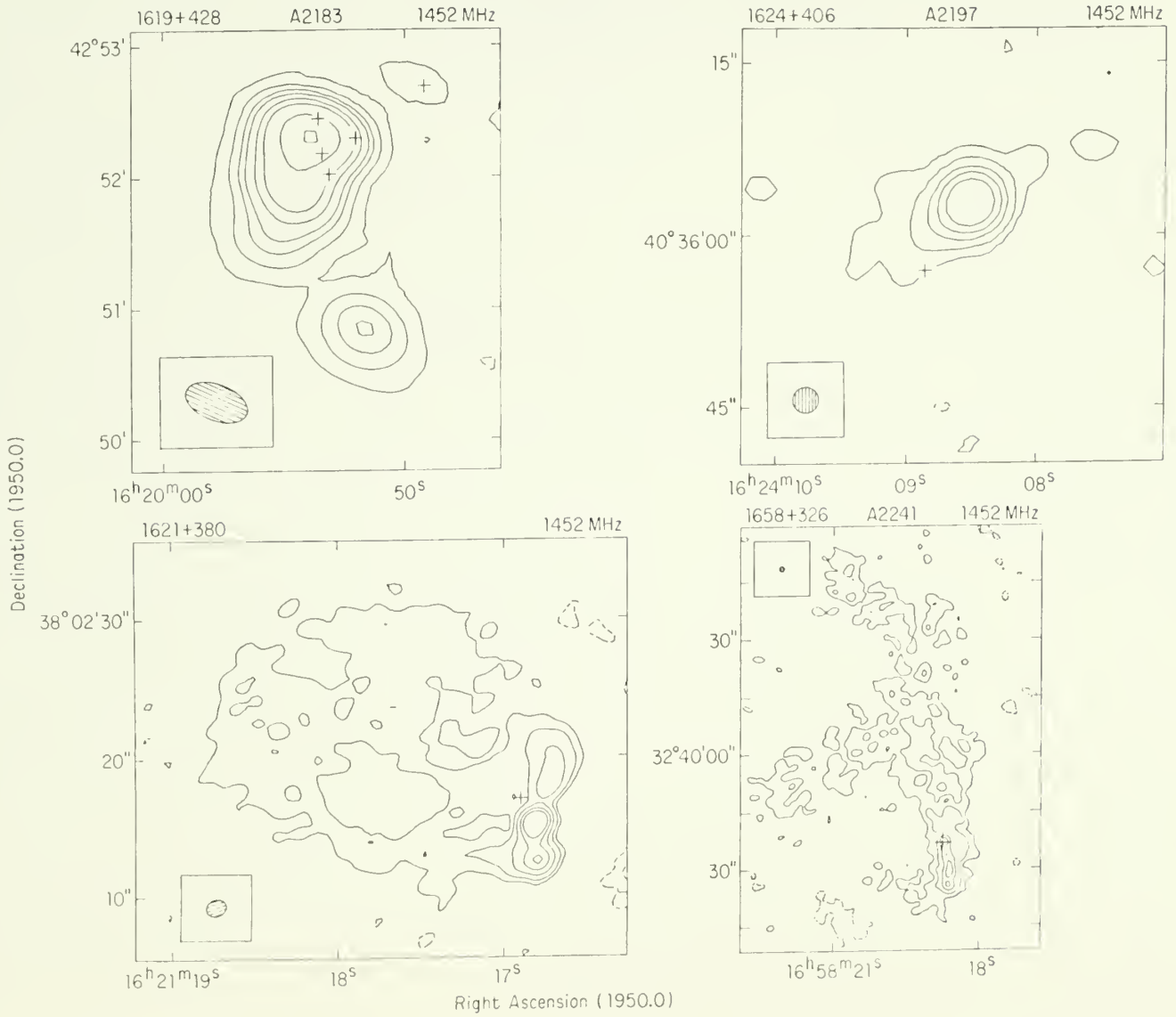
1619+428 A2183 1452 MHz
42°53'
52'
51'
50'
16h20m00s
50s
1624+406 A2197 1452 MHz
15"
40°36'00"
45"
16h24m10s
09s
08s
1621+380 1452 MHz
38°02'30"
20"
10"
16h21m19s
18s
17s
1658+326 A2241 1452 MHz
30"
32°40'00"
30"
16h58m21s
18s
Declination (1950.0)
Right Ascension (1950.0)

Figure 3.2m

B/W radiophotographs of the sources in Figure 3.1m.

1619+428

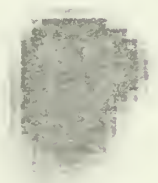

1624+406 1452 MHz

1621+380 1452 MHz

1658+326 1452 MHz

Figure 3.3d

Optical fields of cluster radio sources, reproduced from the E prints of the Palomar Sky Survey (copyright 1960, National Geographic Society - Palomar Sky Survey. Reproduced by permission of the California Institute of Technology). The positions of the objects denoted by the bars are given in Table 3.3. The scale in arcminutes and the orientation of the charts are shown in the top left corner.

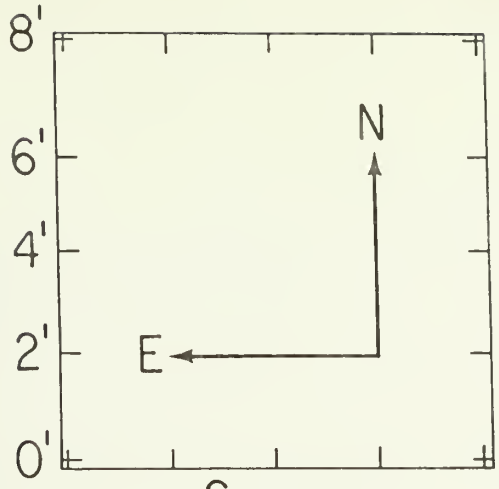

1330+507
A1758

1519+488A,B
A2064

1556+274
A2142

1615+425
A2172

1619+428
A2183

A 2241: Riley (1975) suggested that 1658+326 (4C 32.52E) was a tailed source. Low resolution observations by Bijleveld and Valentijn (1982) showed that the tail splits and bends, as in 1250-150. The tapered map (20."9x14."4) shown here is in agreement with Bijleveld and Valentijn. In addition, the 2."2 resolution map reveals the following features:

(1) a one sided jet directed south from the 3.5 mJy core; and

(2) the originally single tail splits into two tails at a projected distance of ~30" (62 kpc) from the compact core.

A 2250: 1709+397 has been mapped by Rudnick and Owen (1976); Miley and Harris (1977); Simon (1979); Owen et al. (1979); Harris et al. (1980a); and Harris, Kapahi, and Ekers (1980). A single tail is seen in the 1."8x1."4 resolution map of the region of the core. The tapered map (6."7x6."5) shows that the tail forks (as suggested by Miley and Harris) at a distance of ~2.'5 (195 kpc) from the core.

A 2255: 1712+638 is the lesser known of the two NATs in A 2255. It has been mapped by Harris, Kapahi and Ekers (1980) who christened it "The Beaver" because of its "body and tail" morphology. The 4."4x3."6 resolution map shows twin jets bending back from the core towards the diffuse tail. The other twin tail source, 1712+640 (4C 64.20.1), has been studied by Slingo (1974b); Rudnick and Owen (1976); Simon (1979); Owen et al. (1979); and Harris, Kapahi, and Ekers (1980) and so was not reobserved.

Figure 3.1n

See Figure 3.1a. 1658+326: -2, 2, 4, 6, 10, 15, 20, 25, 30, 35, (20.9"x14.4" @64.2°); 1709+397: -0.5, 0.5, 2, 5, 15, 50, (6.7"x6.5" @14.1°); 1712+638: -1.3, 1.3, 2.5, 3.5, 5, (4.4" 3.6" @20°); 1709+397: -0.4, 0.4, 1, 3, 7, 11, (1.8"x1.4" @-67°).

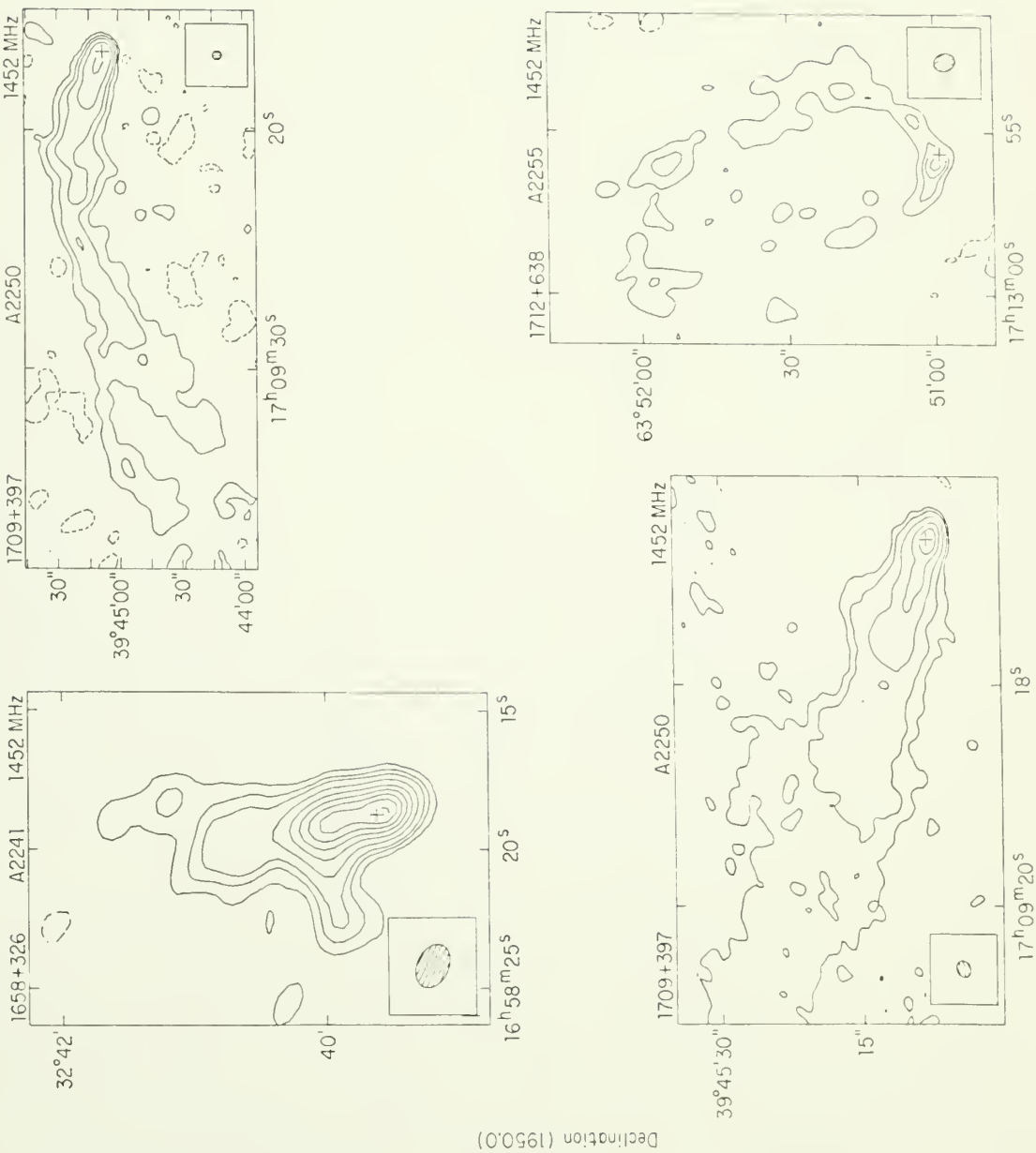
1658+326
A2241
1452 MHz
32°42'
40'
16h58m25s
20s
15s
1709+397
A2250
1452 MHz
39°45'00"
30"
44'00"
17h09m30s
20s
1712+638
A2255
1452 MHz
63°52'00"
30"
51'00"
17h13m00s
55s
1709+397
A2250
1452 MHz
39°45'30"
15"
17h09m20s
18s
Declination (1950.0)
Right Ascension (1950.0)

Figure 3.2n

B/W radiophotographs of the sources in Figure 3.1n.

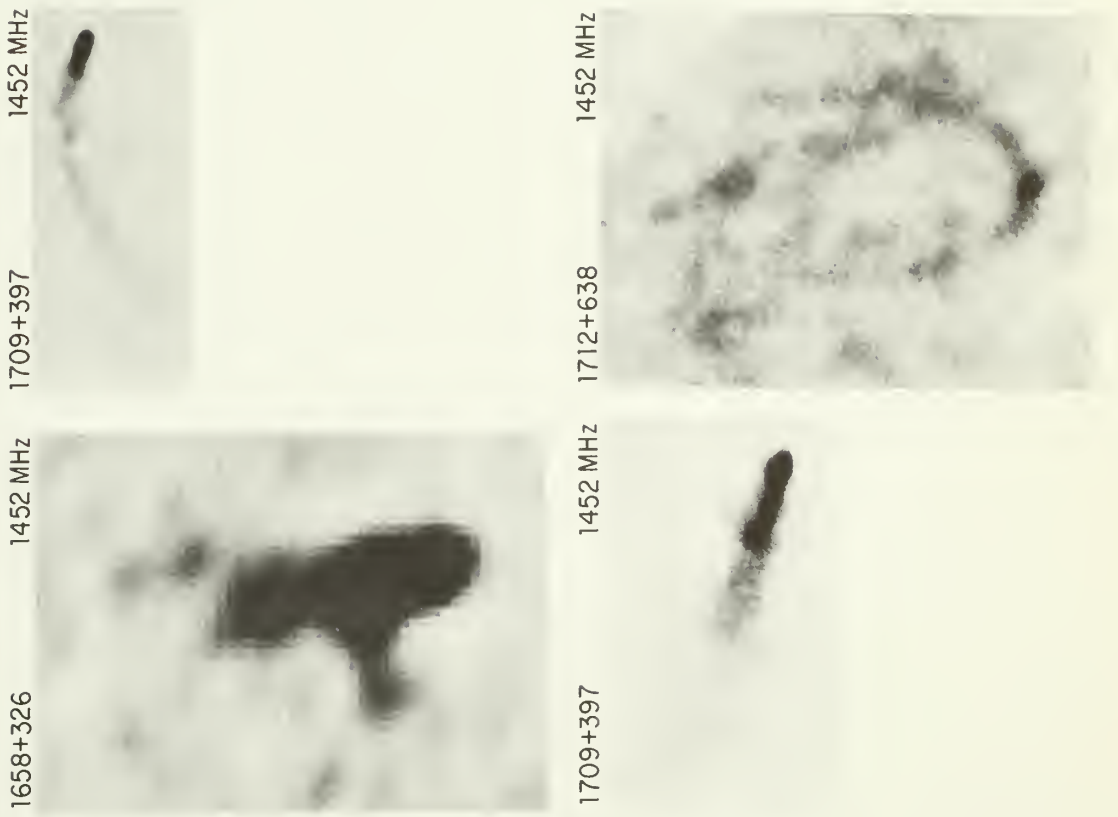
1658+326
1452 MHz
1709+397
1452 MHz
1709+397
1452 MHz
1712+638
1452 MHz

A 2256: A 2256 has been studied in detail by Bridle and Fomalont (1976), and Bridle et al. (1979), who find five NATs along with several other complex sources and a diffuse radio halo. The tapered map (4."0x3."6) of the center of the cluster shows four sources (including three NATs) also mapped at comparable resolution by Valentijn (1981). A close-up of the twin tail source 1705+786 (source B of Bridle et al.) at this resolution is also shown. The other three sources are shown at higher resolution (2."1x1."1). 1706+786 (A), also mapped by Rudnick and Owen (1976), and 1706+787 (C) are both single tail sources. 1707+787 (D) appears to be a bent double similar to 1257+282.

A 2289: 1753+580 was shown to be a twin tail source by Owen et al. (1982b). The source is shown here at 1."6x1."3 resolution. The jets are strikingly asymmetric and differ in brightness by a factor of ~23, with a gap in the west jet where the surface brightness falls below 0.3 mJy/beam.

A 2311: 1850+702 is a twin tail source (Owen et al. 1982b) shown here at 2."4x2."2 resolution. The two jets make a sudden transition to a diffuse tail at ~30" (~50 kpc) behind the core.

A 2319: Observations of 1918+439 by Birkinshaw (1978) and Harris and Miley (1978) suggested that the source was a NAT. The tapered map (7."5x7."4) shows twin tail structure, reminiscent of the early maps of NGC 1265 (e.g., Miley 1973).

Figure 3.1o

See Figure 3.1a. The center of Abell 2256: -0.5, 0.5, 1, 3, 7, 12, 18, 25, (4.0"x3.6" @60°).

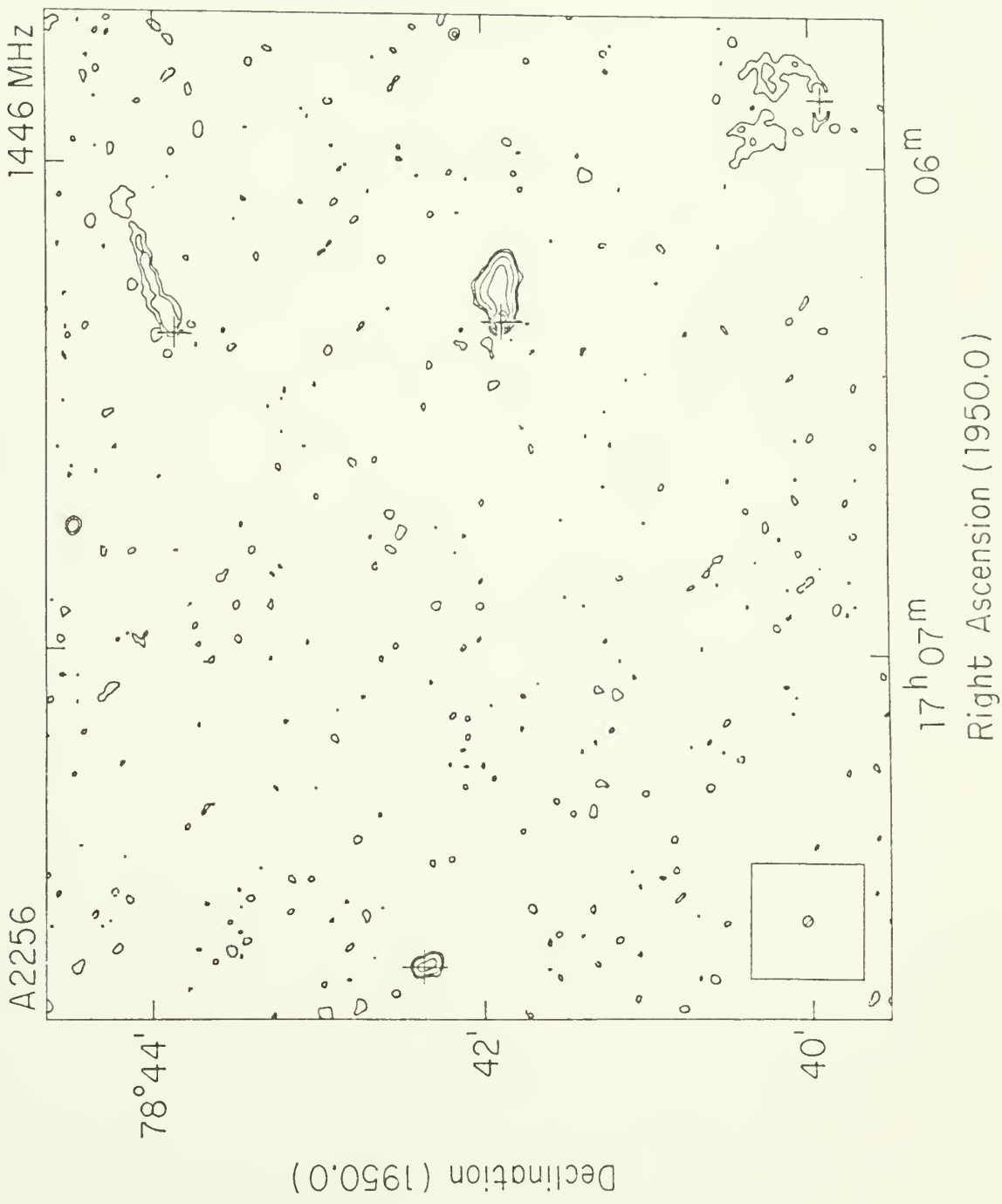
A2256
1446 MHz
78°44'
42'
40'
Declination (1950.0)
17h07m
06m
Right Ascension (1950.0)

Figure 3.2o

B/W radiophotographs of the sources in Figure 3.1o.


1446 MHz
A2256

Figure 3.1p

See Figure 3.1a. 1705+786: -0.5, 0.5, 1, 1.5, 2, 3, (4.0"x3.6" @60°); 1706+787: -0.4, 0.4, 0.8, 1.2, 2, (2.1"x1.1" @71.6°); 1707+787: -0.4, 0.4, 0.6, 0.8, 1, 1.5, (2.1"x1.1" @71.6°); 1706+786: -0.4, 0.4, 1, 2, 4, 7, 11, (2.1"x1.1" @71.6°).


1705+786
A2256
1446 MHz
1706+787
A2256
1446 MHz
1706+786
A2256
1446 MHz
1707+787
A2256
1446 MHz
Declination (1950.0)
Right Ascension (1950.0)

Figure 3.2p

B/W radiophotographs of the sources in Figure 3.1p.

1705+786 1446 MHz

1706+787 1446 MHz

1706+786 1446 MHz

1707+787 1446 MHz

A 2572: 2316+184 (OZ 127) was shown to be a twin tail source by Owen et al. (1982b). The lower resolution 1.4 GHz map by Fanti et al. (1983) (their A 2572-4) suggests that the tail does not extend much beyond what is seen in the 1."4x1."3 resolution map shown here. However, the integrated spectral index is rather steep (~-0.8 between 750 and 1410 MHz; Hoglund 1967). The source exhibits a sudden transition from well collimated jets to a diffuse tail. This source, as well as NGC 1265 and 1850+702 is the best example of the type of morphology expected from a galaxy with a turbulent galactic wake.

A 2593: Lower resolution observations of 2322+143A,B by Owen et al. (1982b) suggested that these two sources might be NATs. The 1."2 resolution map shows a single tail or jet source (2322+143B) with wiggles in the tail. 2322+143A appears to be a straight twin jet source embedded in diffuse emission. The latter source might be a tailed source seen at a very small angle to its direction of motion (perhaps a more extreme version of 1621+380). It could also be a leaky beam (cf. B2 1321+31, Fanti et al. 1982; or NGC 1265, Chap. V). (The faint stripes in the diffuse emission in 2322+143A are probably due to an instability in CLEAN (Cornwell 1983).)

3.4 Discussion

The sources presented in this paper make up a diverse rogues' gallery. It is clear from these observations that the NAT phenomenon

Figure 3.1q

See Figure 3.1a. 1753+580: -0.4, 0.4, 0.8, 1.5, 2.5, 5, (1.6"x1.3" @-55.6°); 1918+439: -1, 1, 2, 3, 4, (7.5"x7.4" @-47°); 2316+184: -0.3, 0.3, 1, 4, 8, (1.4"x1.3" @-38°); 1850+702: -0.4, 0.4, 0.8, 1.5, 4, (2.4"x2.2" @-37°).

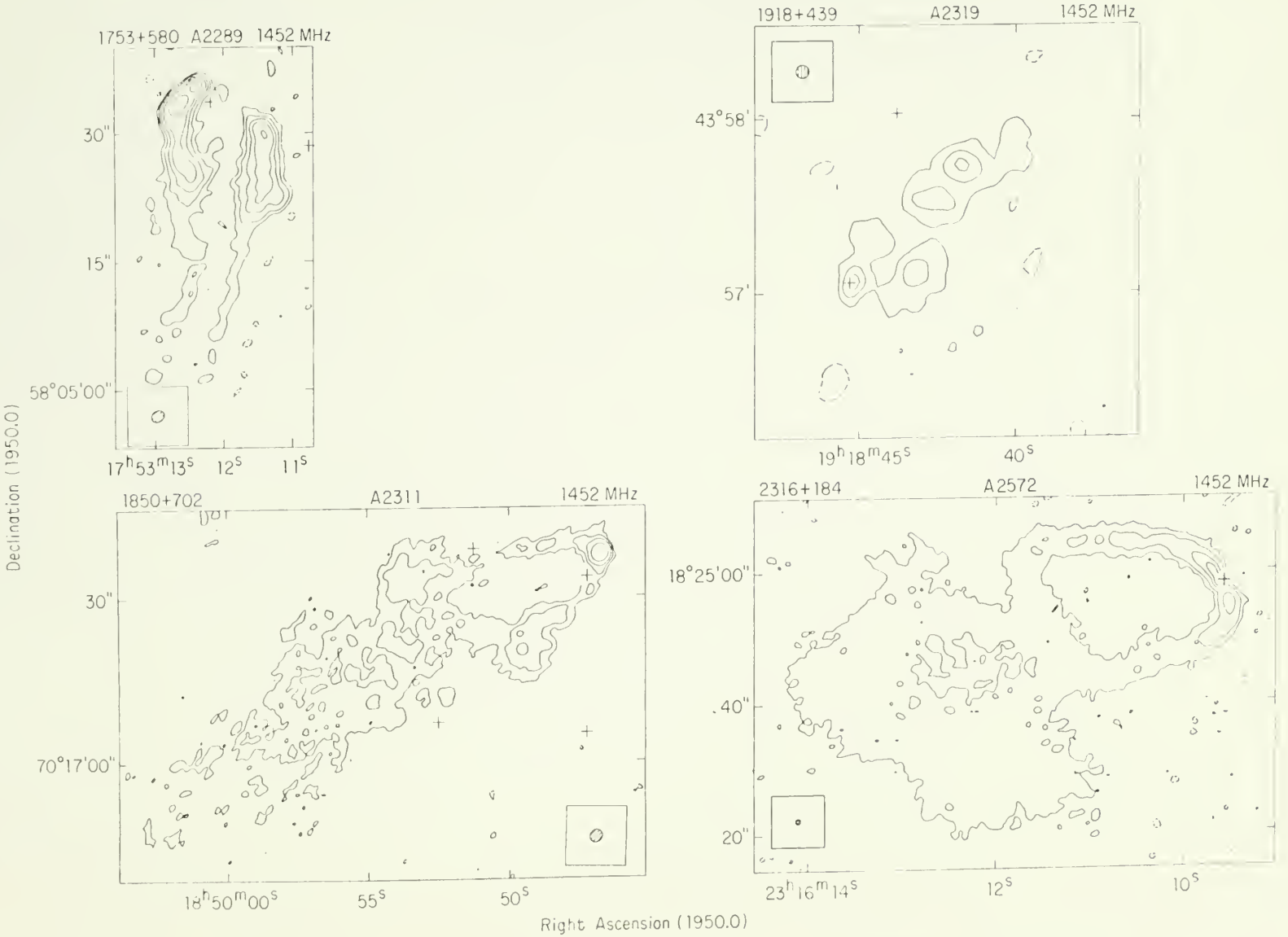
1753+580 A2289 1452 MHz
30"
15"
58°05'00"
17h53m13s 12s 11s
1918+439 A2319 1452 MHz
43°58'
57'
19h18m45s 40s
1850+702 A2311 1452 MHz
30"
70°17'00"
18h50m00s 55s 50s
2316+184 A2572 1452 MHz
18°25'00"
40"
20"
23h16m14s 12s 10s
Declination (1950.0)
Right Ascension (1950.0)

Figure 3.2q

B/W radiophotographs of the sources in Figure 3.1q.

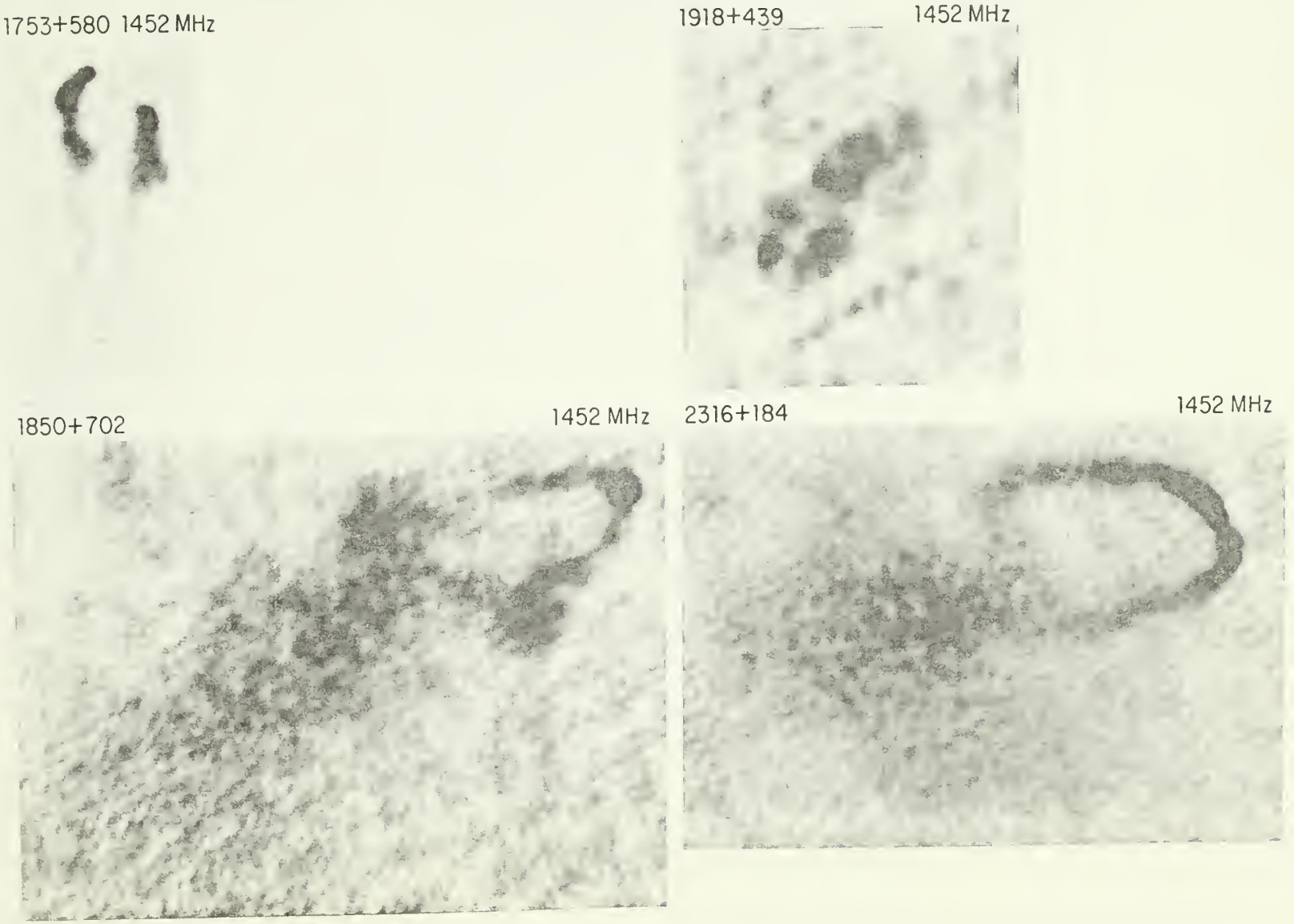
1753+580 1452 MHz
1918+439 1452 MHz
1850+702 1452 MHz
2316+184 1452 MHz

Figure 3.1r

See Figure 3.1a. 2322+143A,B: -0.5, 0.5, 1, 2, 4, 7, (1.2").

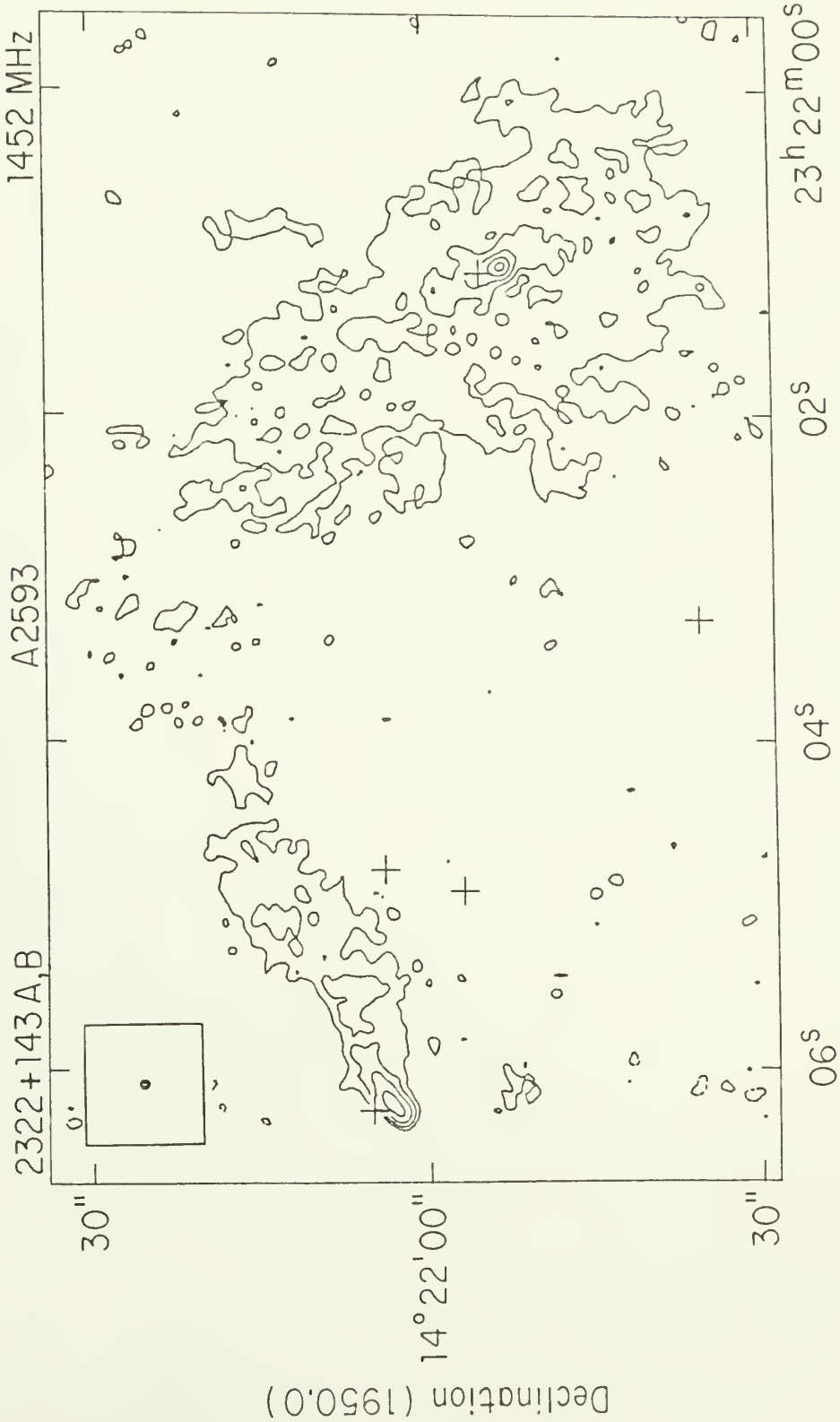
1452 MHz
A2593
2322+143 A,B
30"
14°22'00"
30"
06s
04s
02s
23h22m00s
Declination (1950.0)
Right Ascension (1950.0)

Figure 3.2r

B/W radiophotographs of the sources in Figure 3.1r.

2322+143A,B

1452 MHz

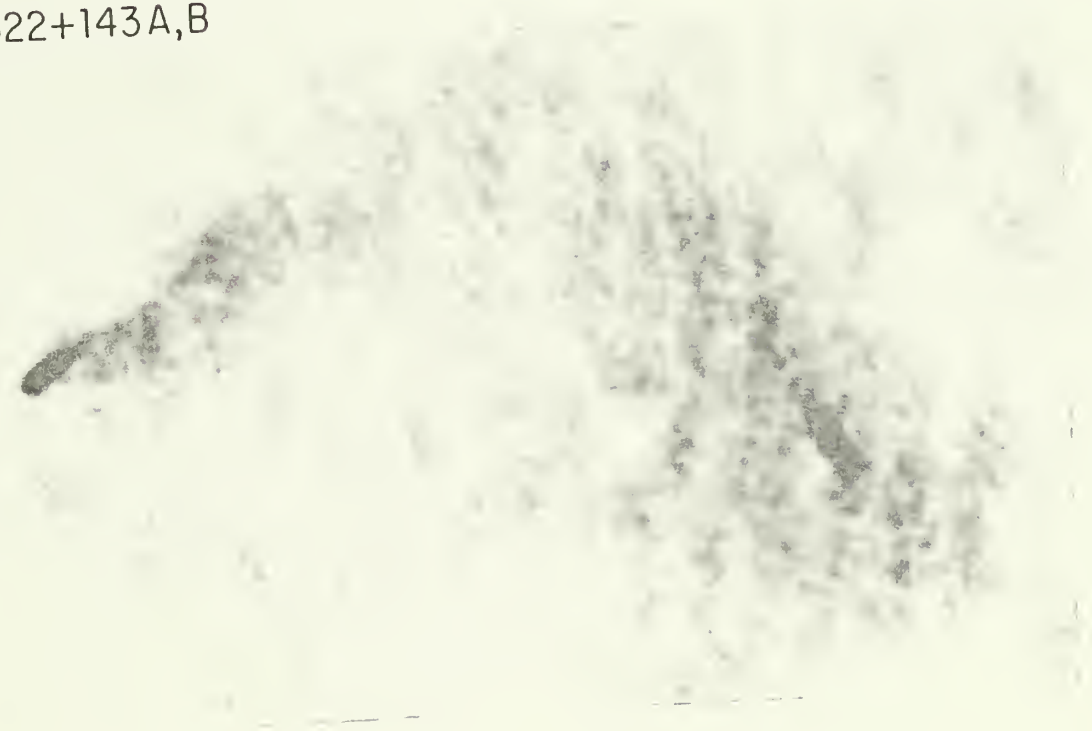

Figure 3.3e

Optical fields of cluster radio sources, reproduced from the E prints of the Palomar Sky Survey (copyright 1960, National Geographic Society - Palomar Sky Survey. Reproduced by permission of the California Institute of Technology). The positions of the objects denoted by the bars are given in Table 3.3. The scale in arcminutes and the orientation of the charts are shown in the top left corner.

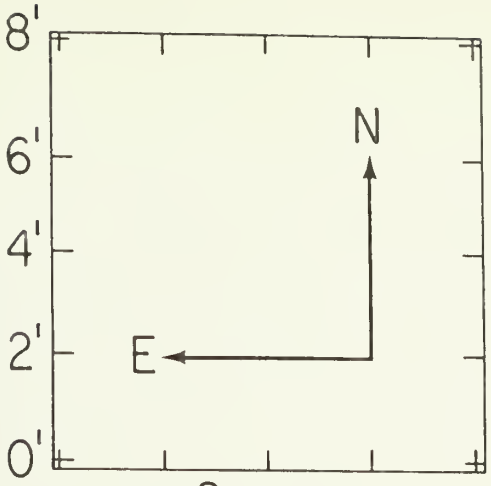

Source
(Cluster)

1753+580
A2289

1850+702
A2311

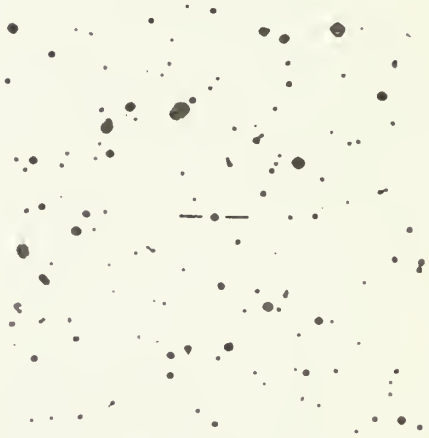

1918+439
A2319

2316+184
A2572

2322+143A,B
A2593

encompasses a much larger variation in morphology than previously thought. The results are summarized below for the various groups of objects.

Narrow angle tail sources

Observations of 41 NATs are presented. Only 10 of them are single tail sources, i.e., 0039-095A, 0309+411, 0905-098, 1339+266B?, 1519+488A, 1556+274, 1624+406?, 1706+786, 1706+787, and 2322+143B. The observations presented here increase the percentage of NATs with twin jets by a factor of 3 (from 25% (e.g., Simon 1978, Valentijn 1979) to 75%). Since some of the single tail NATs may be single jet sources instead of tail sources (e.g., 0905-098; Harris, Costain and Dewdney 1984), it is likely that the actual percentage is even higher.

The remaining twin tail sources appear to fall into two classes based on morphology (i.e., the nature of the jet/tail transition). In one group the jets make a very sudden transition into broad, diffuse tails (e.g., NGC 1265, 1850+702, and 2316+184). In the other group, the jets do not change structure as radically, but expand much more gradually and may eventually merge into a single tail (e.g., 0039+211, 0647+693, 1055+570B, 1256+282, 1619+428, and 1753+580). The possible significance of this is discussed in Chapter IV.

With the exception of NGC 1265, the jets in the twin jet sources are basically unresolved by these observations, with typical upper limits to the jet radius of ~1-2 kpc.

Some of the NATs (e.g., 0039+211, 0431-134, 0907-091, 1621+380, 1712+638, and 2316+184) have jets which are brightest right near the core and become dimmer with increasing distance from the core. This is in contrast with higher luminosity jets which tend to have "gaps" in the jet emission right near the core (e.g., Perley et al. 1980). If these gaps are greater than ~2-3 kpc in size, they would have been resolved by these observations and would have been seen. NGC 1265 is the only clear example of a NAT with such a gap, and high sensitivity observations show weak emission in the gap (Chap. V). It is not yet clear why this difference between high and low luminosity jets exists. One possibility is that the lower luminosity sources have lower Mach numbers and/or beam velocities which allows particle acceleration to "turn on" the jets closer to the core.

Of these 41 NATs, there are 11 sources which exhibit large scale curvature in the tails (i.e., 0314+416 (Miley 1973 and Chap. V), 0335+096, 0431-134, 0905-098, 1108+411, 1244+699, 1250-150, 1256+282 (Willson 1970), 1619+428, 1658+326 (see also Bijleveld and Valentijn 1982), and 1709+397 (see also Miley and Harris 1977)). Possible explanations for this include curved trajectories through the ICM and buoyancy effects (e.g., Cowie and McKee 1975; Gisler and Miley 1979; Burns 1979; Harris 1982).

Although most twin tail NATs have similar brightness ratios between the opposing jets, there are a few with high ratios (e.g., 0039+21) and 1753+580). Since it is unlikely that this difference is produced

by relativistic Doppler boosting (see Chap. VII), the difference must be intrinsic or produced by environmental effects (e.g., differing entrainment, turbulence, development of particle acceleration, etc.).

Wide angle tail sources

Observations are presented here of nine WATs, i.e., 0304-123A, 0327+246B, 0658+330, 0704+351, 1257+282, 1339+266A, 1519+488A, 1615+426, and 1707+787. All are associated with relatively dominant galaxies (rank 1 or 2). Three of them (1257+282, 1339+266A, and 1519+488B) have small radio sizes (<25 kpc), are "V" shaped, have no visible compact core, and may be contained entirely within the extent of the optical galaxy.

cD galaxies

0039-095B (A 85) and 0258+356 (A 407) are radio sources with complex diffuse structure associated with cD galaxies (i.e., very dominant galaxies in the center of the cluster; rank 1).

"Jet" sources

A few sources with complex morphology were mapped whose structure is not obviously either WAT or NAT. 0154+319 and 2322+143A are single and twin jet sources, respectively. 0123-016B is a "double" with extremely distorted jets and diffuse lobes. Finally, 0704+351 appears to be two physically interacting twin jet sources.

CHAPTER IV

THE GLOBAL PROPERTIES OF THE NAT SAMPLE

In this chapter the global and statistical properties of the Narrow Angle Tail (NAT) sample are examined. The statistical analysis complements the very detailed analysis of NGC 1265 (3C 83.1B) in Chapters V and VI. At some level, every individual source is unique. There will be peculiarities and quirks which set each source apart from other members of its class. The purpose of this chapter is to step back and try to understand the general characteristics of NATs and how they reflect the interaction of the radio plasma with its environment. The data presented in Chapter III increase the number of sources for which there are high sensitivity, arcsecond resolution maps by about a factor of 10. This allows, for the first time, a study of the correlations of the properties of NATs as a function of morphology within the class.

The selection criteria for the sample are discussed. Tables of the cluster and radio source properties of 51 NATs in Abell clusters are presented. The global properties of this heterogeneous sample of 51 sources as well as those of a homogeneous subsample of 39 NATs are investigated. The dependence of the probability that a cluster will contain a NAT on cluster richness, Bautz-Morgan type and Rood-Sastry type is examined. The distributions of core power, integrated power, width, velocity, and distance from the cluster center for rank 2 and 3 galaxies are compared. The relationships between core power and integrated power, width and integrated power, length and integrated power, velocity and integrated power, and morphology and width are studied. The nature of single tail sources is discussed. The

implications for the models for tailed sources are examined. Finally, the results are summarized.

4.1 The Sample

A set of two criteria which define a homogeneous and representative (but not complete) sample was established. These criteria came naturally from the Abell cluster survey of Owen et al. (1982a). Fourteen hundred and seventy-eight Abell clusters were searched for radio sources with flux densities $\geq$ 0.1 Jy at 1.4 GHz located within 0.5 corrected Abell radii, A_c of an Abell cluster center,

$$A_c = \frac{103\ q_o^2\ (1 + z)^2}{(q_o z + [(1 + 2q_o\ z)^{1/2} - 1]\ (q_o - 1))} \text{ arcsec} \qquad (4.1)$$

(e.g., Rudnick and Owen 1977), where q_o is the deceleration parameter and z is the cluster redshift. A total of 485 radio sources in the directions of 442 Abell clusters were found. This sample is 100% complete (for declinations north of $\delta = -19°$ for richness class $\geq$ 3 and 98.5% complete for $m_{10} < 17.0$ (Owen et al. 1982a).

The single dish survey of Owen et al. (1982a) has been followed by aperture synthesis observations of the detected sources (Owen et al. 1982b). The VLA snapshot observations of Owen and collaborators have uncovered many tailed sources. At least twenty-one potential NATs from the Owen et al. survey were included in the high resolution observations conducted for the thesis and presented in Chapter III.

By combining the observations of 38 NATs from Chapter III with observations of 13 other sources from the literature, a total of 51 NATs in Abell clusters were collected. Of these sources, 39 satisfied the following criteria which were used to define a homogeneous subsample:

(1) They have a total flux density $\geq$ 0.1 Jy at 1.4 GHz.

(2) They are located within 0.5 corrected Abell cluster radii, A_c, from an Abell cluster center. This second criterion is applied because many radio surveys of sources in the directions of Abell clusters have concentrated on the inner parts of the clusters (e.g., Owen 1974, 1975; Riley 1975; McHardy 1978; Owen et al. 1982a,b). Thus, sources further than about ~0.5 A_c from the cluster center are under-represented in the present statistical samples. The remaining sources failed to meet one or both criteria.

This sample cannot be considered complete because:

(1) Not all of the clusters in Abell's complete subsample have been observed. In addition, as the reduction of the VLA observations of the Owen et al. sample progressed, additional NATs which met the sample criteria were discovered too late to be included in this work.

(2) Some sources may have been missed because they did not appear to be NATs in the earlier maps. Sources whose direction of motion is nearly along the line of sight may have been selected against.

(3) The flux density limit for the homogeneous sample of 0.1 Jy corresponds to a minimum detectable power of $P_{1.4} = 2 \times 10^{24}$ W/Hz at a redshift of 0.1. From the observations of very nearby clusters (e.g., Perseus and Coma), it is known that the powers of NATs can be as low as

10^{23} W/Hz. Thus the intrinsically weaker sources in more distant clusters are selected against.

However, the homogeneous sample of 39 NATs is probably representative of the class of NATs in rich clusters as a whole. Except for the range in total powers, in every case where the properties of the heterogeneous and homogeneous samples are compared, the results are in agreement (see below).

All physical parameters were calculated assuming a Hubble constant of H_o = 75 km sec^{-1} Mpc^{-1} and deceleration parameter of q_o = 0.1. This choice for H_o results in an equivalent linear size for A_c of 2 Mpc.

The "cluster" properties of the 51 NATs are given in Tables 4.1A and 4.2B. The contents of Table 4.1A are as follows. The source name is given in column 1. The cluster number (Abell 1958) is given in column 2. The redshift and a reference are given in column 3. Cluster membership has not yet been confirmed for about half of the NATs. In this work it is assumed that all NATs are members of the coincident clusters. The richness class, R, (Abell 1958) is given in column 4. The Bautz-Morgan (1970) (BM) classification and a reference are given in column 5. For compactness, the notation used is: 1 = BM I, 2 = BM I-II, 3 = BM II, 4 = BM II-III, 5 = BM III, and a colon (e.g., 4:) designates an uncertain classification. The Rood-Sastry (1971) (RS) classification (taken from Struble and Rood 1982, 1983) for the clusters in distance class $\leq$ 5 is given in column 6. The distance of the optical galaxy from the center of the cluster (D_c) in units of corrected Abell radii (Rudnick and Owen 1977) is given in column 7. The coordinates of the cluster

centers were taken from Sastry and Rood (1971) and Bahcall (1975). Abell (1958) estimates that the errors in the cluster center positions are

Table 4.1A

Cluster Properties of NATs in Abell Clusters

Name	Cluster	Z	R	BM	RS	D_c	Rank	In Sample?
0039+211	0084	0.1015 1	1	3: 4	L6a	0.13	2	Y
0039-095A	0085	0.0518 2	1	1 4	cD	0.14	3	N
0039-097	"	"	"	"	"	0.14	3	Y
0053-016	0119	0.0437 2	1	4 5	C12	0.10	3	Y
0053-015	"	"	"	"	"	0.003	2	Y
0123-016A	0194	0.0186 2	0	3 5	L6a	0.02	2	Y
0255+133	0401	0.0748 2	2	1 5	cD	0.26	3	Y
0256+132	"	"	"	"	"	0.43	3	Y
0309+411	0426	0.0183 2	2	4 5	L9	0.62	3	N
0313+411	"	"	"	"	"	0.22	3	Y
0314+412	"	"	"	"	"	0.15	3	N
0314+416	"	"	"	"	"	0.21	3	Y
0431-134	0496	0.0316 2	1	1: 4	cD	0.19	3	Y
0457+054	0526	0.0541 1	1		I_c	0.20	3	Y
0647+693	0562	0.110 1	1	4 4	L8a	0.41	2	Y
0810+665	0629	0.1502 1	1	5 4	C7	0.05	2	Y
0905-098	0754	0.0528 2	2	2 4	cD_s	0.65	3	N
0907-091	"	"	"	"	"	0.49	3	Y
1055+570A	1132	0.1363 2	1	5 4	B	0.15	2	N
1055+570B	"	"	"	"	"	0.13	3	Y
1108+411	1190	0.0738 2	2	3: 4	B	0.09	2	Y
1131+493	1314	0.0341 2	0	5 4	C8	0.15	2	Y
1132+492	1314	"	"	"	"	0.11	3	Y
1142+198	1367	0.0213 2	2	4 4	F	0.20	2	Y
1200+519	1452	0.0631 2	0	5 6	C8	0.23	2	Y
1227+119	1552	0.102 3	1	3 4	B	0.20	2	Y
1244+699	1614	0.157 3	1	5 4		0.18	2	Y
1250-150	1631	0.053 2	0	1 4	C11	0.18	3	Y
1256+282	1656	0.0235 2	2	3 5	B	0.10	3	Y
1330+507	1758	0.280 2	3	5 4		0.27	3	Y
1339+266	1775	0.0709 2	2	3: 7	B_b	~0.0	2	Y
1502+287	2022	0.0564 2	1	5 5	F	0.29	2	Y
1519+488	2064	0.1074 1	0		L7a	0.18	3	N
1556+274	2142	0.0904 2	2	3 4	B_b	0.11	3	Y
1619+428	2183	0.131 3	1	3 4	C8	0.17	3	Y
1624+406	2197	0.0303 2	1	3 5	L8a	0.54	2	N
1638+538	2220	0.1106 2	0	4 7		0.20	2	Y
1658+326[a]	2241E	0.1021 2	0	1 6	cD	0.33	3	Y
1709+397	2250	0.0654 2	1	5: 4	C9	0.17	2	Y

Table 4.1A - Continued

Name	Cluster	Z		R	BM		RS	D_c	Rank	In Sample?
1712+638	2255	0.0821	2	2	4	5	C12	0.76	3	N
1712+640	"	"		"		"	"	0.15	3	Y
1703+787	2256	0.0601	2	2	5	5	B	0.83	3	N
1705+786	"	"		"		"	"	0.11	3	N
1706+786	"	"		"		"	"	0.05	3	Y
1706+787	"	"		"		"	"	0.07	3	N
1712+787	"	"		"		"	"	0.52	3	N
1753+580	2289	0.160	3	1				0.04	3	Y
1850+702	2311	0.079	3	1	5	4	I_s	0.13	3	Y
1918+439	2319	0.0529	2	1	4	4	cD_s	0.31	3	Y
2316+184	2572	0.0395	2	0	5	4	F	0.11	3	Y
2322+143B	2593	0.0440	2	0	3	4	F	0.04	3	Y

Notes to Table 4.1A

(a) A 2241 is actually two superposed clusters (Spinrad and Bahcall 1976), A 2241E (z=0.101) and A 2241W (z=0.056). Spinrad and Bahcall also suggest a revision of the RS type from I_s to cD.

Table 4.1B

Cluster Properties of NATs in Abell Clusters

Name	Cluster $\langle v_r \rangle$ (km/sec)	Ref.	NAT $\langle v_r \rangle - v_{NAT}$ (km/sec)	Ref.
0039+211				
0039-095A				
0039-097				
0053-016	449	24	600	25
0053-015	"		1625	24
0123-016A	435	8	-108	8
0255+133	1294	9	2880	10
0256+132	"		-890	10
0309+411	1396	11		
0313+411	"		130	12
0314+412	"		1037	12
0314+416	"		-2200	12
0431-134				
0457+054				
0647+693				

Table 4.1B - Continued

Name	Cluster $\langle v_r \rangle$ (km/sec)	Ref.	NAT $\langle v_r \rangle - v_{NAT}$ (km/sec)	Ref.
0810+665				
0905-098	1191	13	300	14
0907-091	"		-1777	15,13
1055+570A				
1055+570B				
1108+411				
1131+493	678	9	547	16
1132+492	"		436	16
1142+198	847	11	-52	17
1200+519	503	18	-200	18
1227+119				
1244+699				
1250-150				
1256+282	888	9	99	19
1339+266	1552	20	797	20
1502+287				
1519+488				
1556+274	1241	9		
1619+428				
1624+406	352	21		
1638+538				
1658+326				
1709+397	693	18	759	18
1712+638	1209	22	-715	22
1712+640	"		273	23
1703+787	1274	15		
1705+786	"		1543	18,26
1706+786	"		262	18,26
1706+787	"		244	18,26
1712+787	"			
1753+580				
1850+702				
1918+439	1627	15		
2316+184				
2322+143B				

References for Table 4.1B

1. Owen and White 1983, private communication

2. Sarazin, Rood, and Struble (1982)

3. Owen et al. (1982a)
4. Leir and Van den Bergh (1977)
5. Bautz and Morgan (1970)
6. Simon (1978)
7. McHardy (1979)
8. Chincarini and Rood (1977)
9. Hintzen and Scott (1979)
10. Hintzen, Scott, and Tarenghi (1977)
11. Faber and Dressler (1976)
12. Chincarini and Rood (1971)
13. Melnick and Quintana (1981a)
14. Harris, Costain, and Dewdney (1984)
15. Faber and Dressler (1977)
16. Coleman et al. (1976)
17. Dickens and Moss (1976)
18. Ulrich (1978)
19. Rood et al. (1972)
20. Hintzen (1979)
21. Yahil and Vidal (1977)
22. Hintzen and Scott (1980)
23. Stauffer, Spinrad, and Sargent (1979)
24. Melnick and Quintana (1981b)
25. Grandi (1983)
26. Bridle and Fomalont (1976)

typically a few arcminutes and are slightly higher for the closest clusters. The error in D_c is due almost entirely to the error in the position for the cluster center, since the error in the galaxy positions is about ~1" and is negligible in comparison. Assuming an error of 2' for the cluster center positions, and using the definition of A_c given by Rudnick and Owen (1977), the error in D_c (in units of A_c) is then given by

$$\Delta D_c \simeq \frac{1.17\left[q_o z + \left((1 + 2q_o z)^{1/2} - 1\right)(q_o - 1)\right]}{q_o^2 (1 + z)^2} \quad ; \qquad (4.2)$$

e.g., at $z = 0.01$, $\Delta D_c \simeq 0.01$.

The relative rank of the galaxy (as defined by Rudnick and Owen 1976) is given in column 8. Rank 1 denotes the dominant galaxy in the cluster, rank 2 denotes a galaxy whose brightness is comparable to that of the brightest galaxy, and rank 3 denotes a galaxy which is much fainter than the dominant galaxy. Finally, whether or not the source satisfies the two selection criteria for the homogeneous sample is given in column 9 (Yes or No).

The contents of Table 4.1B are as follows: The source name is given in column 1. The cluster radial velocity dispersion (in kilometers per second) and a reference are given in columns 2 and 3, respectively. The radial velocity of the NAT with respect to the cluster mean (defined to be $V_{mean}-V_{NAT}$) and a reference are given in columns 4 and 5, respectively. Where possible, velocity dispersions which have been corrected for the special relativistic effect pointed out by Harrison (1974) were used.

The radio properties of the 51 NATs are given in Tables 4.2A and 4.2B. The contents of Table 4.2A are as follows. The source name and an alternate name (if it exists) are given in columns 1 and 2, respectively. The total flux density (in jansky) at 1.4 GHz and a reference are given in column 3. Single dish measurements of the total flux density were used preferentially. The $\log_{10}$ of the total monochromatic luminosity (i.e., power) at 1.4 GHz in the rest frame of the source in units of watts per hertz is given in column 4. The $\log_{10}$ of the radio luminosity between 10^8 and 1.5×10^{10} Hz (assuming a spectral index of $\alpha = -0.75$, where $S_\nu \propto \nu^\alpha$) in units of ergs per second is given in column 5. The flux density of the nuclear core (in jansky) at 1.4 GHz and a reference are given in column 6. In those cases where it was judged that the measured core flux density included a significant contribution from nearby emission, the number is given as an upper limit. The $\log_{10}$ of the core power at 1.4 GHz in units of watts per hertz is given in column 7.

The contents of Table 4.2B are as follows. The source name is given in column 1. The measured projected width in kiloparsecs between the two jets (after they have bent) is given in column 2. For the single tail sources, the deconvolved tail diameter is given as an upper limit. A reference to the map used is given where appropriate. The apparent projected length of the source in kiloparsecs is given in column 3. This is the distance from the core to the end of the tails, taken to be the point at which the tail surface brightness falls below the sensitivity of the map. The observed tail length can be a function of observing frequency, (u,v) coverage, resolution, and sensitivity, but

the estimate given here is the best that could be done given the existing data. A lower limit is given for those sources where the flux density measured by an interferometer was significantly less than

Table 4.2A

Radio Properties of NATs in Abell Clusters

Source	Other Name	Total $S_{1.4}$ (Jy)		Log_{10} Total $P_{1.4}$	Log_{10} Lum	Core $S_{1.4}$ (Jy)		Log_{10} Core $P_{1.4}$
0039+211	4C21.05	0.67	1	25.2	42.0	0.034		23.9
0039-095A		0.07		23.6	40.4	0.004		22.3
0039-097		0.12		23.8	40.7	0.007		22.6
0053-016		1.13		24.6	41.5	0.008		22.5
0053-015		1.50		24.7	41.6	0.042		23.2
0123-016A		0.91		23.8	40.7	0.017		22.0
0255+133	4C13.17A	0.70	1	24.9	41.8	0.009	10	23.0
0256+132	4C13.17B	0.19		24.3	41.2	0.003		22.6
0309+411		0.30		23.3	40.2	0.294		23.3
0313+411	IC310	0.67	1	23.6	40.5	0.130	11	22.9
0314+412	CR15	0.02	2	22.1	39.0	-----		----
0314+416	NGC 1265	7.67	1	24.7	41.6	0.012		21.9
0431-134		0.52[a]		24.0	40.9	0.024[b]		22.7
0457+054		0.16		24.0	40.8	$\leq$0.002		$\leq$22.1
0647+693		0.80[a]		25.3	42.2	0.005[b]		23.1
0810+665	4C66.07	0.27	3	25.1	42.0	-----		----
0905-098		0.37		24.3	41.2	0.119		23.8
0907-091		0.39		24.3	41.2	0.031		23.2
1055+570A		0.02		23.8	40.7	$\leq$0.002		$\leq$23.0
1055+570B		0.38	1	25.2	42.0	$\leq$0.0004		$\leq$22.2
1108+411	4C41.23	0.84	1,4	25.0	41.9	0.013		23.2
1131+493	IC708	0.84	5	24.3	41.1	0.21	5	23.7
1132+492	IC711	0.47	5	24.0	40.9	0.034		22.9
1142+198	3C264	5.45	1	24.7	41.5	0.25	12	23.3
1200+519	4CT51.29.1	0.72	1	24.8	41.6	0.05	13	23.6
1227+119		2.11	1	25.7	42.5	0.013	14	23.5
1244+699		0.24	1	25.1	42.0	0.006		23.5
1250-150		0.29	1	24.2	41.1	0.002		22.0
1256+282	5C4.81	0.13		23.13	40.0	0.002		21.3
1330+507		0.16	1	25.5	42.3	0.005		24.0
1339+266B	4C26.41	0.29		24.5	41.3	$\leq$0.007		$\leq$22.9
1502+287		0.87	1	24.7	41.6	0.013	16	22.9
1519+488A		0.05		24.1	40.9	$\leq$0.005		$\leq$23.1
1556+274		0.13	1	24.3	41.2	0.021		23.6
1619+428		0.14	1	24.7	41.6	0.0008		22.5

Table 4.2A - Continued

Source	Other Name	Total $S_{1.4}$ (Jy)		Log_{10} Total $P_{1.4}$	Log_{10} Lum	Core $S_{1.4}$ (Jy)	Log_{10} Core $P_{1.4}$
1624+406		0.06	6	23.0	39.9	0.033	22.8
1638+538	4C53.37	0.63	7	25.2	42.1	0.012 15	23.5
1658+326	4C32.52E	0.28		24.8	41.7	0.0035	22.9
1709+397	4CT39.49.1	0.56	1	24.7	41.6	0.010	22.9
1712+638	Beaver	0.14	7	24.3	41.2	0.006	22.9
1712+640	4CT64.20.1A	0.29	7	24.6	41.5	0.006 13	22.9
1703+787		0.01	8	22.9	39.7	----	---
1705+786		0.06		23.6	40.5	0.002	22.2
1706+786		0.16		24.1	40.9	0.015	23.0
1706+787		0.04		23.5	40.3	0.0016	22.1
1712+787		0.01	8	22.9	39.7	----	---
1753+580		0.22	1	25.1	42.0	0.007	23.6
1850+702		0.30	1	24.6	41.4	0.013	23.2
1918+439		0.09	9	23.7	40.6	$\leq$0.008	$\leq$22.6
2316+184		0.40	1	24.1	41.0	0.015	22.7
2322+143B		0.15		23.8	40.6	0.006	22.4

Notes to Table 4.2A

a. Total flux density at 1.4 GHz extrapolated from 4.9 GHz, assuming a spectral index of $\alpha = -0.7$.

b. Core flux density at 1.4 GHz extrapolated from 4.9 GHz, assuming a spectral index of $\alpha = 0.0$.

Table 4.2B

Radio Properties of NATs in Abell Clusters

Source	Width (kpc)	Ref	Length (kpc)	Ref
0039+211	23.9		247	17
0039-095A	< 2.4		43	
0039-097	26.5		47	
0053-016	17.3		260	
0053-015	25.9		311	
0123-016A	24.3		>48	
0255+133	24.1	10	391	7
0256+132	41.2		135	
0309+411	<0.5		56	2
0313+411	<4.6	11	126	18
0314+412	<3.8	19	43	19
0314+416	19.6		210	18
0431-134	15.3		> 47	
0457+054	40.5		> 71	
0647+693	157.8		>246	
0810+665	11.4	20	109	21
0905-098	<2.1		164	
0907-091	38.5		123	
1055+570A	12.0		> 70	
1055+570B	12.0		> 27	
1108+411	15.5		> 44	
1131+493	31	22	55	22
1132+492	13.4		604	23
1142+198	19.6	12	129	24
1200+519	110	25	167	25
1227+119	57	14	118	14
1244+699	103.4		262	
1250-150	31.5		143	
1256+282	4.9		124	26
1330+507	< 6.4		>153	
1339+266B	0.8		364	25
1502+287	38		202	27
1519+488A	< 1		> 18	
1556+274	< 3.6		>129	
1619+428	9.6		256	
1624+406	14.2	6	81	6
1638+538	135	28	236	28
1658+326	?		212	
1709+397	< 0.9		470	25
1712+638	50.6		260	7
1712+640	18.2	20	212	7
1703+787	<18	8	120	8
1705+786	30		40	
1706+786	< 0.6		30	

Table 4.2B - Continued

Source	Width (kpc)	Ref	Length (kpc)	Ref
1706+787	< 0.6		> 66	
1712+787	<18	8	67	8
1753+580	32.6		>117	
1850+702	28.8		>152	
1918+439	19.4		82	
2316+184	16.5		50	
2322+143B	< 0.4		51	

References to Table 4.2B

1. Owen et al. (1982a)
2. Gisler and Miley (1979)
3. Slingo (1974)
4. Harris et al. (1980a)
5. Wilson and Vallee (1977)
6. Gavazzi and Perola (1980)
7. Harris, Kapahi, and Ekers (1980)
8. Bridle et al. (1979)
9. Birkinshaw (1978)
10. Burns and Ulmer (1980)
11. Gower (1983), private communication
12. Bridle and Vallee (1981)
13. Simon (1979)
14. Laing, Riley, and Longair (1983)
15. Burns and Balonek (1982)
16. Owen et al. (1982b)
17. Riley (1975)

18. Miley (1973)

19. Miley et al. (1972)

20. Owen et al. (1979)

21. Rudnick and Owen (1977)

22. Vallee, Wilson, and Van der Laan (1979)

23. Vallee and Wilson (1976)

24. Hogbom and Carlsson (1974)

25. Miley and Harris (1977)

26. Jaffe, Perola, and Valentijn (1976)

27. Valentijn (1981)

28. Burns and Owen (1980)

that measured by a single dish. A reference to the map used is given where appropriate. Angular sizes were taken from the references and converted to linear sizes assuming the values for H_o and q_o given above.

4.2 Statistical Properties of NATs in Abell Clusters

The global properties of the homogeneous sample of 39 NATs (and in some cases the entire collection of 51 NATs in Abell clusters) are presented and discussed below.

Cluster richness

The Narrow Angle Tail morphology is thought to be due to the interaction of the ICM with quasi-continuous beams of plasma ejected by a rapidly moving galaxy. Thus, it is interesting to know how the nature

of this interaction depends on the properties of the cluster (e.g., richness, Bautz-Morgan type, Rood-Sastry type). This may ultimately lead to clues to the nature of the galaxy-ICM interaction during the course of cluster evolution.

A histogram of the distribution of NATs as a function of cluster richness for both the heterogeneous sample of 51 sources in the directions of Abell cluster and the homogeneous subsample of 39 NATs is shown in Figure 4.1. Both samples have similar distributions. The average number of NATs per cluster in clusters with at least one NAT (using all 51 NATs) for richness class 0, 1, 2, 3 are 1.11, 1.17, 2.0, and 1.0, respectively. Only one richness class 3 cluster (A 1758) has so far been found to contain a NAT. However, the fractional contribution of richness class 1, 2, 3, 4, and 5 to Abell's complete statistical sample of 1683 clusters is roughly 72.8%, 22.7%, 4.04%, 0.4%, and 0.06%, respectively (Abell 1965). Thus, richness class 3 clusters make up about only 4% of the clusters in Abell's statistical sample. Note that there are no richness class 3 clusters closer than distance class 4 ($0.06 < z < 0.1$, Abell 1958). Because of this, the bias against sources of low radio power in distant clusters will result in an artificial deficiency of richness class 3 clusters with NATs. Also, the number of richness class 2 clusters containing NATs is exaggerated by the contribution from two clusters, A 426 (Perseus) and A 2256, which contribute four and five NATs, respectively.

Because of this, the distribution of clusters containing at least one NAT (i.e., counting each cluster only once) is more relevant. The expected number of clusters in each richness class was calculated by

multiplying the number of clusters in the sample by the fractional contribution of each richness class to Abell's statistical sample. The observed and expected distributions are shown in Figure 4.1. The observed numbers of clusters in richness class 1 and 3 are close to those expected. However, there is an excess of richness class 2 clusters with NATs. The observed and expected distributions were compared using a chi-square "goodness-of-fit" test (Conover 1980). The two distributions are marginally different (with a reduced chi-square of 1.32). The probability that this difference is produced by chance is $P \approx 27\%$. Nearly all of the discrepancy is due to the observed excess of NATs in richness class 2 clusters.

Thus, there is a hint that the richer clusters are more likely to contain a NAT than poorer clusters, though this is not statistically significant. Also, there may be a tendency for richer clusters to have more NATs per cluster than poorer clusters. Further observations of richness class 3 clusters at higher sensitivity are needed in order to clarify this point.

Previous work which dealt mainly with strong sources (e.g., the 4C survey) suggested that the probability that a cluster will exhibit detectable radio emission is at best not strongly dependent on cluster richness class (e.g., Fomalont and Rogstad 1966; Tovmassian and Moiseev 1967; Mills and Hoskins 1977; McHardy 1979; Slee, Wilson, and Siegman 1983). Rogstad and Ekers (1969) suggested that this result could be explained if the number of very bright ellipticals in clusters (which also tend to be strong radio emitters) is also not strongly dependent on cluster richness. However, recently White, Owen, and Hanisch (1982)

have found that richer clusters are more likely to contain a radio source, and they suggest that this is possibly because they simply contain more galaxies. This difference with previous results may be due to the higher sensitivity of the Owen et al. (1982a) survey which resulted in the detection of weaker cluster sources. The suggestion that richer clusters are more likely to contain a NAT is also consistent with the larger number of galaxies in richer clusters. However, this result could also be due to a stronger interaction of the radio source with its environment in richer clusters.

There is a tendency for richer clusters to have higher radial velocity dispersions (Bahcall 1981, Struble and Rood 1982) and higher X-ray luminosities (McKee et al. 1980). A correlation may also exist between radial velocity dispersion and X-ray luminosity (e.g., Faber and Dressler 1976, Hintzen and Scott 1979). Thus, it seems likely that radio sources in richer clusters move at higher velocities through a denser ICM than in poorer clusters. Twin jet sources which might be relatively straight in a poorer cluster environment are more likely to be NATs in a richer cluster environment. So, in richer clusters a higher fraction of the radio sources are expected to show a tailed morphology (cf. Ekers et al. 1981).

Bautz-Morgan type

Leir and Van den Bergh (1977) give the distribution of Bautz-Morgan (BM) types (Bautz and Morgan 1970) for the clusters in Abell's complete sample. The BM types for the clusters in distance classes 1 through 4 (which are the most accurately determined) were used to calculate the

expected distribution of clusters containing NATs shown in Figure 4.2. The observed counts for the sources in both the homogeneous sample and the larger heterogeneous sample (for which a BM type has been determined) are presented. Both samples are seen to have similar distributions. In addition, the observed and expected distributions for all clusters with at least one NAT (counting each cluster only once) are shown. The results are:

(1) NATs are definitely found in BM class 1 clusters contrary to the suggestion of McHardy (1979).

(2) NATs are about equally likely to be found in clusters of any BM type. The raw and expected distributions were compared using a goodness-of-fit test. The observed distribution is only slightly different from the expected one (reduced chi-square of 0.86), with a probability of $P \approx 49\%$ that this difference is produced by chance.

(3) All of the NATs in BM class 1 and 2 clusters are rank 3 galaxies (i.e., galaxies much fainter than the brightest galaxy) which is consistent with the results of Simon (1978).

Rood-Sastry type

Histograms of the distribution vs. RS type for all 51 NATs, the subsample of 39 NATs and for 33 Abell clusters containing at least one NAT are shown in Figure 4.3. (Only clusters of distance class ≤ 5 have been classified by Struble and Rood 1982, 1983.) The expected distribution of clusters containing NATs was calculated using the fractional distribution of revised RS types for distance class ≤ 4 given by Struble and Rood (1982) and is also shown in Figure 4.3. There is an

excess of binary, core-halo, and line type clusters and a deficiency of flat and irregular type clusters containing NATs (Fig. 4.3); though only the differences in the observed and expected numbers of binary and irregular clusters are large enough to be statistically significant. These differences are sufficient to cause the observed distribution to differ significantly from that expected if NATs were distributed uniformly among clusters of every RS type. The goodness-of-fit test finds a reduced chi-square of 5.65 with a probability that the difference is produced by chance of $P < 0.1\%$.

The deficiency of NATs in flat and irregular clusters could be at least partially due to the much higher fraction of spiral galaxies in these clusters (e.g., Oemler 1974), since NATs are found in elliptical galaxies. Struble and Rood (1982) have suggested that cD, B, C, and L type clusters are more dynamically evolved than F and I type clusters. If this picture is correct, then these results are consistent with the hypothesis that there is a preference for NATs to be found in more evolved clusters (see also Sparke 1983).

Projected distance from the cluster center

The distribution of projected distance from the cluster center, D_c, in units of corrected Abell cluster radii is given in Figure 4.4 for the homogeneous sample. The median D_c for the whole subsample is 0.17. The distributions for the rank 2 and 3 galaxies were compared to determine whether one group tends to be found closer to the cluster center. If this were the case, the medians of the two distributions would be different. This was examined using a version of a chi-square test

Figure 4.1

The distribution of NATs as a function of cluster richness class for: 51 NATs in Abell clusters; the homogeneous subsample of 39 NATs; clusters with at least one NAT (counting each cluster only once); and the expected distribution of clusters for richness 1, 2, and 3 (calculated using the fractional contribution of each richness class to Abell's (1958, 1965) complete sample of 1683 clusters).

Figure 4.2

The distribution of NATs as a function of Bautz-Morgan type (Bautz and Morgan 1970) for: 51 NATs in Abell clusters; the homogeneous subsample of 39 NATs; clusters with at least one NAT (counting each cluster only once); and the expected distribution of clusters (calculated using the fractional distribution of BM types for distance classes $\leq$ 4 given by Leir and Van den Bergh 1977).

Figure 4.3

The distribution of NATs as a function of revised Rood-Sastry type (Rood and Sastry 1971; Struble and Rood 1982, 1983) for: 51 NATs in Abell clusters; the homogeneous subsample of 39 NATs; 33 clusters with at least one NAT (counting each cluster only once); and the expected distribution of clusters (calculated using the fractional distribution of RS types for distance classes $\leq$ 4 given by Struble and Rood 1982).

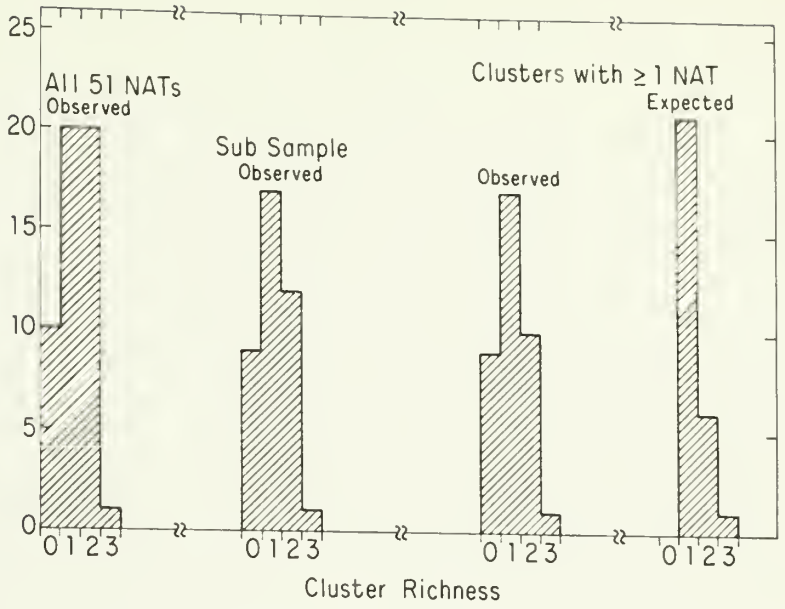
All 51 NATs
Observed
Sub Sample
Observed
Clusters with ≥ 1 NAT
Observed
Expected
25
20
15
10
5
0
0 1 2 3
Cluster Richness

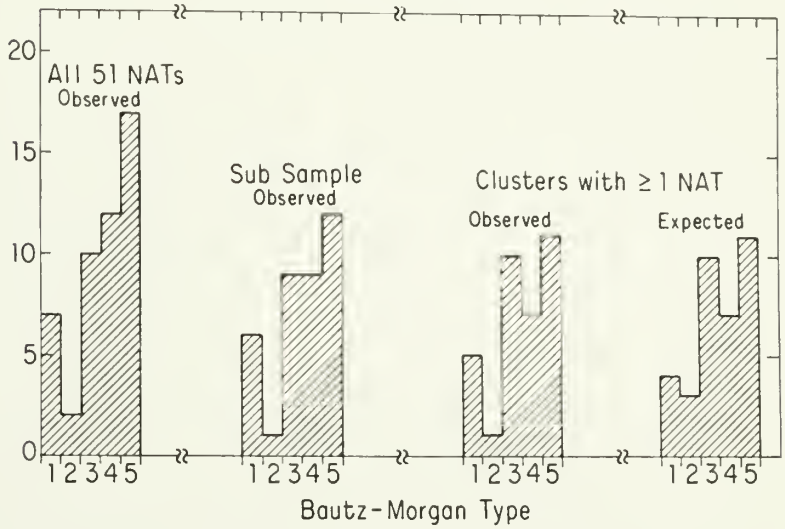
All 51 NATs
Observed
Sub Sample
Observed
Clusters with ≥ 1 NAT
Observed
Expected
20
15
10
5
0
1 2 3 4 5
Bautz-Morgan Type

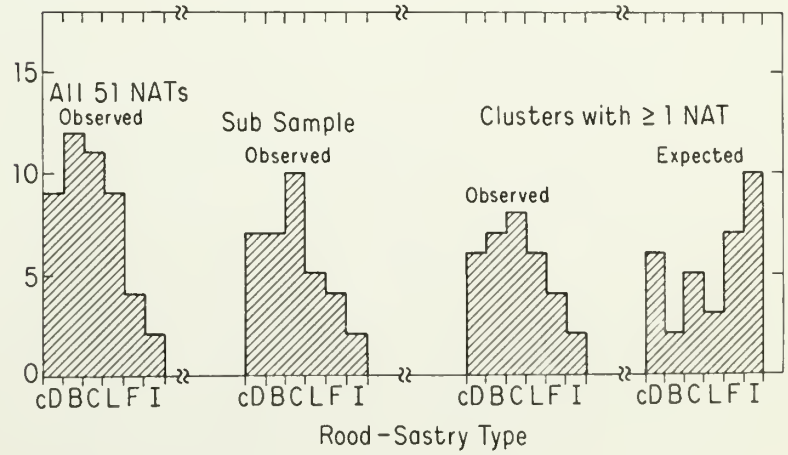
All 51 NATs
Observed
Sub Sample
Observed
Clusters with ≥ 1 NAT
Observed
Expected
15
10
5
0
cDBCLFI
Rood-Sastry Type

called the "median test" (e.g., Conover 1980). The median test examines whether two samples have been drawn from populations with the same median value (the null hypothesis). The probability that the distributions for the rank 2 and 3 galaxies were drawn from populations with the same median is P ≈ 96.3% (reduced chi-square = 2.5×10^{-3}). Thus, the data are consistent with the hypothesis that the rank 2 and 3 NATs have the same distribution of projected distance from the cluster center.

The second hypothesis tested was whether the NATs have a distribution consistent with that of a King (1972) model. This is interesting because the isothermal King model is thought to be a reasonable approximation to the distributions of both the galaxies (e.g., Bahcall 1977, Dressler 1978) and the X-ray emitting gas (Forman and Jones 1982) in clusters. The projected surface density $\sigma(r)$ of galaxies was assumed to be of the form

$$\sigma(r) = \sigma_o \left(1 + \frac{r^2}{r_c^2} \right)^{-1} , \qquad (4.3)$$

where r_c is the core radius, defined to be the distance at which the surface density drops to half of its original value (i.e., $\sigma(r_c) = 0.5\sigma_o$), and σ_o is a normalization constant (e.g., Bahcall 1977), and was chosen such that the total number of galaxies between 0 and $0.5A_c$ was 39, the number of galaxies in the subsample. The correct value for the cluster core radius is at present a matter of controversy and different investigators have obtained different results (even for the same clusters); i.e., Austin and Peach (1974) find

$r_c = 250 \pm 73$ kpc, Bahcall (1975) finds $r_c = 170 \pm 27$ kpc, and Dressler (1978) finds $r_c = 310 \pm 73$ kpc (where the results have been scaled using $H_o = 75$ km sec^{-1} Mpc^{-1}). Quintana (1979) finds that the estimated core radius increases as fainter galaxies are counted and suggests that this is evidence for mass segregation; i.e., the brighter (and hence presumably more massive) galaxies are more centrally concentrated than the fainter galaxies. Averaging these three determinations gives $r_c \approx 244$ kpc.

A King model with core radius of $r_c = 244$ kpc was used and compared to the data using both the median test and the goodness-of-fit test. The goodness-of-fit test resulted in a reduced chi-square of 1.91. This amount of disagreement between the two distributions will be produced by chance with a probability of $P \approx 11\%$. The King model (with $r_c = 244$ kpc) has a larger median value (0.21) than the observed distribution. The median test resulted in a large reduced chi-square of 2.39, i.e., the model and observed distributions were drawn from parent populations with the same median with a probability of $P \approx 13\%$. Thus, a core radius of $r_c = 244$ kpc does not give a very good fit to the data.

A much better fit is obtained using Bahcall's (1975) value of 170 kpc for the core radius. In this case the goodness-of-fit test resulted in a reduced chi-square of 1.57. This amount of disagreement between the two distributions will be produced by chance with a probability of $P \approx 18\%$. This model ($r_c = 170$ kpc) has a median value of 0.18, which is only slightly larger than that of the observed distribution. The median test resulted in a reduced chi-square of 0.27; i.e., the model and observed distributions were drawn from parent populations with the same

median value with a probability of P ≈ 60%. Thus, a King model with a core radius of 170 kpc (H_o = 75 km sec^{-1} Mpc^{-1}) can reproduce the observed median distance from the cluster center, though the observed distribution falls off slightly faster with D_c (beyond the median) than the King model (see Fig. 4.4). However, given that the NATs are in clusters with different core radii, the data appear to be roughly consistent with the hypothesis that NATs have the same spatial distribution in clusters as do other cluster members. It is not unexpected that the distribution of NATs should be more closely fit by the smaller value for the core radius given by Bahcall (1975) since NATs, while not the brightest cluster members, are among the brighter members and should be found preferentially near the cluster centers if some amount of equipartition and mass segregation has occurred (cf. Quintana 1979).

The apparent deficiency of NATs in the region ~0.3-0.5 A_c could be at least partially due to the decrease in the ICM density and temperature with distance from the cluster center (e.g., Forman and Jones 1982). The smaller external pressure would require the radio source to expand much more in order to come into pressure balance with the external medium. The resulting adiabatic losses and lower emissivity (and hence surface brightness) would make such sources harder to detect.

Galaxy velocity

One interesting question is whether the rank 2 and 3 galaxies have similar velocities through the ICM. The brighter (and hence presumably

more massive) galaxies should have lower velocities if there has been significant equipartition of kinetic energy among the cluster galaxies. At this point there are measured radial velocities (with respect to the cluster mean) for only 22 NATs in Abell clusters (listed in Table 4.1B). This is sufficient to give preliminary statistical results.

The distributions of radial velocities for the rank 2 and 3 galaxies are given in Figure 4.5. The median radial velocity for all 22 NATs is 574 km/sec, which is comparable to the velocity dispersions in Abell clusters (e.g., Danese, De Zotti, and Di Tullio 1980). The distribution of velocities for the rank 3 galaxies extends to much higher velocities than for the rank 2 galaxies. However, a median test resulted in a reduced chi-square of 0.21; i.e., the two distributions were drawn at random from parent populations with the same median velocity with a probability of $P \approx 65.1\%$. This suggests that the rank 2 and 3 galaxies have comparable velocities through the ICM. This result should be examined with a much larger sample of radial velocities. Note that the classification of galaxies into relative optical ranks is subjective and depends essentially on the Bautz-Morgan classification of the cluster. It is not clear that the actual differences in galaxy size are very significant and absolute magnitudes will be necessary to answer this question.

Thus, NATs have velocities which are comparable to the cluster velocity dispersions (cf. Ulrich 1978; Baggio, Perola, and Tarenghi 1978). The results of Chapter VII suggest that (within the context of current models for NATs) velocities which are on the order of the cluster velocity dispersions are sufficient to account for both the

Figure 4.4

The distribution of NATs in the homogeneous subsample as a function of distance from the cluster center, D_c, in units of corrected Abell radii, A_c (as defined by Rudnick and Owen 1977 see eq. 4.1), in bins of 0.1 A_c for: rank 2 galaxies; rank 3 galaxies; both rank 2 and 3 galaxies; and a King (1972) model with a core radius of 170 kpc and Abell cluster radius of 2 Mpc (H_o = 75 km sec^{-1} Mpc^{-1}).

Figure 4.5

Radial velocities (kilometers per second) with respect to the cluster mean (22 NATs total) for: rank 2 galaxies; rank 3 galaxies; and both rank 2 and 3 galaxies.

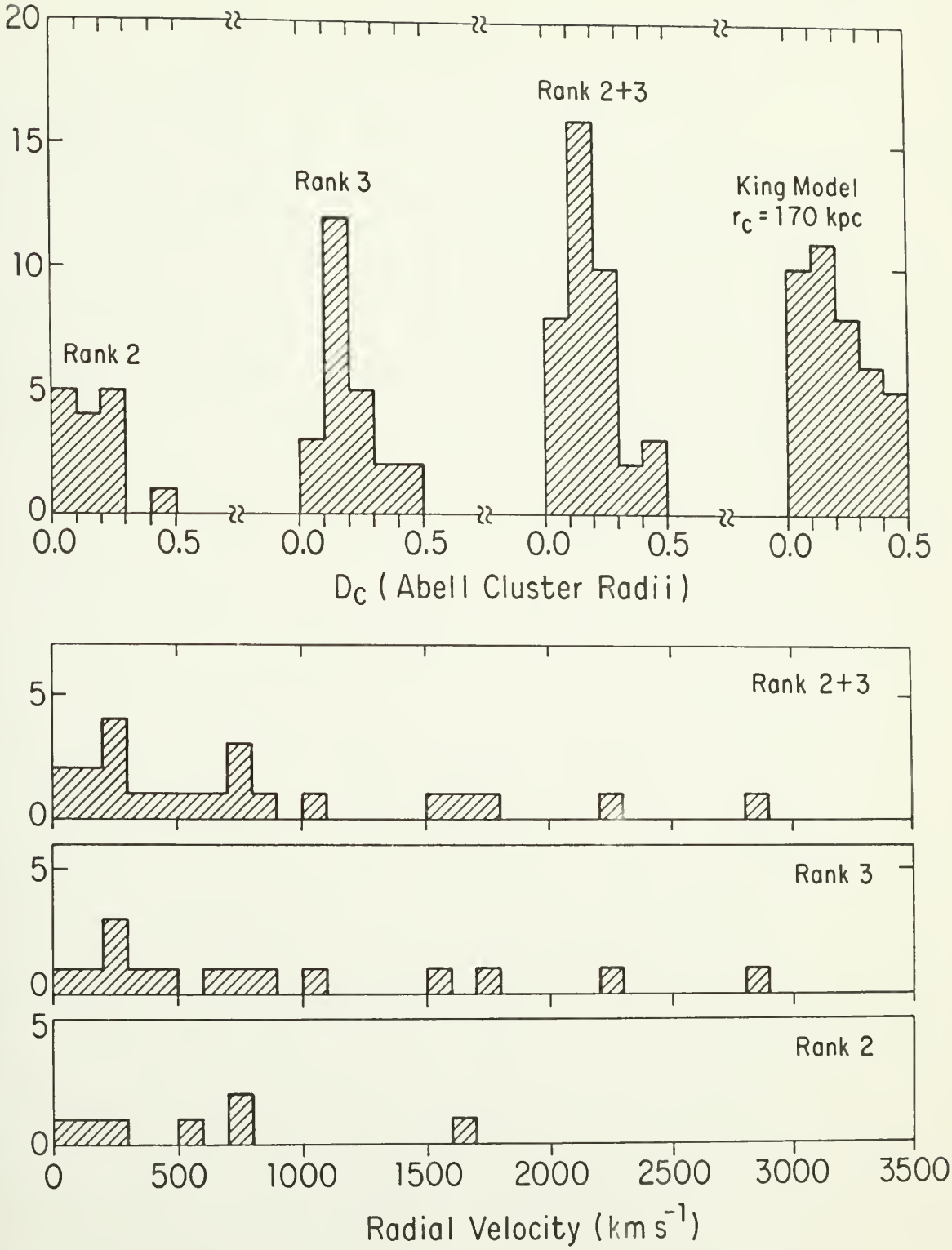
20
15
10
5
0
Rank 2
Rank 3
Rank 2+3
King Model
r_c = 170 kpc
0.0
0.5
D_C (Abell Cluster Radii)
Rank 2+3
Rank 3
Rank 2
0
500
1000
1500
2000
2500
3000
3500
Radial Velocity (km s^{-1})

energetic requirements and morphology of NATs. These results are consistent with the hypothesis that the distorted structure of the NATs is due to their motion through the ICM, as suggested by Miley et al. (1972).

Guindon and Bridle (1978) have studied the relationship between the amount of distortion in the radio structure and the galaxy velocity relative to the ICM for various morphological types of cluster radio sources. They suggested that smaller galaxy velocities are associated with less distorted radio structure (though since their sample was rather small they suggested that this result was in need of confirmation). This is consistent with the suggestion of Owen and Rudnick (1976) that the structure of the Wide Angle Tail sources is produced by relatively low galaxy velocities. The association of the less distorted radio structure with parent galaxies of larger optical luminosity, and hence larger mass (Owen and Rudnick 1976, Simon 1978), is consistent with the more massive galaxies having relatively lower galaxy velocities through the ICM.

Thus, these results are consistent with the hypothesis that NATs are not required to have velocities which are larger than the cluster velocity dispersions, but that the WATs and other more linear sources (associated with more dominant galaxies) are required to have velocities which are much lower than the cluster velocity dispersions. This is also consistent with the hypothesis that some amount of dynamical evolution and energy equipartition has occurred in these clusters (e.g., Owen and Rudnick 1976, Guindon and Bridle 1978).

Nuclear core power and integrated radio power

The currently available single-frequency observations are of sufficient sensitivity and resolution to distinguish an unresolved core from nearby or superposed jet and/or tail emission in 41 out of 51 sources, giving a detection rate of ~80%. The distribution of NATs as a function of $\log_{10}$ nuclear core power at 1.4 GHz for optical ranks 2, 3, and both 2 and 3 are presented in Figure 4.6 for 47 NATs. The upper limits to the core powers in 0314+412, 0810+665, 1703+787, and 1712+787 are very uncertain and are not included. Both the heterogeneous sample and the homogeneous subsample have the same median value (22.91). The rank 2 galaxies (median 23.26 for all 47 NATs) have more powerful cores than the rank 3 galaxies (median 22.66 for all 47 NATs). The median test reveals that the rank 2 and 3 galaxies were drawn from populations with the same median with a probability of $P \approx 1\%$ for the larger sample (reduced chi-square of 6.59) and a probability of $P \approx 0.1\%$ for the subsample (reduced chi-square of 9.73).

The distributions of $\log_{10}$ integrated radio power at 1.4 GHz for both samples are presented in Figure 4.7. The sample of 51 has a smaller median value (24.33) than the homogeneous sample (24.62) reflecting the bias for stronger sources in the selection criteria for the subsample. Thus, the heterogeneous sample of 51 is probably more representative of the distribution of integrated powers among NATs than the subsample. For this reason the larger sample was used in the comparison of the optical rank 2 and 3 galaxies. As for the core powers, the rank 2 galaxies (median 24.74) have higher integrated powers than the rank 3 galaxies (median 24.08). The median test results in a

Figure 4.6

Log_{10} core power (watts per hertz) at 1.4 GHz in the rest frame of the source for the homogeneous sample of 39 galaxies: rank 2 galaxies; rank 3 galaxies; both rank 2 and 3 galaxies combined; and for the heterogeneous sample (minus four sources with very uncertain core powers): rank 2 galaxies; rank 3 galaxies; and both rank 2 and 3 galaxies combined.

Figure 4.7

Log_{10} integrated power (watts per hertz) at 1.4 GHz in the rest frame of the source for the homogeneous sample of 39 galaxies: rank 2 galaxies; rank 3 galaxies; rank 2 and 3 galaxies combined; for all 51 NATs in Abell clusters: rank 2 galaxies; rank 3 galaxies; rank 2 and 3 galaxies combined.

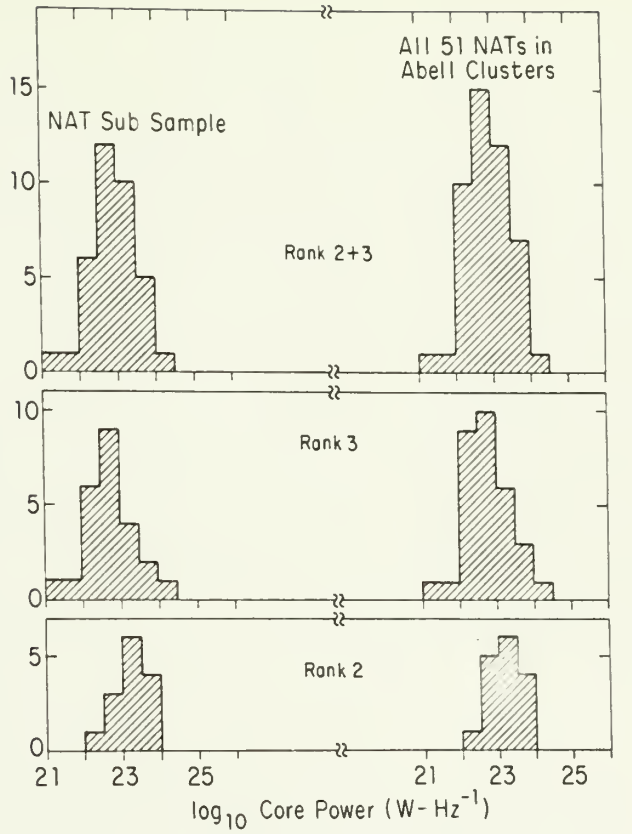
All 51 NATs in
Abell Clusters
NAT Sub Sample
Rank 2+3
Rank 3
Rank 2
15
10
5
0
21
23
25
log10 Core Power (W-Hz-1)

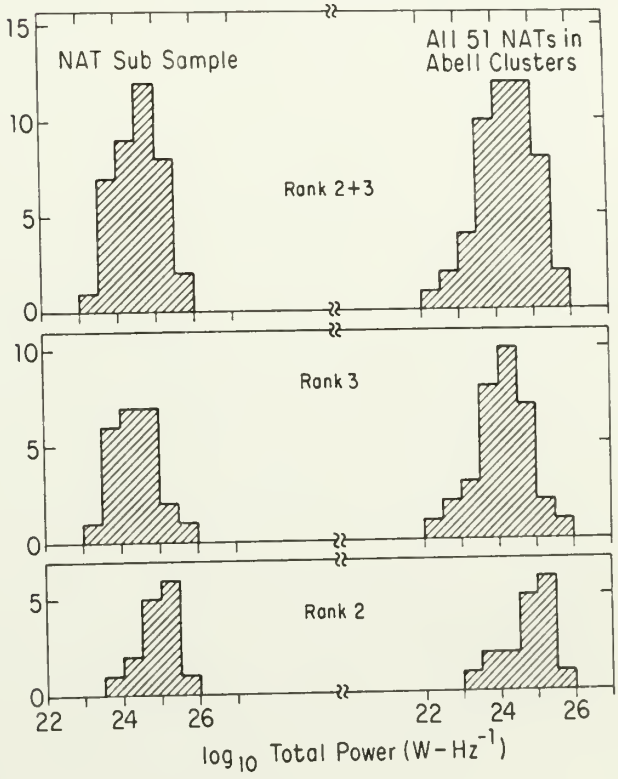
NAT Sub Sample
All 51 NATs in
Abell Clusters
Rank 2+3
Rank 3
Rank 2
15
10
5
0
22
24
26
log10 Total Power (W-Hz-1)

reduced chi-square of 6.63. The probability that this much difference is found in two samples chosen at random from populations with the same median is P ≈ 1%. Thus, this result is also significant. Except for a few sources (i.e., 0309+411, 0905-098, 1131+493, 1556+274, and 1624+406) the core powers are only a very small fraction (~0.01) of the integrated radio powers (see Chap. III and Table 4.2). Thus, the result that rank 2 galaxies have larger total powers than rank 3 galaxies is independent of the result that rank 2 galaxies also have larger core powers.

The observed distribution of $\log_{10}$ total powers is rather narrow with a mean of 24.25 and a dispersion or root-mean-square of 0.74. The selection effects in the survey will remove some NATs from the low power tail and will artificially narrow the distribution. The shape of the low power part of the distribution cannot be determined without additional observations to a much lower limiting power.

Nuclear core power vs. integrated power

The previous results suggest that the rank 2 galaxies tend to produce more powerful radio sources with more powerful nuclear cores than rank 3 galaxies. Is there a correlation between the integrated power of the radio source and the power of the core in NATs? Earlier work (e.g., Fanti and Perola 1977, Bridle and Fomalont 1978) concluded that there was not a significant correlation between the core and integrated powers. However, more recent work (with data of higher resolution and sensitivity) has suggested that there is a significant correlation. Burns and Gregory (1982) found a correlation between the

integrated flux densities at 2.7 GHz and core flux densities at 4.9 GHz for a sample of 4C radio galaxies in poor clusters. Feigelson amd Berg (1983) and Fabbiano et al. (1984) found a correlation between the core powers at 5 GHz and the integrated powers at 178 MHz in samples of 16 and 40 3CR radio galaxies, respectively. A correlation between total power at 1.4 GHz and core power at 5 GHz is also evident in a sample of 94 radio sources with jets (Bridle 1984).

Figure 4.8 suggests that there is a correlation between the $\log_{10}$ of the core power and the $\log_{10}$ of the integrated power at 1.4 GHz for the 47 NATs for which core powers (or upper limits) can be calculated. The nonparametric Spearman rank test (e.g., Conover 1980) was used to test for a positive correlation. Conservative ranks for the cores with upper limits were chosen (i.e., those ranks which would most weaken the apparent correlation). This resulted in a value for ρ of 0.47. Such a high correlation would be produced by chance in a population of 47 objects with a probability of $P \leq 0.1\%$. Thus, the correlation is significant. A least-squares fit of a straight line to the data produces a slope of 0.50 ± 0.12, i.e., $P_{core} \propto P_{total}^{1/2}$. This slope was also found for a sample of B2 and 3CR sources, though with much less significance (Fanti and Perola 1977).

However, it is possible that the apparent correlation is due at least in part to selection effects, (e.g., the effect of the decreasing linear resolution as a function of redshift). The measured flux density of the cores of the more distant galaxies may contain a higher contribution from emission near the core than the nearby galaxies. Because of the flux density limit in the sample, the more distant

galaxies are preferentially the ones with larger integrated powers. Thus, this selection effect could produce a spurious correlation between core power and integrated power. Note that an intrinsic correlation between core and integrated power could also produce a correlation between core power and redshift in this essentially flux-limited sample.

The plot of $\log_{10}$ core power vs. redshift (Fig. 4.9) suggests a correlation between these two quantities with the more distant galaxies having brighter cores. With a conservative choice of ranks for the cores with upper limits, the Spearman rank test results in $\rho = 0.23$. This amount of correlation would be produced by chance with a probability of $P \sim 6\%$. Thus, this correlation is of marginal significance and suggests that this selection effect is not very important. One possible experiment would be to observe the cores of these sources with the same linear resolution. It would be useful to do this at 6 cm, since at the higher frequency there would be less of a contribution to the measured flux density of the core from nearby steep spectrum structure.

At this point, it appears that there is a correlation between the core power and integrated powers of NATs. This result extends the range of integrated powers and source morphologies over which this relationship has been found. It seems somewhat surprising that this relationship should exist at all, because the need for in situ particle reacceleration in jets, hotspots, and diffuse tails might be expected to "decouple" the extended emission from that in the core. In addition, the details of the particle acceleration mechanism may be different in sources such as classical doubles and Narrow Angle Tails. This suggests

Figure 4.8

Log_{10} core power vs. log_{10} integrated power watts per hertz at 1.4 GHz for 47 of the 51 NATs in Abell clusters.

Figure 4.9

Log_{10} core power at 1.4 GHz watts per hertz vs. redshift for 47 NATs in the heterogeneous sample.

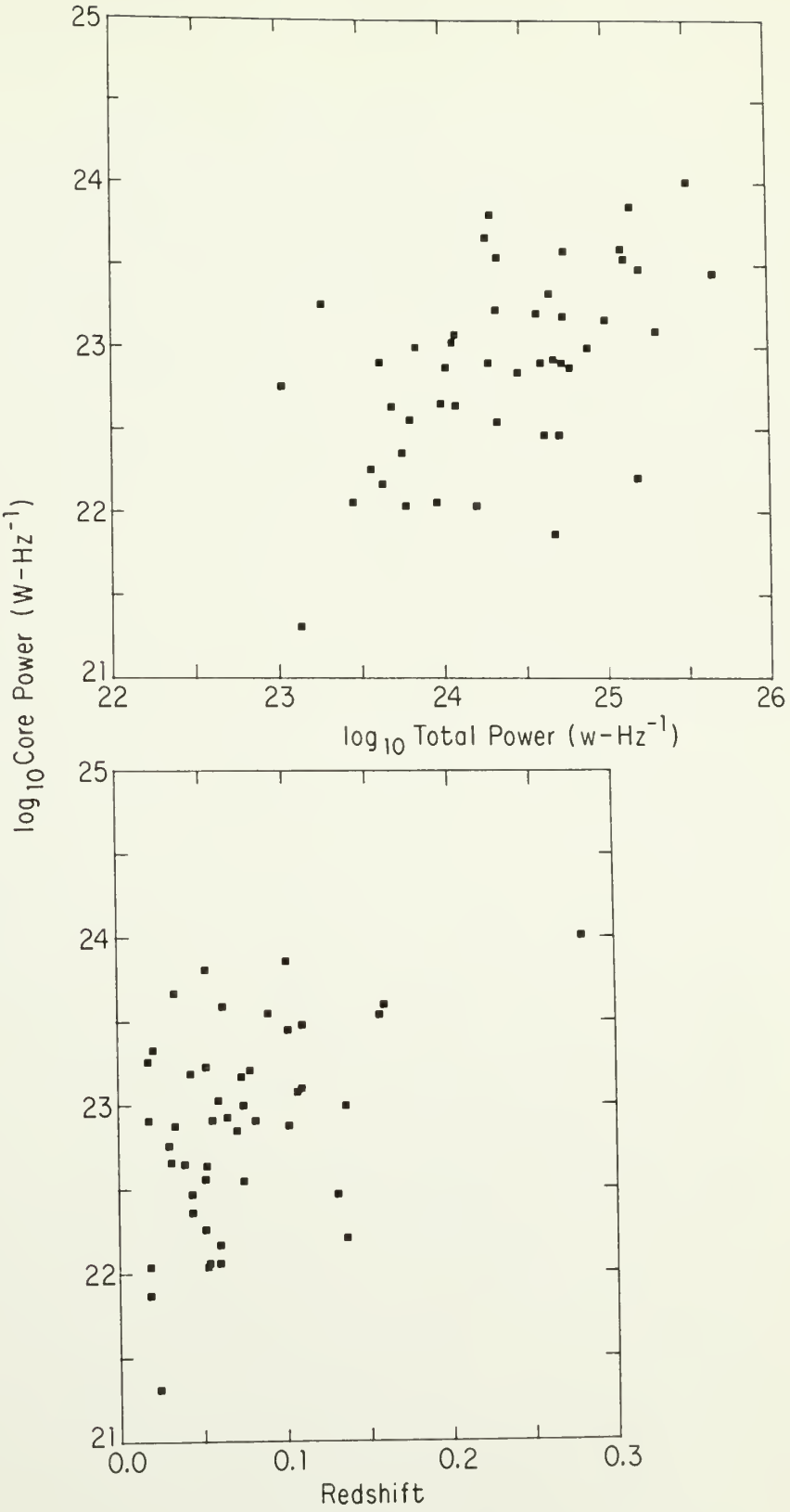
25
24
23
22
21
22
23
24
25
26
log 10 Core Power (W-Hz-1)
log 10 Total Power (w-Hz-1)
25
24
23
22
21
0.0
0.1
0.2
0.3
Redshift

that the relationship between core and integrated power is based on something which is fairly universal and independent of the details of the particle acceleration mechanism. The brightness of the core may be related to such parameters as the amount of kinetic energy flux produced by the core and/or the number of "seed" relativistic electrons which are initially produced in the core and later reaccelerated (many times) in the extended structure.

Another clue is that the apparent correlation between the core and total power may be related to a correlation of both of these parameters with the optical magnitudes. Auriemma et al. (1977) examined the bivariate optical-radio luminosity function for elliptical galaxies and concluded that brighter optical galaxies tend to be stronger radio sources. Fabbiano et al. (1984) also find a correlation between nuclear core power at 5 GHz and the galaxy optical luminosity. The results presented here that rank 2 galaxies have stronger cores and total powers than rank 3 galaxies is consistent with this. However, a detailed discussion of this question will have to be deferred until accurate absolute magnitudes for these NAT galaxies are available. Note that such a correlation would explain the upper limit to the observed distribution of total powers (Fig. 4.7). The upper limit to the radio power might correspond to an effective upper limit to the optical magnitude (i.e., size and/or mass) of a galaxy which could move fast enough to produce a NAT source.

Projected widths

The projected width, defined here to be the projected linear distance (in kiloparsecs) between the two jets after they have bent, is shown in Figure 4.10 for the sources in the homogeneous sample (minus 1658+326). The median width for the entire homogeneous sample is 19.6 kpc (which coincidentially is the width of NGC 1265). The median widths for the rank 2 and 3 galaxies are 25.1 and 16.9 kpc, respectively. The median test results in a reduced chi-square of 4.26, and suggests that these distributions were drawn from populations with the same median value with a probability of $P \approx 5\%$.

The distributions of projected widths for the heterogeneous sample (minus 1658+326) are shown in Figure 4.11. The median for the larger sample is 18, which is very close to that of the homogeneous subsample. The median test resulted in a lower reduced chi-square of 1.67, i.e., the rank 2 (median 24.3) and rank 3 (median 16.5) galaxies in the heterogeneous sample are drawn from populations with the same median value with a probability of $P \approx 20\%$. Thus, at this point the data are roughly consistent with the hypothesis that NATs associated with rank 2 and 3 galaxies have comparable widths, though there is a hint that more dominant galaxies (rank 2) have larger widths.

There are two peaks in the observed distribution of projected widths: one at 0-5 kpc and one at 15-20 kpc. Simple Monte Carlo calculations (using 10^4 trials) were performed in order to examine the effects of projection upon the data. The expected distribution of projected widths (given a random distribution of angles) is shown in Figure 4.12 for different values of the assumed intrinsic width. The

Figure 4.10

Projected width (kiloparsecs) of the homogeneous sample (minus 1658+326) for galaxies of: rank 2; rank 3; rank 2 and 3 combined. The width is defined to be the distance between the jets after they have bent. The deconvolved tail diameter is used for single tail NATs.

Figure 4.11

Projected width (kiloparsecs) of the heterogeneous sample (minus 1658+326) for galaxies of: rank 2; rank 3; rank 2 and 3 combined. The width is defined to be the distance between the jets after they have bent. The deconvolved tail diameter is used for single tail NATs.

Figure 4.12

The expected fractional distribution of projected widths from Monte Carlo calculations using 10^4 trials, assuming a random distribution of angles and an intrinsic width of: 10 kpc, 20 kpc, 30 kpc, and 40 kpc.

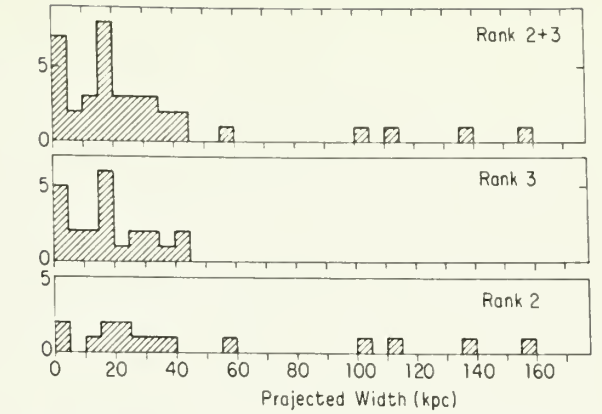
Rank 2+3
Rank 3
Rank 2
0 20 40 60 80 100 120 140 160
Projected Width (kpc)

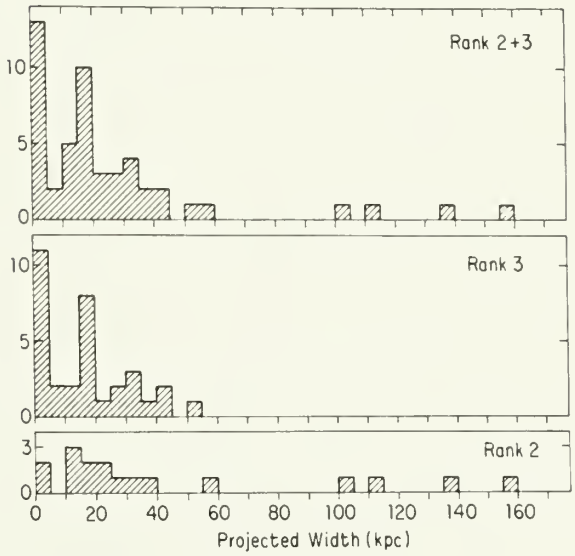
Rank 2+3
Rank 3
Rank 2
0 20 40 60 80 100 120 140 160
Projected Width (kpc)

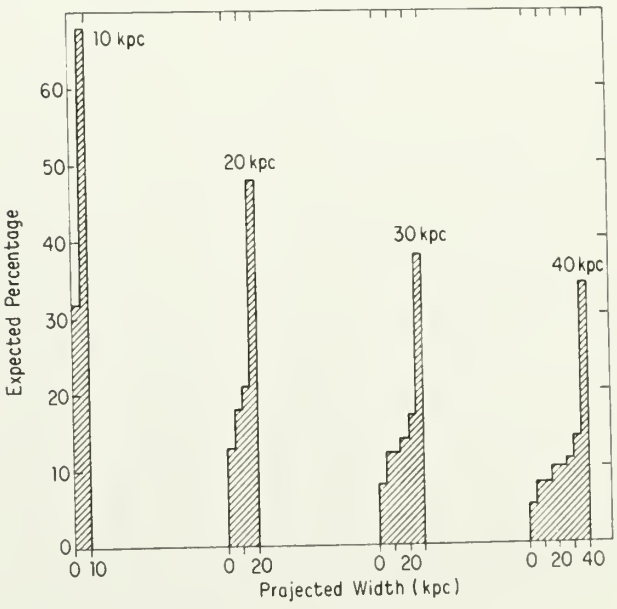
10 kpc
20 kpc
30 kpc
40 kpc
Expected Percentage
0 10
0 20
0 20
0 20 40
Projected Width (kpc)

predicted distribution has a peak at the intrinsic width and a broad, rather flat tail extending to a projected width of 0.0. For an intrinsic width of 20 kpc, only 13% of the sources are expected to have projected widths less than 5 kpc. Since there are 30 sources with projected widths less than 20 kpc in the heterogeneous sample (see Fig. 4.11), there should be less than four single tail sources (i.e., sources with widths less than 5 kpc). However, 13 single tail sources (widths < 5 kpc) are observed, i.e., a factor of ~3 greater than expected. This difference is shown to be significant by a goodness-of-fit test which compared the observed distribution (below 20 kpc) in the heterogeneous sample (Fig. 4.11) with the expected distribution assuming (for simplicity) an intrinsic width of 20 kpc. A distribution of intrinsic widths less than 20 kpc will produce a larger number of single tail sources. The goodness-of-fit test resulted in a reduced chi-square of 8.33. The probability that this much difference between the two distributions is produced by chance in $P \leq 0.1\%$. A similar test assuming an intrinsic width of 10 kpc also fails to account for the number of NATs with widths less than 10 kpc. Thus, the distribution of intrinsic widths must extend both to small (<5 kpc) and large (~60 kpc, perhaps >100 kpc) widths in order to account for the observed distribution.

Single tail NATs or one-sided jets?

The question of the nature of single tail sources was first addressed in detail by Simon (1978). The large increase in the number of high resolution maps of NATs since then allows this question to be

readdressed with further success. Part of the excess number of sources with widths <5 kpc may be due to a subset of sources in which the beams are swept back almost immediately after ejection from the nucleus. This may occur in galaxies in which there is very little ISM in the galaxy to protect the beam from the full force of the ICM. If low momentum flux jets are produced in galaxies without a significant ISM, the jets will be bent back very quickly. Since there is no ISM to provide a turbulent wake, the jets must provide the kinetic energy to power the luminosity in the tail. Since the jets have low kinetic energy flux, the source luminosity will be low. This hypothesis is consistent with the data on single tail sources, since they tend to have much lower integrated radio powers than other NATs. The median $\log_{10}$ power at 1.4 GHz for the 12 single tailed sources with widths < 5 kpc is 23.95, and is lower than the median for the 51 NATs as a whole (24.33). The median test results in a reduced chi-square of 6.93, i.e., the probability that the single and twin tail NATs are drawn at random from parent populations with the same median powers is $P \leq 1\%$. One prediction of this model is that there should be very little ISM in the parent galaxy of a single tail NAT.

Another possibility is that the single tail NATs are located nearer to the cluster center than the twin tail NATs. The single tail sources would then be moving faster near perigee (closest approach to the cluster center) on their orbit through the cluster. Also, the external medium is denser near the cluster center. Thus, the ram pressure forces would be stronger and the beams would be bent sooner. Using all 51 NATs, this hypothesis was tested. The median projected distance, D_c,

from the cluster center is slightly smaller for the single tail sources (0.145) than for the twin tail sources (0.18). However, the median test results in a reduced chi-square of 1.54 (a probability of being produced by chance of P ≈ 22%) and, thus, the difference is not statistically significant.

One alternate possibility is that the single tail sources are relatively stationary, one-sided jets. (Additional velocity information may help to answer this question.) However, one-sided jets are usually associated with high luminosity objects ($\log_{10} P_{1.4} > 24.5$ W/Hz, e.g., Bridle and Perley 1984), while these single tail sources are relatively weak. Also, stationary, one-sided jets might be expected to build up diffuse lobes. Unless these sources are observed at a special point in their lifetime, the lack of diffuse lobes also argues against their being one-sided jets. Thus, it seems more likely that low power, single-sided sources without lobes are NATs rather than one-sided jets. (See, however, Harris, Costain, and Dewdney 1984.)

Some of the single tail NATs may be sources in which the beams are ejected parallel to the direction of motion of the galaxy (e.g., 1615+351, Ekers et al. 1978; Chap. III; 2247+11, Hardee, Eilek, and Owen 1980). If the beam which is ejected directly into the direction of motion is disrupted and is not able to convert its kinetic energy into radio luminosity, then this would account for the lower radio luminosities of these single tail sources (R. Ekers 1983, private communication). Can this amount of energy be "hidden" in a nonobservable form? A conservative assumption would be that all the energy goes into heating a single, relatively small, volume of gas. (If

the energy is spread out along the galaxy's path, then the problem becomes even easier.) Over the source lifetime, t_s, the radio luminosity, L_{rad}, would go instead into heating a volume of gas in front of the galaxy, giving $L_{rad}t_s \approx nkTV$, where n, T, and V are the density, temperature, and volume of the hot "lobe" of gas, and k is the Boltzmann constant. Using $L_{rad} = 10^{40}$ ergs/sec and $t_s = 10^8$ yrs, which are typical values for NATs, and taking a volume comparable to that of the galaxy, $V = (4\pi/3)(10 \text{ kpc})^3$, gives $nT \approx 2\text{x}10^3$ K cm^{-3}, which is comparable to the conditions in the ICM, i.e., if $n \sim 10^{-4}$ cm^{-3}, then $T \sim 2\text{x}10^7$ K. Such a lobe of hot gas would produce undetectable amounts of optical line emission and thermal X-ray emission.

Thus, even if all the energy in the forward beam went into heating a relatively small volume of gas, it would be undetectable by current observational techniques. This provides a way to decrease the radio luminosity of single tail sources by a factor of ~2, assuming that the kinetic energy in the beam can be dissipated as heat in the external medium.

A new class of NAT?

There is a gap in the observed distribution of widths between 60 and 100 kpc (Fig. 4.11). The four sources (0647+693, 1200+519, 1244+699, and 1638+538) with widths greater than 100 kpc have properties intermediate between those of NATs and WATs. These sources are all associated with relatively dominant galaxies (rank 2) and are relatively powerful ($\log_{10} P_{1.4} \sim 24.8$-$25.3$ W/Hz). In addition, the tails of these sources have structure more typical of the WATs (i.e., bends at

significant angles to the axis of symmetry) than the swept back appearance more typical of NATs.

Projected width vs. integrated power and galaxy velocity: a comparison with the models

The dependence of the radius of curvature and the tail luminosity on the beam and galaxy parameters is reviewed in Chapter VII. In NATs without a significant ISM, if all other parameters (i.e., ICM density, ρ_{icm}, galaxy velocity, v_g, beam radius, r_b) are held constant, a more powerful beam (i.e., larger beam velocity, v_b and/or beam density, ρ_b) will have a larger radius of curvature and will produce a more powerful radio source than a weaker beam (Begelman, Rees, and Blandford 1979) (BRB). Thus it might be expected that there would be a correlation between radius of curvature (i.e., width) and integrated radio power.

On the other hand, in sources where there is a significant ISM, the luminosity in the tail can be provided by the turbulent galactic wake instead of by the kinetic energy in the beam (Jones and Owen 1979). (The plasmon in a channel model for NATs (Christiansen, Pacholczyk, and Scott 1981) also depends on the existence of an ISM and will be considered here to be a limiting case of the Jones and Owen model.) In this case, if all other parameters were held constant (ρ_b, v_b, and ρ_{icm}), then galaxies with larger velocities and/or ISM radii would have more energetic wakes ($L \propto r_s^2 v_g^3$, where r_s is the radius of the ISM in the parent galaxy), and thus larger integrated powers than galaxies with lower velocities or smaller ISM radii. In the Jones and Owen model, the radius of curvature would depend on the radius of the ISM, since the

beams would not bend significantly until near the edge of the ISM. Since NATs with a larger ISM radius would tend to have more energetic wakes, NATs with larger radii of curvature would tend to have larger integrated radio powers. Thus, both models predict a positive correlation between integrated radio power and width.

The $\log_{10}$ integrated power at 1.4 GHz vs. the projected width (for 50 sources) is plotted in Figure 4.13. The larger heterogeneous sample was used here because of the stronger bias against low intrinsic power in the homogeneous sample. One source, 1658+326, was omitted because its width could not be estimated reliably. The lack of sources in the lower right-hand corner of Figure 4.13 may be real. The size of the ISM radius depends upon parameters such as the stellar mass loss rate and galaxy velocity. Jones and Owen estimate that given the range of input parameters the plausible range of values for the ISM radius is ~4-50 kpc. Thus, in sources with very large widths (> 100 kpc), the jets probably extend into the ICM. If this is the case, then their bending is described by the BRB model. Sources with large widths are produced either by very low galaxy velocities or very powerful jets. If the jets are very powerful, then the source luminosity is expected to be high. Thus, unless the galaxy velocities are very low, very wide sources should be relatively luminous. This is in fact what is observed in Figure 4.13.

The Spearman rank test results in $\rho = 0.41$, which will be produced by chance in a random sample of 50 objects with a probability of $P \approx 0.3\%$. So, there is a correlation; i.e., the sources with larger widths tend to have larger integrated radio powers, which is consistent with both models. This is also consistent with the result that rank 2 galaxies

have larger integrated radio powers (and possibly larger widths) than rank 3 galaxies.

In the Jones and Owen model, a larger galaxy velocity will produce a more energetic wake and, assuming the same value for the efficiency, a higher integrated radio luminosity. Therefore, in this model a correlation is expected between the galaxy velocity and the integrated radio power. In the BRB model, higher momentum flux (i.e., larger $\rho_b v_b^2$) beams will produce a brighter radio source. However, such beams will be harder to bend, and high momentum flux beams will not produce a NAT unless the galaxy velocity is also high. Thus, in the BRB model high luminosity NATs should also have higher galaxy velocities. A correlation between galaxy velocity and integrated radio power would be interesting, but cannot be used to discriminate between the two models. A plot of $\log_{10}$ total power at 1.4 GHz vs. galaxy velocity for the 22 NATs in Abell clusters with measured velocities is shown in Figure 4.14. There is no strong correlation apparent. The Spearman rank test results in $\rho = 0.30$ ($P \approx 9\%$) and confirms this impression. Hence, there is no significant correlation between galaxy velocity and integrated radio power in these data.

It is possible that the sample is composed of both groups of sources: those with a significant ISM and those without. The twin tailed NATs were subjectively divided into two groups based on their morphology. The 18 sources which resemble NGC 1265 (i.e., the jets make a very sudden transition into bright, broad, diffuse tails) were selected and plotted in Figure 4.15. The 12 twin tail sources in which the jets did not exhibit such a rapid transition (non-diffuse tailed)

Figure 4.13

Log_{10} integrated power at 1.4 GHz (watts per hertz) vs. width (kiloparsecs) for 50 NATs.

Figure 4.14

Log_{10} integrated power at 1.4 GHz (watts per hertz) vs. velocity with respect to the cluster mean (kilometers per second) for 22 NATs.

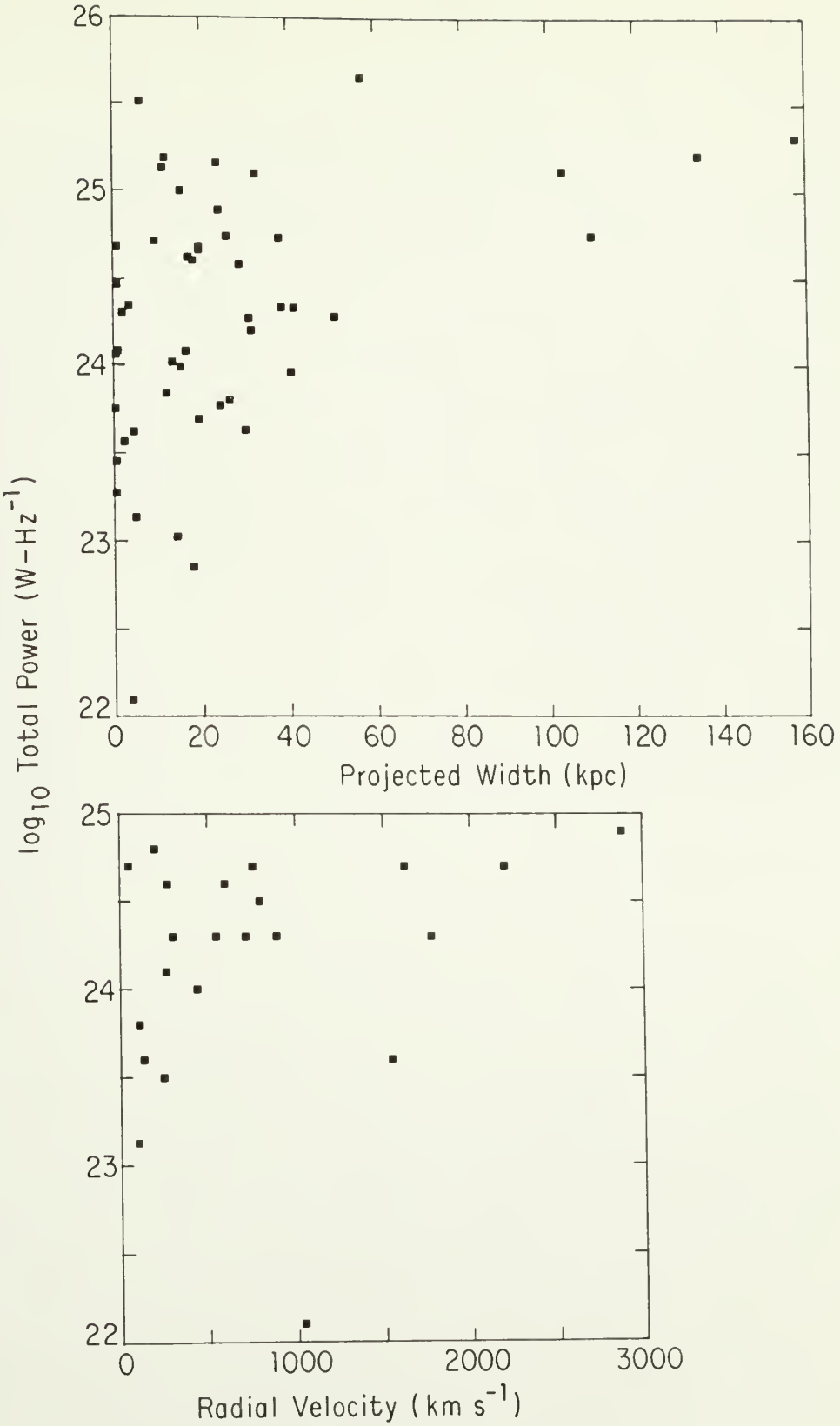
26
25
24
23
22
0
20
40
60
80
100
120
140
160
Projected Width (kpc)
log10 Total Power (W-Hz-1)
25
24
23
22
0
1000
2000
3000
Radial Velocity (km s-1)

are plotted in Figure 4.16. This morphological classification is subject to several selection effects (e.g., sensitivity to low surface brightness structure, resolution, projection, etc.), but it is the best that could be done with the present data. In both of these subgroups there is less correlation than in the combined sample. In the non-diffuse tail group, the Spearman rank correlation is $\rho = 0.43$ ($P \approx 8\%$), and for the diffuse tail group, $\rho = 0.04$ (no correlation at all!). The most conservative conclusion that can be drawn from this is that the variation of the other parameters is sufficient to wash out any correlation in the smaller subgroups. Also, the single tail NATs which tend to have both small widths and low radio powers have been omitted from the two subgroups. The presence of the single tail NATs in the larger sample of 50 NATs may enhance the correlation. There are, however, two interesting differences between the two subgroups:

(1) Over half (7 out of 12) of the non-diffuse tailed sources are rank 2 galaxies, while a much smaller fraction (6 out of 18) of the diffuse tailed galaxies are rank 2. The significance of the suggestion that the non-diffuse tail sources are more likely to be rank 2 than the diffuse tail sources was examined using a 2x2 contingency table test (based on the binomial distribution; see Conover 1980) which resulted in a statistic $T = -1.35$ ($P \approx 9\%$). Thus, the data are not consistent with the hypothesis that non-diffuse tail sources are more likely to be rank 2 than diffuse tail sources.

(2) The diffuse tailed sources have a narrow range of widths (~15-50 kpc, mean = 24.4, rms = 9.5) which is comparable to the expected width of the ISM (see Jones and Owen 1979), while the other group has a

Figure 4.15

Log_{10} integrated power at 1.4 GHz (watts per hertz) vs. width (kiloparsecs) for 18 NATs which exhibit a very sudden transition between the jets and the tails (i.e., the diffuse tailed NATs).

Figure 4.16

Log_{10} integrated power at 1.4 GHz (watts per hertz) vs. width (kiloparsecs) for 12 NATs which exhibit a very gradual transition between the jets and the tails (i.e., the non-diffuse tailed NATs).

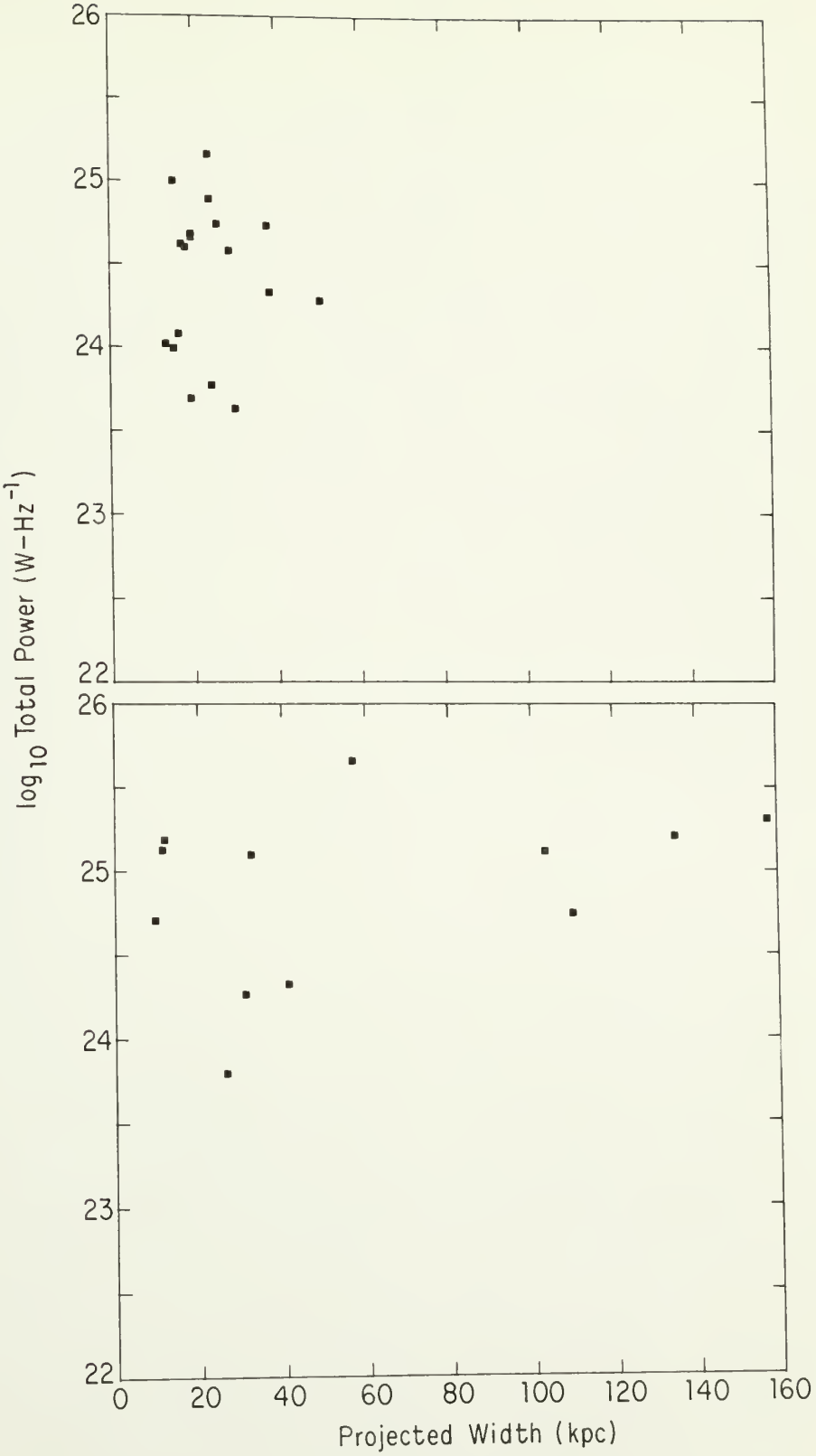
26
25
24
23
22
log10 Total Power (W-Hz-1)
26
25
24
23
22
0
20
40
60
80
100
120
140
160
Projected Width (kpc)

somewhat broader distribution of widths (~10-60 kpc, mean = 27.7, rms = 15.5). (If the four sources with widths >100 kpc are included, the range of widths in the non-diffuse tailed sources is increased to ~10-160 kpc.)

The existence of this remarkable difference in the morphology of the jet-tail transition is consistent with the hypothesis that the sources fall into two groups, which differ in the degree to which the galaxy has an appreciable ISM. Those sources whose morphology is similar to that of NGC 1265 might be formed in galaxies with a significant ISM. NATs may abruptly form broad, bright, diffuse tails only if the beams can be bent back into a turbulent galactic wake. The upper limit to the range of widths in the diffuse tailed sources would then come directly from the upper limit to the radius of the ISM in these galaxies. Sources in which the beams extend much further from the galaxy will miss the galactic wake entirely, and may form a diffuse tail very gradually unless instabilities or entrainment are very important. The lower limit (~15 kpc) to the distribution of widths in the diffuse tailed sources may come from the fact that the ISM will protect the beam from the full force of the oncoming ICM. The beam will not be bent significantly until it reaches the outer regions of the ISM, where it will be bent more sharply (see Jones and Owen 1979). Thus, the width of the diffuse tailed sources would directly reflect the width of the ISM in the parent galaxy.

If the existence of an ISM and a turbulent wake are not important then other possibilities must be considered. An alternate possibility is that fluid instabilities and internal turbulence are the causes of

the rapid jet-tail transitions (e.g., Benford, Ferrari, and Trussoni 1980, Baan and McKee 1983). If this is the case, then the different characteristic widths to the two groups would be fortuitious. Also, the reason for the difference in the development of the instabilities in the two groups of sources would be an interesting question.

Lengths

The length of the tail is taken to be the distance from the core to the point furthest from the core where the tail disappears into the noise. The observed tail length can be a function of observing frequency, (u,v) coverage, resolution, and sensitivity. Because of this, the results of this section must be viewed with caution. In sources where all of the total flux density is present in the interferometer map, the observed length should be the true length of the tail (at that frequency). In sources where the total flux density is not seen in the map, the tail length is given as a lower limit (Table 4.2B).

The distributions of projected lengths (in kiloparsecs) for ranks 2, 3, and 2 and 3 combined for the NATs in the homogeneous sample are given in Figure 4.17. The corresponding distributions for the 51 NATs in the heterogeneous sample are shown in Figure 4.18. (Lower limits are shown as arrows.) The median length of the sample of 51 NATs (123.5 kpc) is only slightly smaller than that of the subsample (132 kpc). Such a relationship could be due to a dependence of the observed tail length on radio power (see discussion below). Figure 4.17 suggests that the rank 2 galaxies (median 185 kpc) are slightly longer than the rank 3 galaxies

(median 128 kpc). However, this difference is not statistically significant. Application of the median test resulted in a reduced chi-square of 0.74 for the subsample, which would be produced by chance with a probability of P ≈ 39%. For the heterogeneous sample, the conclusions are similar. The median test resulted in a reduced chi-square = 0.63 (P ≈ 43%). Thus, the rank 2 and 3 galaxies appear to have comparable observable lengths. There are several possible reasons for this.

(1) If the tails are all simply passive wakes, then the tail length, L, is given by $L = v_g t_1$, where v_g is the galaxy velocity and t_1 is a time scale which is the larger of either the radiative loss time or the lifetime of the turbulence which is capable of particle acceleration in the turbulent wake. The turbulence lifetime may be the larger time scale since there is evidence for *in situ* particle acceleration in the tails of some NATs (e.g., Ekers *et al.* 1978; Wilson and Vallee 1977; Baggio, Perola, and Tarenghi 1978; Simon 1979; and Downes 1980). The time scale for decay of turbulence in a wake depends on how quickly the energy in the largest eddies can cascade down to smaller size scales where the viscosity and thus the energy dissipation are more important (e.g., Landau and Lifshitz 1959, Chap. 3). The decay time scale goes roughly as $t_1 \propto d/v$ (Landau and Lifshitz 1959, p. 143), where d is the characteristic size of the largest turbulent eddies (in this case the width of the galaxy) and v is the characteristic velocity of the eddies (i.e., the galaxy velocity if it is subsonic, or the sound speed of the ICM if the galaxy velocity is supersonic). Thus, if the galaxy velocities are at least transsonic in the ICM (which is required by the

bending models), the larger galaxies would tend to have a longer turbulence decay time scale and thus longer tails than the smaller galaxies.

(2) Within the context of the beam/plasmon models for NATs, the required beam or plasmon velocities are typically a factor of ~10 higher than the respective galaxy velocities (Chap. VII). If the beams in rank 2 galaxies are not disrupted by a turbulent galactic wake (e.g., because the jets carry more thrust or because the turbulence is negligible behind larger galaxies due to a lower galaxy velocity), then the tails may have some significant velocity with respect to the ICM. In that case, the tail lengths would be longer than otherwise expected in rank 2 galaxies.

(3) A plot of the tail length vs. $\log_{10}$ integrated power at 1.4 GHz for the 51 NATs is shown in Figure 4.19. There is a definite suggestion that the more powerful sources are longer. The Spearman rank test results in a value for ρ of ~0.50, which will be found in an uncorrelated population of 51 objects with a probability of $P < 0.1\%$.

A possible selection effect is that in the brighter radio sources the tails can be traced further from the galaxy before they are lost in the noise. Since the rank 2 galaxies tend to be more powerful radio soures than the rank 3 galaxies, a larger fraction of the tail length of rank 2 galaxies might be observed. If rank 2 galaxies have intrinsically shorter tails than rank 3 galaxies, this selection effect might cause the observed tail lengths to be comparable.

(4) If the rank 2 galaxies have lower galaxy velocities than the rank 3 galaxies, then the result that the observed lengths are

Figure 4.17

Projected length (kiloparsecs) for the homogeneous subsample of 39 NATs for galaxies of: rank 2, rank 3, ranks 2 and 3 combined. Lower limits are shown as arrows.

Figure 4.18

Projected length (kiloparsecs) for the heterogeneous sample of 51 NATs for galaxies of: rank 2, rank 3, ranks 2 and 3 combined. Lower limits are shown as arrows.

Figure 4.19

Projected length (kiloparsecs) vs. $\log_{10}$ integrated power at 1.4 GHz (watts per hertz) for the heterogeneous sample of 51 NATs in Abell clusters.

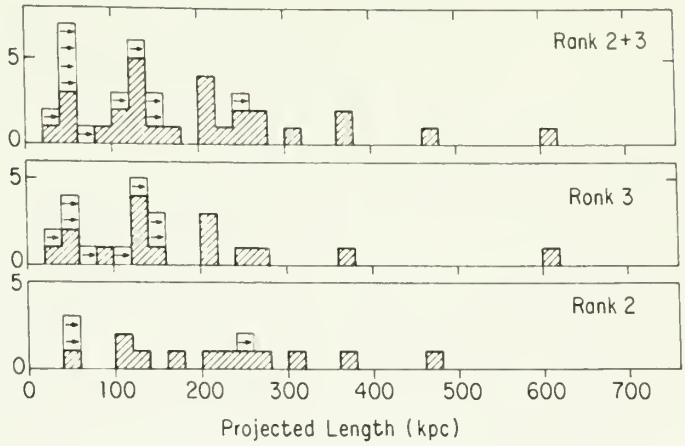
Rank 2+3
Rank 3
Rank 2
0
5
0
100
200
300
400
500
600
700
Projected Length (kpc)

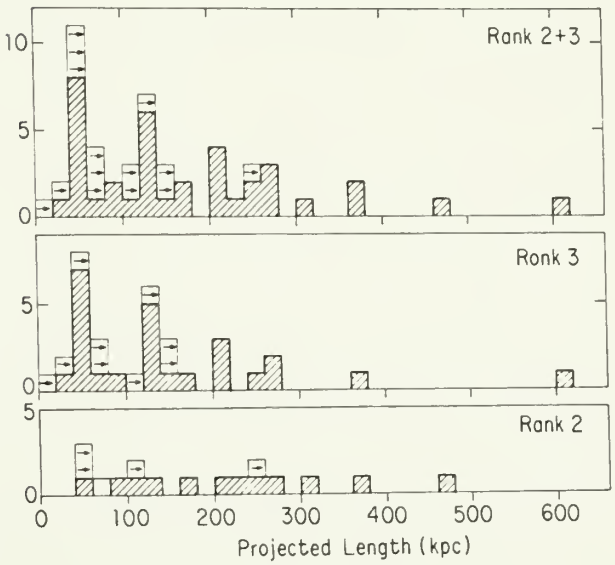
Rank 2+3
Rank 3
Rank 2
0
5
10
0
100
200
300
400
500
600
Projected Length (kpc)

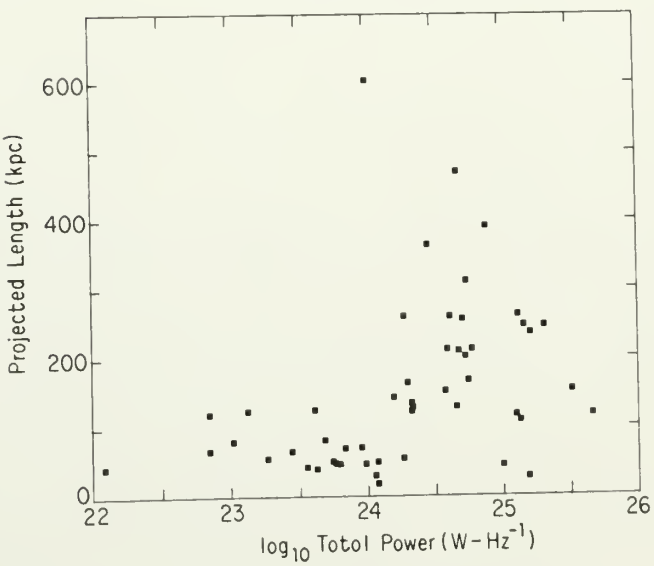
Projected Length (kpc)
0
200
400
600
22
23
24
25
26
log10 Totol Power (W-Hz-1)

comparable might be due to one or more of the effects discussed above. However, at this point the data suggest that the rank 2 and 3 galaxies have comparable velocities through the ICM. If this result is confirmed, then it would suggest that these effects are not important, and that the lengths are comparable simply because the galaxies travel comparable distances within the appropriate time scale, t_1, which must also be comparable.

4.3 Summary

The global properties of both a heterogeneous sample of 51 NATs in the directions of Abell clusters and a well-defined homogeneous subsample of 39 NATs have been presented and the implications for models of NATs have been discussed. Except for the distributions of total powers, the two samples give identical results, though the correlations tend to be stronger in the homogeneous sample. This suggests that the correlations found here are not dependent on the range of radio powers considered. The results are as follows:

(1) NATs are about equally likely to be found in clusters of any Bautz-Morgan type.

(2) There is a weak suggestion that richer clusters contain more NATs per cluster than poorer clusters and that richer clusters are more likely to contain NATs than poorer clusters.

(3) There are significant differences between the expected and observed number distributions as a function of Rood-Sastry type. There is an excess of binary clusters with NATs and a deficiency of irregular

clusters with NATs. If the evolutionary scenario suggested by Struble and Rood (1982) is correct, this result would be consistent with the hypothesis that NATs are found preferentially in more evolved clusters.

(4) Rank 2 and 3 galaxies are found at comparable projected distances from the cluster center. The observed distribution is roughly consistent with that expected for an isothermal King (1972) model with a core radius of 170 kpc (H_o = 75 km sec^{-1} Mpc^{-1}).

(5) Rank 2 and 3 NATs have comparable velocities through the ICM. This result is based on velocities for 22 NATs and needs to be reexamined with a larger sample.

(6) NATs associated with rank 2 galaxies have stronger nuclear cores and greater integrated powers than rank 3 galaxies. There is a hint that rank 2 galaxies have larger widths than rank 3 galaxies. The two ranks appear to have comparable observable lengths.

(7) There is a tentative correlation between core power and integrated power at 1.4 GHz.

(8) The observed distribution of $\log_{10}$ integrated powers is rather narrow, with a mean and root-mean-square of 24.25 and 0.74, respectively. Because the selection effects truncate the low power end of the distribution, a larger sample of NATs down to a much lower limiting radio power is necessary to determine the true shape of the distribution.

(9) There must be a population of sources with intrinsic width <5 kpc in order to explain the low end of the distribution of projected widths. Some of these apparently single tailed sources may be one-sided jets, though it is more likely that they are NATs in galaxies without a significant ISM in which the jets are swept back over a very short size

scale. Some single tail NATs may be sources in which one beam is ejected into the direction of motion of the galaxy and is disrupted without producing significant radio luminosity.

(10) There is a gap in the distribution of NAT widths between 60-100 kpc. The four sources with widths > 100 kpc have properties intermediate between those of NATs and WATs (i.e., they have larger integrated radio powers and are associated with more dominant galaxies, cf. Owen and Rudnick 1976).

(11) The NATs can be divided into two classes based on how rapidly the transition between collimated jets and a broad tail occurs. Galaxies which exhibit a very rapid transition (e.g., NGC 1265) have projected widths in the range ~15-50 kpc. This is comparable to the expected width of the ISM in these galaxies, and is consistent with the hypothesis that the beams in these sources are disrupted by a turbulent galactic wake (cf. Jones and Owen 1979).

(12) There is a correlation between the integrated power at 1.4 GHz and the projected width in a heterogeneous sample of 50 NATs. There is no correlation in smaller subgroups consisting of either diffuse tailed NATs or non-diffuse tailed NATs.

(13) There is no correlation between galaxy velocity and $\log_{10}$ integrated radio power at 1.4 GHz.

(14) The sources with larger integrated radio powers tend to be longer.

The correlations found here are consistent with the hypothesis (first suggested by Miley et al. 1972) that the morphology of Narrow Angle Tail sources is due to the interaction of the intracluster medium

with radio luminous plasma ejected by a moving galaxy. At this point, the statistical results are consistent with both of the continuous beam models (Begelman, Rees, and Blandford 1979; Jones and Owen 1979) and the plasmon in a channel model (Christiansen, Pacholczyk, and Scott 1981) for the structure and energetic requirements of NAT sources. The data are consistent with (but do not prove) the hypothesis that NATs are formed in galaxies with varying amounts of ISM. The generally smooth total intensity structure and fairly constant tail widths (in individual sources) over distances of a few hundred kiloparsecs favors a gas removal mechanism in these ellipticals which has little impact on the transport of energy from the core over the $\sim 10^8$ yr lifetime of these sources.

CHAPTER V

MULTI FREQUENCY OBSERVATIONS OF NGC 1265 (3C 83.1B)

In this chapter, the details of the VLA observations and data reduction at 21, 6, and 2 cm are discussed. Maps of the jets and tails with a wide range of resolutions (0."45-12") are presented, and the total intensity, spectral index, and polarization structure of NGC 1265 are discussed. These data are unprecedented in their sensitivity and frequency coverage at this resolution and reveal many interesting features in this prototypical NAT. An analysis of the data within the context of quasi-continuous beam models for NATs is presented in Chapter VI.

5.1 The Observations and Data Reduction

A summary of the observational parameters is given in Table 5.1. The date of the observations is given in column 1. The VLA array, and the number of antennas used, is given in column 2. The observing frequency and bandwidth (in megahertz) are given in columns 3 and 4, respectively. The calibrator used to set the flux density scale, and its flux density (in jansky) are given in column 5. As discussed in Chapter II, the flux density scale of Baars et al. (1977) was used. The total integration time (in hours) is given in column 6.

The flux densities of 3C 138 at 6 cm determined 5 months apart differ by ~4% (see Table 5.1). The measurements tabulated in the VLA calibrator manual are roughly consistent with a variability at that

Table 5.1

The Parameters of the Observations

Date	Array	Frequency (MHz)	Bandwidth (MHz)	Calibrator	(Jy)	Time (Hours)
11-05-80	A 25	4873	25	3C 286	7.33	4.8
06-05-81	B 27	4873	25	3C 138	4.20[a]	6.0
10-05-81	D 27	4885	50	3C 138	4.05[b]	2.1
11-09-81	C 26	1413	25	3C 138	8.67[b]	2.3
11-12-81	C 27	14965	50	3C 286	3.46	10.0
03-20-82	A 27	1418	25	3C 286	14.73	10.4
03-21-82	A 27	1418	25	3C 286	14.73	10.4

Notes to Table 5.1

a. Based on previous measurements tabulated in the VLA calibrator book and from M. and H. Aller (1981, private communication).

b. Determined relative to 3C 286 on 11-12-81 assuming flux densities for 3C 286 of 7.41 and 14.77 Jy at 4885 and 1413 MHz, respectively.

level. Alternately, there could have been errors in the application of the flux density scale.

Using the techniques described in Chapter II, the calibration and preliminary editing were carried out on the DEC-10 and the mapping and image processing was carried out on a VAX 11/780 at the VLA using the NRAO Astronomical Image Processing System (AIPS). The phase reference center used for all the observations of NGC 1265 was:

$\alpha = 03^h\ 14^m\ 57.^s25$, $\delta = 41°\ 40'\ 52.''00$ (epoch 1950.0).

The 21 cm data

Observations at 21 cm in the A configuration were obtained on two consecutive days (March 20 and 21, 1982) for a total integration time of 20.8 hours. The two data sets were calibrated and the data reduced in an identical manner. 3C 84 was observed for 1 minute every 14 minutes to calibrate the antenna amplitudes, phases, and instrumental polarization. 3C 84 is very strong (~14 Jy at 21 cm and ~60 Jy at 6 and 2 cm; e.g., O'Dea, Dent, and Balonek 1984) and is only ~30' away from NGC 1265 and is thus an ideal calibrator and was used for all the ~1" resolution observations. (At ~1" resolution the halo component of 3C 84 is essentially resolved out.) The solutions for the antenna polarizations obtained on both days were identical within the errors. Both 3C 286 and 3C 138 were observed in order to check the reliability of the ionospheric Faraday rotation corrections. Initially, the position angle corrections determined using 3C 138 and 3C 286 disagreed by about 15°. The Faraday rotation correction reduced the discrepancy to about 4° on both days. This residual error may be due to an inadequate model for the earth's magnetic field or to variations in the ionospheric electron density.

When the two data sets were mapped, a spurious ~1 mJy feature was discovered at the phase reference center. This was thought to be due to DC offsets in some correlators. This problem was solved by clipping the visibility data with amplitudes above 150 mJy after a 10^4 CLEAN component model for NGC 1265 was subtracted from the visibility data. Also, both 3C 84 and 3C 83.1A, which are nearby strong sources, were subtracted from the visibility data. These procedures reduced the

root-mean-square noise in the total intensity maps from ~0.22 mJy/beam to ~0.09 mJy/beam. Self-calibration of the phases did not improve the data; and the unself-calibrated data was used.

NGC 1265 was observed at 21 cm in the C configuration for a total integration time of 2.3 hours on November 9, 1981. Since 3C 84 has considerable extended structure on a scale of ≥10", it could not be used as a calibrator in the 20 cm, C configuration or 6 cm, D configuration observations. For this reason, the point source 0300+471 was used instead to calibrate the antenna amplitudes, phases, and instrumental polarization. Fourteen minute scans of NGC 1265 were alternated with 2 minute observations of 0300+471. Because 3C 286 was below the horizon during this short observing run, 3C 138 was used as both the absolute flux density standard and the polarization position angle calibrator. The bootstrapped flux density of 0300+471 was 1.5 Jy, which is consistent with other measurements. The corrections to ionospheric Faraday rotation were determined to be ~4° during the entire observing run. Since the uncertainty in this correction is probably about that size, the corrections were not applied.

It was found that interference was present throughout the C configuration observing run. Visibility points with discrepant amplitudes or a very high root-mean-square were edited out. Confusion from 3C 84 was also a problem. When a large field surrounding NGC 1265 was mapped, 3C 84 appeared at the edge of the map with a peak surface brightness of ~0.1 Jy/beam and a total flux density of ~2.5 Jy. The peak surface brightness and total flux density of 3C 84 were reduced to ~0.04 Jy/beam and 0.2 Jy, respectively, by subtracting the Fourier

transformed CLEAN components of 3C 84 from the visibility data. The phases were self-calibrated using a CLEAN component model for NGC 1265 and the nearby strong (~1 Jy) background point source 3C 83.1A. High points in the visibility data were clipped after a source model of 10^4 CLEAN components was subtracted from the data. These techniques improved the data significantly, though the root-mean-square noise in the final CLEANed map was still relatively high (~2.4 mJy/beam). The data from the A and C array observations were combined and I, Q, and U maps were made. The maps were CLEANed deeply and restored with a 1."2 (Full Width to Half Maximum; FWHM) circular gaussian CLEAN beam. A set of maps were also made using only the A array data. A 40 kλ taper (kλ = 10^3 wavelengths) was applied to the (u,v) data in order to produce maps at a resolution of 3."2 which could be used to study the properties of the first ~1.'5 of the diffuse tails. A map was made using only the C configuration data (~12") in order to study the large scale structure of the source.

There were two remaining problems in the 21 cm total intensity maps.

(1) Broad rippled centered on 3C 83.1A due to incomplete removal of the sidelobes of 3C 83.1A; and

(2) A low level high spatial frequency ripple at position angle ~-45° in the 1."2 resolution map due to some bad data at the longest spacings. The high frequency rippled were present in maps deconvolved using both the "Prussian Helmet CLEAN" devised by Cornwell (1983a) and a maximum entropy algorithm (Cornwell 1983b).

These problems are important only for the parameters derived for the diffuse tails. Further attempts to solve these problems are planned.

The 6 cm data

NGC 1265 was observed at 6 cm in the A configuration on November 5, 1980 for a total integration time of 4.8 hours. Observations of NGC 1265 at 21 and 6 cm (for 5 and 6 minutes, respectively) were alternated with 1.5 minute observations of 3C 84 at both frequencies for a period of 12 hours. However, there were severe problems with the 20 cm data during this run, and only the 6 cm data were useable. The observations of 3C 84 were used to calibrate the antenna complex gains and instrumental polarization. 3C 286 was used as both the absolute flux density standard and the absolute polarization position angle calibrator.

The phases of the visibility data were self-calibrated using a CLEAN component model. High points in the data were clipped and 3C 83.1A was subtracted from the visibility data. A small improvement in the map was achieved and the final value for the root-mean-square noise was ~0.07 mJy/beam.

NGC 1265 was observed for a total integration time of 6 hours at 6 cm on June 5, 1981 in the B configuration. To calibrate the antenna amplitudes, phases, and instrumental polarization, 3C 84 was observed for 2.5 minutes every 12.5 minutes. 3C 138 was used as both the absolute flux density calibrator and the polarization position angle

calibrator. The bootstrapped flux density of 3C 84 was 60.3 Jy which was consistent with other measurements.

The phases were self-calibrated using a CLEAN component model. 3C 83.1A was subtracted from the visibility. The root-mean-square noise in the final CLEANed total intensity map was ~0.07 mJy/beam.

NGC 1265 was observed for an integration time of 2.1 hours at 6 cm on October 5, 1981 in the D configuration. 0300+471 was observed for 2 minutes every 14 minutes and was used to calibrate the antenna gains and instrumental polarization. 3C 138 was used as both the absolute flux density standard and the absolute position angle calibrator. The bootstrapped flux density of 0300+471 was 2.6 Jy which was consistent with other measurements.

3C 84 and 3C 83.1A were subtracted from the visibility data. Self-calibration of the phases did not improve the data. The root-mean-square noise in the final CLEANed total intensity map was ~0.26 mJy/beam.

The data from all three arrays were combined to produce the highest resolution (0."45) maps with an root-mean-square noise of 0.06 mJy/beam. The data from the B and D arrays were combined, and the resulting I, Q, and U maps at 1."2 and 3."2 resolution CLEANed deeply to produce the maps used in the comparison with the 20 cm A+C array maps. The root-mean-square noise in the final CLEANed, untapered 1."2 resolution total intensity map was 0.06 mJy/beam. The high frequency ripple seen in the 1."2 resolution 21 cm (A+C) data is also seen in the 6 cm (B+D) data. Because of the importance of comparing 6 and 2 cm maps using data

with the same (u,v) coverage, additional 6 cm maps were made at 1."2 and 3."2 resolution using only the B configuration data.

The 2 cm data

NGC 1265 was observed at 2 cm for a total integration time of 10 hours on November 12, 1981 in the C configuration. 3C 84 was observed for 2.5 minutes every 14.5 minutes and was used to calibrate the antenna gains and instrumental polarization. 3C 286 was used as the primary flux density standard and the absolute polarization position angle calibrator.

These data were used to produce I, Q, and U maps at 1."2 and 3."2 resolution, which were compared with the 6 cm, B configuration maps. When NGC 1265 was mapped, a spurious ~5 mJy feature was found at the phase reference center. As in the 21 cm A array data, this was probably due to DC offsets in the amplitudes of some correlators. A 2000 CLEAN component source model was Fourier transformed and subtracted from the visibility data, which was then clipped at a level of 0.3 Jy. This removed the spurious feature and reduced the root-mean-square noise in the map from 0.3 mJy/beam to 0.18 mJy/beam. Self-calibration was not attempted.

The effect of "bandwidth smearing" on the maps

The reference center was chosen to be in the approximate center of the "horseshoe" defined by the jets. As discussed in Chapter II, the bandwidth smearing effect is a radial smearing and increases with distance from the phase center. Structure perpendicular to the jet axis

will be smeared and the peak intensity reduced by roughly the same amount everywhere along the jets. Because the phase center is very close to the jets (~20-30 arcsec) for the frequency-bandwidth-array combinations used in these observations, the magnitude of the effect is small. For the worst case (the 21 cm A-array data), the beam is broadened and the peak intensity is reduced by ~2% at the position of the jets. All other frequency-array combinations are degraded by less than 1%.

5.2 The Total Intensity and Polarization Structure

In this section maps at 21, 6, and 2 cm and one dimensional profiles of various jet parameters are presented. The total intensity, spectral index, and polarization structure are discussed. A correction for the attenuation by the primary beam was applied to the maps. A scale of 0.35 kpc/arcsec was used ($z = 0.0183$ (Noonan 1981, Tifft 1978)); $H_o = 75$ km sec^{-1} Mpc^{-1} and $q_o = 0.1$). The parameters of the maps are given in Table 5.2. The map wavelength, λ, (in centimeters) is given in column 1. The VLA arrays combined to produce the map are given in column 2. The root-mean-square noise in the CLEANed total intensity and polarization maps (Stokes parameters I and Q) are given in columns 3 and 4, respectively. The FWHM (in arcseconds) and the position angle of the CLEAN beam are given in column 5.

The total intensity structure

Edge brightening. The 6 cm total intensity map at 0."45 resolution made by combining the data from the A, B, and D arrays, is shown in Figure 5.1. A B/W radiophotograph blow-up of a portion of the map, showing the structure of the inner bright spots or "knots" in more detail is shown in Figure 5.2. Note that because of the additional structure revealed in this map, the knots are described with a nomenclature slightly different from that used by Owen, Burns and

Table 5.2

Map Parameters

λ (cm)	Arrays	ICLN rms (mJy/beam)	QCLN rms (mJy/beam)	CLEAN Beam "	"	°
21	A+C	0.115	0.046	1.2		
21	A+C	0.204	0.049	3.2		
21	C	2.4		12.9	x 11.4	-4.4
6	A+B+D	0.058	0.064	0.45		
6	B+D	0.059	0.045	1.2		
6	B+D	0.169	0.054	3.2		
6	B	0.084		1.2		
6	B	0.150	0.082	3.2		
2	C	0.177	0.190	1.2		
2	C	0.20	0.22	3.2		

Rudnick (1978). The knot W2 of OBR is seen to consist of two knots, labeled here W2 and W3, which are connected by an edge brightened bridge. At this resolution the transverse total intensity structure of the jets is very asymmetric. The knots appear to be edge brightened on the "front" or south edge. The transverse profiles taken across E1 and W2 also show this asymmetry (Fig. 5.3).

Figure 5.1

A contour plot of total intensity at 6 cm (0."45, A+B+D). Contour levels are -0.2, 0.2, 0.5, 1.0, 2.0, and 10.0 mJy/beam. The knots and warm spots are labeled. The CLEAN beam FWHM is shown as a shaded circle.

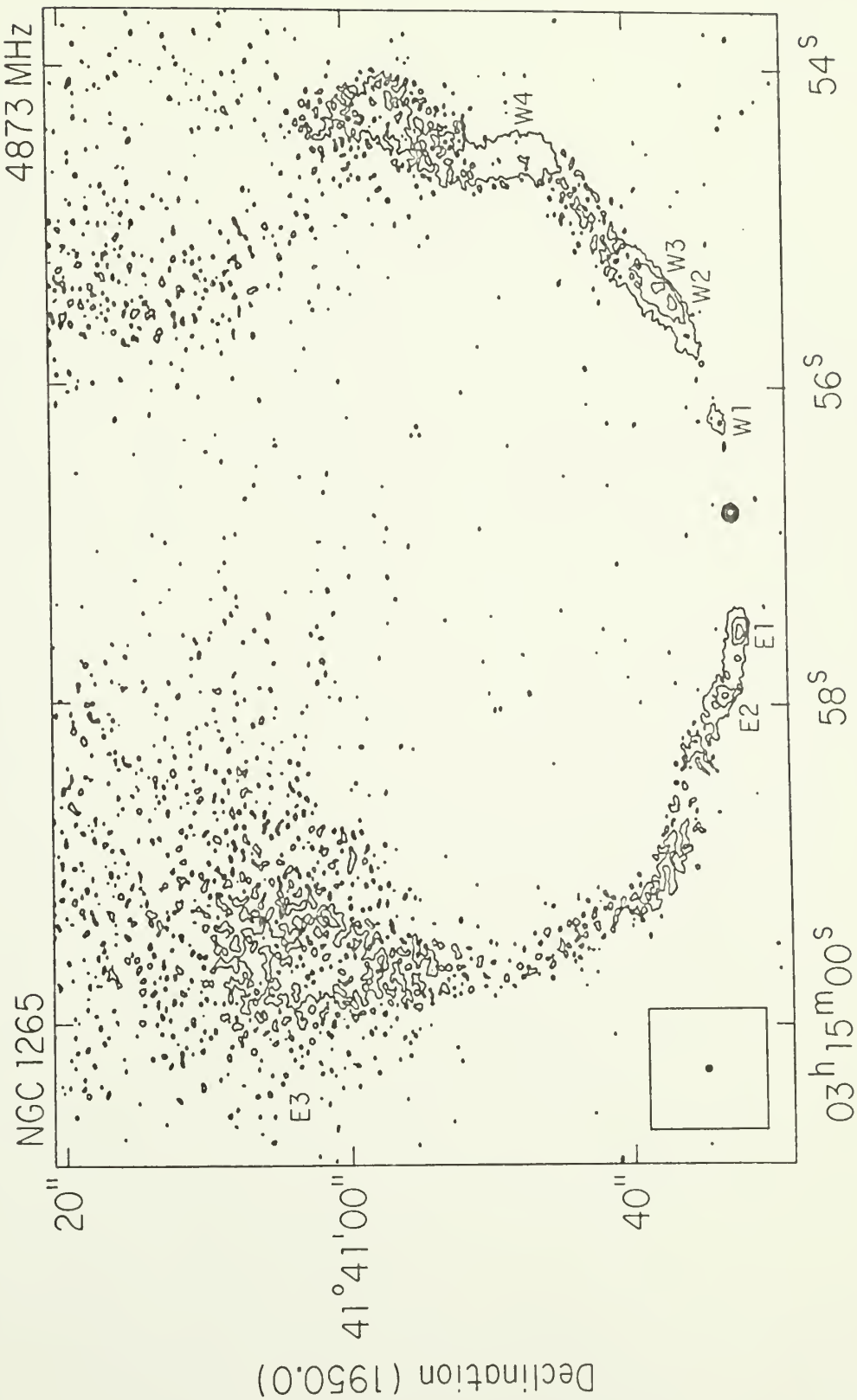
NGC 1265
4873 MHz
E3
E2
E1
W1
W2
W3
W4
20"
40"
41°41'00"
Declination (1950.0)
03h15m00s
58s
56s
54s
Right Ascension (1950.0)

Figure 5.2

A B/W radiophotograph at 6 cm (0."45, A+B+D) showing the structure of the inner knots in more detail.

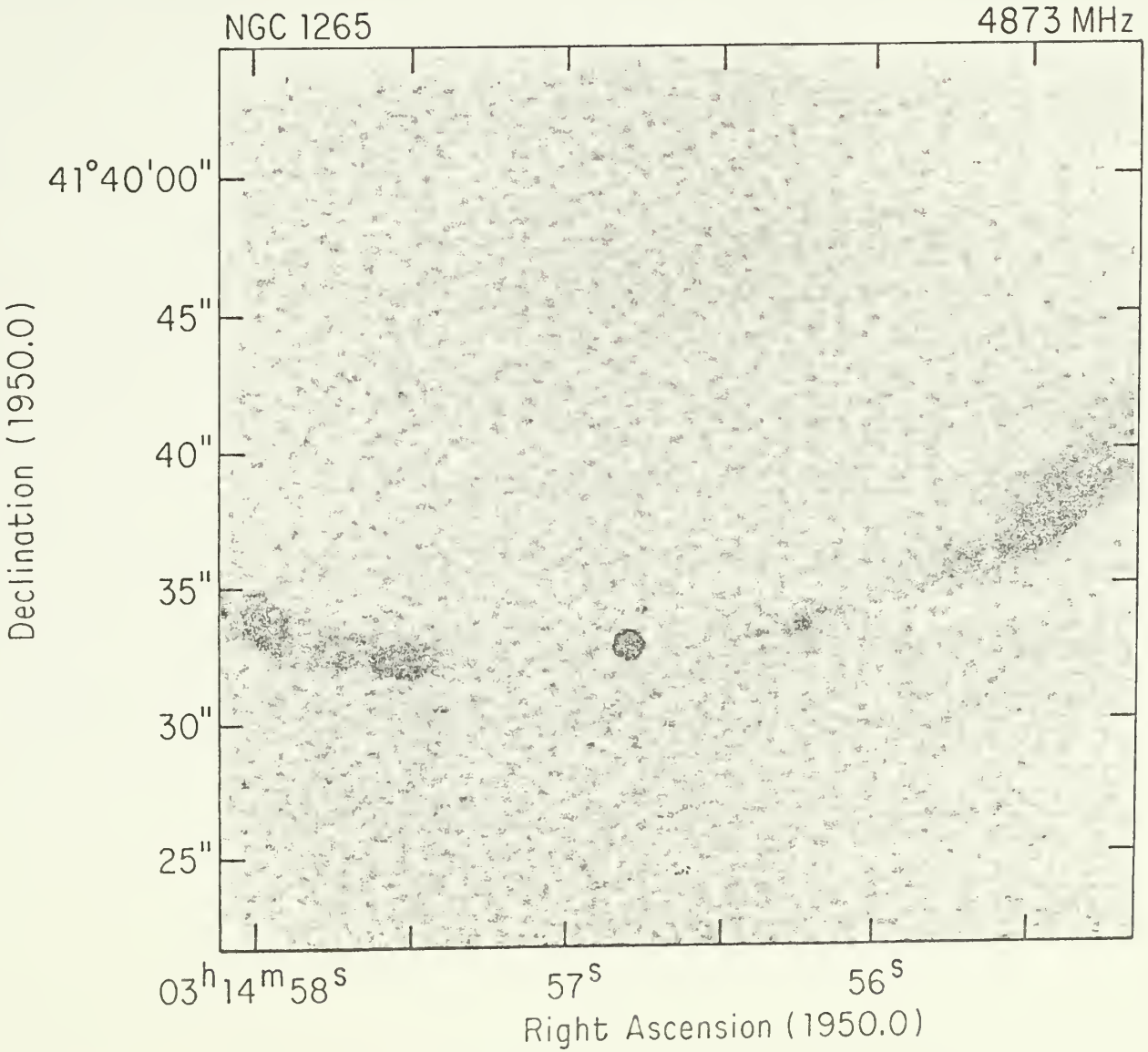
NGC 1265
4873 MHz
41°40'00"
45"
40"
35"
30"
25"
Declination (1950.0)
03h14m58s
57s
56s
Right Ascension (1950.0)

Figure 5.3

Transverse profiles of total intensity at 6 cm (A+B+D) across the edge brightened knots E1 and W2. The FWHM of the CLEAN beam (0."45) is shown.

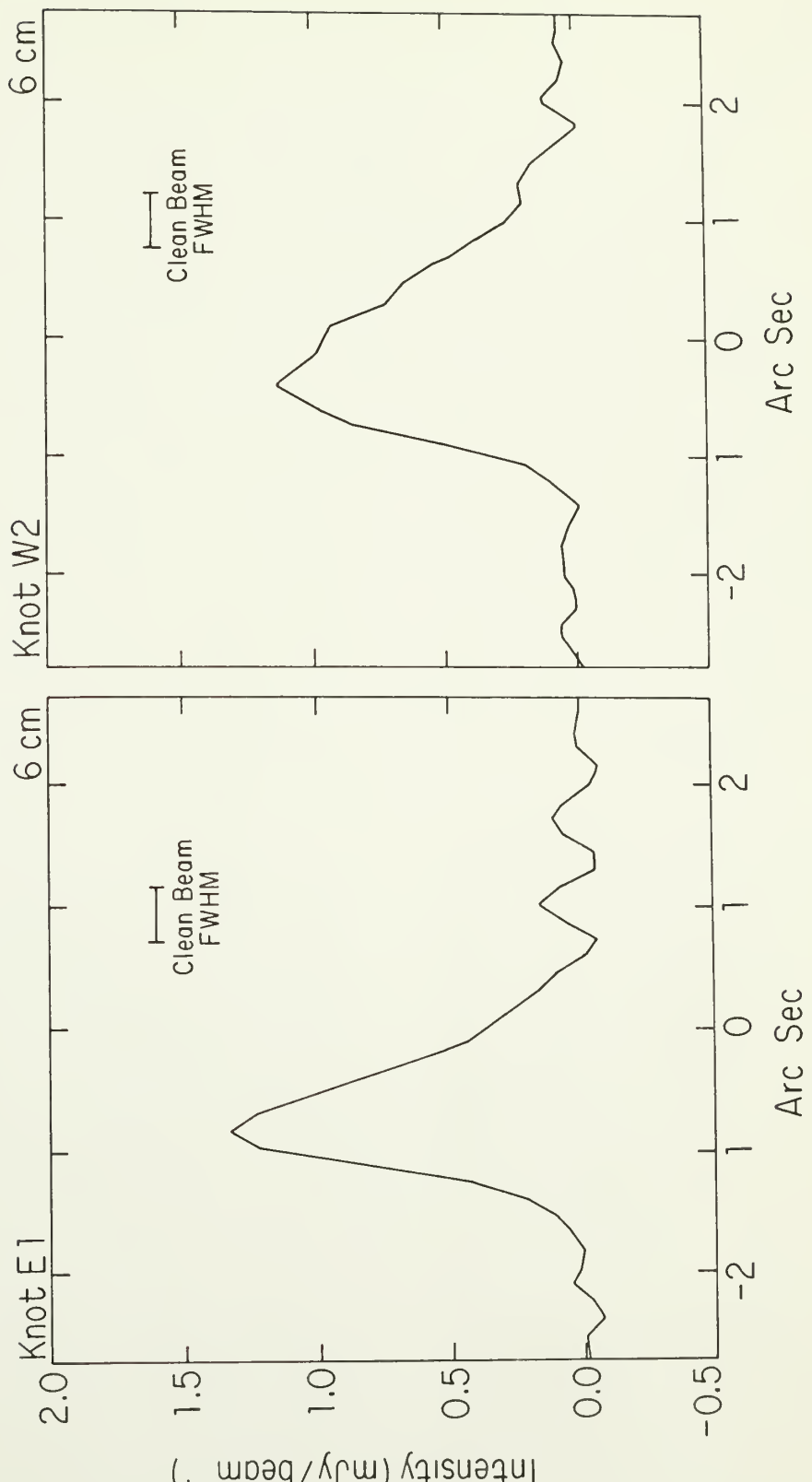
Knot E1
6 cm
Clean Beam
FWHM
Knot W2
6 cm
Clean Beam
FWHM
Intensity (mJy/beam^{-1})
2.0
1.5
1.0
0.5
0.0
-0.5
-2
-1
0
1
2
Arc Sec
Arc Sec

The arcsecond scale structure. Contour plots of the total intensity 1."2 resolution maps at 21 cm (A+C), 6 cm (B+D), and 2 cm (C array) are shown in Figures 5.4, 5.5, and 5.6, respectively. Radiophotographs (in B/W) of these maps are shown in Figures 5.7, 5.8, and 5.9, respectively. The brightness profile along the jets of the ridge of maximum brightness at 6 cm (B+D) is shown in Figure 5.10 for the east and west jets. The 21 and 6 cm maps show that the jets are continuous from the compact core to the point where they expand into the diffuse tails ~10 kpc directly behind the core. There is a hint that the west jet splits as it expands into the diffuse tail.

The jets are initially very weak (~0.4-0.5 mJy/beam at 21 cm) until the position of the knots W1 and E1 at a distance of 2 and 3 kpc, respectively, from the core. At the knots W1 and E1, the jet surface brightness increases by a factor of ~7 and ~16, respectively. However, along most of the length of the jets the brightness profile is very smooth with little variation (especially along the east jet). Ignoring the bright inner knots, the jet surface brightness changes by only about 20% and 50% along the east and west jets, respectively. Because of the weaker flux density and higher noise, the 2 cm map shows only the compact core (whose flux density continues to rise with increasing frequency) and the knots.

The diffuse jet "cocoon." At 21 cm (A+C) there is a halo or "cocoon" of diffuse emission surrounding the west jet, and to a lesser extent the east jet (see Fig. 5.4). This feature is seen in the dirty map, in the deeply CLEANed map, and in a map deconvolved using a maximum entropy algorithm (Cornwell 1983b). Thus, it is unlikely to be

Figure 5.4

A contour plot of total intensity at 21 cm (1."2, A+C). Contour levels are -0.3, 0.3, 0.7, 1.5, 3.0, 6.0, and 10.0 mJy/beam. The CLEAN beam FWHM is shown as the shaded circle.

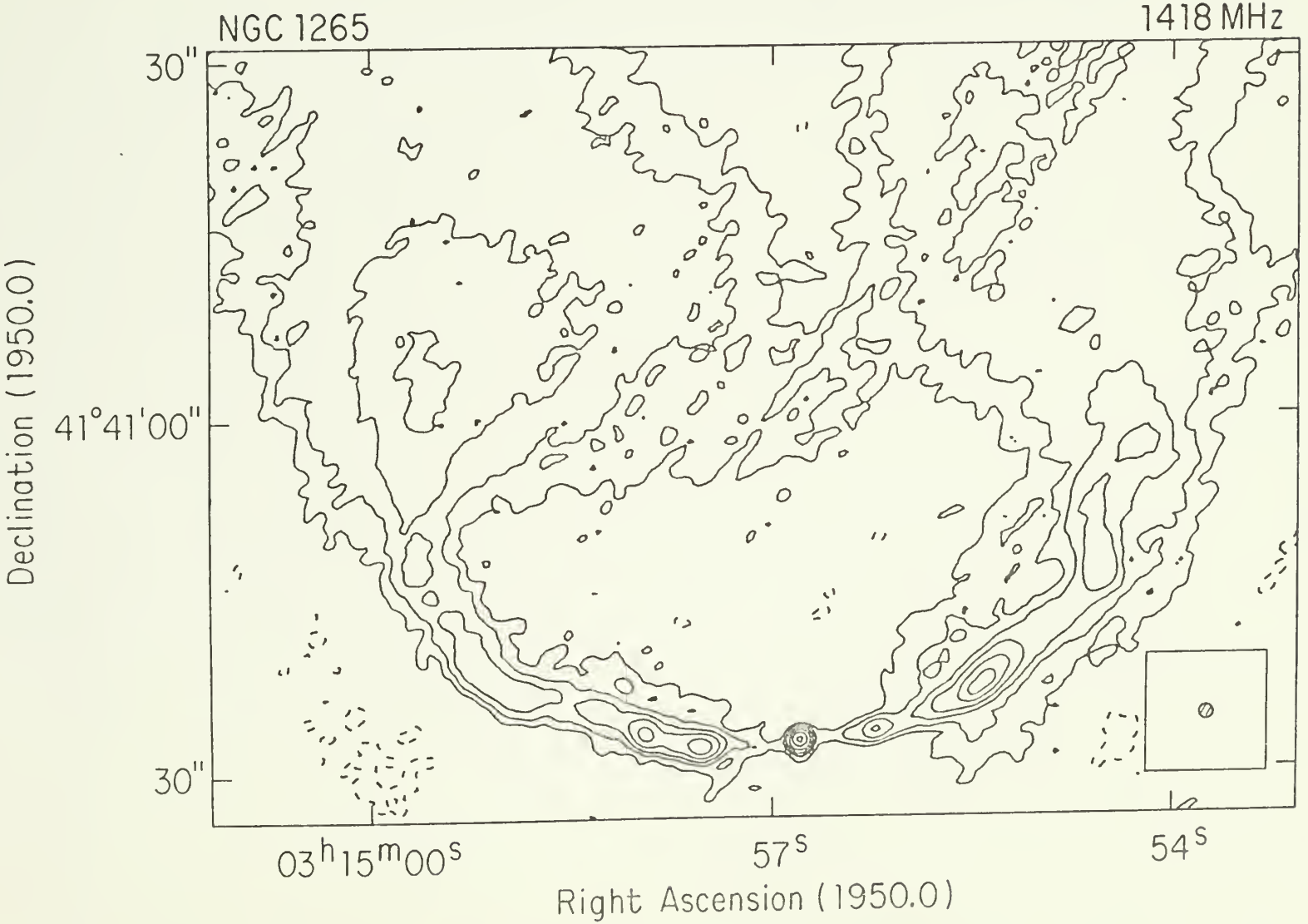
NGC 1265
1418 MHz
30"
41°41'00"
30"
Declination (1950.0)
03h15m00s
57s
54s
Right Ascension (1950.0)

Figure 5.5

A contour plot of total intensity at 6 cm (1."2, B+D). Contour levels are -0.2, 0.2, 0.7, 1.5, 3.0, 5.0, and 10.0 mJy/beam. The CLEAN beam FWHM is shown as the shaded circle.

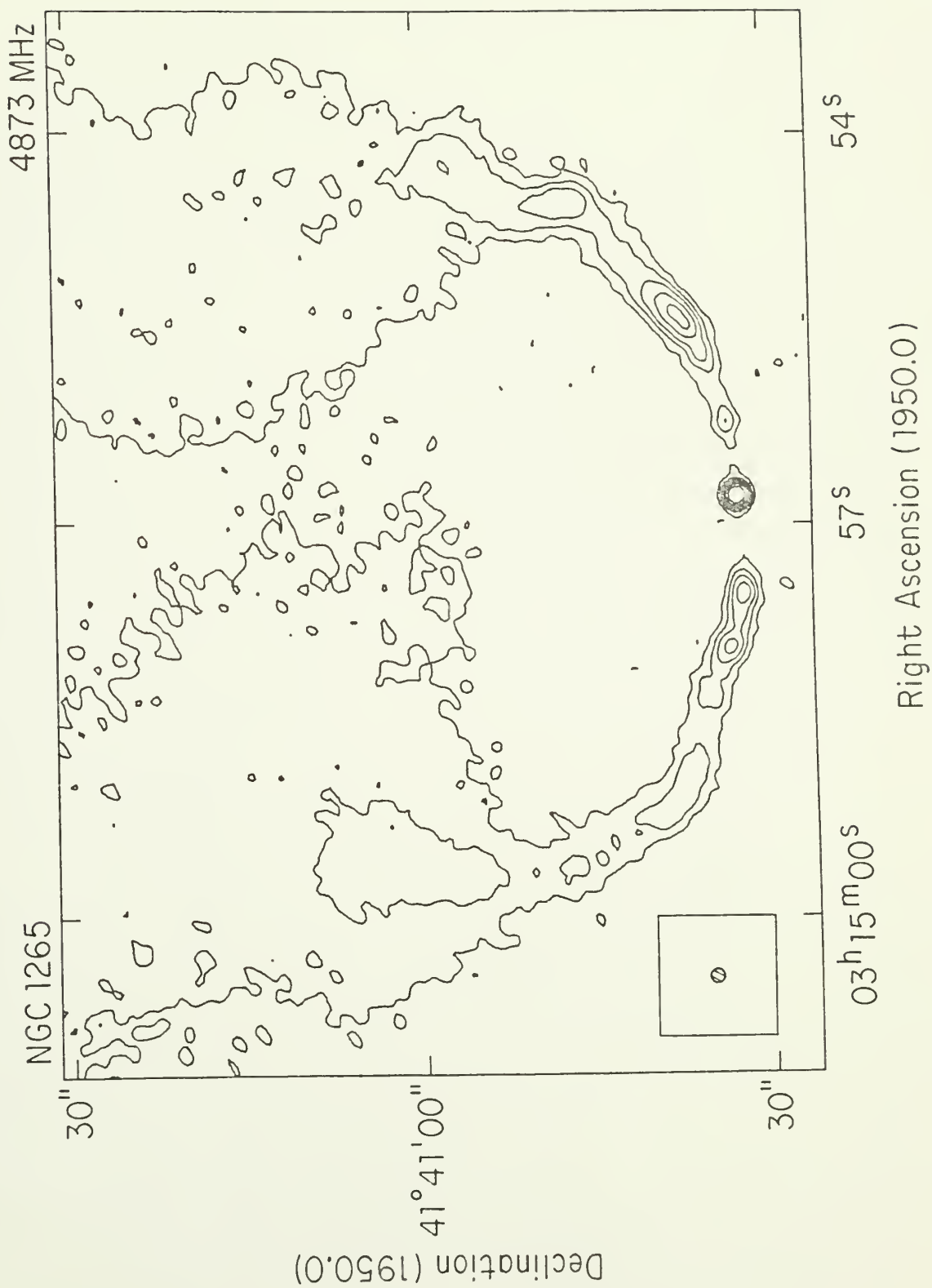
4873 MHz
NGC 1265
30"
41°41'00"
30"
03h15m00s
57s
54s
Declination (1950.0)
Right Ascension (1950.0)

Figure 5.6

A contour plot of total intensity at 2 cm (1."2, C). Contour levels are -0.5, 0.5, 1.0, 1.5, 2.0, 3.0, 5.0, and 7.0 mJy/beam. The CLEAN beam FWHM is shown as the shaded circle.

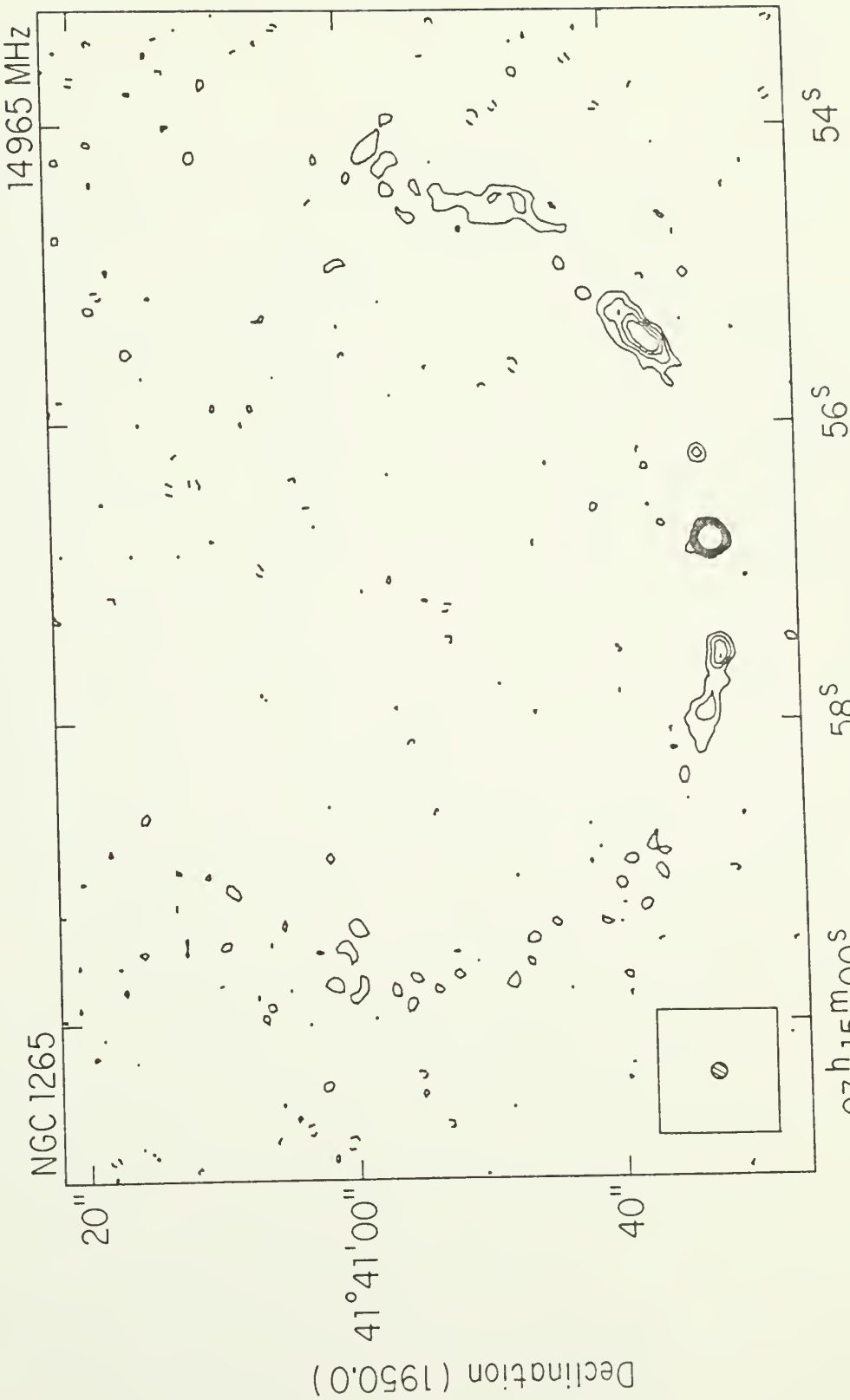
14965 MHz
NGC 1265
20"
40"
41°41'00"
Declination (1950.0)
03h15m00s
58s
56s
54s
Right Ascension (1950.0)

Figure 5.7

A B/W radiophotograph of total intensity at 21 cm (1."2, A+C) showing the jets, cocoon, and diffuse tails.

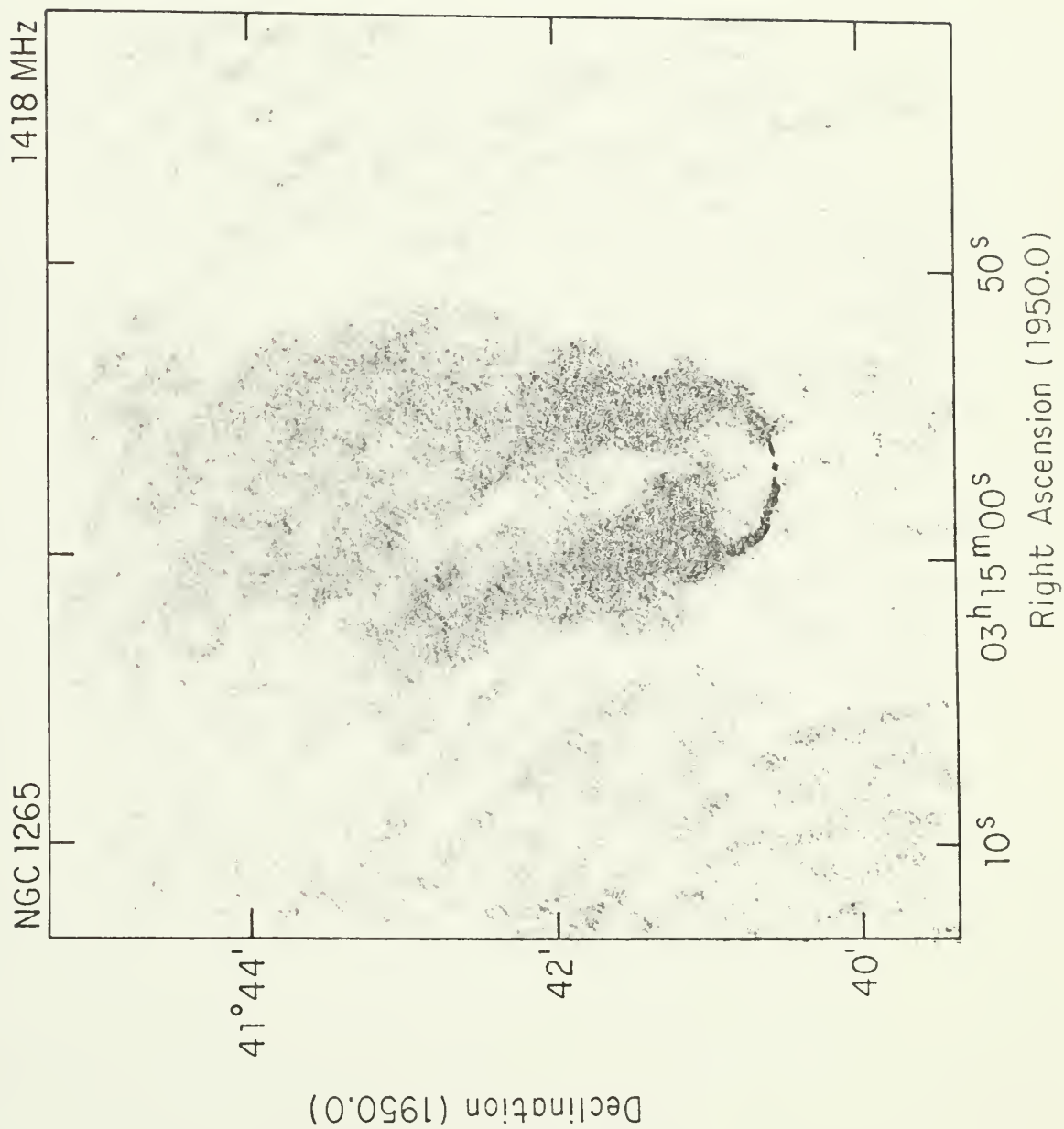
NGC 1265
1418 MHz
41°44'
42'
40'
Declination (1950.0)
10s
03h15m00s
50s
Right Ascension (1950.0)

Figure 5.8

A B/W radiophotograph of total intensity at 6 cm (1."2, B+D) showing the jets and diffuse tails.

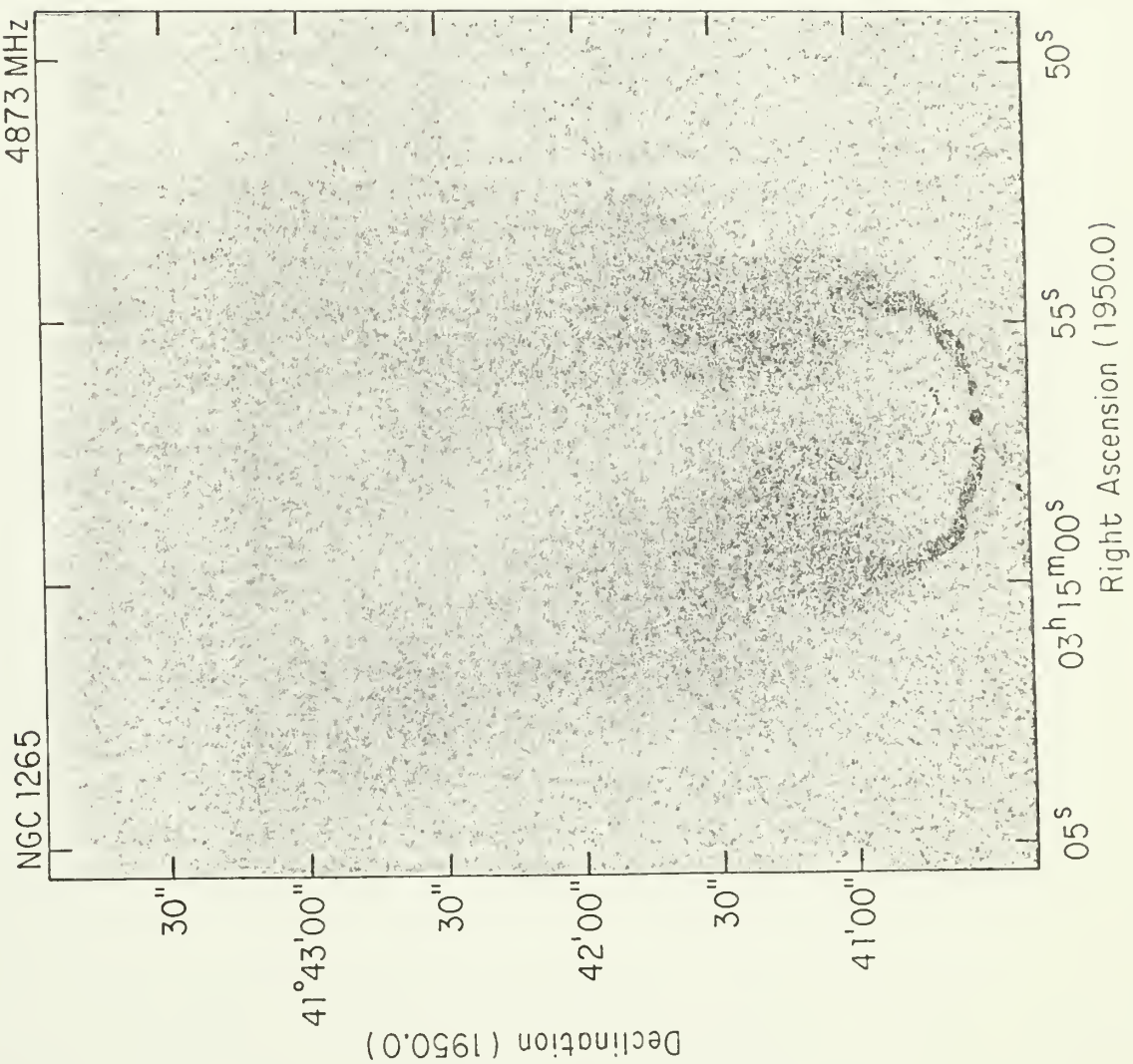
NGC 1265
4873 MHz
30"
41°43'00"
30"
42'00"
30"
41'00"
Declination (1950.0)
05s
03h15m00s
55s
50s
Right Ascension (1950.0)

Figure 5.9

A B/W radiophotograph of total intensity at 2 cm (1."2, C) showing the jets.

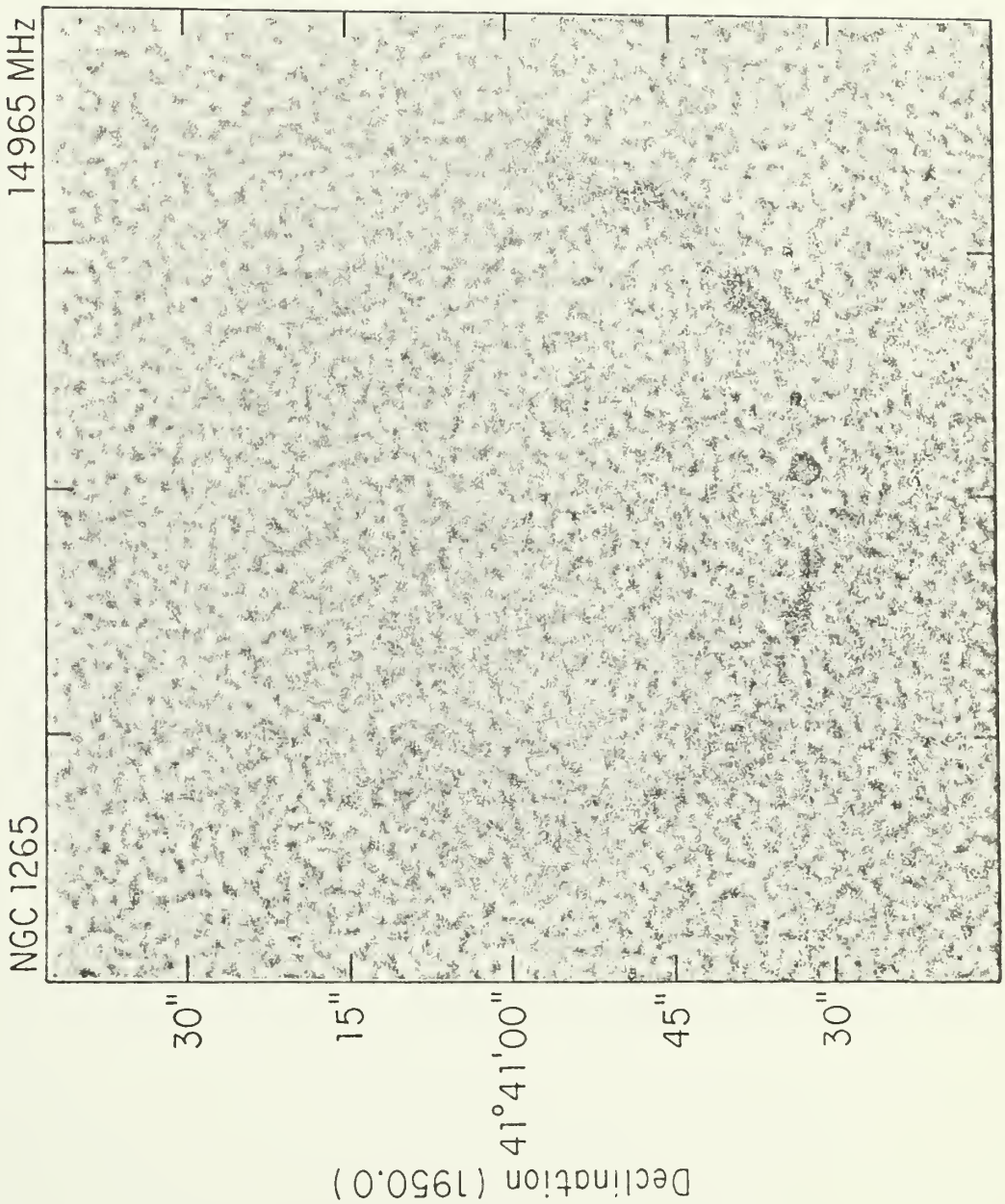
NGC 1265
14965 MHz
30"
15"
41°41'00"
45"
30"
Declination (1950.0)
03h14m59s
57s
55s
Right Ascension (1950.0)

Figure 5.10

One dimensional profiles of total intensity at 6 cm (1."2, B+D) along the ridge of maximum brightness of the east (top) and west (bottom) jets. Distance is given in kiloparsecs from the nuclear core, assuming a scale of 0.35 kpc/arcsec. The error bars are less than the size of the symbols.

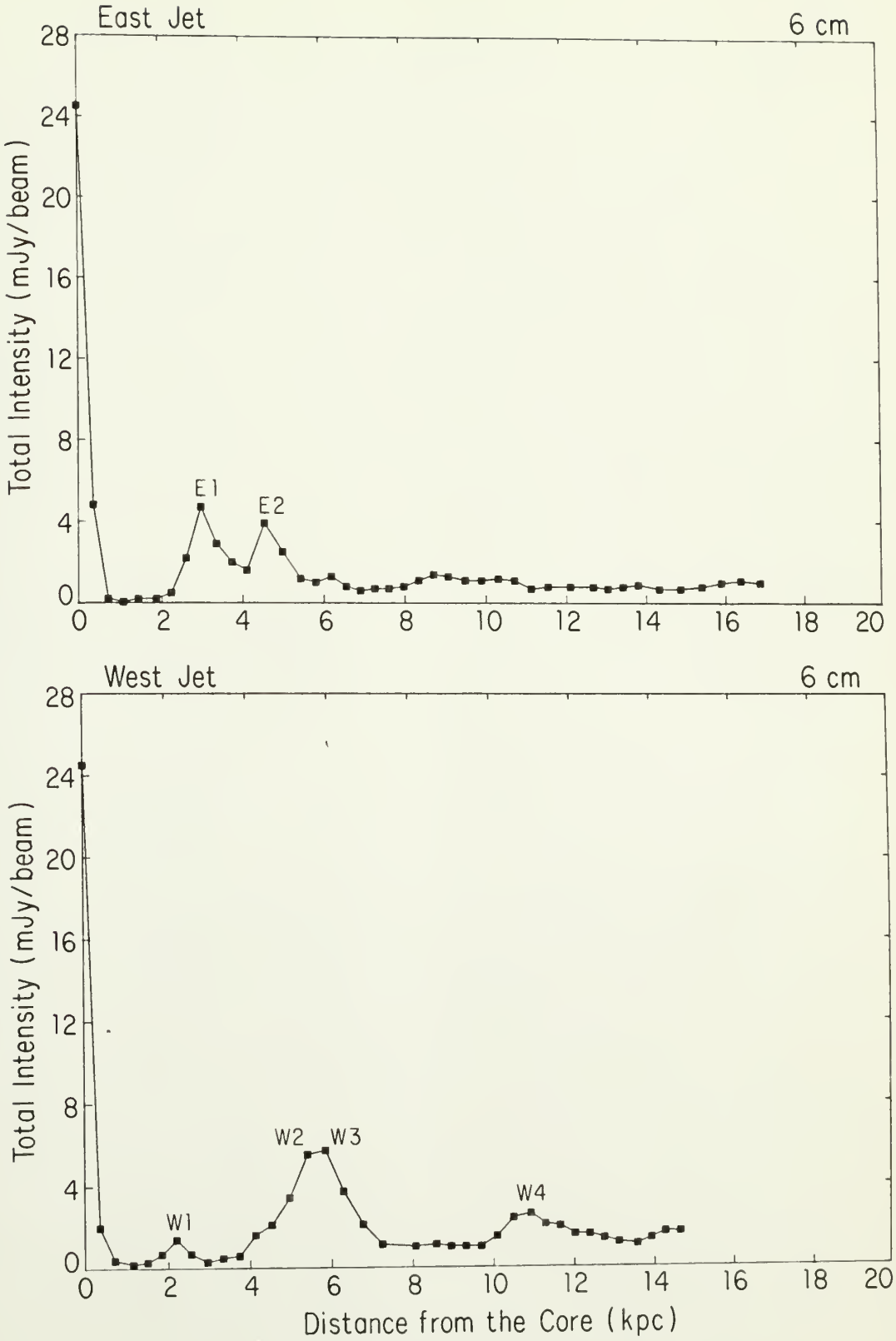
East Jet
6 cm
Total Intensity (mJy/beam)
E1
E2
West Jet
6 cm
Total Intensity (mJy/beam)
W1
W2
W3
W4
Distance from the Core (kpc)

an artifact produced by the deconvolution algorithm. Also, the cocoon is not simply proportional to the peak intensity in the source, since it is not seen around the ~12 mJy core (the strongest point in the map). Thus, the diffuse emission is probably real.

The cocoon extends ~1-2" from the west jet at a level of ~0.4-1 mJy/beam and ~0.5-1" from the east jet at a level of ~0.4 mJy/beam, with the larger extent on the inside of the "horseshoe" formed by the jets. The cocoon is not edge brightened as the jets are, but trails off into the noise in both directions. This diffuse emission is not seen in the 6 cm (B+D) maps (at a 3 sigma upper limit of 0.18 mJy/beam), implying that it has a spectral index steeper than $\alpha \approx -1$. The 6 cm (B+D) data are certainly sensitive to diffuse emission on this scale since the diffuse tails show up so well.

The 3 sigma upper limit to the polarized flux density at 21 cm is 0.15 mJy/beam. Thus, the upper limit to the fractional polarization of the cocoon is ~30-15% for total intensities in the range ~0.5-1 mJy/beam.

The jet collimation structure. Transverse profiles of the jet surface brightness (extending ~2 beamwidths into the noise on either side) were obtained at roughly 1" intervals along the jets. The 6 cm (B+D) map was used since a better baseline could be obtained due to the lack of diffuse emission surrounding the jets. Some experimentation showed that the results of fitting a gaussian to the jet profile were less sensitive to lumpiness in the baseline than was a straightforward calculation of the second moment. The jet profiles are not gaussian, but the gaussian fit provides a well defined characteristic size which

can be used to describe the jet collimation structure. The gaussian FWHM, ϕ_o was obtained and deconvolved using the relation

$$\phi = [\phi_o^2 - \phi_b^2]^{1/2} \qquad (5.1)$$

where ϕ_b is the FWHM of the gaussian CLEAN beam. Where the jet was unresolved, the jet FWHM was taken to be $< 0.5\ \phi_b$ (e.g, Burns 1979, Burns, Owen, and Rudnick 1979). For an unresolved cylinder, the jet radius, r_j, is given by $r_j < 0.425\ \phi_b$, while for a resolved cylinder, $r_j = 0.85\ \phi$ (e.g., Burns et al.). The deconvolved gaussian FWHM (ϕ) along the east and west jets is shown in Figure 5.11.

Over much of the length of the jets, the ratio of the peak brightness to the 3 sigma noise is only ~10. This introduces some scatter into the FWHM measurements. Thus, although the general trends in ϕ are reliable, the detailed structure should be viewed with caution. Along the east jet between ~11-14 kpc from the core, where the signal-to-noise ratio is especially poor, the FWHM data were smoothed with a 3 point boxcar filter.

To first order, between ~3-10 kpc from the core, both jets expand at a constant collimation angle (defined to be arctan ($\Delta\phi/\Delta X$), where X is the distance from the core) of ~8°. The west jet is unresolved at 1."2 resolution (except at W1) until about 3 kpc from the core. The collimation shoulder at ~10-12 kpc from the core occurs at the position of the sharp kink in the jet at W4. Between ~12 and 14 kpc, the west jet expands with a collimation angle of ~60°. The FWHM data for the east jet are a bit noisier, and the spikes in the collimation structure

Figure 5.11

The deconvolved FWHM and estimated error of a gaussian fit to the transverse total intensity structure at 6 cm (1."2, B+D) along the east (top) and west (bottom) jets.

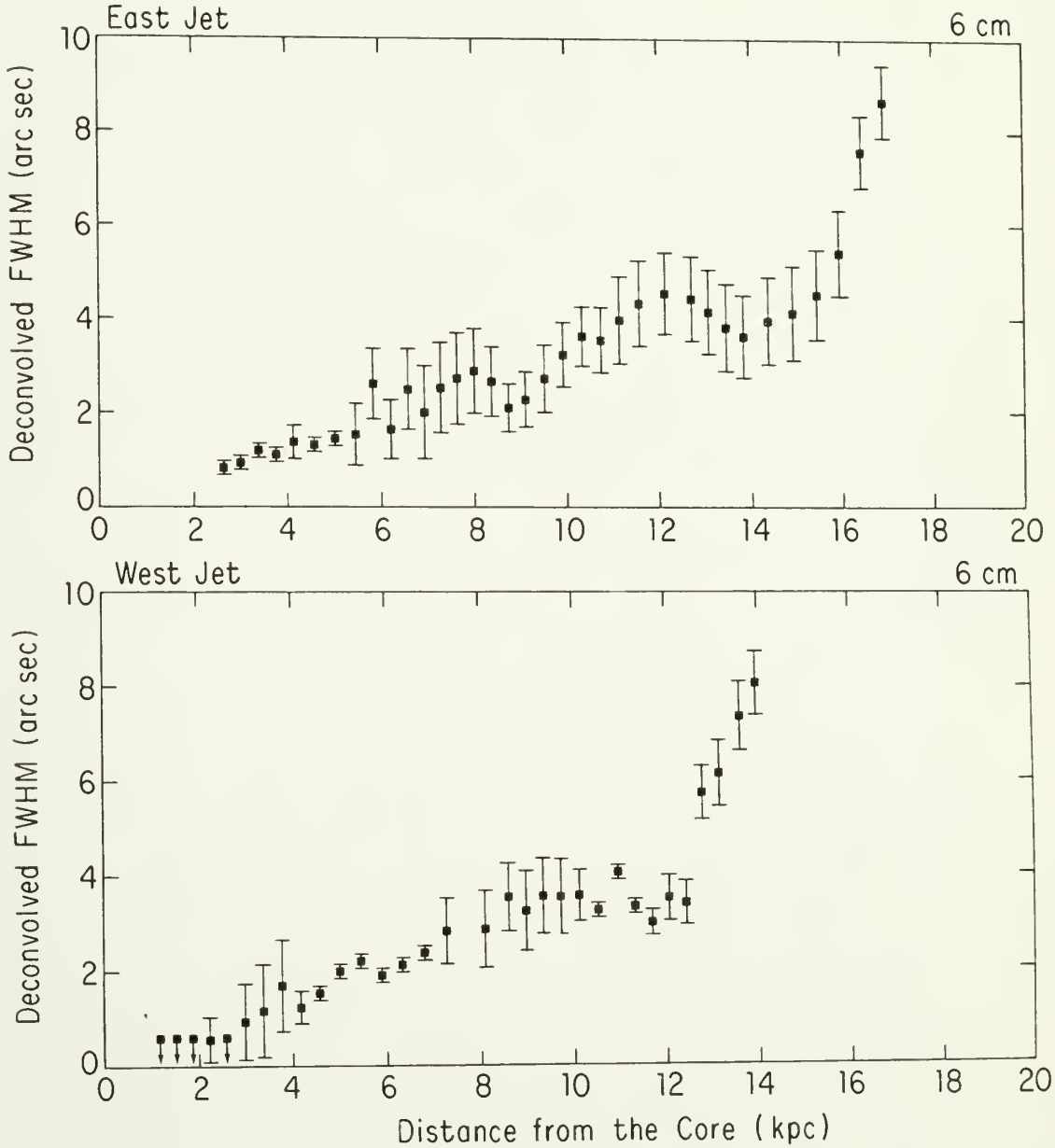
East Jet
6 cm
Deconvolved FWHM (arc sec)
West Jet
6 cm
Deconvolved FWHM (arc sec)
Distance from the Core (kpc)

are not significant. There may be collimation shoulders (where the jet temporarily narrows) at 8-9 kpc and at 12-14 kpc from the core. Beyond 14 kpc from the core, the east jet expands more rapidly with a collimation angle of ~60°.

Wiggles in the jets. There are asymmetric wiggles in the jets. The wiggle in the west jet appears to have a larger amplitude and shorter wavelength than the wiggle in the east jet. There is a suggestion that the wiggles, most notably in the west jet, continue into the tails even after the jets expand by about an order of magnitude.

The large scale structure. A contour plot and a B/W radiophotograph of the 21 cm, C array map are shown in Figures 5.12 and 5.13. The figures show the large scale structure seen by Miley (1973) (but with a resolution greater than twice his). The two jets can be distinguished and are seen to expand ~10 kpc behind the core and appear to merge or overlap at that point. However, beyond this point, the tails seem to narrow and diverge from one another, maintaining separate identities for an additional ~1' (~20 kpc). At a distance of 3-4' behind the core, the tails merge or overlap once again. At this point, the tail narrows and bends to the northwest (pointing directly away from the cluster center). The extensions to the northeast and southwest seen by Gisler and Miley (1979) at 610 MHz are not seen here. The present 21 cm observations (with a minimum baseline of ~80 m) are sensitive to structure on size scales of $\leq$ 4'. Thus at ~12" resolution, these features must have a surface brightness $<$ 7 mJy/beam (3 sigma) at 21 cm. If this structure is not resolved out by these observations, it must have a spectral index steeper than ~-1.2.

Figure 5.12

A contour plot of total intensity at 21 cm (12."9 x 11."4 @ -4°4, C) showing the large scale structure of the source. Contour levels are at -10, 10, 30, 50, 100, 200, and 300 mJy/beam. The CLEAN beam FWHM is shown as the shaded ellipse.

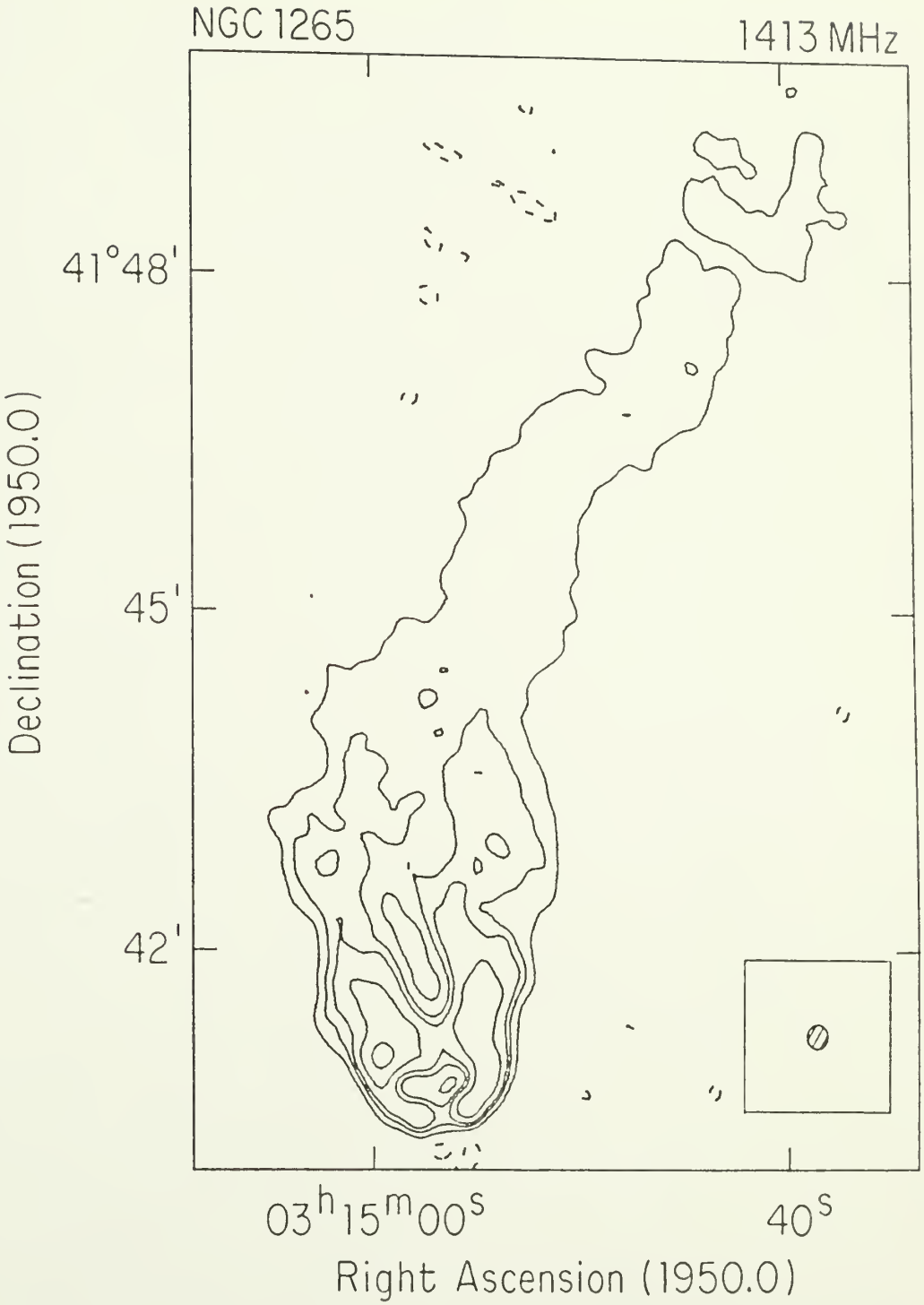
NGC 1265
1413 MHz
41°48'
45'
42'
Declination (1950.0)
03h15m00s
40s
Right Ascension (1950.0)

Figure 5.13

A B/W radiophotograph of total intensity at 21 cm (12."9 x 11."4 @ -4°.4, C), showing the large scale structure of the source.

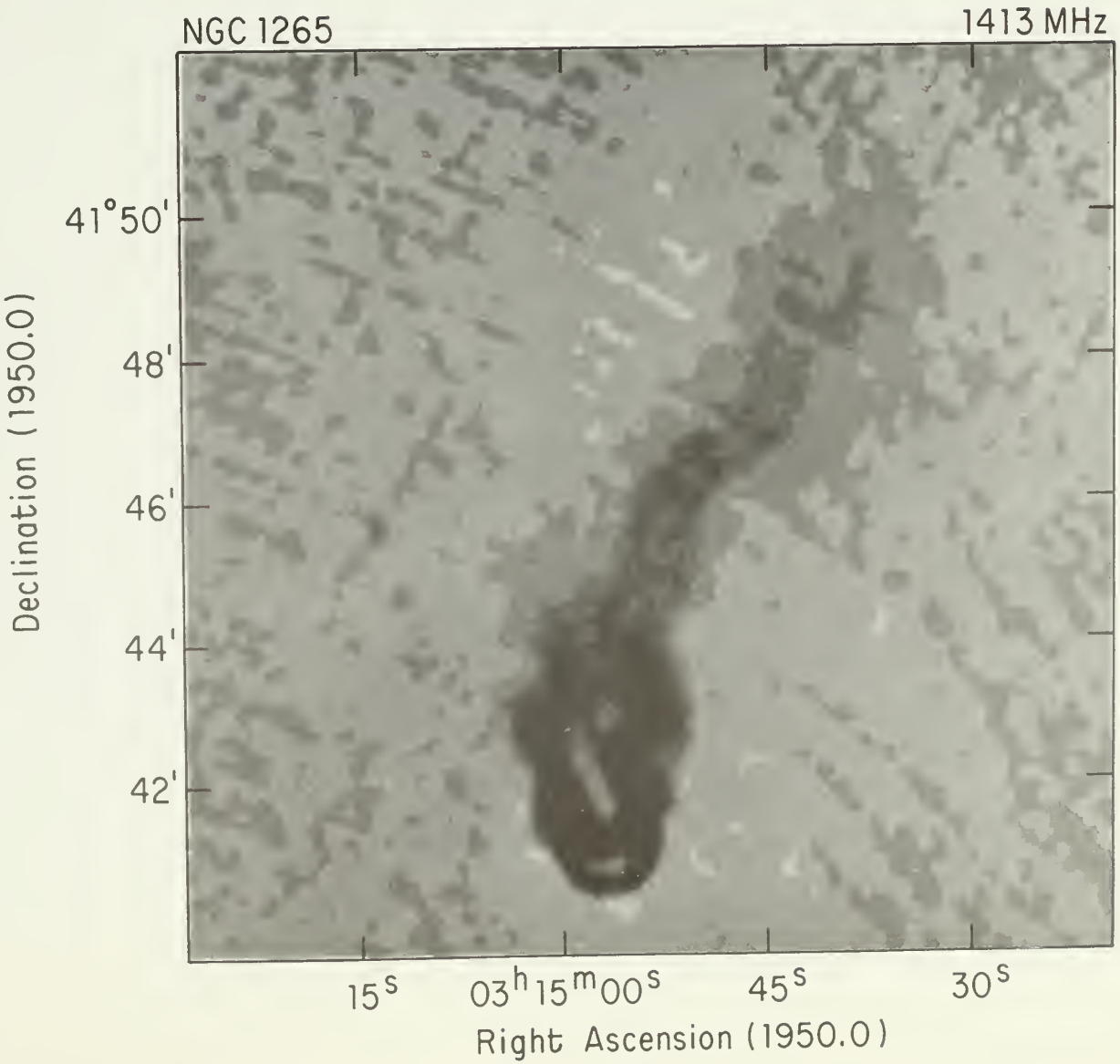
NGC 1265
1413 MHz
41°50'
48'
46'
44'
42'
Declination (1950.0)
15s
03h15m00s
45s
30s
Right Ascension (1950.0)

The spectral index structure

The spectral index distribution between 6 cm (B+D) and 21 cm (A+C) at 1."2 resolution along the maximum brightness ridge in the east and west jets is shown in Figure 5.14. (The spectral index, α, is defined such that $S_\nu \propto \nu^\alpha$.) The error in the spectral indices were calculated using both the root-mean-square errors and an additional error of 2% of the total intensity at each frequency. This additional error takes into account possible errors in the flux density scale and corresponds to a minimum error in spectral index of 0.03 at these frequencies. The weighted mean spectral index is -0.63 ± 0.01 and -0.65 ± 0.01 along the east and west jets, respectively. There is no systematic gradient in spectral index along the jets as a whole. There is a suggestion in the data that the knots have a flatter spectral index (~ -0.55) than the rest of the jets, and that there is a temporary steepening between W1 and W2. However, these features are at about the 2 sigma level of significance.

The spectral index between 6 cm (B) and 2 cm (C) along the east and west jets is shown in Figure 5.15. The 6 and 2 cm maps have been tapered to a resolution of 3.2 arcseconds in order to increase the signal-to-noise ratio. The weighted mean spectral index is -0.64 ± 0.03 and -0.68 ± 0.02 along the east and west jets, respectively.

Any comparison of the 6-2 cm spectral index maps with the 21-6 cm spectral index maps must be done with caution because of the differences in the (u,v) coverages in the two sets of maps. However, the data are consistent with a straight spectral index between 21 and 2 cm (except at W1). The steepening between W1 and W2 and the flattening of the

Figure 5.14

The one dimensional distribution of spectral index at 1."2 resolution between 21 cm (A+C) and 6 cm (B+D) along the ridge of maximum brightness for the east (top) and west (bottom) jets. Distance is given in kiloparsecs from the core.

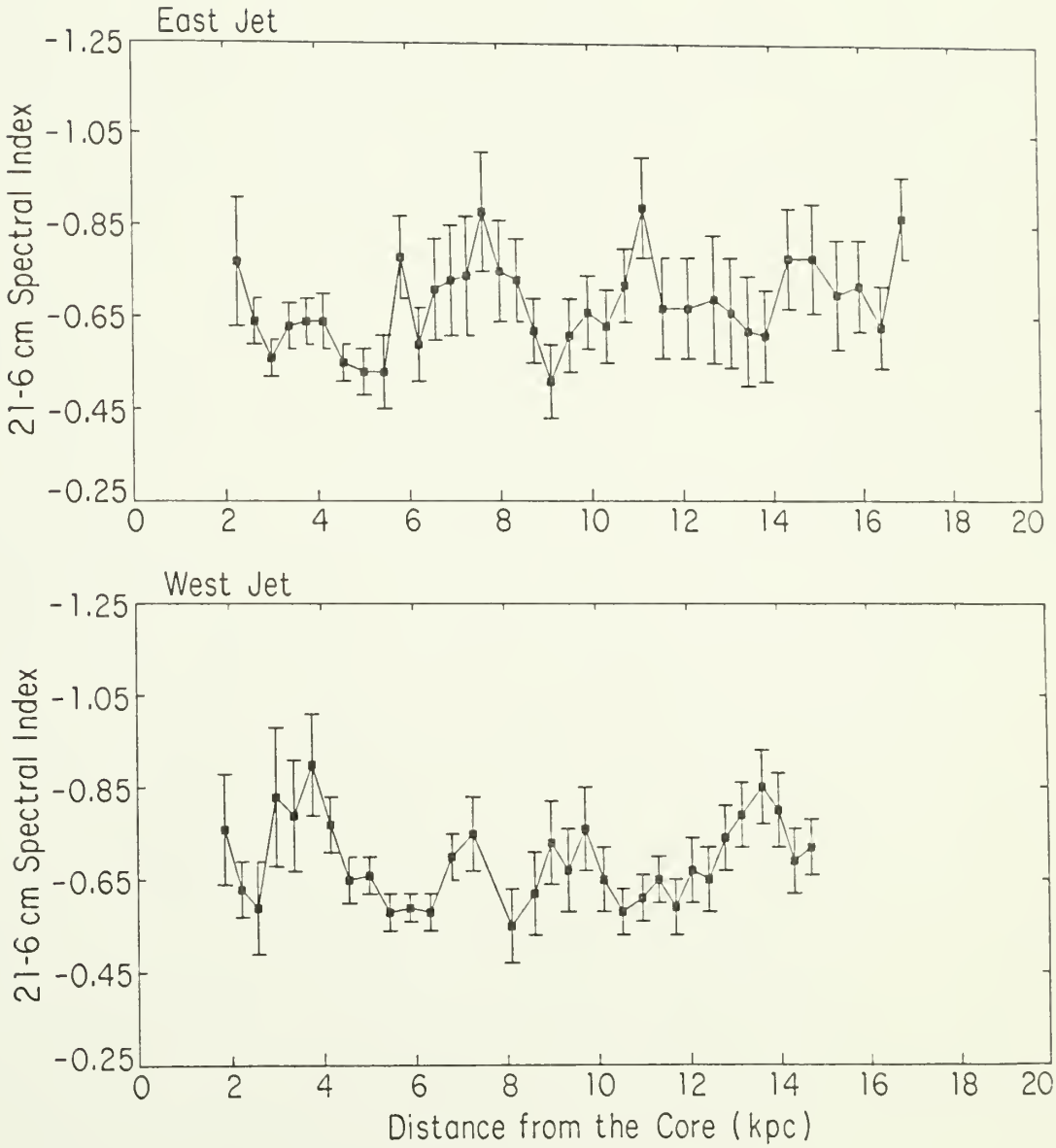
East Jet
-1.25
-1.05
-0.85
-0.65
-0.45
-0.25
21-6 cm Spectral Index
0
2
4
6
8
10
12
14
16
18
20
West Jet
-1.25
-1.05
-0.85
-0.65
-0.45
-0.25
21-6 cm Spectral Index
0
2
4
6
8
10
12
14
16
18
20
Distance from the Core (kpc)

Figure 5.15

The one dimensional distribution of spectral index at 3."2 resolution between 6 cm (B) and 2 cm (C) along the ridge of maximum brightness for the east (top) and west (bottom) jets. Distance is given in kiloparsecs from the core.

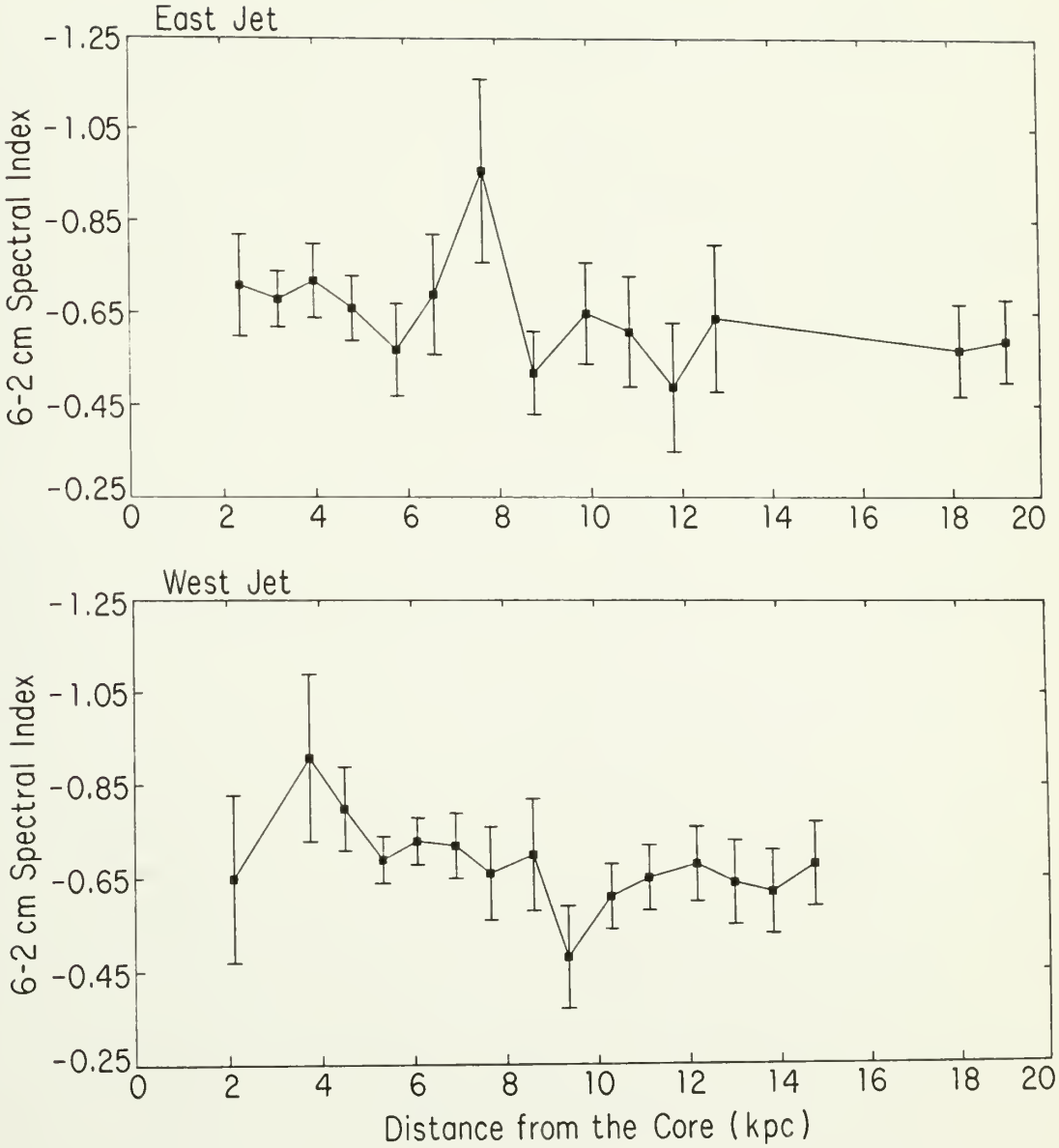
East Jet
6-2 cm Spectral Index
-1.25
-1.05
-0.85
-0.65
-0.45
-0.25
0
2
4
6
8
10
12
14
16
18
20
West Jet
6-2 cm Spectral Index
-1.25
-1.05
-0.85
-0.65
-0.45
-0.25
0
2
4
6
8
10
12
14
16
18
20
Distance from the Core (kpc)

spectral index at the knots noted above in the 21-6 cm data are also present in the 6-2 cm spectral index data, and this supports the reality of these features.

The spectrum of the compact core is presented in Figure 5.16. The spectral index between 20 and 6 cm and 6 and 2 cm is 0.59 ± 0.03 and 0.30 ± 0.03, respectively.

Knot W1. The knot W1 is unusual in that it has a flat spectral index between 6 and 2 cm (Fig. 5.16). A two-dimensional gaussian was fit (using the AIPS task IMFIT) to W1 in the 21 cm (A array, 1."2), 6 cm (B array, 1.2"; and A+B+D array, 0."45), and 2 cm (C array, 1."2) primary beam corrected maps. Parameters of the fits are given in Table 5.3. The wavelength of the map, λ, (in centimeters) is given in column

Table 5.3

Parameters of Knot W1

λ (cm)	Peak (mJy/beam)	Gaussian Size arcsec	arcsec	degrees
21	2.83	2.57 (0.29)	x 0.63 (0.12)	@ 105°4
6	1.42	<1.77	x <1.77	
6[a]	0.58	<1.30	x <1.30	
2	1.34	<0.67	x <0.67	

Notes to Table 5.3

a. at 0."45 resolution

1. The peak surface brightness (in milli-jansky/beam) from the gaussian fit is given in column 2. The deconvolved gaussian FWHM (in arcseconds)

Figure 5.16

The spectrum between 2 and 21 cm of the nuclear core (top) and knot W1 (bottom).

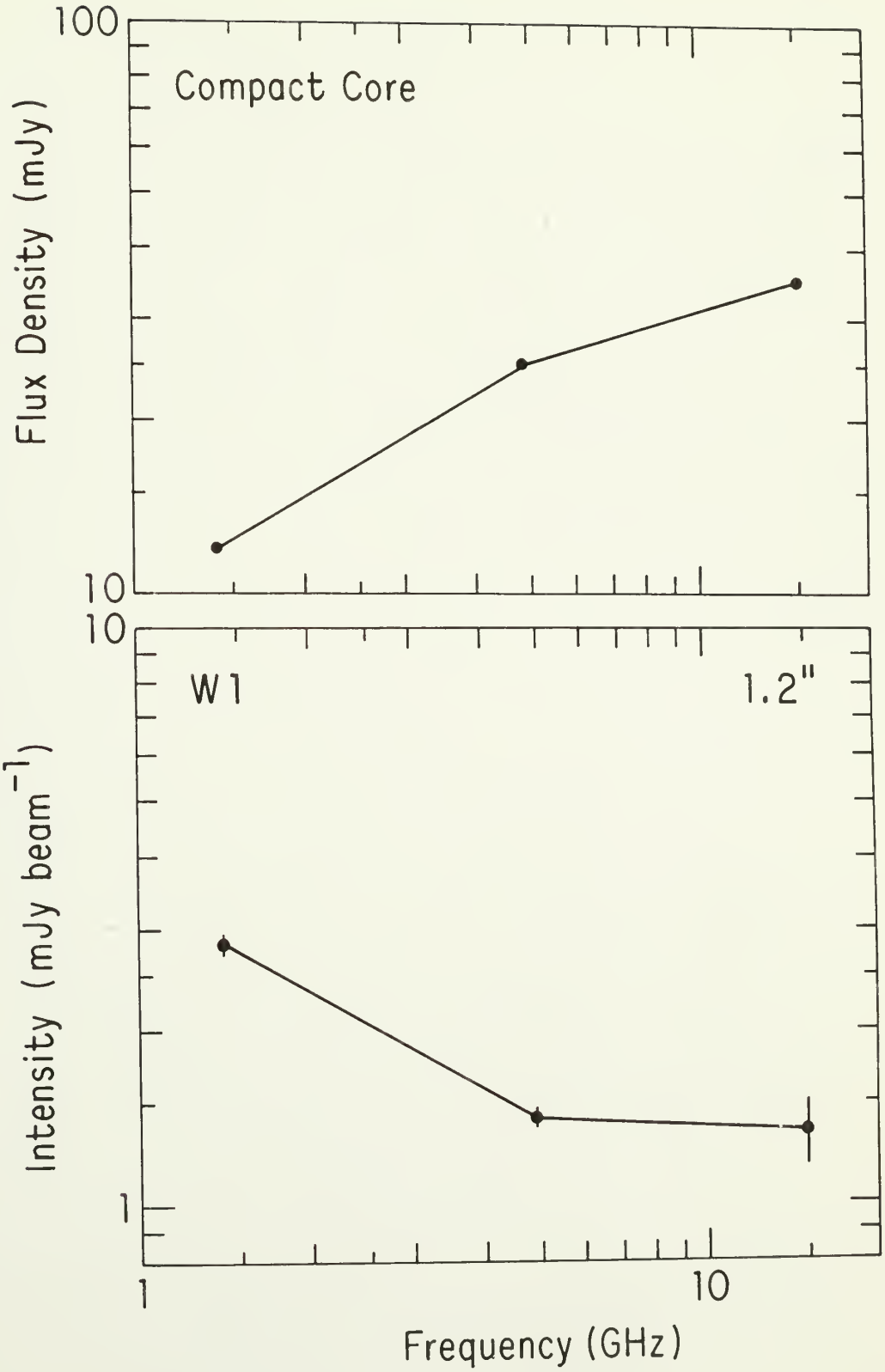
100
Compact Core
Flux Density (mJy)
10
10
W1
1.2"
Intensity (mJy beam^{-1})
1
1
10
Frequency (GHz)

and their errors and position angle (in degrees) are given in columns 3, 4 and 5. The upper limits are obtained by deconvolving the fit FWHM plus the one sigma error.

At 1."2 resolution, the spectral index and its error (calculated as described above) between 21-6 cm and 6-2 cm is -0.56 ± 0.07 and -0.05 ± 0.15, respectively. The contribution of the steep spectrum component to the flux density at 6 and 2 cm is unknown. Thus, observations at a higher frequency are needed to deconvolve the total flux density spectrum and determine the spectrum of the "flat" component. The relatively high flux density at 2 cm is not due to an error in CLEAN, since the knot has the same flux density in both the dirty and CLEANed maps at all three wavelengths. Various mechanisms which could produce the observed spectral index are discussed in Chapter VI.

The polarization structure

The positive bias in the polarized flux density, S_p, was removed using the relationship given by Wardle and Kronberg (1974),

$$S_p = S_{p,obs} \left[1 - SN^{-2}\right]^{1/2} , \qquad (5.2)$$

where $S_{p,obs}$ is the observed polarized flux density,

$$S_{p,obs} = \left[Q_{obs}^2 + U_{obs}^2\right]^{1/2} \qquad (5.3)$$

Q_{obs} and U_{obs} are the observed Stokes parameters, and SN is the signal-to-noise ratio. This correction was applied to the data using a

version of the AIPS program CORMS revised by the author. The polarization position angle, χ, was calculated in the usual way, i.e.,

$$\chi = 1/2 \arctan (U/Q). \qquad (5.4)$$

In all the maps and profiles shown in this section, the fractional polarization has been "blanked" (i.e., set to a null value) below a signal-to-noise ratio of 3. In order of decreasing resolution, the polarization structure is as follows:

The jets. At 0."45 resolution, polarized flux density with a signal-to-noise ratio $\geq$ 2 an be seen only at the positions of the brightest portions of the jets, i.e., the knots. A contour plot of total intensity at 6 cm (A+B+D, 0."45) with electric field position angles superposed (with length proportional to fractional polarization) is shown in Figure 5.17. Typical values of the fractional polarization and root-mean-square error are shown at selected locations. The position angles are perpendicular to the edge of the jet along the edge brightened region at W2-W3.

In order to increase the signal-to-noise ratio in the polarization at the W2-W3 knot group, maps were made in which the CLEAN components were restored with a very elliptical beam (0."45 x 2."0 at a position angle of -45°). This increased the sensitivity by averaging along the axis of the jet without losing transverse resolution. A total intensity map with polarization position angles superimposed, and with length proportional to fractional polarization, is shown in Figure 5.18. In this map the fractional polarization is seen to be edge brightened, varying from ~25-30% on the edges to $<$ 5% in the center. The electric

Figure 5.17

A contour plot of total intensity at 6 cm (0."45, A+B+D) and polarization position angle, χ, with length proportional to fractional polarization. The position angles are "blanked" where the signal-to-noise ratio in both polarized flux density and fractional polarization is less than 3. This corresponds to a maximum one sigma error in χ of 10°. Typical values of the fractional polarization and its one sigma error are shown in selected locations. The CLEAN beam FWHM is shown as the shaded circle. The scale of the polarization vectors is also shown. Contour levels are -0.2, 0.2, and 0.5 mJy/beam.

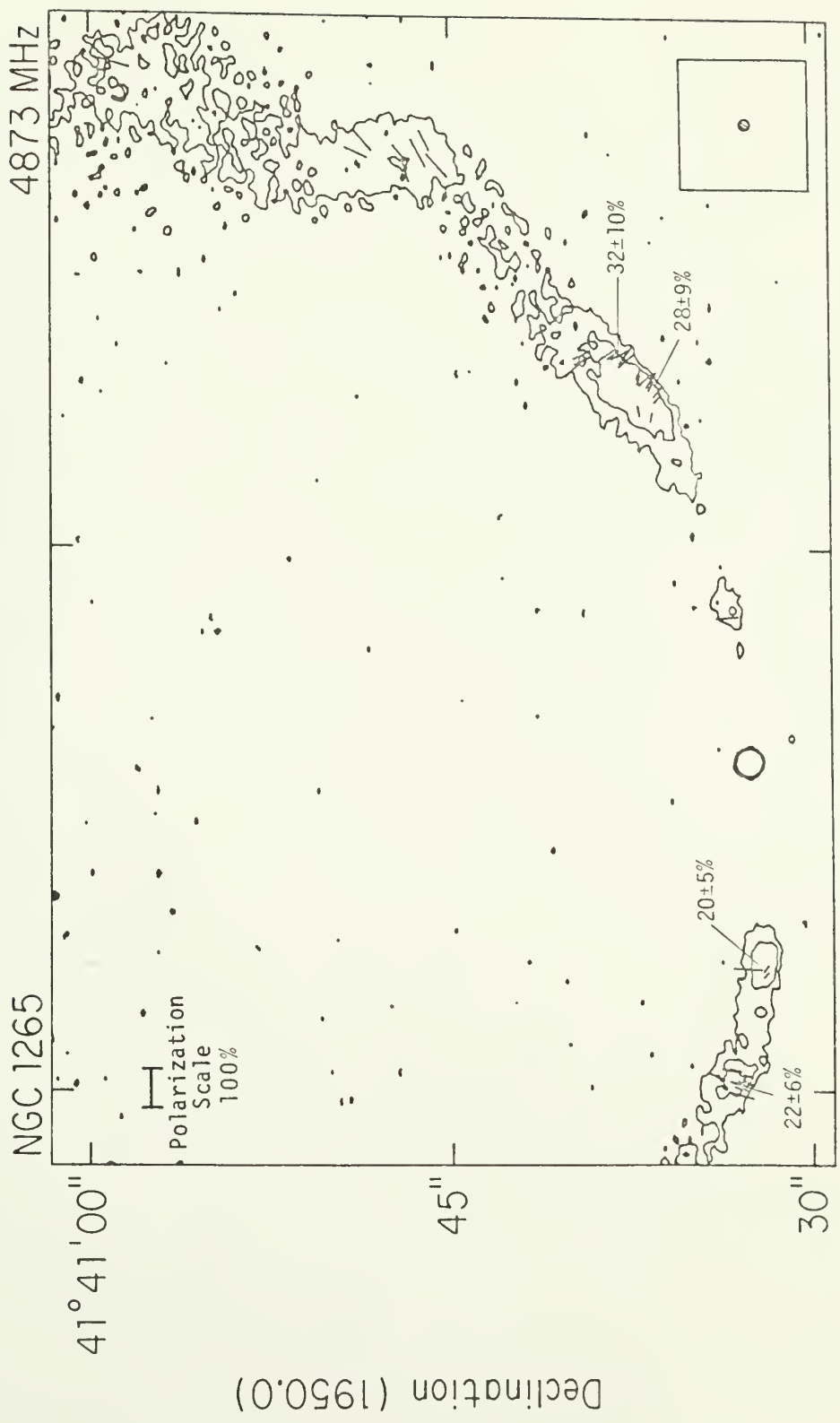
NGC 1265
4873 MHz
Polarization Scale 100%
32±10%
28±9%
20±5%
22±6%
41°41'00"
45"
30"
03h14m58s
56s
Declination (1950.0)
Right Ascension (1950.0)

Figure 5.18

A contour plot of total intensity at 6 cm (0."45 x 2."0 @ -45°, A+B+D) and polarization position angle, χ, with length proportional to fractional polarization. The position angles are "blanked" where the signal-to-noise ratio in both polarized flux density and fractional polarization is less than 3. The CLEAN beam FWHM is shown as the shaded ellipse. The scale of the polarization vectors is also shown. Contour levels are -0.2, 0.2, 0.5, 1.0, 2.0, and 3.0 mJy/beam.

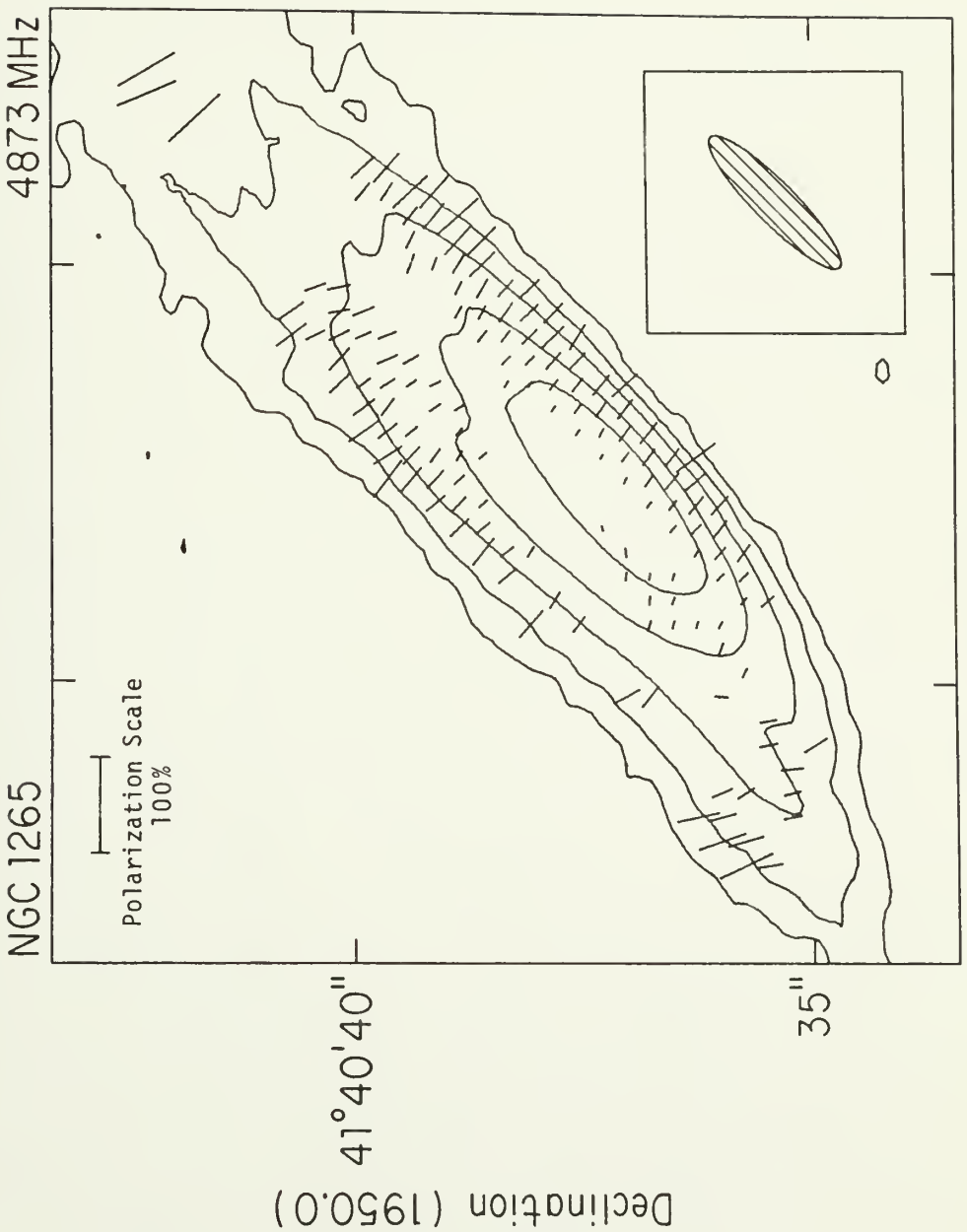
NGC 1265
4873 MHz
Polarization Scale
100%
41°40'40"
35"
Declination (1950.0)
03h14m55.6s
55.2s
Right Ascension (1950.0)

field is perpendicular to the jet axis on both sides of the jet. There is a hint that the position angle rotates by ~45° in the center of the jet.

B/W radiophotographs at 1."2 resolution of the fractional polarization are shown in Figure 5.19 at 21 cm (A+C) and in Figure 5.20 at 6 cm (B+D), respectively.

The polarization structure is complex and two dimensional. At both wavelengths, both the polarized flux density and fractional polarization are fairly symmetrically edge brightened over much of the inner two-thirds (~10-12 kpc) of the jets. The polarization structure of the last one-third of the jets is less clear, partially due to a lower signal-to-noise ratio. However, the fractional polarization is not symmetrically edge brightened in this region as it is closer to the core. In the last third of the jets, portions of the east jet are edge darkened in fractional polarization, while the west jet is edge brightened on the east side.

The knots tend to have lower fractional polarization than the rest of the jets.

The contrast in the W2-W3 knot group is especially sharp, with a change in fractional polarization at 21 cm from ~4% in the center to ~25% at the edges. The fractional polarization at 6 cm at 1."2 resolution is comparable to that seen at 0."45 resolution. One dimensional profiles of the fractional polarization or 3 sigma upper limits (filled squares) along the ridge of maximum brightness in the east and west jets are shown in Figure 5.21 at 21 cm and Figure 5.22 at 6 cm. These profiles show that except at a few points the fractional

Figure 5.19

A B/W radiophotograph of fractional polarization at 21 cm (1."2, A+C). Only values with a signal-to-noise ratio greater than 3 are shown.

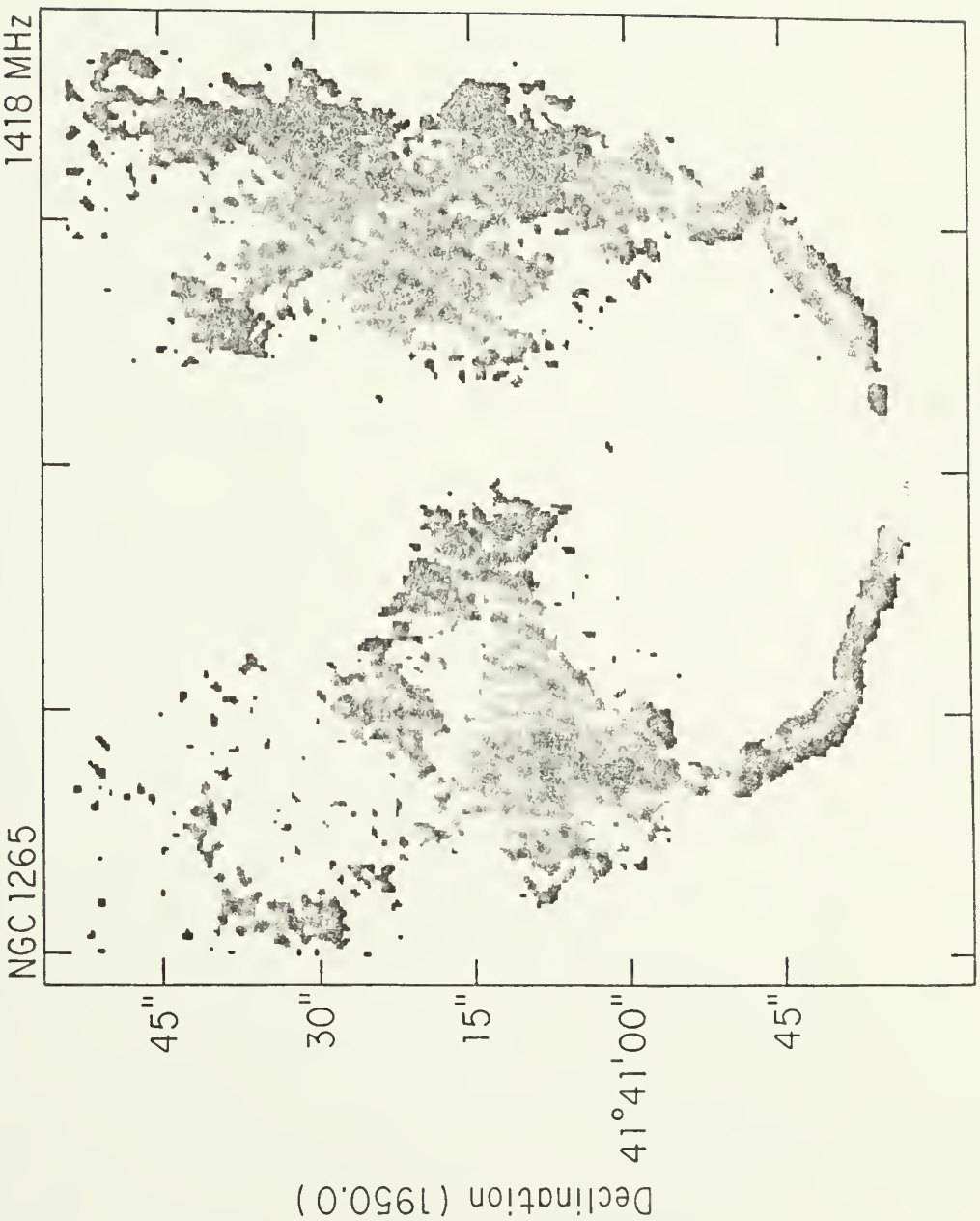
NGC 1265
1418 MHz
45"
30"
15"
41°41'00"
45"
03h15m01s
59s
57s
55s
Declination (1950.0)
Right Ascension (1950.0)

Figure 5.20

A B/W radiophotograph of fractional polarization at 6 cm (1."2, B+D). Only values with a signal-to-noise ratio greater than 3 are shown.

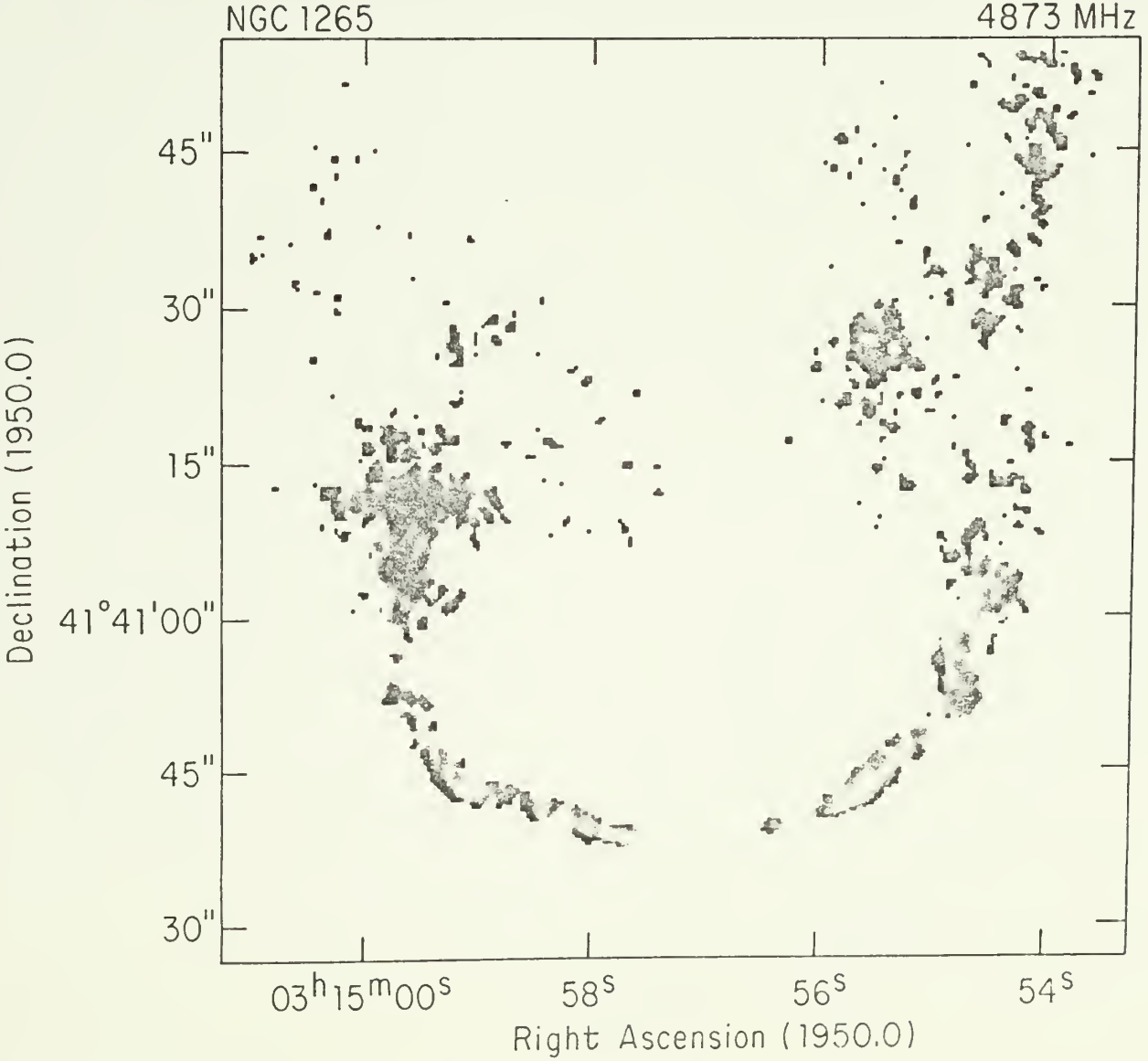
NGC 1265
4873 MHz
45"
30"
15"
41°41'00"
45"
30"
Declination (1950.0)
03h15m00s
58s
56s
54s
Right Ascension (1950.0)

Figure 5.21

The one dimensional distribution of fractional polarization at 21 cm (1."2, A+C) for the east (top) and west (bottom) jets. Three sigma upper limits are also shown.

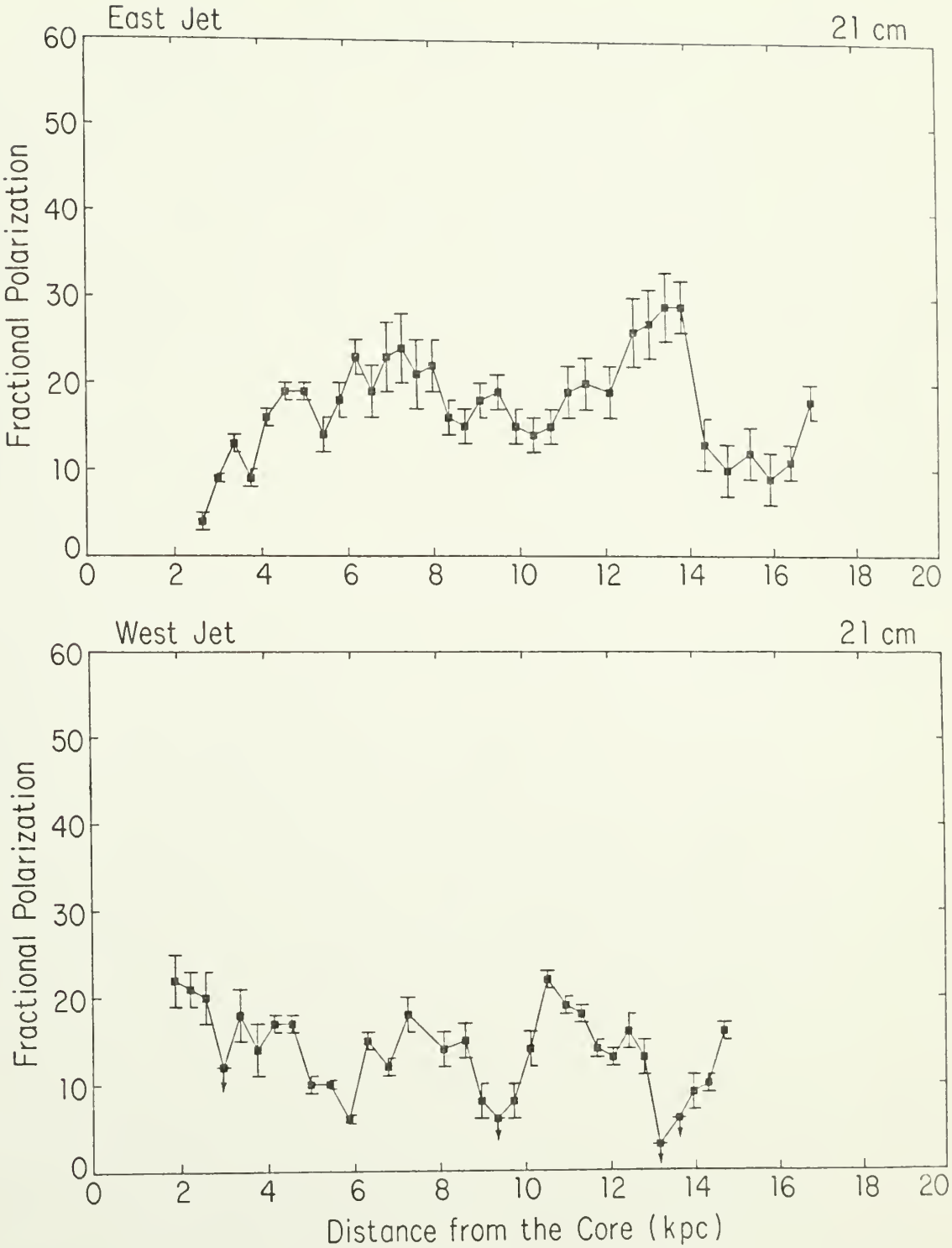
East Jet
21 cm
Fractional Polarization
0
10
20
30
40
50
60
0
2
4
6
8
10
12
14
16
18
20
West Jet
21 cm
Fractional Polarization
Distance from the Core (kpc)

Figure 5.22

The one dimensional distribution of fractional polarization at 6 cm (1."2, B+D) for the east (top) and west (bottom) jets. 3 sigma upper limits are also shown as filled squares.

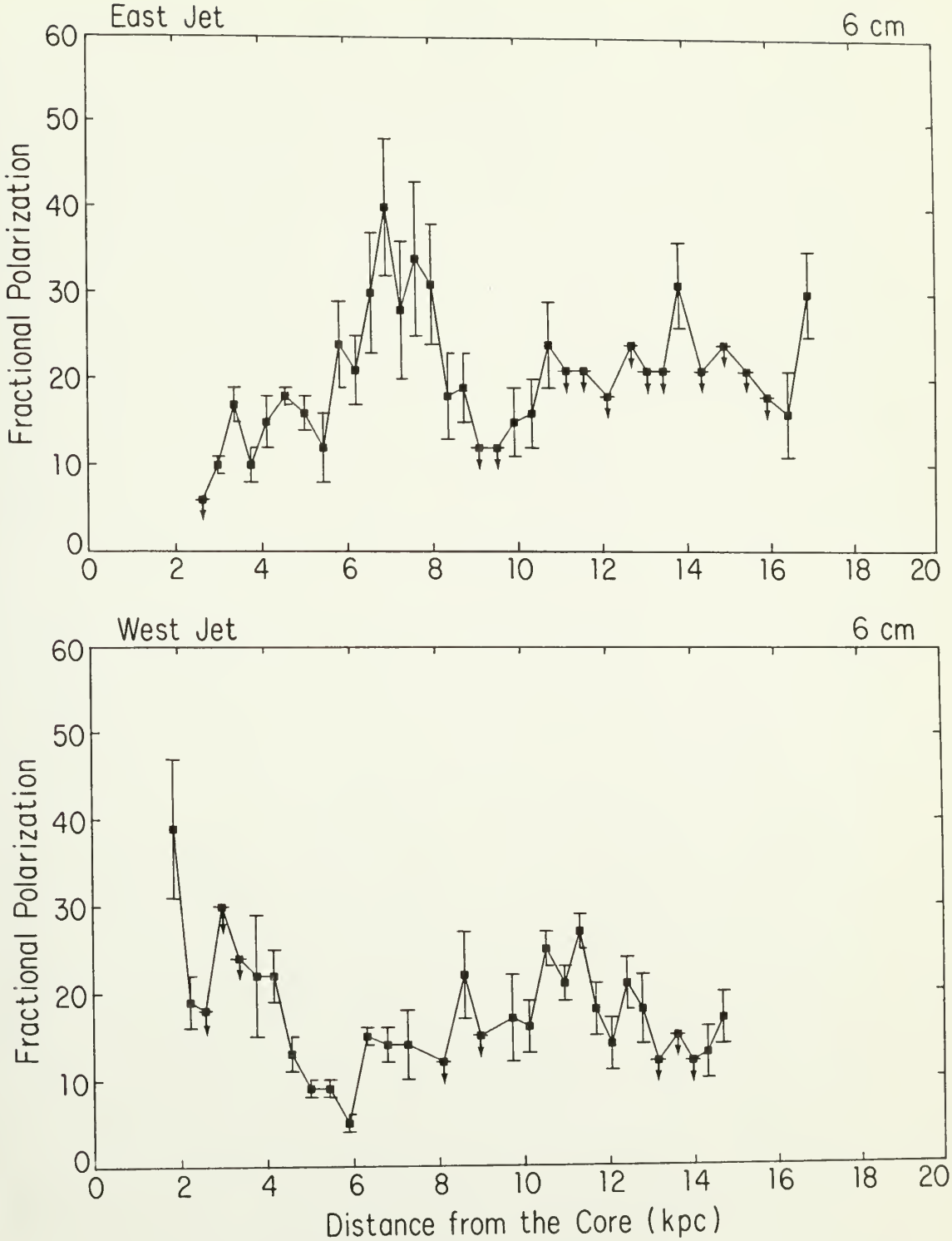
East Jet
6 cm
Fractional Polarization
0
10
20
30
40
50
60
0
2
4
6
8
10
12
14
16
18
20
West Jet
6 cm
Fractional Polarization
Distance from the Core (kpc)

polarizations at 6 and 20 cm are identical within the root-mean-square errors. The fractional polarization is mostly in the range ~10-25%, though there are significant excursions above (to ~35%) and below (to ~4%) this range. Along the west jet (at 21 cm where the SN is higher) the fractional polarization drops from ~16% to ~5% at three places: at W2-W3, and just before and after the kink in the jet (at W4). Along the east jet, the fractional polarization rises from ~4% at E1 to ~20% at E2, climbs to ~26% just before the regime of rapid expansion, and drops to ~11% during the regime of rapid expansion beyond 14 kpc from the core.

The electric field vectors (i.e., polarization position angles) with length proportional to fractional polarization are shown superimposed on total intensity maps at 21 cm (A+C) and 6 cm (B+D) at 1."2 resolution in Figures 5.23 and 5.24. (The position angles are "blanked" where the signal-to-noise ratio in both the fractional polarization and polarized flux density is less than 3.) It will be argued in Chapter VI that because of the lack of depolarization and the small values of rotation measure observed between 6 and 21 cm, the position angles at 6 cm are close to the intrinsic values. The position angles at 6 cm seen at 1."2 resolution agree with those seen at 0."45. The electric field is mostly transverse (i.e., perpendicular) to the jet axis along the inner two-thirds (~10-12 kpc) of both jets. The region of mostly perpendicular field is followed in the last one-third of the jets with regions of more complex position angle structure. In the east jet, the position angles are mostly parallel to the jet axis. In the west jet, the position angles are mostly parallel in the jet center and

Figure 5.23

A contour plot of total intensity at 21 cm (1."2, A+C) and polarization position angle, χ, with length proportional to fractional polarization. The position angles are "blanked" where the signal-to-noise ratio in both polarized flux density and fractional polarization is less than 3. The CLEAN beam FWHM is shown as the shaded circle. The scale of the polarization vectors is also shown. Contour levels are -0.3, 0.3, 1.0, 3.0, and 8.0 mJy/beam.

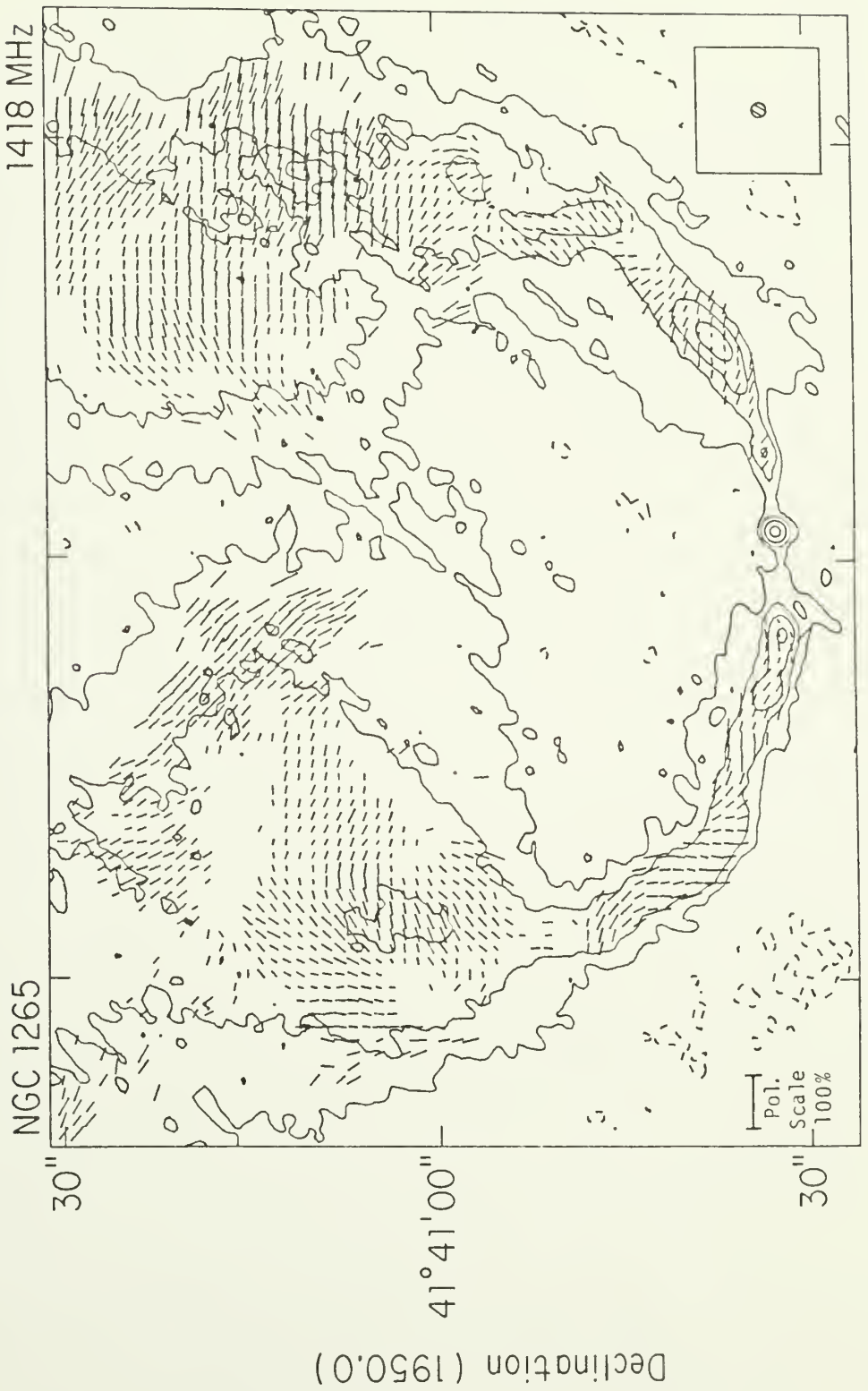
1418 MHz
NGC 1265
30"
41°41'00"
30"
03h15m00s
57s
54s
Pol. Scale 100%
Declination (1950.0)
Right Ascension (1950.0)

Figure 5.24

A contour plot of total intensity at 6 cm (1."2, B+D) and polarization position angle, χ, with length proportional fractional polarization. The position angles are "blanked" where the signal-to-noise ratio in both polarized flux density and fractional polarization is less than 3. The CLEAN beam FWHM is shown as the shaded circle. The scale of the polarization vectors is also shown. Contour levels are -0.2, 0.2, 0.8, and 3.0 mJy/beam.

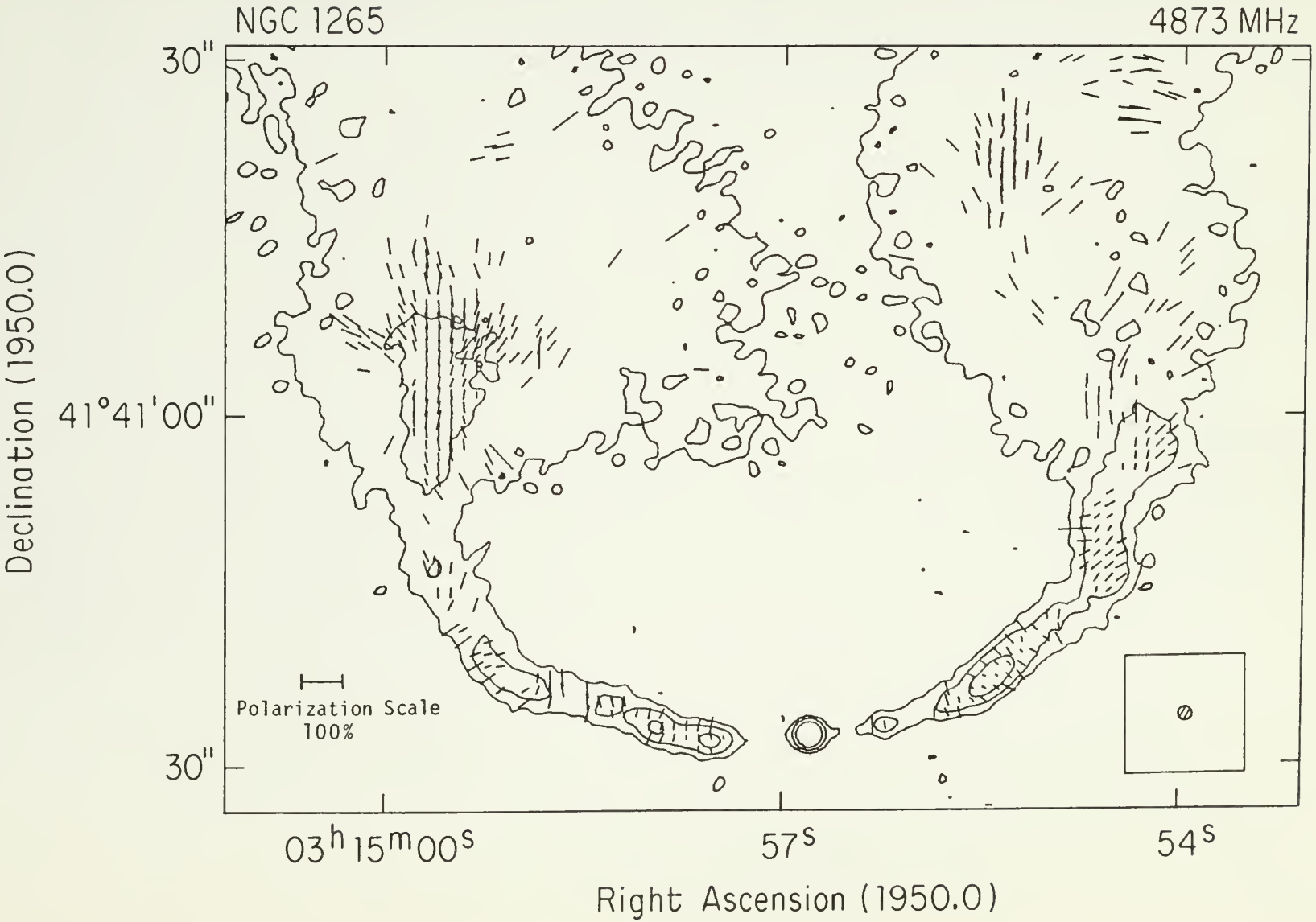
NGC 1265
4873 MHz
30"
41°41'00"
30"
Declination (1950.0)
Polarization Scale
100%
03h15m00s
57s
54s
Right Ascension (1950.0)

perpendicular on the edges. The transition between perpendicular and parallel field occurs near the point where both jets begin to bend more rapidly, though this may only be a coincidence.

A contour plot of total intensity with position angles superimposed of the W2-W3 knot group at 6 cm (1."2, B+D) is shown in Figure 5.25. The edge brightening in fractional polarization is also seen in this figure, though there is only a suggestion of a position angle rotation associated with the frequency independent decrease in polarization of the knot center.

The two wavelength rotation measure, RM, is defined to be

$$RM = (\chi_1 - \chi_2)/[57.3\ (\lambda_1^2 - \lambda_2^2)]\ \text{rad m}^{-2} \qquad (5.5)$$

where χ is the position angle (in degrees) at a wavelength of λ (in m). The RM between 6 cm (B+D) and 21 cm (A+C) along the east and west jets is presented in Figure 5.26. The error shown was calculated using both the statistical errors in Q and U, and an assumed 5° error at 21 cm due to the uncertainty in the ionospheric Faraday rotation corrections. Only position angles with statistical errors less than 10° (i.e., a signal-to-noise ratio 3 in polarized flux density) at both frequencies were used in the calculation of the rotation measure. Note that a difference of π radians between 1418 and 4873 MHz corresponds to an RM of 76.2 rad m^{-2}. This value was added to some negative values of RM in order to minimize the size of the jumps in RM.

There is no evidence (at 1."2 resolution) for any significant RM structure across the jets. Along the west jet the RM varies smoothly

Figure 5.25

A contour plot of total intensity at 6 cm (1."2, B+D) and polarization position angle, χ, with length proportional to fractional polarization of the knot group W2-W3. The position angles are "blanked" where the signal-to-noise ratio in both polarized flux density and fractional polarization is less than 3. The CLEAN beam FWHM is shown as the shaded circle. The scale of the polarization vectors is also shown. Contour levels are -0.2, 0.2, 0.8, and 3.0 mJy/beam.

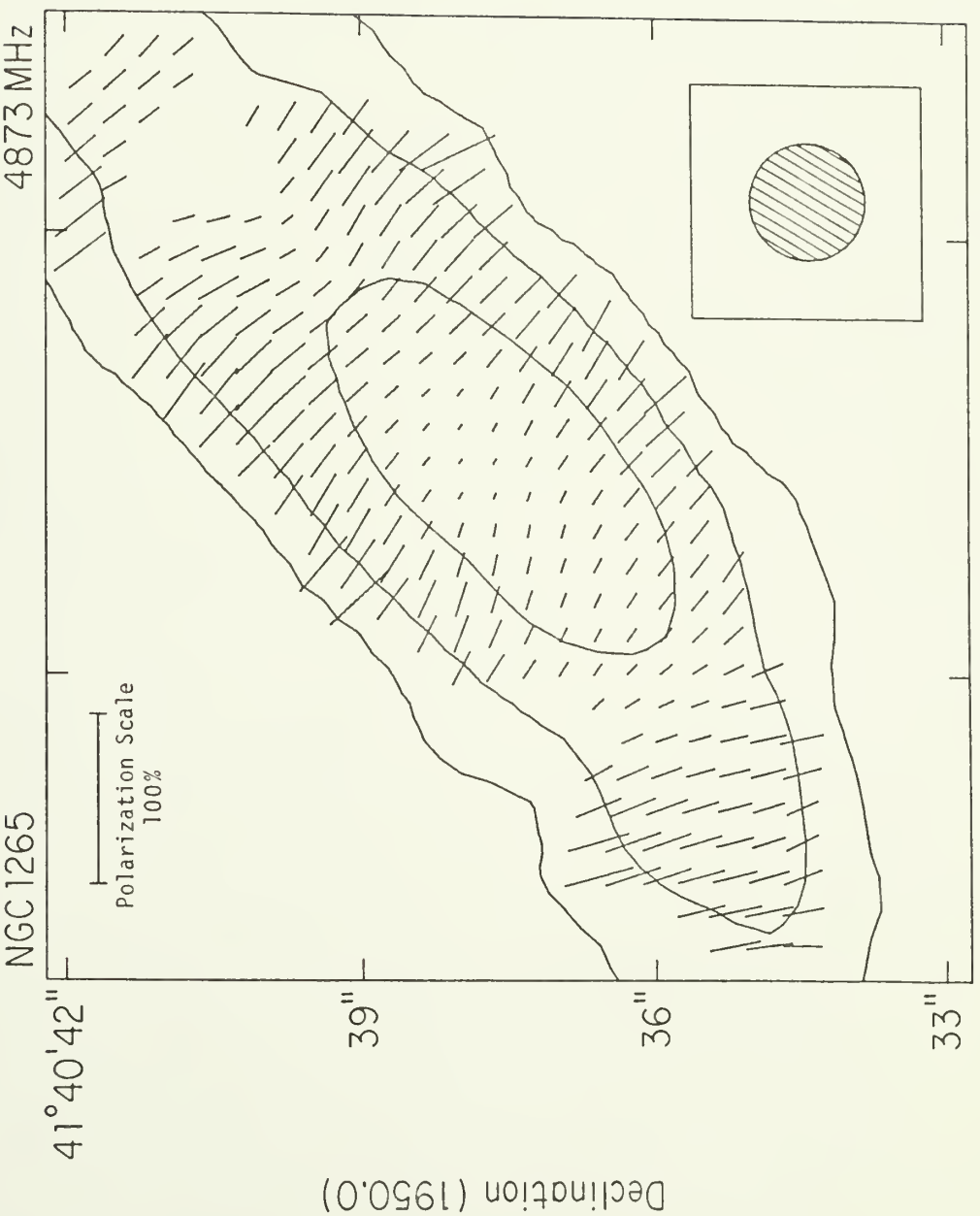
NGC 1265
4873 MHz
Polarization Scale
100%
41°40'42"
39"
36"
33"
Declination (1950.0)
03h14m55.6s
55.2s
Right Ascension (1950.0)

Figure 5.26

The one dimensional distribution at 1."2 resolution of rotation measure between 21 (A+C) and 6 (B+D) cm along the ridge of maximum brightness of the east (top) and west (bottom) jets. Distance is given in kiloparsecs from the nuclear core.

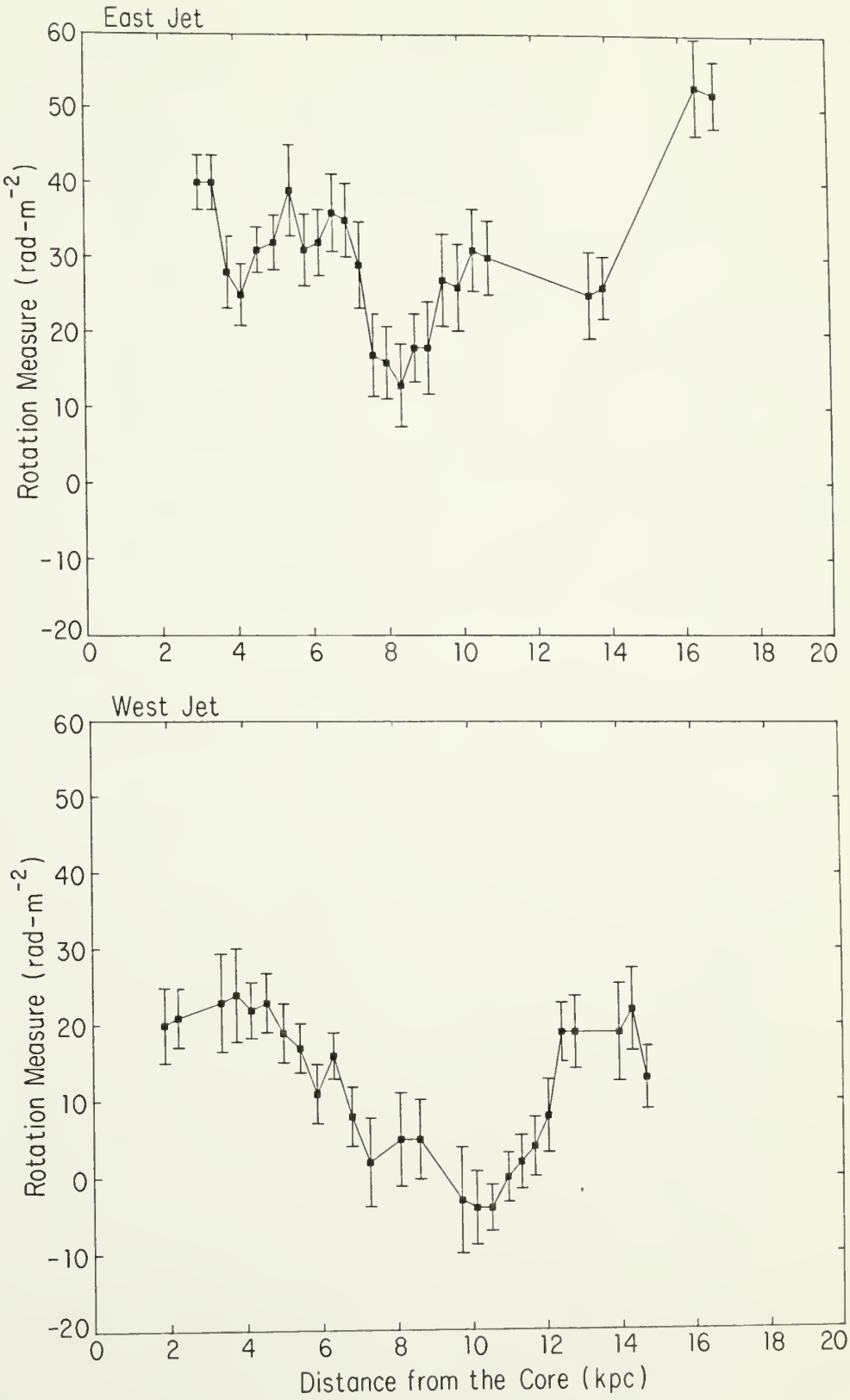
East Jet
West Jet
Rotation Measure (rad-m^{-2})
Distance from the Core (kpc)
60
50
40
30
20
10
0
-10
-20
0
2
4
6
8
10
12
14
16
18
20

from ~23 rad m^{-2} at ~2 kpc from the nucleus to ~-4 rad m^{-2} at 10 kpc from the nucleus to ~20 rad m^{-2} at 12-15 kpc. In contrast, along the east jet, the RM is ~25-35 rad m^{-2} from ~3 kpc to ~7-8 kpc from the core where it drops to ~13 rad m^{-2} and then increases to ~30 rad m^{-2} by 10 kpc from the core. The changes in RM are not associated with any particular variations in the fractional polarization along the jets. Ignoring the spikes, both of the drops in the RM and the largest gradients in RM occur at the positions of the shoulders in the collimation structure. Perley, Bridle, and Willis (1984) have also observed variations in RM associated with the collimation structure of NGC 6251. However, in NGC 1265, the changes in RM occur over a larger size scale than the changes in collimation. Also, since there are only two examples of a positional coincidence between RM and collimation in NGC 1265, it is possible that in this source the association is produced by chance.

Because of the weak flux density and higher noise level at 2 cm, there is no significant polarized flux density with a signal-to-noise ratio $\geq$ 2 at 2 cm at 1."2 resolution.

However, a map at 3."2 resolution produced by applying a 40 kλ taper to the (u,v) data at 2 cm does show significant polarized flux density at the positions of the knots. One dimensional profiles of the fractional polarization at 3."2 resolution are shown for the east and west jets in Figure 5.27 at 6 cm (B) and Figure 5.28 at 2 cm (C). The position angles of the electric vectors are shown superimposed on total intensity maps in Figures 5.29 and 5.30 at 6 and 2 cm, respectively. The fractional polarization and position angles at 6 cm at 1."2 and 3."2

Figure 5.27

The one dimensional distribution of fractional polarization at 6 cm (3."2, B) for the east (top) and west (bottom) jets. Three sigma upper limits are also shown. Distance is given in kiloparsecs from the nuclear core.

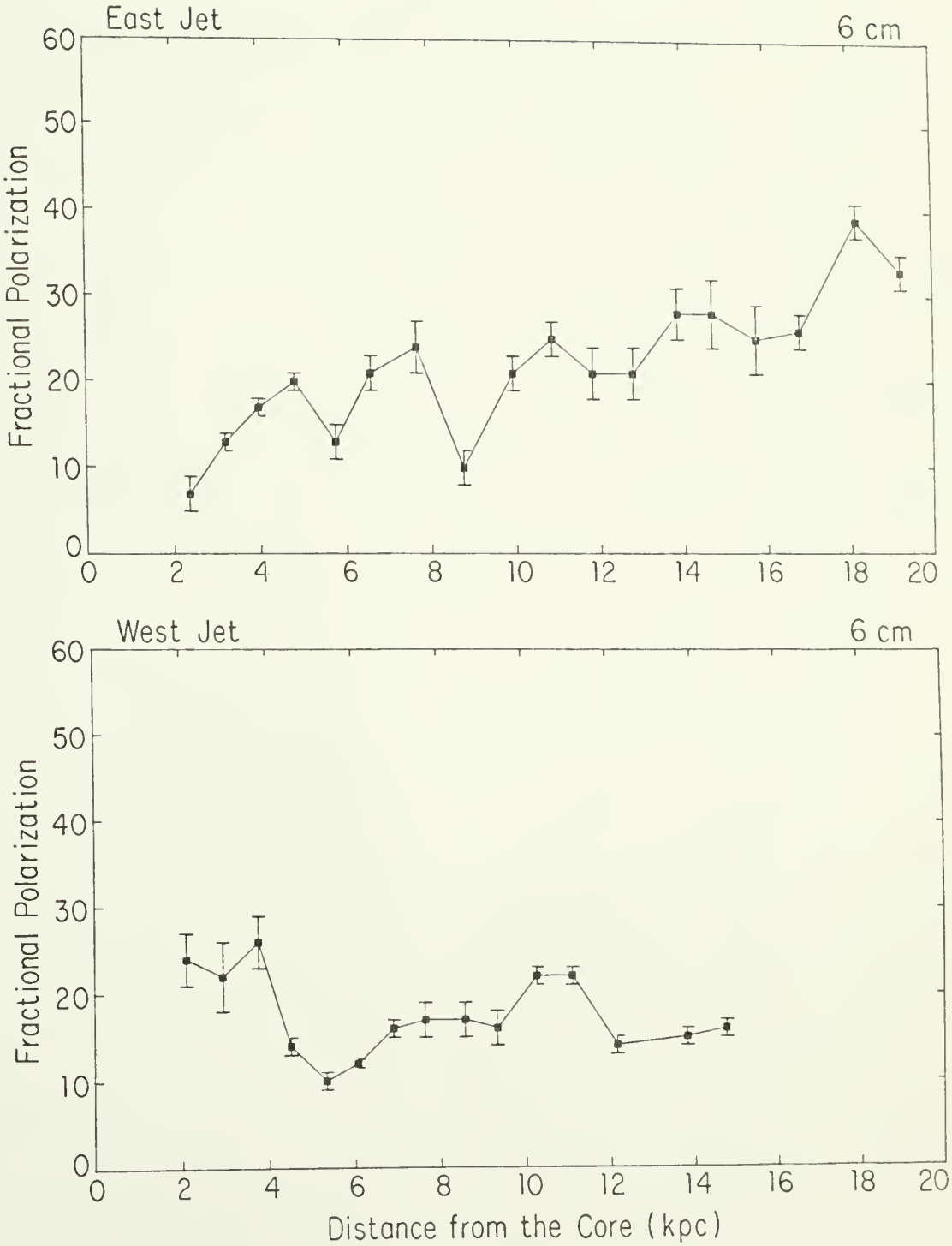
East Jet
6 cm
Fractional Polarization
0
10
20
30
40
50
60
0
2
4
6
8
10
12
14
16
18
20
West Jet
6 cm
Fractional Polarization
Distance from the Core (kpc)

Figure 5.28

The one dimensional distribution of fractional polarization at 2 cm (3."2, C) for the east (top) and west (bottom) jets. Three sigma upper limits are also shown. Distance is given in kiloparsecs from the nuclear core.

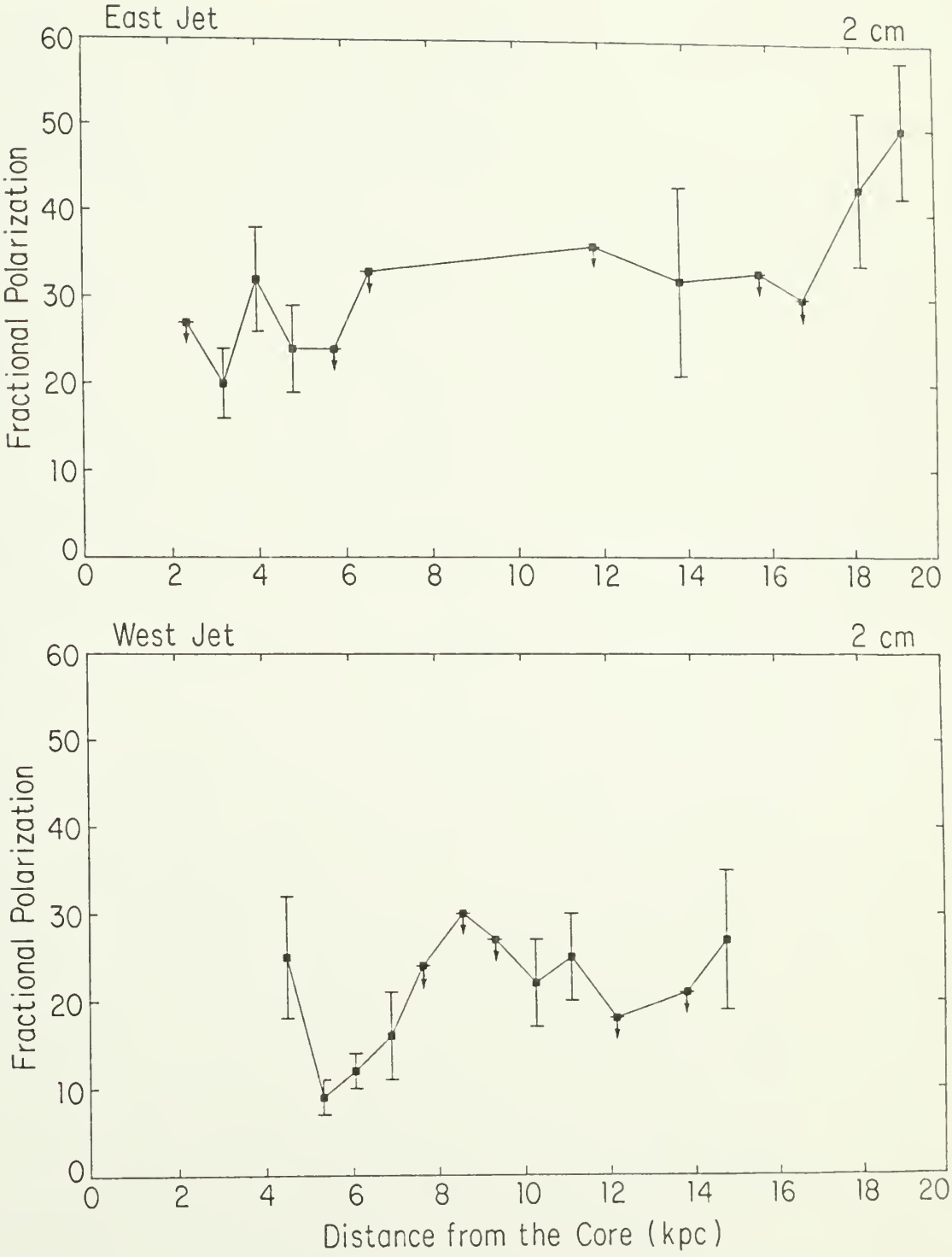
East Jet
2 cm
Fractional Polarization
0
10
20
30
40
50
60
0
2
4
6
8
10
12
14
16
18
20
West Jet
2 cm
Fractional Polarization
Distance from the Core (kpc)

Figure 5.29

A contour plot of total intensity at 6 cm (3."2, B) and polarization position angle, χ, with length proportional to fractional polarization. The position angles are "blanked" where the signal-to-noise ratio in both polarized flux density and fractional polarization is less than 3. The CLEAN beam FWHM is shown as the shaded circle. The scale of the polarization vectors is also shown. Contour levels are -0.5, 0.5, 3.0, and 8.0 mJy/beam.

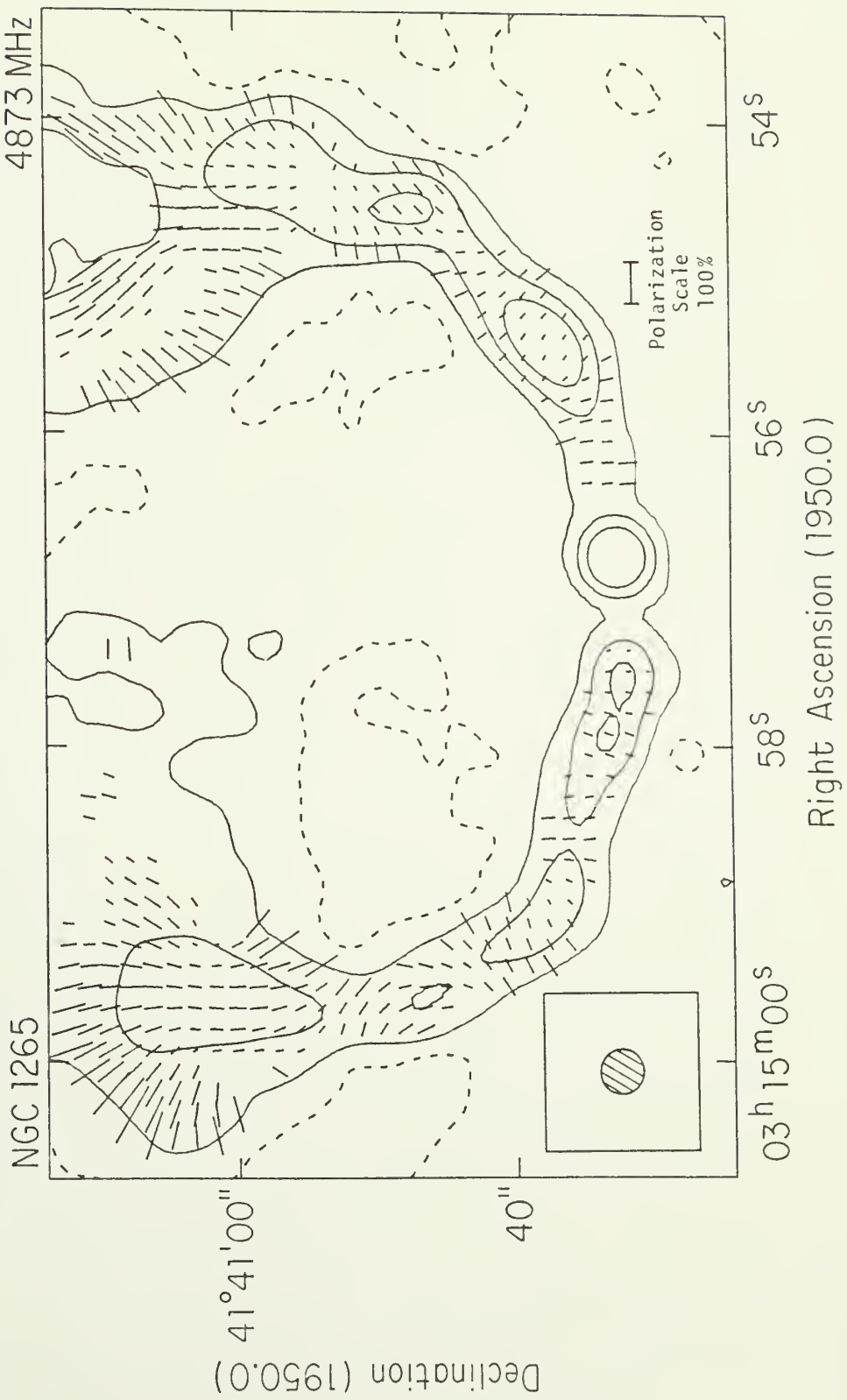
4873 MHz
NGC 1265
Polarization
Scale
100%
41°41'00"
40"
03h15m00s
58s
56s
54s
Declination (1950.0)
Right Ascension (1950.0)

Figure 5.30

A contour plot of total intensity at 2 cm (3."2, C) and polarization position angle, χ, with length proportional to fractional polarization. The position angles are "blanked" where the signal-to-noise ratio in both polarized flux density and fractional polarization is less than 3. The CLEAN beam FWHM is shown as the shaded circle. The scale of the polarization vectors is also shown. Contour levels are -0.6, 0.6, 1.5, 3.0, and 15.0 mJy/beam.

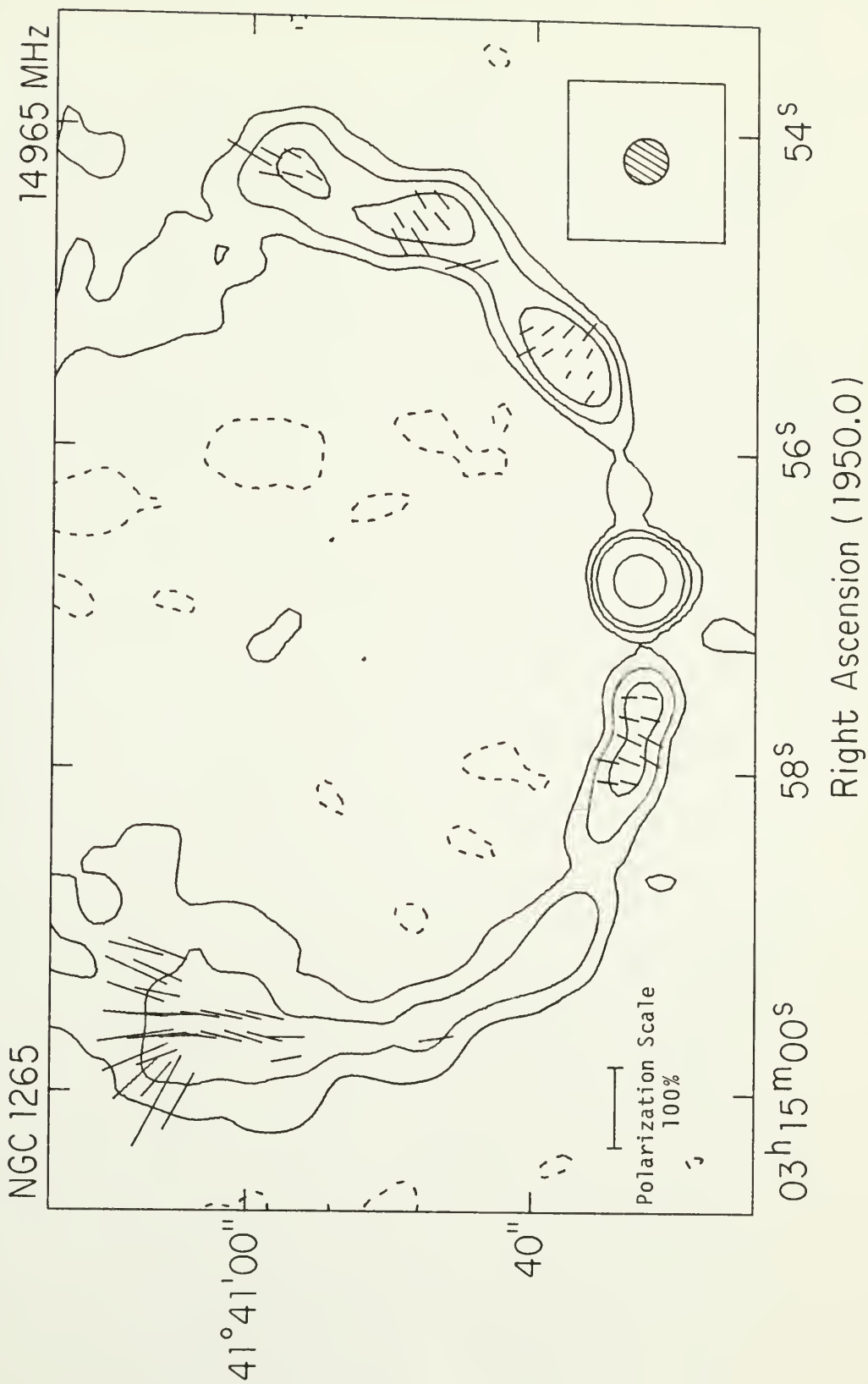
NGC 1265
14965 MHz
41°41'00"
40"
03h15m00s
58s
56s
54s
Right Ascension (1950.0)
Polarization Scale
100%

resolution are in good agreement and are consistent with the data at 2 cm at 3."2 resolution.

At 3."2 resolution there is polarization information for the bright portions of the jets at 3 wavelengths. This allows a more accurate calculation of the RM than in the 2 wavelength case, since the $n\pi$ ambiguity is reduced. Also, the wavelength dependence of the position angle, χ, can be determined. This is especially important in determining the location of the RM structure, which is discussed in Chapter VI. The position angles were obtained from tapered maps at 3."2 resolution at 21 cm (A+C), 6 cm (B), and 2 cm (C) at six locations with a signal-to-noise ratio in polarized flux density > 3 at 2 cm. (At 3."2 resolution the 6 cm maps made using the B+D and B data sets give the same position angles.) A least-squares fit was obtained to the equation

$$\chi = \mathrm{RM}\ \lambda^2 + \chi_o \quad \mathrm{rad} \quad , \tag{5.6}$$

where χ_o is the intrinsic (zero wavelength) position angle. The results for RM and χ_o are given in Table 5.4. The name of the location (see Fig. 5.1) is given in column 1. The rotation measure (with an uncertainty of 2.6 rad m^{-2}) is given in column 2. The intrinsic position angle (with an uncertainty of 1°.2) is given in column 3. The total position angle rotation at 21 cm is given in column 4. The position angle, χ, is plotted vs. λ^2 in Figure 5.31 for the six locations, and the fits are shown as solid lines. The fits are all very good, and the fitted relationships go through all the one sigma error bars. Thus, the data are consistent with $\chi \propto \lambda^2$ between 2 and 21 cm for

Figure 5.31

Plots of position angle, χ, vs. λ^2 at 2, 6, and 21 cm for six locations on the jets where the signal-to-noise ratio in polarized flux density at 2 cm (3."2 resolution) is greater than 3. The fit rotation measures are shown as solid lines (see text). Note the excellent agreement between the fit and the data.

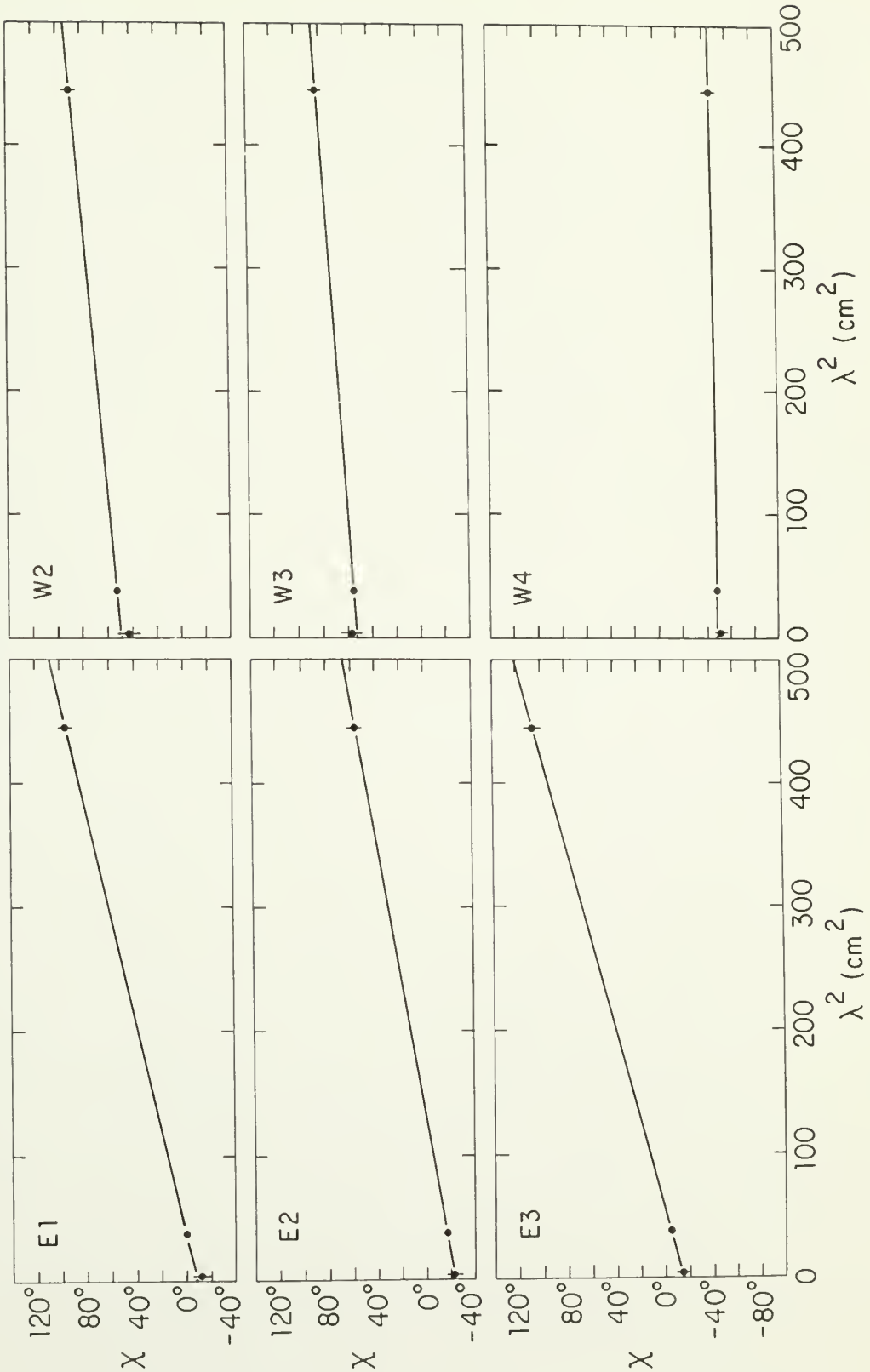
E1
E2
E3
W2
W3
W4
χ
120°
80°
40°
0°
-40°
-80°
0
100
200
300
400
500
λ² (cm²)

up to ~120° of rotation. The derived RMs are in excellent agreement with those found earlier between 6 and 21 cm (see Fig. 5.26). This

Table 5.4

Estimates of the Three Wavelength RM

Location	RM (rad m^{-2})	X_o (degrees)	Rotation at 21 cm (degrees)
E1	41.0	- 9.0	105
E2	31.0	-24.0	80
E3[a]	48.0	-15.0	122
W2	16.0	48.0	42
W3	12.0	53.0	31
W4	1.0	-49.0	2

Notes to Table 5.4

a. The warm-spot in the east jet/tail transition (see Fig. 5.1).

suggests that additional ambiguities of $n\pi$ are unnecessary and that the RM structure shown in Figure 5.26 is correct.

The tails. A 40 kλ taper was applied to the 21 cm (A+C) and 6 cm (B+D) data in order to study the polarization structure of the jet-tail transition and the first ~1.'5 of the tails with a resolution of 3."2. A B/W radiophotograph of the polarized intensity at 21 cm is shown in Figure 5.32. In general, the polarized intensity has a wispy, filamentary appearance and is brightest near the edges of the tails. A contour plot of total intensity at 6 cm with the electric field position angles superimposed (with length proportional to fractional polarization) is shown in Figure 5.33. Because of the large scale ripples discussed earlier, the signal-to-noise ratios in the total intensity and fractional polarization in the diffuse tails are higher at

Figure 5.32

A B/W radiophotograph of polarized intensity at 21 cm (3."2, A+C) showing the filamentary structure in the tails. A correction has been applied for the positive bias (see text).

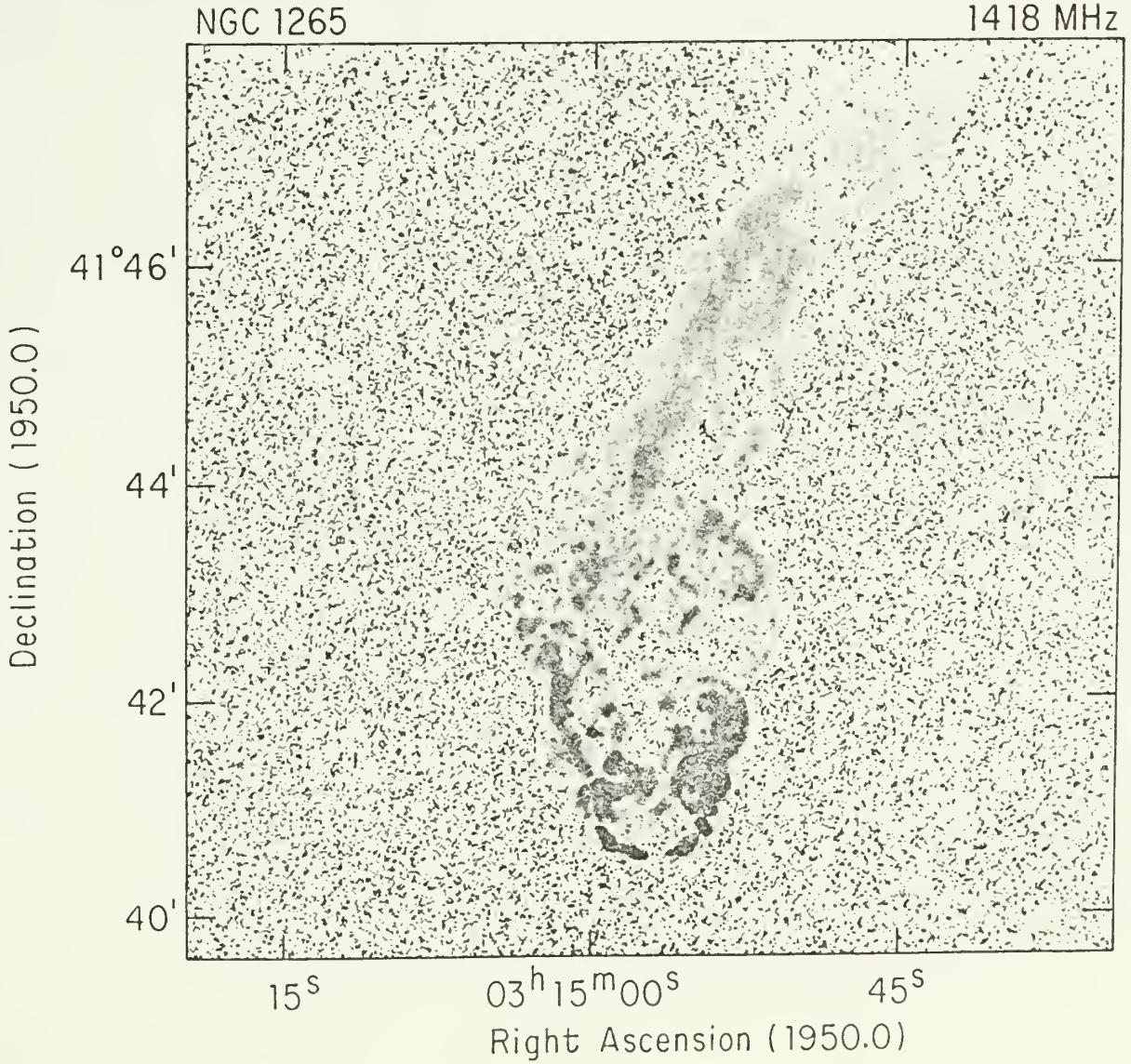
NGC 1265
1418 MHz
41°46'
44'
42'
40'
Declination (1950.0)
15^s
03^h15^m00^s
45^s
Right Ascension (1950.0)

Figure 5.33

A contour plot of total intensity at 6 cm (3."2, B+D) and polarization position angle, χ, with length proportional to fractional polarization. The position angles are "blanked" where the signal-to-noise ratio in both polarized flux density and fractional polarization is less than 3. The CLEAN beam FWHM is shown as the shaded circle. The scale of the polarization vectors is also shown. Representative values of the fractional polarization and its one sigma error are shown in selected areas. Contour levels are -0.4, 0.4, and 3.0 mJy/beam.

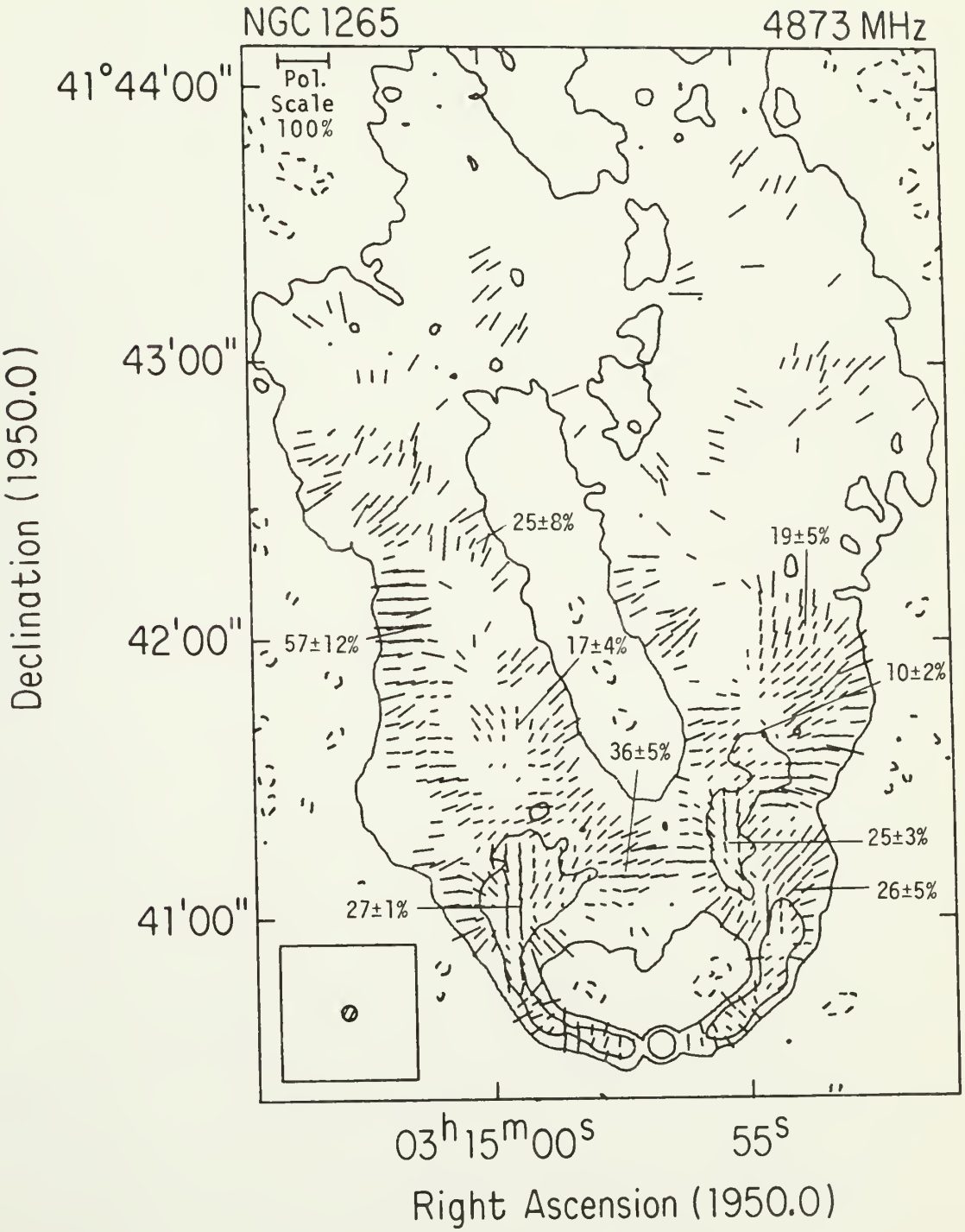
NGC 1265
4873 MHz
Pol. Scale 100%
41°44'00"
43'00"
42'00"
41'00"
Declination (1950.0)
25±8%
19±5%
57±12%
17±4%
10±2%
36±5%
25±3%
26±5%
27±1%
03h15m00s
55s
Right Ascension (1950.0)

6 cm than at 21 cm. At selected places, typical values for the fractional polarization and root-mean-square error are given. As seen in the jets, the fractional polarization tends to increase towards the edges of the tails. At the positions of the warm spots (i.e., the brighter regions) in the jet-tail transition in both tails, the electric field is oriented parallel to the tails. A shell of electric field oriented radially outward surrounds both warm spots. Further down the tails, the electric field is oriented predominantly perpendicular to the tails.

A contour plot of total intensity at 21 cm, with electric field position angles superimposed with length proportional to fractional polarization, is shown in Figure 5.34. Representative values of the rotation measure and error (calculated as described above) are given for selected areas. The RM fluctuates from point to point, however, there are not significant systematic trends in RM either across or along the tails. The RM in the tails tends to be systematically higher (by ~20-30 rad m^{-2}) than that along the jets.

5.3 Summary

Total intensity and polarization measurements with arcsec resolution at 2, 6, and 21 cm of NGC 1265 (3C 83.1B) have been presented. These data are unprecedented in their sensitivity and frequency coverage at this resolution and have revealed many interesting features in this prototype NAT. The basic observational results are summarized below.

Figure 5.34

A contour plot of total intensity at 21 cm (3."2, A+C) and polarization position angle, χ, with length proportional to fractional polarization. The position angles are "blanked" where the signal-to-noise ratio in both polarized flux density and fractional polarization is less than 3. The CLEAN beam FWHM is shown as the shaded circle. The scale of the polarization vectors is also shown. Representative values of the rotation measure and its one sigma error are shown in selected areas. Contour levels are -0.6, 0.6, 2.0, and 10.0 mJy/beam.

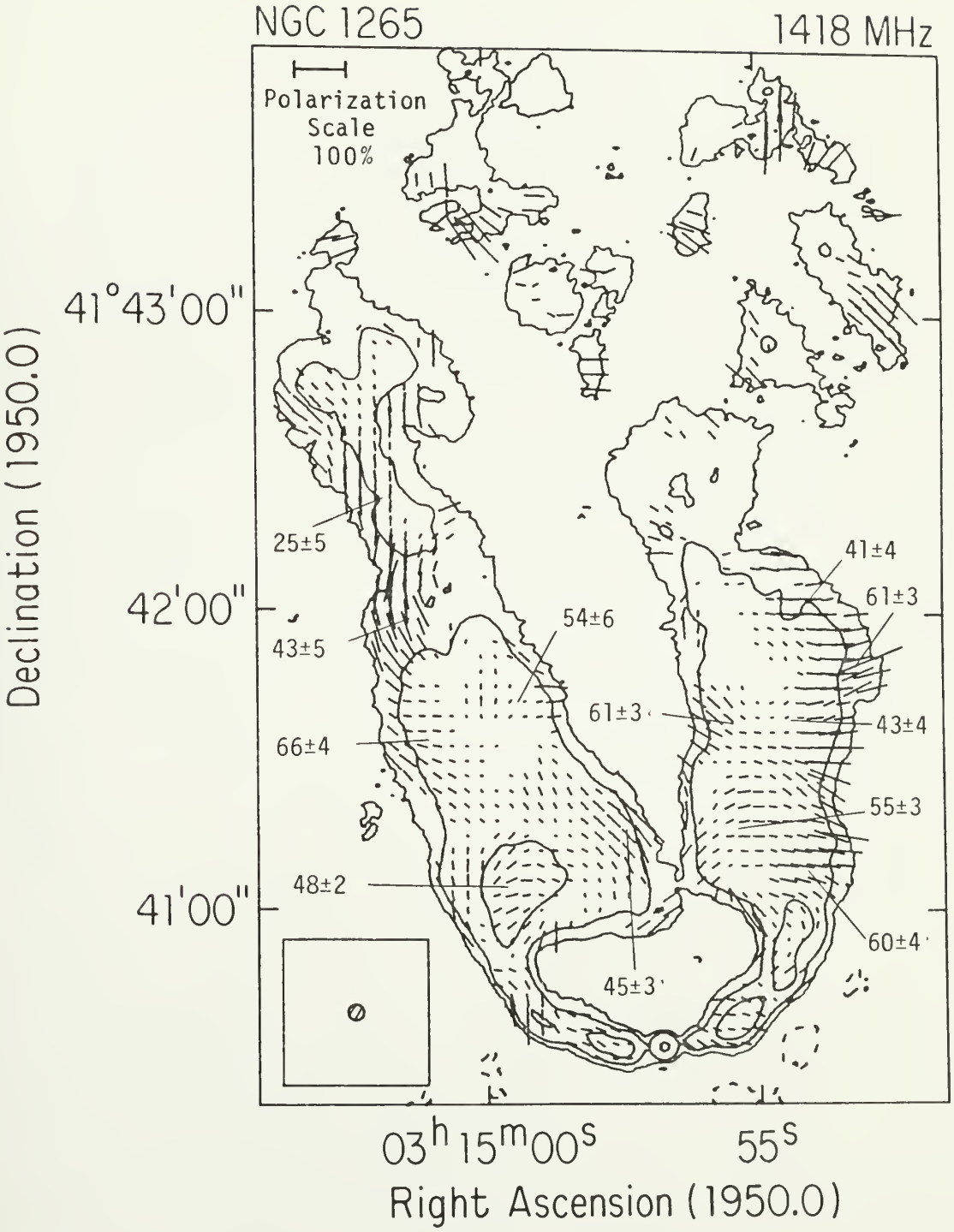
NGC 1265
1418 MHz
Polarization
Scale
100%
41°43'00"
42'00"
41'00"
Declination (1950.0)
25±5
43±5
66±4
48±2
54±6
61±3
45±3
41±4
61±3
43±4
55±3
60±4
03h15m00s
55s
Right Ascension (1950.0)

(1) At 0."45 resolution the transverse total intensity structure of the inner knots in the jets is very asymmetric and is brightest on the south side (i.e., the leading or "front" edge).

(2) The jets are continuous from the compact core to the broad diffuse tails. In the inner ~2-3 kpc from the core, the surface brightness is a factor of ~10 less than that of the first bright knots (E1 and W1).

(3) At 21 cm there is a diffuse "cocoon" of emission around the jets. The cocoon is not seen at 6 cm and must therefore have a spectral index steeper than $\alpha \simeq -1$. The fractional polarization of the cocoon at 21 cm is < 15-30%.

(4) The jets expand with variable expansion rate, but with a typical collimation angle of ~8°. There are shoulders or regions of a flattening in the expansion at ~10-12 kpc from the core, just before the rapid expansion into the tails.

(5) There are asymmetric wiggles in the jets.

(6) There are no significant gradients in spectral index along the jets and the mean value is $\alpha \simeq -0.65$. The knots may have a slightly flatter spectral index (~-0.55) than the rest of the jets. Except for the knot W1, the data are consistent with a straight spectral index between 21 and 2 cm.

(7) The knot W1 has a normal spectral index (~-0.56) between 21 and 6 cm and a very flat spectral index (~-0.05) between 6 and 2 cm.

(8) The fractional polarization along the jets at 2, 6, and 21 cm is typically ~15-25%. There is no evidence for Faraday depolarization (within the errors) at 6 or 21 cm.

(9) Over the inner roughly two-thirds of the jets, the fractional polarization is edge brightened, and the apparent intrinsic polarization position angle is perpendicular to the jet axis. Over the last one-third of the jets, the fractional polarization is more complex, and the position angle tends to be mostly parallel to the jet axis in the center (and perpendicular on the edges in the west jet).

(10) The knots tend to have lower fractional polarization than the rest of the jets. In particular, the W2-W3 knot shows a very strong, frequency independent decrease in the knot center (or equivalently edge brightening) of both the polarized flux density and fractional polarization. There may be a slight position angle rotation in the center of the jet associated with the decrease in polarization.

(11) The rotation measure along both jets varies by > 30 rad m^{-2} over a size scale of ~10" (i.e., ~3 kpc). At 3."2 resolution, $\chi \propto \lambda^2$ between 2 and 21 cm. Total position angle rotations at 21 cm in the range ~80°-120° are observed at three locations along the jets.

(12) The fractional polarization in the tails is edge brightened. The position angles tend to be perpendicular to the tails, though there is a fair amount of disorder or scatter in the position angles.

CHAPTER VI

ASTROPHYSICAL IMPLICATIONS OF THE OBSERVATIONS OF NGC 1265

In this chapter the multifrequency radio observations of NGC 1265 (0314+416, 3C 83.1B) presented in Chapter V are interpreted and discussed within the context of current models for radio jets and in particular bent jets in Narrow Angle Tail (NAT) sources. The basic physical parameters of the radio jets are estimated. An interpretation of the polarization data is given and the possible geometry of the magnetic field in the jets is discussed. The properties of a possible ISM are investigated. The data are used to constrain the possible physics of the jets and astrophysical arguments are made concerning the nature of the interaction of the radio jets with their environment. Finally, the results are summarized.

6.1 Basic Physical Parameters

Jet luminosity

At 21 cm the average total flux density (i.e., the sum divided by two) of the jets (from the core to the point where they start to merge with the tails) is ~0.226 Jy. The radio luminosity is given by

$$L_{rad} = 1.2\times10^{27} D^2 S_o \nu^{-\alpha}(1+z)^{-1/2} \qquad (6.1)$$
$$\left[\nu_u^{1+\alpha} - \nu_l^{1+\alpha}\right]/(1+\alpha) \text{ erg sec}^{-1},$$

where z is the galaxy redshift, D is the distance to the source (in megaparsec). S_o is the flux density (in jansky) at a frequency ν_o (in hertz), α is the spectral index, and ν_u and ν_l are the upper and lower

frequency cutoffs (in hertz). The radio luminosity of the jets was calculated assuming a spectral index of -0.65 between lower and upper frequency cutoffs of 100 MHz and 15 GHz. The average radio luminosity of the jets is $L_{rad} = 1.1 \times 10^{40}$ ergs sec^{-1}.

Minimum pressure and magnetic field

The internal pressure, P_{int}, in the radio jets consists of contributions from the thermal particles, relativistic particles, and the magnetic field. The pressure due to the thermal particles is not known (because the thermal particle density and temperature are difficult to estimate) and will be assumed for the moment to be negligible. Lower limits to the contribution to the pressure from the relativistic particles and magnetic field can be calculated from synchrotron radiation theory (e.g., Pacholczyk 1970, Burns, Owen, and Rudnick 1979). The minimum pressure, P_{min}, is given by

$$P_{min} = \phi B^2_{minP}/(8\pi) + (1/3)E_{minP}/V \text{ dynes cm}^{-2} \qquad (6.2)$$

where

$$B_{minP} = \left[2\pi(1+k)C_{12}L/(V\phi)\right]^{2/7} \text{ gauss} \qquad (6.3)$$

is the magnetic field at minimum pressure, and

$$E_{minP} = \left[V\phi/(2\pi)\right]^{3/7} \left[L(1+k)C_{12}\right]^{4/7} \text{ ergs} \qquad (6.4)$$

is the particle energy (electrons and protons) at minimum pressure, and k is the ratio of proton to electron energy, V is the source volume, C_{12} is a constant which depends on the spectral index and the energy

cutoffs, and ϕ is the volume filling factor (assumed to be one here). The total energy, including both the particles and magnetic fields, is obtained by multiplying equation 6.4 by (5/4). The typographical errors in equation A10 of Burns et al. for the minimum pressure have been corrected here in equation 6.2. The minimum pressure and magnetic field were calculated assuming:

(1) The radio spectrum extends from 100 MHz to 15 GHz, with a spectral index of -0.65. (Only the upper cutoff is important if $\alpha < -1$.)

(2) The protons and electrons have equal energies (k = 1).

(3) The jets are cylinders uniformly filled with relativistic particles and magnetic fields (ϕ = 1).

Over most of the length of the jets, P_{min} is about $1\text{-}3\times10^{-11}$ dynes cm^{-2}, and increases to $\sim6\text{-}9\times10^{-11}$ dynes cm^{-2} in the inner knots. B_{minP} is typically ~10-15 μG (μG = 10^6 gauss) and increases to ~20-30 μG at the inner knots. For comparison, the ram pressure from the ICM is $\rho_{icm}v_g^2 \simeq 7\times10^{-11}$ dynes cm^{-2} for $n_{icm} = \rho_{icm}/m_H$ 5×10^{-4} cm^{-3}, where m_H is the mass of the hydrogen atom, and assuming the galaxy velocity is v_g = 3000 km sec^{-1}; while the static thermal pressure from the cluster gas is (for T = 7×10^7 K, Mushotzky and Smith 1980) $n_{icm}kT = 5\times10^{-12}$ dynes cm^{-2}.

The particle lifetime

The electron lifetime at a frequency ν (Hz) due to both synchrotron losses in a magnetic field, B, (gauss) and to inverse Compton losses off of the microwave background (with equivalent magnetic field

$B_R = 4(1 + z)$ μG, where z is the galaxy redshift) is given by (Van der Laan and Perola 1969),

$$t_1 \simeq \frac{2.6 \times 10^4 B^{1/2}}{(B^2 + B_R^2)[(1 + z)\nu]^{1/2}} \text{ yrs.} \qquad (6.5)$$

For B = 15 μG, an electron radiating at 15 GHz will have a lifetime of $t_1 \simeq 3 \times 10^6$ yrs. Thus, relativistic electrons created in or near the core could travel the entire ~20 kpc length of the jets within their lifetime for bulk jet velocities of $v_b > 0.02c$.

6.2 The Magnetic Field in the Jets

The galactic coordinates of NGC 1265 are l = 150.16 and b = -13.12, which is a region of small, positive rotation measure, RM, (i.e., $0 < RM < 60$ rad m^{-2}; Simard-Normandin et al. 1981; Mitton 1972). For a foreground RM of 60 rad m^{-2}, the rotation at 6 cm will be 12°. The RM's calculated for NGC 1265 using data at 2, 6, and 21 cm (for which $\chi \propto \lambda^2$) are all less than 60 rad m^{-2} and most are less than 40 rad m^{-2}. Thus, because of the small foreground rotation and the lack of internal depolarization, the position angles at 6 cm will be within a few degrees of their intrinsic values. Then for transparent synchrotron radiation, the projected magnetic field direction will be perpendicular to the observed position angles at 6 cm.

The apparent projected magnetic field is parallel to the jet axis along roughly the inner two-thirds of both jets. Along roughly the last third of the west jet, the projected magnetic field is mostly parallel

to the axis along the edges and perpendicular to the axis in the center of the jet. Along the last third of the east jet, the projected magnetic field is mostly perpendicular to the jet axis.

The field parallel to the jet axis in the inner approximate two-thirds of the jets is in contrast to what is usually seen in symmetric low power radio jets (Bridle 1982, Bridle and Perley 1984). Generally, low power jets have apparent projected fields perpendicular to the jet axis. However, in beams which are confined by and interact very strongly with an external medium (as suggested by the bending) a velocity gradient or shear will be set up across the beam, with the velocity decreasing towards the edges of the beam. This shear will stretch out an initially tangled field along the beam axis, resulting in a jet with a mostly parallel magnetic field. The development of a perpendicular field region further down the jets could be due to the gradual expansion of the beam since the parallel component varies as

$$B_{\parallel} \propto r_b^{-2} \tag{6.6}$$

(if magnetic flux is conserved) and the perpendicular (azimuthal) component varies as

$$B_{\perp} \propto v_b^{-1} r_b^{-1}, \tag{6.7}$$

(e.g., Blandford and Rees 1974, Bicknell and Henriksen 1980). Thus, in the simple case of conservation of magnetic flux, because the beam expands, the perpendicular component will eventually dominate. However, in NGC 1265 it appears that magnetic flux is not conserved (see Sec. 6.10) and these simple laws will not be obeyed.

Tangential field

Laing (1981) has calculated the expected total intensity and polarization structure due to an initially tangled magnetic field which has been sheared tangentially to the beam surface (his model B). He finds that the polarization structure is a strong function of the inclination angle, δ, of the jet to the line of sight. Thus, in principle, the observed polarization structure of the jets can be used to constrain the source geometry. However, there are two problems with this in practice.

(1) The intensity distribution across the jets in NGC 1265 is asymmetric (probably because the beam adjusts hydrostatically to the external pressure gradient), while Laing's profiles for the tangential field all have symmetric total intensity structure, by assumption of axial symmetry.

(2) The jet is only slightly resolved over much of its length. The available resolution is 1."2, while the deconvolved jet width varies from ~0."5 - 3". There is polarization information at 0."45 resolution at 6 cm for the bright inner knots, though these data do not reveal any new structure.

A computer program was written in which the formula given by Laing (1981) were used to calculate the theoretical profiles for a jet with radius 0.5", 1."0 and 1."5 for a variety of inclination angles. The profiles were then numerically convolved with a gaussian with FWHM of 1."2. Laing finds that the tangential field geometry results in a projected magnetic field which is perpendicular to the jet axis in the center of the jet and is parallel to jet axis on the edges for any

inclination different from 90°. However, the effect of convolution with a gaussian beam is to increase the range of inclination angle over which the projected magnetic field is exclusively parallel to the jet axis. For a jet with a radius of 1."5 convolved with a 1."2 beam, the projected field is parallel to the jet axis for the range of inclinations $45° \leq \delta \leq 135°$. This regime of parallel, projected magnetic field is accompanied by edge brightened fractional polarization as is seen in NGC 1265. The parallel field region in the jets is the region over which nearly all of the bending occurs. Thus, if this model is correct, the jets in NGC 1265 must be within ~45° of the plane of the sky. Since the measured radial velocity with respect to the cluster mean is ~2200 km sec^{-1} (Chincarini and Rood 1971), this requires the total velocity to be $\geq$ 3100 km sec^{-1}, which is a plausible value.

A related geometry would be a magnetic field which is confined to a plane perpendicular to the jet axis, with sheared edges (Laing 1980). As long as the sheared edges are large compared to the perpendicular field in the jet core, the polarization would be indistinguishable from that of the completely tangential field model because of the limited resolution. The essential difference in the jet physics between the two models is whether or not a strong shear extends from the edges all the way in to the jet axis.

There are two other possible field geometries which should be considered--a helical field with constant pitch angle, γ_o, filling a cylinder (suggested by Fomalont et al. 1980 for the jets in 3C 31), and a field suggested by Chan and Henriksen (1980, CH) which is parallel to the jet axis on the axis and has a helical pitch angle which increases

with radius from 0.0 on the axis to a constant value, γ_o, at the beam surface. Laing (1981) also gives the formula for the total intensity and polarization structure for these two field geometries. Convolved profiles were calculated for a range of inclination angles and helical pitch angles and were compared with the data. One general feature of these models is that for a wide range of pitch angles, as the inclination angle becomes increasingly smaller or larger than 90° (i.e., for a jet out of the plane of the sky), the total intensity and polarization profiles become increasingly asymmetric.

Helical field

The convolved helical field model can qualitatively reproduce the polarization structure of the inner two-thirds of the jets (i.e., edge brightened fractional polarization with projected magnetic field parallel to the axis) for inclination angles in the range $80° \leq \delta \leq 110°$ and helical pitch angles in the range $30° \leq \gamma_o \leq 110°$. Outside of this narrow range, the helical field model either requires the projected field to be perpendicular to the jet axis over some part of the profile, or else does not reproduce the observed edge brightening in the fractional polarization. This would require that the jets be no more than about 10° out of the plane of the sky. The spatial velocity of NGC 1265 would then be $\geq 1.2 \times 10^4$ km sec^{-1}, which seems much too high.

The last third of the east jet (with a relatively flat fractional polarization profile and predominantly perpendicular projected field) could be qualitatively reproduced by a helical field with $75° \leq \delta \leq 105°$ and $\gamma_o \simeq 90°$. On the other hand, the perpendicular projected field

structure in the jet center with parallel projected field on the edges seen in the last third of the west jet can be reproduced by inclination angles $30° \leq \delta$. However, even for the convolved profile, this would require two minima in the fractional polarization profile which are not observed.

CH field

The polarization of the CH field is qualitatively similar to that of the simple helical field (Laing 1981). However, for the region of parameter space where the projected magnetic field is exclusively parallel to the jet axis, the CH field produces a flatter fractional polarization profile. (For a given δ and γ_o, the edge brightening in fractional polarization is much less for the CH field than it is for the helical field.) Thus, the polarization structure of the inner two-thirds of the jets can be qualitatively reproduced for $85° \leq \delta \leq 95°$ and $50° \leq \gamma_o \leq 60°$. And the source must be within about 5° of the plane of the sky, requiring a total velocity for NGC 1265 of $\geq 2.5 \times 10^4$ km sec^{-1}.

The last third of the east jet can be qualitatively reproduced by $70° \leq \delta \leq 110°$ and $\gamma_o \simeq 90°$. As in the case of the helical field model, the CH field cannot reproduce the polarization of the last third of the west jet.

Thus, the pure helical field and CH field models cannot provide a consistent description of the polarization structure of the jets in NGC 1265. However, this should not be too surprising given that both fluid turbulence and shearing are expected to occur within the jets. It

is unlikely that a well-ordered magnetic field geometry could exist under such conditions unless such things as rotation or a beam current were very important (cf. CH). More realistic models which include some amount of random field (see Perley, Bridle, and Willis 1984) should be considered. Faraday depth effects cannot be invoked to alter these conclusions since no depolarization is seen.

At this point, the magnetic field geometry which most plausibly reproduces the polarization data is that of an initially tangled field which has been sheared so as to be tangential to the edges of the jet.

6.3 Upper Limits on Faraday Depolarization within the Jets

In this section the limits on Faraday depolarization will be used to set constraints on the internal particle density in the jets. The observed rotation measure, on the other hand, appears to be produced externally and provides information on the jet's external environment.

The lack of depolarization between 6 and 21 cm can be used to set an upper limit to the internal Faraday depth through the center of the jets, F_c, where

$$F_c = 1600\ n_e\ B_\mu\ \lambda^2\ L \text{ rad} , \tag{6.8}$$

and where n_e is the thermal particle density in cm^{-3}, B_μ is the net component of the magnetic field along the line of sight in μG, λ is the wavelength in m, and L is the path length through the center of the jets in kiloparsec; and $F_c = 2RM\lambda^2$, where RM is the rotation measure (e.g., Cioffi and Jones 1980). The simplifying assumptions will be made that

the jets are cylinders homogeneously filled with relativistic particles, magnetic fields, and thermal particles and that both the large-scale magnetic field orientation and the amount of disorder in the field are uniform within any beam width. The last two assumptions concerning the magnetic field are consistent with the tangled tangential field discussed above. Cioffi and Jones (1980) have considered the effects of geometry and resolution on the observed Faraday rotation and depolarization in transparent synchrotron sources, and their results will be used in the interpretation of the polarization data. The knot E2 has the highest signal-to-noise ratio in fractional polarization and will be used for this calculation. Note that this will give the lowest possible upper limit to the internal Faraday depth. Elsewhere along the jet, where the signal-to-noise ratio is lower, higher values of F_c are permitted. E2 is mostly unresolved (deconvolved FWHM of ~1."3 compared to a resolution of 1."2), so the results of Cioffi and Jones for an unresolved cylinder seen from the side are applicable.

At 6 and 21 cm, the fractional polarization at E2 is 18 ± 1% and 19 ± 1%, respectively (i.e., they are equal within their errors). The depolarization ratio (P_{21}/P_6) is thus 1.06 ± 0.08. A conservative estimate of the maximum permissible Faraday depth would be that required to produce a 3σ difference in the depolarization ratio between 21 and 6 cm (i.e., reducing the depolarization ratio from 1.06 to 0.82). Using Figure 1b from Cioffi and Jones, a Faraday depth of $F_c \simeq 1.9$ rad would be required (assuming that the 18% fractional polarization at 6 cm is unaffected by Faraday or beam depolarization). Then using $B_\mu = 25$ from minimum pressure and L = 0.8 kpc, the upper limit to the internal

thermal particle density is $n_e < 1 \times 10^{-3}$ cm^{-3}. Note that if there are many reversals of the magnetic field direction along the line of sight, a higher thermal particle density is permitted. This loophole is in fact the most serious uncertainty in the interpretation of polarization measurements of jets. The observed fractional polarization is given by

$$p = [(3q + 3)/(3q + 7)]B_o^2/(B_o^2 + B_r^2), \qquad (6.9)$$

where $q \equiv (1 - 2\alpha) \simeq 2.3$ for $\alpha \simeq -0.65$, and B_o and B_r are the ordered and random components in the magnetic field (Burn 1966). If the observed fractional polarization of ~20% is not affected by Faraday or beam depolarization, then $B_r \simeq 1.6\ B_o$, i.e., the random component of the field dominates. This problem may be affecting the derived density, n_e.

In an unresolved cylinder, a central Faraday depth of 1.9 rad at 21 cm will produce a rotation in position angle of $\Delta\chi \simeq 24°$; while at 6 cm the corresponding Faraday depth is $F_c \simeq 0.16$ rad, which will result in a rotation of $\Delta\chi \simeq 2°$. Thus the apparent rotation measure between 6 and 21 cm is 9.5 rad m^{-2}. Note that this is an upper limit to the apparent rotation measure produced within the jets and would only be reduced by possible reversals in the magnetic field direction. The polarization data at 6 cm at 0."45 resolution provide a consistency check on these results. The lack of position angle rotation across E2 is consistent with the low estimated central Faraday depth at this wavelength ($F_c \simeq 0.16$ rad). Also the value of the fractional polarization of ~22% ± 6% is consistent with a lack of beam depolarization on the scale of ~0."45 - 1."2 (~0.16 - 0.42 kpc).

6.4 Foreground RM Structure Along the Jets

The change in RM along the jets (see Chap. V) are at least a factor of three larger than can be produced within the jets. Also, the position angles at 2, 6, and 21 cm are consistent with $\chi \propto \lambda^2$ over a range of position angle rotation of up to ~120°. Since the maximum rotation obtainable from an unresolved cylinder is ~45° (Cioffi and Jones 1980), this suggests that the rotation occurs in a foreground screen. There are four possible locations for this screen: our Galaxy, the Perseus cluster, a sheath around the jets, and, finally, an ISM within NGC 1265. Each of these possible locations will be considered in turn.

The Galaxy

The root-mean-square variations in NGC 1265 occur over a size scale of several arcseconds. At this point there is no evidence for any structure in the Galactic RM on such a small scale (Simard-Normandin et al. 1981). Also, Burn (1966) has considered the properties of the Galactic clouds which would be required to produce observable amounts of Faraday rotation on sufficiently small scales. He finds that implausible conditions are required. Thus, it seems that any contribution from our galaxy to the RM of NGC 1265 is likely to be uniform over the ~1' scale of the jets.

The Perseus cluster

Jaffe (1980) has considered the morphology of the magnetic field in clusters of galaxies. He suggests that turbulent, galactic wakes are capable of generating a tangled cluster magnetic field of order 1 μG. The dominant wavelength in the tangled field is expected to be ~20 kpc. Thus, any line of sight through the cluster will go through many reversals in the direction of the magnetic field. This will tend to wash out any differential RM structure (e.g., Burn 1966). There should be significant RM structure in the cluster only if the cell size of the tangled field is comparable to the path length. However, in that case, the RM would still be uniform over the relatively small scale of the RM variations in NGC 1265. Thus, although the Perseus cluster may contribute to the foreground RM, it is unlikely that the RM variations in NGC 1265 are produced in the cluster magnetic field.

A sheath around the jets

An additional possibility is that the RM occurs in a sheath around the jets. The possible origins of such a sheath or cocoon are discussed below. But whatever its origin, because radio emission is seen, there must be a magnetic field outside the jets. Since the RM variations are of comparable magnitude of both jets, the Faraday depth through the sheath must be comparable, i.e., similar path lengths, magnetic fields, and particle densities.

The strength of the magnetic field in the sheath can be estimated from the minimum pressure conditions. The exact geometry and spectrum of the diffuse halo are uncertain, however, the estimate of the magnetic

field depends on the luminosity and volume to only the 2/7 power. It is assumed that the sheath is cylindrically symmetric around the jets, with a radius of ~2 kpc (i.e., the approximate size of the radio cocoon around the west jet). A cylindrical volume of radius 0."6 and length 13" is taken through the halo (i.e., taking the simple slab geometry). Then, choosing a spectral index of $\alpha = -1.1$, and upper and lower frequency cutoffs of 1.4 GHz and 100 MHz, gives $B_{minP} \sim 6$ μG and $P_{min} \sim 3 \times 10^{-12}$ dynes cm^{-2}. Taking a smaller volume or a lower low-frequency cutoff would increase the value of B_{minP} and P_{min}. However, this pressure is a factor of ~10 too low to confine the radio jets. This suggests that minimum pressure conditions do not exist in the cocoon, and that the pressure is dominated either by relativistic protons and magnetic fields or by thermal particles. For the purposes of this calculation, it will be assumed that the magnetic field and relativistic protons in the cocoon contribute enough pressure to confine the radio jets and that the magnetic field in the cocoon is comparable to that in the jets, i.e., $B \sim 15$ μG. So, if $B_\mu = 15$ and $L = 2$ kpc, the electron density needed to provide RM in $n_e \simeq 1 \times 10^{-3}$, which is higher than the estimated particle density in the ICM.

Thus, the data are roughly consistent with the hypothesis that the RM is produced in a sheath around the jets if there is an ISM of some kind.

An ISM in NGC 1265

The RM variations along the jets have a size scale which is comparable to the expected size of the ISM in NGC 1265 (JO). Also,

there is evidence for RM structure due to an ISM in NGC 6251 (Perley, Bridle, and Willis 1984) and in M84 (Laing and Bridle 1983). (The origin and morphology of the magnetic field in an elliptical galaxy are uncertain; however, a detailed investigation of these problems is beyond the scope of this thesis.) If the ISM is responsible for producing the RM structure, then 30 rad $m^{-2} \simeq 800\ n_e\ B_\mu\ L$. If $L \simeq 10$ kpc and $n_e < 0.3\ cm^{-3}$ (from the upper limits on the Hα flux density), then the net component of the field along the line of sight is $B_\mu > 0.01$ μG.

If there is not a significant ISM, i.e., the galaxy contains a significant magnetic field, but the density is that of the ICM ($n_{icm} \simeq 5 \times 10^{-4}\ cm^{-3}$), then the required magnetic field is $B_\mu \sim 8$ μG. This value for the magnetic field seems rather high, since if the galaxy is swept free of an ISM, it is hard to imagine how the galaxy could maintain such a high magnetic field.

At this point there do not seem to be any considerations which rule out the possibility that the RM is produced in an ISM in the galaxy NGC 1265. The large-scale gradient in the RM could be due to either a change in the path length, the orientation of the B field, the density of the ISM, or various combinations of these possibilities.

6.5 Constraints on an ISM in NGC 1265

If there is an ISM in NGC 1265, and if it confines the radio jets, then $P_{int} \simeq n_e kT \simeq 3 \times 10^{-11}$ dynes cm^{-2} (from the minimum pressure calculation), where n_e is the electron density (in cm^{-3}), T is the temperature (in kelvins), and k is the Boltzmann constant. Also, its

radius should be comparable to the bending scale size of the jets (JO, see also Chap. IV) giving $r_s \simeq R \simeq 10$ kpc. A lower limit to the temperature can be obtained from the upper limit to the Hα flux density of $F_{H\alpha} < 5\times10^{-14}$ ergs cm^{-2} sec^{-1} (Gisler and Butcher 1983, private communication) which corresponds to an Hα luminosity of $L_{H\alpha} < 3.1\times10^{40}$ erg sec^{-1} for a distance to NGC 1265 of 72 Mpc. If the ISM is approximated by homogeneous sphere of radius, r_s, then (using cgs units)

$$L_{H\alpha} = (4\pi/3) j_{H\alpha} r_s{}^3 n_e{}^2 \ , \qquad (6.10)$$

where $j_{H\alpha}$ is the Hα emissivity for Case B (i.e., large opacity in Lα). The numerical calculations of Ferland (1980) were used to estimate a power law approximation to $j_{H\alpha}$ at temperatures near 10^6 K which are expected in the ISM (e.g., Jones and Owen 1979). Using Ferland's calculations gives

$$j_{H\alpha} = 2.29\times10^{-27}(T/10^6)^{-1.27} \text{ ergs sec}^{-1} \text{ cm}^{-3} \qquad (6.11)$$

which should be good to ~10% in the range $5\times10^5 \leq T \leq 5\times10^6$ K. Then the Hα luminosity is given by

$$L_{H\alpha} = 4.0\times10^{-19} n_e{}^2 r_s{}^3 T^{-1.27} \text{ ergs sec}^{-1}, \qquad (6.12)$$

or, substituting $n_e = P_{int}/kT$

$$L_{H\alpha} = 2.1\times10^{13} P_{int}{}^2 r_s{}^3 T^{-3.27} \text{ ergs sec}^{-1} \qquad (6.13)$$

and the limit on the temperature becomes

$$T > [2.1\times10^{13} r_s^{3} P_{int}^{2} L_{H\alpha}^{-1}]^{0.306} , \qquad (6.14)$$

which gives $T > 8\times10^{5}$ K if $P_{int} = 3\times10^{-11}$ dynes cm^{-2}.

The current 3σ upper limit to the X-ray flux from NGC 1265 is 2.6×10^{-13} erg cm^{-2} sec^{-1} in the energy band 0.4 to 3.0 keV (corrected for instrumental response but not for absorption in the direction of the Perseus cluster) from an ~8000 second observations with the IPC of the Einstein Observatory (Fabricant et al. 1979). This corresponds to an X-ray luminosity in this energy band of $L_x < 1.6\times10^{41}$ ergs sec^{-1} and can also be used to set limits to the temperature of a possible ISM. The upper limit will be compared with the predicted X-ray luminosity due to thermal bremsstrahlung from a homogeneous sphere of radius r_s of fully ionized hydrogen. At X-ray energies below 1 keV, the observed emission must be corrected for photoelectric absorption by atoms in our galaxy along the line of sight to the source. The absorption is given by $\sim e^{-\sigma(E)N_H}$, where σ(E) is the energy dependent absorption cross section and N_H is the column density of neutral hydrogen. The energy dependence of the absorption cross section is complicated by the contribution from trace elements such as carbon, nitrogen, and oxygen, but is given approximately by

$$\sigma(E) \simeq 2\times10^{-22}(E)^{-8/3} \text{ cm}^{-2}, \qquad (6.15)$$

where E is in kiloelectron volts (e.g., Longair 1981, p. 51). The column density of neutral hydrogen in the direction of the Perseus cluster (from a fit to the X-ray spectrum of the cluster) is $N_H \simeq 3.2\times10^{21}$ cm^{2} (Mushotzky et al. 1978). This column density produces an

opacity of ~0.6 (i.e., an attenuation of ~50%) at an energy of 1 keV. The absorption increases rapidly below 1 keV and reaches the 1/e point at ~0.85 keV. Thus, the effective energy band of the observations is roughly ~1-3 keV. The X-ray luminosity obtained by integrating the free-free emissivity (e.g., Spitzer 1978, p. 57) over the energy band 1-3 keV gives

$$L_x = 1.75\times10^{38} g_{ff} T^{1/2} n_e^2 r_s^3 \left[\exp(-1.2\times10^7/T) - \exp(-3.5\times10^7/T)\right] \text{ erg sec}^{-1} , \quad (6.16)$$

where g_{ff} is the gaunt factor ($g_{ff} \simeq 1.3$ for $T \sim 10^6$-10^7 K), r_s is in kiloparsecs and T is in kelvins. Substituting $n_e = P_{int}/kT$ results in

$$Lx = 9.2\times10^{69} g_{ff} P_{int}^2 T^{-1.5} r_s^3 \left[\exp(-1.2\times10^7/T) - \exp(-3.5\times10^7/T)\right] \text{ erg sec}^{-1} . \quad (6.17)$$

The X-ray luminosity given by equation 6.17, using $P_{int} = 3\times10^{-11}$ dynes cm^{-2} and r_s = 10 kpc, is plotted in Figure 6.1. The X-ray upper limit as well as the lower limit on the temperature from the Hα measurements are also shown. The upper limit to the X-ray luminosity is too high to constrain parameter space any further. A more sensitive upper limit would be very useful.

Then, using the lower limit of $T > 8\times10^5$ K gives an electron density of $n_e < 0.3$ cm^{-3}. If the ISM is responsible for producing the RM structure, then 30 rad m^{-2} $\simeq$ 800 n_e $B_\mu L$. If L $\simeq$ 10 kpc and $n_e <$ 0.3 cm^{-3}, then the net component of the field along the line of sight is $B_\mu > 0.01$ μG. If the RM is produced in a ~2 kpc sheath around the jets,

Figure 6.1

The predicted X-ray luminosity in the energy band 1 to 3 keV as a function of the temperature of the ISM. Also shown are the current 3σ upper limit to the X-ray emission (Fabricant et al. 1979) and a lower limit to the ISM temperature of 10^6 K from the upper limits to the Hα luminosity (Gisler and Butcher, 1983, private communication).

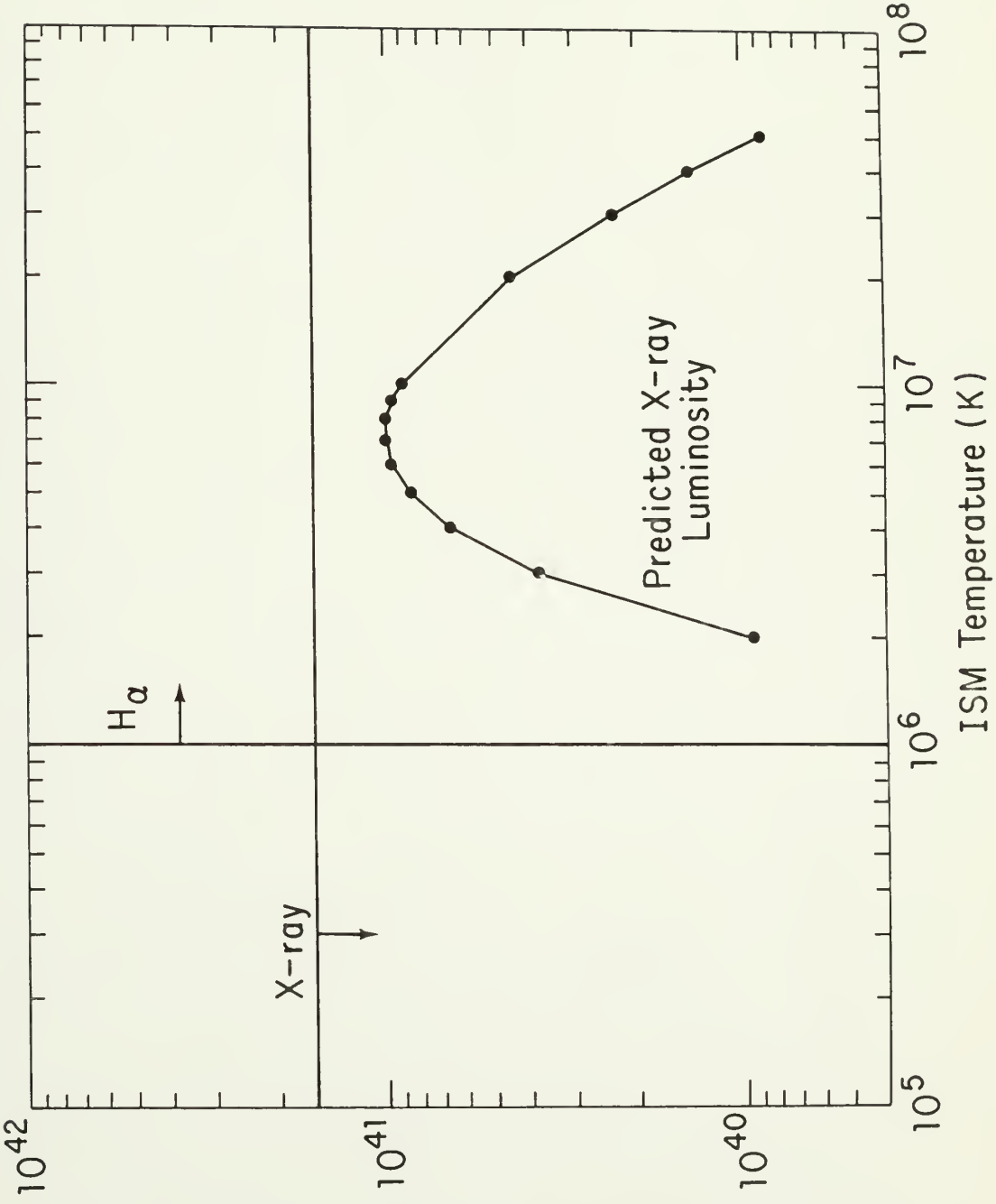
X-ray Luminosity (ergs sec^{-1})
10^{42}
10^{41}
10^{40}
H_α
X-ray
Predicted X-ray Luminosity
10^5
10^6
10^7
10^8
ISM Temperature (K)

the RM due to the ISM must be much smaller, requiring a much smaller net ISM magnetic field along the line of sight, i.e., $B_\mu < 0.01$ μG.

A crude upper limit to the ISM magnetic field comes from the requirement that the field is tied to the gas in the ISM (i.e., the pressure from the magnetic field is less than that of the thermal particles). If the ISM also confines the radio jets, then $B < (8\pi P_{int})^{1/2} \simeq 30$ μG.

The total amount of gas in solar masses within a sphere of radius 10 kpc is roughly $M_{gas} \sim n_e\ 10^{11}\ M_\odot$. Then, for a density of $n_e < 0.3$, the mass of gas is $M_{gas} < 3\times10^{10}\ M_\odot$. This is higher than that expected based on the numerical calculations (e.g., Gisler 1976; Lea and De Young 1976; Shaviv and Salpeter 1982) and suggests that the temperature of the ISM is higher than the current lower limit of 8×10^5 K.

6.6 Edge Brightening and the Beam Mach Number

One observational constraint on the beam Mach number, M, comes from the fact that in the quasi-continuous beam models, the beam experiences a transverse pressure gradient. The beam fluid will come into hydrostatic equilibrium with the external pressure gradient in the sound crossing time $t_c \simeq r_b/c_s$, where r_b is the beam radius and c_s is the sound speed. In that time the beam fluid also travels a distance $d = v_b t_c$, where v_b is the beam velocity. If the observed edge brightening (Figs. 5.1-5.3) is due to a density gradient across the jet produced by this effect, then $M = v_b/c_s \leq d/r_b$, where d is taken to be the distance from the core where the jet first appears to edge brighten, i.e., the

knot E1, giving $M \leq 14$. This is an upper limit to the Mach number since the signal-to-noise ratio interior to E1 is too low to determine whether the edge brightening occurs any sooner. Also, it is not clear at what distance from the core the beam first experiences the external pressure gradient. (If there is a significant ISM, the pressure gradient in the very center of the galaxy is expected to be radial (JO); i.e., the jet will not feel a transverse pressure gradient until some distance from the core.) If there is an ISM, then the observations suggest that the region of radial pressure gradient is no more than ~3 kpc. The knots E1 and W1 can be connected by a straight line which goes through the core. Just beyond these knots the jets start to bend.

The upper limit of ~3 kpc to the size of the radial pressure zone in the center of the galaxy can be compared with the numerical results (Lea and De Young 1976, Shaviv and Salpeter 1982). Lea and De Young do not show the details of the velocity fields in the inner part of their model galaxy. However, Shaviv and Salpeter show velocity fields in the inner part of the galaxy for one of their models in which they take viscosity into account. The pressure gradients are radially outward for the inner ~1-2 kpc but become parallel to the galaxy velocity within ~3 kpc from the center of the model galaxy. Unknown scaling factors are required to make a quantitative comparison between the model and the data. However, the models are at least qualitatively consistent with the existence of transverse pressure gradients in the inner parts of the galaxy.

For a naked beam (i.e., one not immersed in a significant ISM, Begelman, Rees, and Blandford 1979); $M = (R/h\gamma)^{1/2} \simeq 5$ (cf. Chap. VII), where R is the size scale of the bending ($R \simeq 10$ kpc), h is the size scale of the pressure gradient ($h \simeq r_b \simeq 210$ pc), and γ is the adiabatic index, taken to be 5/3 for a beam with a nonrelativistic equation of state. If there is instead a pressure gradient due to a significant ISM (Jones and Owen 1979), then requiring $R \simeq h$ gives $M \simeq 1$. Thus both predicted Mach numbers are consistent with the observations.

6.7 The Diffuse Radio Cocoon

The existence of a sheath of diffuse emission around the jets can be used to examine the nature of the interaction between the jets and their immediate surroundings.

One possibility is that the particles escape or diffuse out of the jets. The diffusion speed will depend on the geometry of the magnetic field outside the jets. The current observations are not sensitive enough to detect any polarization in the cocoon (in fact, the halo is not even detected at 6 cm). The 3σ upper limit to the fractional polarization in the cocoon at 21 cm is ~15-30% (see Chap. V). If the sheath surrounds the jets, then such a low fractional polarization cannot be due to Faraday depolarization in the sheath, since the jets (which would then be seen through a depolarized screen) show no evidence of depolarization. This suggests that either the field in the sheath is highly tangled or that the geometry of the field is such that the polarization from different parts of the sheath cancel out.

Streaming

For completeness, the two cases of streaming along and diffusion across the magnetic field lines will be considered. If the magnetic field is well ordered and is perpendicular to the jet surface, then within the particle radiative loss lifetime, t_l, the particles will travel a distance $x = vt_l$, where v is the particle velocity. Assuming a magnetic field in the cocoon of 15 μG gives a synchrotron and Inverse Compton lifetime of $t_l \simeq 1 \times 10^7$ years for particles radiating at 1.4 GHz. Since the particle spectrum has steepened from ~-0.65 to at least ~-1 by the time the halo can be distinguished from the jets (i.e., a distance of ~210 pc), the upper limit to the streaming velocity is $v < 2 \times 10^6$ cm sec^{-1}. If the jets were exposed to the ICM, the halo would be quickly stripped away (except in the jet "shadow") since the particle speed is much less than the observed galaxy velocity ($v_g > 2.2 \times 10^8$ cm sec^{-1}; Chincarini and Rood 1971). Thus, the existence of the halo on both sides of the jets suggests that the particles stream or diffuse into a static external medium (e.g., an ISM).

If the particle velocity is limited to the Alfven velocity by scattering of the particles by Alfven waves (e.g., Wentzel 1974), then $v_A = B/(4\pi\rho)^{1/2} < 2 \times 10^6$ cm sec^{-1}. If this is the case, the required electron density in the cocoon (for a 15 μG field) is $n_e = \rho/m_H < 3$ cm^{-3} which is higher (by a factor of ~10) than the current upper limits to the electron density outside the jets. If, on the other hand, the thermal pressure in the cocoon is greater than the magnetic field pressure (i.e., $n_e kT < B^2/8\pi$), then the limiting streaming velocity will be the much higher proton sound speed (Holman, Ionson, and Scott 1979).

This condition requires $B < 30$ μG, if $n_e kT \simeq P_{int} \simeq 3 \times 10^{-11}$ dynes cm^{-2}, which is consistent with the current estimates. Then the required cocoon electron density is $n_e < \gamma P_{int}/(m_H c_s^2) \simeq 8$ cm^{-3}, which is much higher (by a factor of ~30) than the upper limits to the electron density outside the jets. The requirement that the electron density is $n_e < 0.3$ cm^{-3} (from the constraints on the Hα luminosity) gives $v_A > 6 \times 10^6$ cm sec^{-1} and $c_s > 10^7$ cm sec^{-1}. Thus, if the particles stream along the field lines, their velocity would be much too high to produce the observed spectral steepening.

Diffusion

If the magnetic field is oriented parallel to the jet surface or is tangled (a more realistic case), the electrons must diffuse across the field lines. In that case, the distance over which the particle spectrum will steepen is given by $x = (2\kappa_D t_1)^{1/2}$, where κ_D is the diffusion constant (e.g., Eilek 1982). Then for $B = 15$ μG, $t_1 \simeq 1 \times 10^7$ years, and $x < 210$ pc, the upper limit to the diffusion constant is $\kappa_D < 7 \times 10^{26}$ cm^2 sec^{-1}.

What does this value of κ_D reveal about the properties of the medium through which the particles diffuse? In the interest of obtaining a simple solution to this question, the following assumptions will be made.

(1) The fluctuations in the magnetic field, δB, are produced by fluid turbulence in the medium.

(2) The fluctuations are small compared to the ordered background field, B_o.

(3) Their power spectrum is given by $W(k) = W_o k^q$, where k is the wave number.

The general form q = -3/2 for a fully developed MHD turbulence (Kraichnan 1965) will be examined first. The total energy density in the turbulent field is given by

$$\delta B^2/8\pi = \int_{k_{min}}^{k_{max}} W(k)\, dk \ , \tag{6.18}$$

where k_{max} and k_{min} are the maximum and minimum wave number, respectively (Eilek 1982). Then if $k_{max} >> k_{min}$, integrating equation 6.18 gives

$$W_o \simeq \delta B^2 k_{min}^{1/2}\ (16\pi)^{-1}. \tag{6.19}$$

The diffusion constant is given by

$$\kappa_D = 4\pi c W(0)/B_o \tag{6.20}$$

(Jokipii 1966; Eilek 1982), where c is the velocity of light and W(0) is the energy density in the field at zero wave number. Following Eilek (1982), the assumption will be made that the power spectrum flattens below k_{min} so that $W(0) \simeq W_o k_{min}^{-3/2}$. Making this substitution into equation 6.20 gives

$$\kappa_D \simeq c\delta B^2\ \lambda_{max}/(B_o{}^2 8\pi), \tag{6.21}$$

where $\lambda_{max} = 2\pi/k_{min}$ is the largest size scale in the turbulence. The value for λ_{max} is uncertain; but if the turbulence is produced through the interaction of the external medium with the jet, then the largest

characteristic size might be the jet radius, $r_b \simeq 800$ pc. Taking $\lambda_{max} = 800$ pc and $\kappa_D = 7 \times 10^{26}$ cm^2 sec^{-1} gives $(\delta B/B_o)^2 \sim 2 \times 10^{-4}$; i.e., the energy in the turbulence is only a negligible fraction of the total energy in the field. This would predict a fractional polarization (eq. 6.9) of ~76%, which is much higher than the upper limit of ~15% and suggests that the tangling in the field is not described by this model.

Eilek (1982) used $q = -1/2$, which she obtained for the case where Alfven waves are generated by Kelvin-Helmholtz instabilities in a jet/medium interface. In this case, the diffusion coefficient is given by

$$\kappa_D = (c/8\pi)(\delta B/B_o)^2 \, (\lambda_{min}\lambda_{max})^{1/2}, \qquad (6.22)$$

where λ_{min} is the minimum wavelength in the turbulence and will be determined by the size scale over which the energy is dissipated in particle acceleration (Eilek 1982). Within the context of Eilek's model, λ_{min} will be given by the Larmor radius of the lowest energy electrons which are accelerated by the Alfven waves. Assuming that the spectrum of the particles extends to a frequency of 10^8 Hz, and using a magnetic field of 15 μG, gives $\lambda_{min} \simeq 1 \times 10^{11}$ cm. Taking $\lambda_{max} = 800$ pc as before, and $\kappa_D = 7 \times 10^{26}$ cm^2 sec^{-1}, gives $(\delta B/B_o)^2 \sim 30$. This will be a lower limit if the spectrum extends below 10^8 Hz. However, the model breaks down for $(\delta B/B_o)^2 \geq 1$ (i.e., the assumption that $\delta B < B_o$ is violated). Thus, it seems that this model also does not describe the conditions in the cocoon.

These two solutions bracket the desired range of parameter space, i.e., $\delta B \sim B$, which is necessary to produce the large amount of disorder in the field suggested by the low fractional polarization. If the magnetic field in the cocoon is indeed tangled due to turbulence, then the parameters of the turbulence are probably intermediate between the two cases considered here.

Particle acceleration in the external medium

An additional possibility for the origin of the cocoon is that it is formed by particles in the external medium which are accelerated through turbulence generated by instabilities in the jet/ISM boundary. In Eilek's (1982) model, the size scale of the acceleration region is comparable to the Larmor radius of the electrons ($\sim 10^{12}$ cm for particles radiating at 1.4 GHz) and is much smaller than the size of the cocoon (~2 kpc). Thus, the particles are also required to diffuse away from the jet to produce the observed cocoon. However, in this case, the injection spectrum of the particles is unknown and a diffusion speed cannot be directly inferred.

Is the cocoon part of the beams?

One possibility is that the cocoon is actually a low brightness part of the beam; i.e., the diffuse emission represents matter moving with bulk velocity v_b. In this picture, the bright ridge or jet is simply the luminous core of the beam. Several lines of argument suggest that this is not the case.

(1) If the difference in the observed extents of the cocoon around the two jets (a factor of ~3) actually represents a difference in the size of the beams, then this would require different densities and velocities in the two beams, since they have similar radio luminosities and bending scale lengths. The east beam would have a density smaller than the west beam by a factor of ~81 in the JO model and ~3 in the BRB model, and a velocity larger by a factor of ~9 and ~3 in the JO and BRB models, respectively. The BRB model is less sensitive to changes in the beam radius since the pressure gradient also scales as the beam radius. In the JO model, the pressure gradient is the radius of the ISM and is fixed, so changing the beam radius has a much more dramatic effect on the derived beam parameters.

It seems unlikely that beams with such different radii, velocities and densities would have similar radio luminosities and bending scale lengths. This suggests that the observed extent of the cocoons is irrelevant to the properties of the beams; or that the observed size of the cocoons are not simply related to their real size. This could be simply because the cocoons are external to and separate from the beams.

(2) If the cocoons were part of the beams, then the external pressure gradient should produce an asymmetric brightness profile or edge brightening. However, the edge brightening is seen only in the jets and not in the cocoons.

(3) The sudden change in total intensity, spectral index, and polarization at the jet/cocoon boundary is hard to explain if they are both parts of the same continuous fluid beam. The properties of the

beam should be smoothed out over a sound crossing time. Why is this boundary so well defined?

Thus, several lines of argument suggest that it is plausible that the cocoons are not part of the beams but are probably composed of particles from the jets which have diffused into a static external medium. The difference in the extent of the cocoons around the two jets may be due to a difference in the diffusion rate from the beams, though there is no a priori reason why this should be the case.

6.8 The Collimation Structure of the Jets

Since the beams are expected to be in pressure balance with the external medium, the variation of the internal pressure along the jets can be used to infer information about the properties of the external medium, and thus the mechanism responsible for the bending. In addition, within the context of the quasi-continuous beam models, the variation of the internal pressure and bending scale length with jet radius may give clues to the conditions within the jets themselves.

Ram pressure bending

The ram pressure bending model of BRB is based on the following simple assumptions (see also the discussion by Vallee, Bridle, and Wilson 1981, and Baan and McKee 1983). It is assumed that the total number density of particles flowing through the beam per unit time is conserved, i.e., $n_b r_b^2 v_b = \text{const}$; that the equation of state of the beam fluid is adiabatic, i.e., $P_b \propto n_b^\gamma \propto r_b^{-2\gamma} v_b^{-\gamma}$, where P_b is the

pressure in the beam and γ is the adiabatic index ($\gamma = 5/3$ for a nonrelativistic gas); and that the beam velocity is constant. The ram pressure on the beam then varies as $P \propto P_o \cos^2\phi$, where P_o is the pressure at the stagnation point (where the beam surface is perpendicular to the galaxy velocity) and ϕ is the angle between the normal to the beam surface at the stagnation point and the normal to the beam surface at any given point (i.e., $\phi = 0°$ at the stagnation point and $\phi \sim 70°$ at the end of the beam). In order for the beam to be bent the internal pressure must be comparable to the external ram pressure, i.e., $P_b \propto r_b^{-2\gamma} v_b^{-\gamma} \sim P \propto \cos^2 \phi$. Thus, the internal pressure in the beam decreases with increasing distance along the beam. A change in ϕ of ~70° requires a decrease in internal pressure of ~10. The internal pressure in the beam is uncertain; however, it is probably not much larger than the estimated minimum pressure, or else the beam would not be in pressure balance with the external ram pressure and would not be bent. The estimated change in internal pressure, assuming minimum pressure conditions in the jets, is roughly the required factor of ~10.

However, the jets expand by roughly a factor of ~6 over this distance. (Here it is assumed that the beam radius is roughly that of the bright jet.) If the beam velocity remains roughly constant then the pressure should drop by a factor of $\sim 6^{10/3} \sim 400$. This is clearly not observed and suggests that one or more of the assumptions of the model are incorrect. Various possible modifications to the basic model will be considered.

(1) One possibility is that the beam velocity is not constant. A decrease in beam velocity of $\sim 40^{3/5} \sim 9$ would be required to produce a

decrease in internal pressure of ~10. Using Euler's equation, the bending scale length, is given by $R \propto n_b r_b v_b^2 \propto v_b r_b^{-1}$, where the assumption that mass is conserved has been used. To some extent the bending scale length is defined only in the steady state, however, as a beam slows down and expands it will bend much faster. An increase in beam radius of ~6 and a decrease in beam velocity of ~9 would decrease the bending scale length by ~54, while a factor of < 2 is consistent with the data. This points out a basic contradiction with this set of assumptions. The velocity must decrease in order to satisfy the constraint on the pressure, yet the velocity must increase to satisfy the constraint on the bending scale length.

(2) Another possibility is that the assumption that the total number density is conserved is incorrect (e.g., entrainment occurs and momentum flux is conserved, $n_b r_b^2 v_b^2 = \text{const}$). In this case the internal pressure will vary as $P_b \propto r_b^{-2\gamma} v_b^{-2\gamma}$; i.e., the dependence of the pressure on the beam radius is the same as before, however, in this case, the velocity need only decrease by a factor of $40^{3/10} \sim 3$. The bending scale length is then given by $R \propto r_b^{-1}$ and is independent of velocity. Thus, an increase in radius of a factor of ~6 would correspond to a decrease in the bending scale length of ~6. This is an improvement over the previous situation, but is still not good enough.

(3) A third possibility is that the equation of state of the beam is non-adiabatic. This would be the case if kinetic energy is dissipated along the beam, which heats the gas and increases the pressure. Dissipation of the beam kinetic energy is also required in order to explain the very flat dependence of the intensity on the beam

radius (see Sec. 6.10). A slower dependence ($\gamma < 5/3$) of the pressure on the density is needed to explain the observations. $\gamma = 1$ (an isothermal jet) is not sufficient and still requires a large decrease in beam velocity and much greater changes in bending scale length than are observed. If either mass or momentum flux are conserved and if the velocity is roughly constant, then an index of $\gamma \simeq 0.6$ is consistent with the observed dependence of the pressure on the beam radius. However, the predicted bending scale length is still much too small. Using a value of $0 < \gamma < 0.6$ will require the velocity to increase in order to satisfy the constraint on the pressure. This will also reduce the problem of the observed bending radius being too large. However, it is not clear why the beam velocity should increase, especially since the beam is required to dissipate kinetic energy to reaccelerate particles.

(4) A fourth possibility is that the observed jet radius does not accurately represent the true beam radius. However, this only introduces another problem. The internal pressure, which is calculated using the observed jet radius, is consistent with the estimated external ram pressure. Using a different beam radius would result in a pressure which was inconsistent with the jet being in pressure balance with the external medium. Also, it was argued above that it is likely that the cocoon is not part of the beam, but is produced by the diffusion of relativistic particles from the jet into the ISM.

An additional argument against the BRB model is that the east jet is relatively straight between knot E2 and the first sharp bend in the jet. In the BRB model, the jet radius should be relatively constant over this region since the external pressure ($\propto \cos^2 \phi$) is also roughly

constant. However, the jet expands steadily over this region. This could be due to an increase in the internal pressure of the beam due to dissipation of the bulk kinetic energy. The dissipation of bulk kinetic energy should in turn bend the beam faster. Yet, the beam is relatively straight over this region. Since the beam has already been bent at knot E1, the lack of bending in this region cannot be due to the beam having a large Mach number. If anything, the dissipation of kinetic energy will heat the gas, raising the sound speed and lowering the Mach number.

Thus, the version of a ram pressure bending model suggested by BRB is based on assumptions which appear to be incorrect. None of the modifications suggested here are able to satisfactorily reconcile the discrepancies.

Bending in an ISM

In the JO model, both the curvature of the jets and the pressure in the jets will depend on the complex distributions of density, temperature, and velocity of the gas in the ISM. The numerical calculations of Lea and De Young (1976) illustrate the expected variation of the ISM properties within the galaxy. Unknown scaling factors are required to make a direct qualtitative comparison between the data and the model. The internal pressures obtained by Lea and De Young are less than $\sim 10^{-12}$ dynes cm^{-2} and are insufficient to confine the radio jets. However, these calculations suggest that there will be a drop in pressure by a factor of ~10 between the center and the edge of their model galaxy. This is consistent with the estimated variation in the internal pressure in the jets in NGC 1265. The velocity fields

calculated by Lea and De Young (1976), and Shaviv and Salpeter (1982) suggest an increase in the pressure gradients towards the edge of the galaxy. This is also consistent with the observed factor of ≤ 2 decrease in the bending scale length at the edge of the galaxy (~10 kpc from the core).

Also, the mostly steady expansion of the jets along their entire length is consistent with the radial pressure gradients expected in an ISM. Thus, the order of magnitude of the pressure gradient and the shape of the bending are consistent with the parameters of the ISM derived in the numerical models. However, as in the BRB model, the functional form of the variation of the internal pressure with beam radius depends on the equation of state of the gas, as well as which conservation laws are obeyed. If the same assumptions are made, the same problems are encountered. These considerations suggest the following results.

(1) The basic morphology of the source, the steady expansion of the jets, and the order of magnitude of the observed pressure gradient along the jets are consistent with the existence of an ISM. This result is also consistent with the assumption that the jets are in pressure balance with the external medium and adjust continuously to the changing external pressure.

(2) The basic assumptions about the conditions within the jets are incorrect. One possibility is that the usual assumption that the equation of state is adiabatic, i.e., $P_b \propto n_b^{\gamma}$, where $\gamma = 5/3$, is incorrect. In this case, the observations are more consistent with $\gamma \sim 0.6$. This would be consistent with significant dissipation of kinetic energy along the beam. The second possibility is that the

equation of state is adiabatic, but that neither mass flux nor momentum flux are conserved. In this case, the correct relationship between density, radius, and velocity is an open question.

The hypothesis that the beams are bent by some form of direct ram pressure bending cannot be totally ruled out by these considerations. However, the explicit model suggested by BRB is based on assumptions which are incorrect, and this version of the model must be ruled out. Alternative versions of ram pressure models should be considered.

6.9 Wiggles

The wiggles in the jets could be due to any of several possible causes (e.g., precession of the central collimator (Icke 1982), a helical instability (Hardee 1982), or a time dependent variation in the momentum flux in the beam (Baan and McKee 1983)).

Precession

Icke (1982) has fit the wiggles in the jets in 3C 129 (Rudnick and Burns 1982) with a simple ballistic model. The model ignores bending of the beams and instead requires the beams to be strongly decelerated by ram pressure, coming to rest over a time scale of $\sim 5 \times 10^6$ years (similar to the independent plasmon model, e.g., Jaffee and Perola 1973). Icke finds that a precession period of $\sim 9 \times 10^6$ years gives a good fit to the data. This is interesting because this suggests that the central engine/collimator is a solid body whose precession is due to another body (e.g., Begelman, Blandford, and Rees 1980).

Thus it is worthwhile to examine the possibility that the wiggles in NGC 1265 are also due to precession. This seems unlikely since near the nucleus the jets do not possess the S-shape produced by precession. Also the amplitude of the wiggles for the two jets are different. In addition, using arguments similar to those in Jones and Owen (1979), it can be shown that the ballistic model considered by Icke is inconsistent with the energetic requirements of the source since jets which are very strongly decelerated are unable to power the radio luminosity in the tails.

In a ballistic model for the jets in NGC 1265, the beams must be completely stopped by the time they reach a distance of ~10 kpc from the core since the distance between the jets remains roughly constant at this point. All the kinetic energy in the beam has then been transformed into internal energy. Some small fraction of this energy will be in a form which can be used to accelerate particles since much of the energy will be dissipated as heat in the external medium (Eilek 1979). The total internal energy in the beam at the stopping distance must be less than twice the initial kinetic energy since the beams are at least slightly transsonic (see Chap. VII). Then, the upper limit to the internal energy in a piece of stopped beam is given by twice the kinetic energy of an independent plasmon of similar size which has stopped at that distance. This internal energy must be sufficient to power the observed radio luminosity of the tails over the lifetime of the source given a reasonable efficiency for conversion of the internal energy into radio luminosity.

Owen, Burns, and Rudnick (1978) find that in order to fit the structure of NGC 1265, an initial plasmon kinetic energy of $E_p < 4x10^{54}$ ergs is required. It is assumed here that roughly $2E_p$, $8x10^{54}$ ergs, is deposited per kiloparsec of length of the source. This assumes that the galaxy velocity and energy output of the source have remained roughly constant over the lifetime of the source, which is consistent with the smooth intensity structure of the tails. After expansion by a factor of ~10 to form the tails, the internal energy is reduced to an internal energy per kiloparsec of $U_{int} \sim 8x10^{53}$ ergs kpc^{-1}. The observed radio luminosity per kiloparsec of the 210 kpc tail (averaged over the tail) is $L_{rad} \sim 10^{39}$ ergs sec^{-1} kpc^{-1} (Miley et al. 1975). In order to provide the observed radio luminosity over the lifetime of the source, t_s, the internal energy must satisfy $U_{int} \simeq t_s L_{rad} \varepsilon^{-1}$, where ε is the efficiency of the conversion of the internal energy into radio luminosity. Taking $U_{int} = 2x10^{53}$ ergs kpc^{-1}, $L_{rad} = 10^{39}$ ergs sec^{-1} kpc^{-1}, and a source lifetime, given by the 210 kpc projected length of the tail divided by the ~3000 km sec^{-1} galaxy velocity, of $t_s = 2x10^{15}$ sec requires an efficiency of $\varepsilon \sim 3$, i.e., 300%. This is probably at least a factor of ~300 too high (e.g., Eilek 1979).

The radio luminosity in the tails can only be provided by beams which have a high velocity as they enter the tails (BRB) or by a turbulent galactic wake (JO). However, the existence of an ISM is inconsistent with Icke's model, which requires that the beams interact directly with the ICM in order to produce a ballistic trajectory. Thus, the simple ballistic precession model suggested by Icke (1982) cannot

explain the wiggles in NGC 1265. Precession per se is not ruled out, but is probably unlikely based on the symmetry of the jets. However, a hydrodynamic model should be considered.

Helical instability

The development of Kelvin-Helmholtz instabilities in radio jets has been considered by Benford (1981); Cohn (1983); Ferarri et al. (1978, 1981, 1982) Fiedler and Jones (1983); Hardee (1979, 1982, 1984); and Ray (1981, 1982). In particular, the case of a helical (or fire hose) instability in a gradually expanding jet (which seems relevant to NGC 1265) has been studied by Hardee (1982, 1984). He finds that the helical wavelength, λ_h, which grows fastest is given by

$$\lambda_h/r_b = 4.2M/\{1 + \zeta^{1/2}\} - 2.5 \ , \qquad (6.23)$$

where M is the Mach number, r_b is the beam radius; and $\zeta = n_b/n_{ext}$, where n_b and n_{ext} are the beam and external particle densities, respectively. This expression might predict λ_h to within about a factor of two (if propagation effects are not important), but may not apply to bent beams (Hardee 1983, private communication). One additional problem is that only about half a wavelength is visible in the jets, but a rough estimate gives $\lambda_h/r_b \sim 12$. Then for the case of an ISM (JO), taking M = 2 gives $n_b \sim 0.2\ n_{ism}$; and taking M = 3 gives $n_b \sim 0.02\ n_{ism}$. (M = 1 is outside the range of parameter space over which equation 6.23 is valid.) If the external density in the ISM is $n_{ism} < 0.3$ cm^{-3} (from the constraints on the Hα luminosity), then the required beam particle density is $n_b < 5\times10^{-2}$ cm^{-3} for M = 2, and $n_b < 5\times10^{-3}$ cm^{-3} for M = 3.

As both of these limits are higher than the upper limit derived from the lack of depolarization, a stronger limit on ISM density would be useful.

For the case of a naked jet (BRB), taking M = 5 also gives $n_b \sim 0.2\ n_{icm}$. If the external density in the ICM is $n_{icm} \simeq 5\times10^{-4}$, then the beam particle density is $n_b \sim 10^{-4}$ cm^{-3}, which is well below the limit imposed by the polarization. In fact, requiring $n_b < 2\times10^{-3}$ cm^{-3} gives an upper limit to the beam Mach number of $M < 10$. Although it is not yet clear that this analysis is applicable, it is interesting that the numbers look reasonable for the case of the naked jet and that the jets turn out to be less dense than the external medium.

Variations in momentum flux

Another possibility is that the wiggles are due to changes in the jet momentum flux (Christiansen, Pacholczyk, and Scott 1981; Baan and McKee 1983). From Euler's equation (see Chap. VII), the momentum flux in the beam is directly proportional to the bending scale length, i.e.,

$$\rho_b v_b^2 \propto R. \tag{6.24}$$

Thus, a decrease in momentum flux results in a decrease in the bending scale length. Variation in the beam momentum flux would result in slightly different trajectories for different pieces of the beam, resulting in apparent wiggles (Baan and McKee 1983). The observed amplitude of the wiggles is about ~5% of the bending scale length, R. Thus, variations in momentum flux of ~5% (eq. 6.24) are required to account for the observed oscillations. One way to vary the momentum flux is simply to eject multiple plasmons into a channel in the ISM

(CPS). This would naturally produce variations in the bending scale length of the channel.

There are, however, two potential problems with this model. One problem arises if the change in momentum flux is due to a change in the energy output of the central engine. Then, if the variation in momentum flux of both jets is comparable, the wiggles might be expected to be roughly symmetric, since the change in the bending scale length would be roughly the same for each jet. This is clearly not the case, so some asymmetry in the energy output of the central engine or some environmental effect may be required. Unequal dissipation of energy along the jets is unlikely since the two jets have roughly equal brightness distributions and radio luminosities. The second potential problem is that if the variations in the bending scale length are larger than the beam radius, this becomes a ballistic model. The individual pieces of the beam will interact independently with the external medium and the independent plasmon model becomes relevant. However, the independent plasmon model has been ruled out for the case of NGC 1265 by JO. The amplitude of the wiggle at the end of the west jet is just large enough that this might be a problem.

6.10 Particle Acceleration in the Jets

The dependence of the intensity on the jet radius can be used to infer the existence of particle acceleration in the jets. The variation of the peak surface brightness with jet FWHM, Φ, for the east and west jets is shown in Figure 6.2. Except for a "spike" in brightness at the

Figure 6.2

The peak intensity along the jet vs. the deconvolved gaussian FWHM for the east (top) and west (bottom) jets.

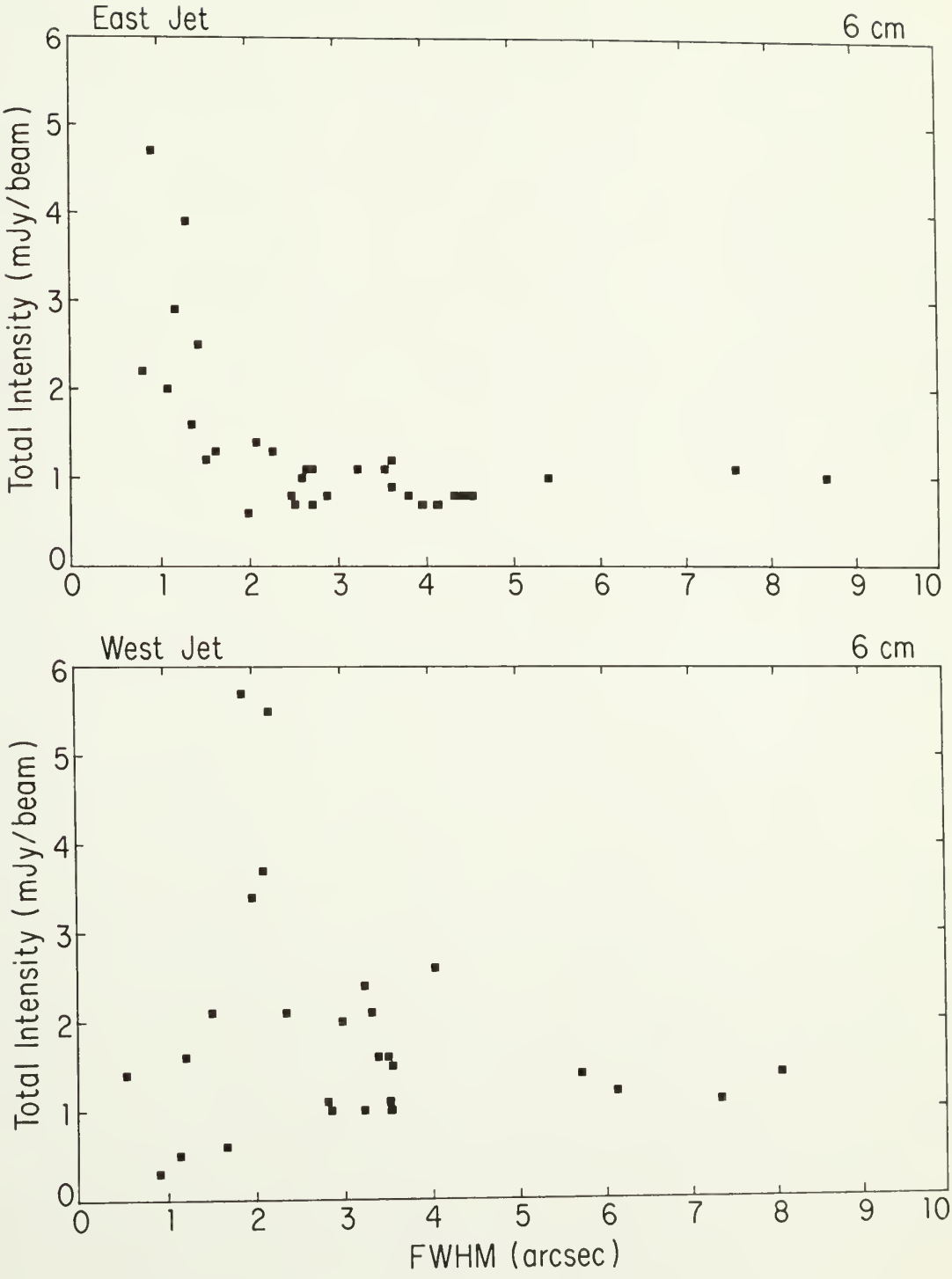
East Jet
6 cm
Total Intensity (mJy/beam)
0
1
2
3
4
5
6
0
1
2
3
4
5
6
7
8
9
10
West Jet
6 cm
Total Intensity (mJy/beam)
FWHM (arcsec)

positions of the knots E1-E2 and W2-W3, the brightness varies very slowly with FWHM and is very flat. For the east jet, $I_\nu \propto \phi^{-0.6}$ (using all the points) and $I_\nu \propto \phi^{-0.2}$ (if the knots E1 and E2 are ignored). For the west jet $I_\nu \propto \Phi^{0.1}$ (using all points) and $I_\nu \propto \Phi^{0.3}$ (if W2-W3 is ignored); i.e., the intensity increases with increasing FWHM. This increase of intensity with FWHM is also seen in the bright jet in NGC 6251 (Perley et al. 1984). The intensity, I_ν, of transparent synchrotron radiation from a power law distribution of electron energy $N(E) = N_o E^{-q} dE$, in a jet of radius, r_b (where $r_b \propto \Phi$) is

$$I_\nu \propto N_o B^{(q+1)/2} r_b \tag{6.25}$$

(e.g., Pacholczyk 1970). Following Perley et al. (1984), the effects of adiabatic expansion and magnetic flux conservation on the intensity of an expanding jet will be considered. Integrating the relativistic electron density between the upper and lower energy cutoffs, E_u and E_l, gives the total number density of relativistic particles, N_t, i.e., $N_t \propto N_o[E_l^{1-q} - E_u^{1-q}]$ and

$$N_o \propto N_t E_l^{q-1} \ , \tag{6.26}$$

if $q > 1$ and $E_u \gg E_l$. If the total number density of radiating particles is conserved $N_t \propto v_b^{-1} r_b^{-2}$. The change in particle energy due to adiabatic expansion or contraction of the volume occupied by the relativistic particles in the jet is $E \propto r_b^{-2/3} v_b^{-1/3}$. This gives

$$N_o \propto r_b^{-(2q+4)/3} v_b^{-(q+2)/3}. \tag{6.27}$$

Then, for a jet where the magnetic field is mostly parallel to the jet

axis, combining equations 6.6, 6.25, and 6.27 and taking an electron energy index of $q = (1-2\alpha) = 2/3$ ($\alpha = -0.65$) gives

$$I_\nu(r_b) \propto r_b^{-(q+2)/3} v_b^{-(5q+4)/3} \propto r_b^{-1.43} v_b^{-5.17} \qquad (6.28)$$

and for a jet where the magnetic field is mostly perpendicular to the jet axis, combining equations 6.7, 6.25, and 6.27 gives

$$I_\nu(r_b) \propto r_b^{-(7q+5)/6} v_b^{-(5q+7)/6} \propto r_b^{-3.08} v_b^{-3.52}. \qquad (6.29)$$

If the beam velocity is constant, then the intensity would decline much faster with increasing radius than the observed very flat dependence. If the velocity is not constant, a variation of $I_\nu \propto r_b^{-0.5}$ (observed in the east jet) would be produced if $v_b \propto r_b^{-3.26}$ for $B_\parallel$ or $v_b \propto r_b^{-0.98}$ for $B_\perp$. Since the jets expand by a factor of ~5 over the $B_\parallel$ region, this would require a decrease in velocity of a factor of ~200. This is very unlikely because of the very gradual bending over this region. From Euler's equation, the bending scale length is given by $R \propto \rho_b v_b^2 h$, where h is the scale height of the external pressure gradient, and ρ_b is the mass density of the beam (see Chap. VII). If the total number density is conserved as the jet slows down and expands, then $\rho_b \propto r_b^{-2} v_b^{-1}$ and $R \propto v_b r_b^{-2} h \propto r_b^{-5.26}$ (assuming $v_b \propto r_b^{-3.26}$; i.e., $I_\nu \propto r_b^{-0.5}$) for a jet in an ISM and $R \propto r_b^{-4.26}$ for a naked jet ($h \sim r_b$). Thus a change in r_b of a factor of ~5 would result in a change in R of at least ~1000, which is clearly not observed.

If the beam slows down due to entrainment of matter from an external medium and momentum flux is conserved (i.e., $\rho_b v_b^2 r_b^2 = \text{const}$) then $R \propto h r_b^{-2}$ for a jet in an ISM or $R \propto r_b^{-1}$ for a naked jet. This is

not as extreme as the previous case, but still requires very large changes in the bending scale of ~25 or ~5, respectively, which are not observed.

Thus the observed I_ν vs. r_b relationship cannot be due simply to a change in beam velocity. The alternative is that if the beam velocity is roughly constant, either particle acceleration compensates for adiabatic losses and/or amplification of the magnetic field compensates for the effects of magnetic flux conservation. It will be argued that both are required.

For the case where adiabatic losses are unimportant, i.e., $E \propto v_b^{-1/3}$ (no dependence on r_b), equations 6.28 and 6.29 become

$$I_\nu(r_b) \propto r_b^{-(q+2)} v_b^{-(q+2)/3} \propto r_b^{-4.30} v_b^{-1.43} \tag{6.30}$$

$$I_\nu(r_b) \propto r_b^{-(q+3)/2} v_b^{-(5q+7)/6} \propto r_b^{-2.65} v_b^{-3.08} \tag{6.31}$$

for $B_\parallel$ and $B_\perp$, respectively. For the case where the magnetic field remains constant as a function of radius, i.e., $B_\parallel \sim$ const and $B_\perp \propto v_b^{-1}$, equations 6.28 and 6.29 become

$$I_\nu(r_b) \propto r_b^{-(2q+1)/3} v_b^{-(q+2)/3} \propto r_b^{-1.87} v_b^{-1.43} \tag{6.32}$$

$$I\nu(r_b) \propto r_b^{-(2q+1)/3} v_b^{-(9q+7)/6} \propto r_b^{-1.87} v_b^{-4.62} \tag{6.33}$$

for $B_\parallel$ and $B_\perp$, respectively. If the beam velocity remains roughly constant (as argued above), then <u>all</u> of these equations predict too steep a decline of I_ν with r_b. Neither neglect of adiabatic losses nor violation of conservation of magnetic flux by itself can reproduce the observed behavior. This suggests that both <u>in situ</u> particle

acceleration and amplification of the magnetic field must occur all along the jets in NGC 1265.

6.11 The Flat Spectrum Knot W1

The flattening of the spectrum of knot W1 between 6 and 2 cm is very unusual and puzzling (see Sec. 5.2 and Fig. 5.16). The spectrum is suggestive of the composite spectrum of some quasars which contain both a self-absorbed compact core and steep spectrum extended structure. It appears that W1 consists of two spectral components, a steep spectrum component (consistent with the typical jet spectrum), and an additional component which has a low frequency turnover (i.e., peak) near or above a wavelength of 2 cm. In this section the nature of the component with the inverted spectrum is examined and various possible physical mechanisms for producing the spectrum are considered.

HII region

One possibility is that the knot is an HII region. Hardee, Eilek, and Owen (1980) have suggested that in the galaxy NGC 7385 (2247+11) there is an HII region associated with a radio feature which could be a knot or lobe. The observed intensity at 2 cm can be used to set limits on the thermal electron density required to produce such an HII region. The monochromatic power, P_ν, due to thermal bremsstrahlung from a spherical HII region with radius R_{HII} would be

$$P_\nu = S_\nu D^2 4\pi = (1/3)\ (4\pi)^2 j_\nu R_{HII}^3 \ , \qquad (6.34)$$

where S_ν is the flux density at frequency ν, D is the distance to the source, and j_ν is the free-free emissivity at frequency ν. Then using the expression for the free-free emissivity given by Spitzer (1978, p. 57), and assuming that the HII region is fully ionized hydrogen, gives (using cgs units)

$$n_e \simeq [4.4\times10^{37} S_\nu D^2 T^{1/2} R_{HII}^{-3} g_{ff}^{-1}]^{1/2} , \qquad (6.35)$$

where g_{ff} is the gaunt factor ($g_{ff} \simeq 1.3$ at $T \sim 10^4$ K). Then assuming $T = 10^4$ K and using $S_\nu = 1.34$ mJy, and $R_{HII} < 120$ pc, gives $n_e > 200$ cm^{-3}. The predicted Hα luminosity, at a temperature of 10^4 K, is given by

$$L_{H\alpha} = 2.3\times10^{-21} n_e^2 R_{HII}^3 T^{-0.8} \text{ ergs sec}^{-1} \qquad (6.36)$$

(Spitzer 1978, p. 89) and is $L_{H\alpha} \simeq 3\times10^{42}$ ergs sec^{-1}, which is two orders of magnitude larger than the current upper limit for the entire galaxy (Gisler and Butcher, 1983). The pressure in the HII region is $nkT > 3\times10^{-10}$ dynes cm^{-2}, which is higher than any pressure available in the ISM to confine the knot. The predicted Hα luminosity can be reduced by raising the temperature of the gas. A temperature of $T \sim 10^7$ K and a corresponding density of $n \sim 1\times10^3$ cm^{-3} are required in order to produce the observed flux density at 2 cm without producing too much Hα luminosity. However, the required particle density is a factor of $\sim10^6$ higher than the upper limit to the particle density with the jets. Thus, a mechanism for producing a particle density which is much higher than any available ambient density is required. The pressure in the HII region is then $nkT \simeq 10^{-6}$ dynes cm^{-2}, which is a factor of $\sim3\times10^5$ higher

than that in the radio jets or in the ISM. The next sections will consider the possibility that the component with the inverted spectrum between 6 and 2 cm is a synchrotron component with a low frequency turnover due to an external or otherwise special absorption mechanism.

Free-free absorption

Another possibility is that the low frequency turnover is due to free-free absorption from thermal particles either mixed in with the relativistic electrons or in front of them. Both situations require similar emission measures, though their frequency dependences below the turnover are very different (e.g., Pacholczyk 1977, Melrose 1980). Then using the standard equation for the free-free opacity (Spitzer 1978, p. 57) and requiring an opacity of ~1 at 6 cm predicts an emission measure of $n_e^2 L \simeq 9 \times 10^7$ cm^{-6} pc for T = 10^4 K. Using a higher temperature results in an even higher emission measure. If the path length is comparable to the knot radius (i.e., L ≃ 120 pc), then $n_e \simeq$ 900 cm^{-3}. Such a high particle density would violate the constraints on the Hα luminosity. The particle density can be reduced by increasing L since $n_e \sim L^{-1/2}$, however, this cannot give much of an improvement since L cannot be made much larger than the knot itself (a factor of $\sim 2^{1/2}$ improvement). This is because if the entire knot is covered, the steep spectrum component would also be cut off and the knot would also be completely depolarized. In addition, this density is already four times more than is needed to account for the knot with an HII region.

Synchrotron self-absorption

If the core had ejected a compact energetic object (e.g., Valtonen and Byrd 1980), it might have a self-absorbed spectrum. Alternatively, conditions in the jet might be such that the radiation could become self-absorbed. The magnetic field of a self-absorbed synchrotron component is given by

$$B = 2.85\times10^{-5}\ \nu_m{}^5\theta^4 S_m{}^{-2}\ \text{gauss}\ , \qquad (6.37)$$

where ν_m is the frequency at the spectral peak in gigahertz, θ is the angular width in milliarcseconds (mas), and S_m is the flux density in jansky at the spectral peak. Taking ν_m = 15 GHz, $S_m = 1.34\times10^{-3}$ Jy, and choosing θ = 1 mas, which is typical of compact energetic objects (e.g., Kellermann and Pauliny-Toth 1981) gives $B \simeq 10^7$ G, which corresponds to a pressure $B^2/8\pi \simeq 6\times10^{12}$ dynes cm^{-2}, which are implausible conditions for radio knots. Taking a value for θ closer to the upper limit of 0."7 from the VLA observations results in much more extreme conditions. However, such a high field could presumably be bound to a massive object.

Less extreme conditions are obtained by using a smaller angular size for the component. The lower limit to the angular size obtained by requiring the brightness temperature to be less than 10^{12} K (due to inverse Compton quenching) is

$$\theta > 0.03\ S_\nu{}^{1/2}\ \lambda_{mas}\ , \qquad (6.38)$$

where S_ν is the flux density in jansky and λ is the observing wavelength in centimeters (O'Dell et al. 1978). Taking $S_\nu = 1.34\times10^{-3}$ Jy and λ =

2 cm gives the extremely small size $\theta > 2\times10^{-3}$ mas ($\sim2\times10^{15}$ cm $\sim$ 140 AU.) This results in a magnetic field (eq. 6.37) of $B > 2\times10^{-4}$ G and a pressure $B^2/8\pi > 2\times10^{-9}$ dynes cm^{-2} which are both high compared to the typical values, but not as extreme as other possibilities. These conditions might not be unexpected if an ejected compact object continued to accelerate particles and amplify the magnetic field in its vicinity. Another possibility is that the region is moving relative to the bulk velocity of the beam and is confined by ram pressure. Taking a beam particle density of $n_b \sim 10^{-4}$ cm^{-3} gives a velocity of $v \sim 0.1c$.

The Tystovich-Razin effect

If there are sufficient thermal particles mixed in with the relativistic particles, the Tystovich-Razin effect will cause the spectrum to be cutoff below a frequency given by $\nu_R \simeq 20\ n_e/B$ (e.g., Pacholczyk 1977, p. 65). Using $\nu_R = 5\times10^9$ Hz, and B = 25 μG, requires $n_e \simeq 6200$ cm-3, which is a factor of $\sim10^6$ higher than the upper limit to the thermal particle density in the jet. The required particle density is also higher than that needed to produce the observed spectrum using an HII region. The dominant effect would be that of the addition of the free-free emission to the spectrum. Thus, it is unlikely that the Tystovich-Razin effect is responsible for the observed spectrum.

Cutoff to electron spectrum

If the low energy cutoff to the relativistic electron spectrum occurs at an energy, E, there will be a cutoff in the synchrotron spectrum below a frequency given by $\nu_c \simeq 6.27\times10^{18}\ B\ E^2$ (e.g.,

Pacholczyk 1970, p. 85). For $\nu_c = 15 \times 10^9$ Hz and B = 25 μG, $\Gamma = E/m_e c^2 \simeq 7 \times 10^3$, which is a fairly high energy for a low energy cutoff. Below ν_c the flux density, $S_\nu \propto \nu^{0.3}$. Observations at higher frequencies are needed to test this hypothesis since the spectrum of the "flat" component is not known.

Induced Compton scattering

Another possibility is that induced Compton scattering from thermal electrons either mixed in with the relativistic electrons or else just in front of them will cause a turnover in the spectrum (Sunyaev 1970, 1971). Heating of the nonrelativistic electrons results in a transfer of photons from higher to lower frequencies. The change with time of the spectrum $I(\nu)$ due to this process is given by

$$dI(\nu)/dt = 4\pi\sigma_T n_e c \nu m_e^{-1} \left[d(I(\nu)/\nu)^2/d\nu \right] , \qquad (6.39)$$

where σ_T is the Thomson scattering cross-section, n_e is the electron density, and m_e is the electron mass (Melrose 1980, p. 101). In the steady-state this process is balanced by emission from the source with a frequency dependence given by $I_s(\nu) = I_o \nu^\alpha$; i.e., $dI(\nu)/dt \propto \nu^\alpha$ and this process is important at low frequencies. Adding this term to the right-hand side of equation 6.39 and setting $d_I(\nu)/dt = 0$ gives $I(\nu) \propto \nu^{1+\alpha/2}$ below the turnover in the spectrum.

In order to produce the observed spectral turnover in W1, a large opacity (i.e., $\sigma_T r n_e > 71$, where r is the source radius) is required. Then the electron density is given by

$$n_e = [\nu_b{}^{2-\alpha} 32\pi^2 m_e / \{3(1-\alpha) r P_o\}]^{1/3} / (\sigma_T) \qquad (6.40)$$

(in cgs units) where ν_b is the frequency at the peak in the spectrum, m_e is the electron mass, α is the spectral index above the turnover, and P_o is defined such that $P_\nu = P_o \nu^\alpha$ is the spectral power (Sunyaev 1971). Note that here $\alpha < 0$ contrary to Sunyaev's usage and equation 6.40 for n_e has been altered to take this into account. Then for ν_b = 15 GHz, r = 120 pc, α = 0.65, S_ν = 1.34 mJy, and $P_o = S_\nu\, 4\pi\, D^2 \nu_b{}^{-\alpha}$, the required particle density is $n_e \simeq 2\times10^6$ cm^{-3}. Such a high particle density would produce too much free-free emission at 2 cm (eq. 6.34) unless the temperature was implausibly high ($T > 5\times10^{19}$ K).

Plasma frequency

The turnover in the spectrum might be caused by a very high plasma frequency if the thermal particle density were high enough (i.e., $n_e \simeq [2\pi\nu_b/5.6\times10^4]^2$, e.g., Pacholczyk 1970, p. 54). However, for a plasma frequency of 15×10^9 Hz a thermal particle density of 3×10^{12} cm^{-3} is required which is again much too high. The free-free emission would dominate for any plausible value of the temperature.

Cyclotron absorption

The possibility that the low frequency cutoff seen in some synchrotron sources is due to cyclotron absorption was suggested by O'Dell and Sartori (1970). They point out that all of the electrons in a synchrotron source radiate most of their energy at frequencies above the cyclotron frequency. Since the radiation at frequencies below the

cyclotron frequency is due to the low frequency emission tail of the highest energy electrons, this provides a natural cutoff to the synchrotron spectrum. The cutoff frequency is given by $\nu_b \simeq 3 \times 10^6 B/\xi$ Hz, where B is the magnetic field in gauss, and ξ is the average value of $\sin\Psi$, and Ψ is the electron pitch angle. A cutoff frequency of 15 GHz requires $B/\xi \simeq 1.6 \times 10^3$ G, which seems much too high.

Particle acceleration

Eilek and Henriksen (1984, EH) have investigated the particle energy spectrum produced through turbulent acceleration in radio sources. They consider the case where fluid turbulence in radio sources produces Alfvén waves through the Lighthill radiation mechanism (see Henriksen, Bridle, and Chan 1982). Resonant acceleration of the particles by the Alfvén waves is expected to boost them to relativistic energies. EH find a stable solution where the particle energy distribution goes to an asymptotic form which corresponds to a synchrotron spectral index in the range -0.5 to -1.0. In addition, they find that the solution is unstable to occasional, short time scale perturbations which temporarily flatten the spectral index. These flattenings of the spectrum will last for the particle radiative loss time scale.

Particle acceleration would thus provide a possible mechanism for producing the flattened spectral index observed in knot W1. The very flat dependence of the intensity on the jet radius suggests that some form of particle acceleration is needed throughout the jets. The steep spectrum between 21 and 6 cm could be produced by more "normal" jet

material surrounding the knot. Thus, this mechanism would not have to reproduce the kink in the spectrum at 6 cm. However, the inverted spectrum between 6 and 2 cm would have to be reproducible by such a model. One possiblity is that there is a low energy cutoff to the electron energy spectrum produced by the acceleration.

One problem with this idea is that the high energy electrons will contribute greatly to the internal pressure, P_{int}. The maximum allowable internal pressure will require an upper energy cutoff in the electron distribution. The expressions for the radio luminosity, minimum pressure, magnetic field, and relativistic particle energy (equations 6.1, 6.2, 6.3, and 6.4) can be rearranged to give:

$$\nu_u \simeq [6.7\text{x}10^{30} P_{min}^{7/4} V(1+\alpha)(1+z)^{1/2}/\{S_o \nu_o^{-\alpha} D^2\} + \nu_l^{(1+\alpha)}]^{1/(1+\alpha)} \text{ Hz}, \quad (6.41)$$

where ν_u and ν_l are the corresponding upper and lower frequency cutoffs in hertz, S_o is the flux density (in jansky) at a frequency, ν_o (in hertz), D is the distance to NGC 1265 (in megaparsecs), V is the source volume (in kpc^3), and α is the spectral index. For $\nu_l = 10^8$ Hz (the exact value is not important if $\alpha > -1$), $\alpha = -0.05$, and taking the other parameters appropriate to W1 gives an upper frequency cutoff of $\nu_u \simeq$ 10 GHz if $P_{min} = 10^{-10}$ dynes cm-2, and $\nu_u \simeq$ 100 GHz if $P_{min} = 3.5\text{x}10^{-10}$ dynes cm^{-2}. Choosing a more inverted spectrum ($\alpha > -0.05$) only increases the pressure. Thus, in order to produce the observed emission at 15 GHz the internal pressure must already be higher than any external pressure available to confine the knot. This result is independent of the particle acceleration mechanism. This suggests that

the knot is out of pressure balance and is expanding at the sound speed. This will result in significant adiabatic losses over the sound crossing time, t_c. In that case, the flat spectrum component in the knot will be observable roughly for the smaller of either the sound crossing time of $t_c > 2000$ years (assuming $c_s = 0.2c$ as an upper limit) or the radiative loss time which is $t_l \simeq 10^6$ years for particles radiating at 15 GHz in a 25 μG field (eq. 6.5). Then within the context of the model of EH, the particle acceleration time scale t_a must be smaller than this minimum time scale. At present there are no theoretical considerations which would prohibit an acceleration time scale as small as 2000 years (Eilek 1983, private communication).

In the EH model, particles of a given energy are accelerated by turbulence (i.e., resonant Alfvén waves) of a particular wavelength,

$$\lambda_t = 2\pi\Gamma m_e c^2/eB \ , \tag{6.42}$$

where e is the electron charge, m_e is the electron mass, c is the speed of light, Γ is the Lorentz factor, and B is the magnetic field. Thus, the maximum particle energy corresponding to the upper frequency cutoff is constrained by the largest size scale of the turbulence. The particle energy is given by

$$E = \Gamma m_e c^2 = c\nu_G m_e \lambda_t/2\pi \ , \tag{6.43}$$

where ν_G is the electron gyrofrequency. Electrons of energy $\Gamma m_e c^2$ radiate at a characteristic frequency given by

$$\nu_c \simeq 6.27\times10^{18} B(\Gamma m_e c^2)^2 \qquad (6.44)$$

(e.g., Pacholczyk 1970, p. 85). Substituting equation 6.43 into 6.44 gives

$$\nu_c \simeq 3.6\times10^{-2} B^3 \lambda_t^2 \text{ Hz} , \qquad (6.45)$$

where B is in gauss, and λ_t is in centimeters. The Lorentz factor of electrons, whose characteristic frequency (in a 25 μG field) is 15 GHz, is $\Gamma \simeq 10^4$. These electrons would be accelerated by turbulence with a size scale of $\lambda_t \simeq 5\times10^{12}$ cm $\simeq$ 0.3 AU, which is much smaller than the 120 pc radius of the knot. The largest wavelength in the turbulence is expected to be roughly the Taylor scale, $\lambda_T \simeq r_b(15/Re)^{1/2}$, where r_b is the jet radius and Re is the Reynolds number (EH). The Reynolds number in a turbulent radio jet is uncertain, but values in the range $\sim10^7$-10^{11} have been suggested (Henriksen, Bridle, and Chan 1982, EH). Taking Re = 10^{11} gives $\lambda_T \simeq 10^{16}$ cm, and the flat spectrum should extend to much higher frequencies ($\nu_c \simeq 6\times10^{16}$ Hz). Thus it would be interesting to know whether the flat spectrum extends to a wavelength of 1.2 cm. The HII region model should also extend with a flat spectrum to higher frequencies, while all the absorption models should eventually steepen to $\alpha \sim -0.65$ above 2 cm.

At this point, there are three possible explanations for the spectrum of knot W1 which require the relatively least implausible conditions: a self-absorbed synchrotron component associated with a compact (~140 AU) object; a hot ($T \sim 10^7$ K), dense ($n \sim 1\times10^3$ cm^{-3}) HII region; and particle acceleration which produces a flat spectrum electron population with a low energy cutoff. For all three mechanisms,

there is the problem with the internal pressure being too high, though this may not be a problem if the possibility that the knot is a transient phenomenon is allowed. In that case, the probability that the knot would be seen at all is very small. Alternately, the high pressure could be maintained in a steady state by, e.g., heating of the thermal gas, or continuing particle acceleration and magnetic field amplification by turbulence, shocks, and/or a compact object.

6.12 Summary

The observations of NGC 1265 have been interpreted within the framework of current models for radio jets; i.e., the jets represent the radio emission from quasi-continuous beams composed of thermal particles, relativistic particles (electrons and protons), and magnetic fields. The observations are consistent with this general picture and the results are the following.

6.1. The bulk velocity of the beam is nonrelativistic, $v_b < 0.2c$, (see Chap. VII), and the beam is at least slightly transsonic ($M \sim 1\text{-}5$). Thus the equation of state of the beam fluid is nonrelativistic; i.e., the thermal particles greatly outnumber the relativistic particles.

6.2. The polarization structure of the jets is consistent with that produced by an initially tangled magnetic field which has been sheared tangentially to the beam surface (cf. Laing 1981).

6.3. Within the context of the homogeneous cylinder model of Cioffi and Jones (1980), the upper limit to the thermal particle density is $n_e < 1 \times 10^{-3}$ cm^{-3}.

6.4. The differential rotation measure structure along the jets appears to be due to a foreground screen which is most likely located either in an ISM or in a sheath around the jets. If the RM is due to the ISM, then for a magnetic field of 1 μG the required electron density is 4×10^{-3} cm^{-3}, which is a factor of ~10 higher than that in the ICM.

6.5. The steep spectrum radio cocoon around the jets (seen at 21 cm) is consistent with diffusion of relativistic electrons from the jets into a static external medium with a tangled magnetic field. It is unlikely that the cocoon represents a low brightness part of a continuous beam.

6.6. Both the RM structure, the collimation structure, and the existence of the radio cocoon around the jets are most easily explained if NGC 1265 possesses an ISM. Combining the X-ray, optical, and radio data results in a radius of $r_s \sim 10$ kpc, a density of $n_e \leq 0.3$ cm^{-3}, a temperature of $T \geq 8 \times 10^5$ K, and a magnetic field of $0.01\ \mu G < B < 30\ \mu G$.

6.7. The wiggles are roughly consistent with helical instabilities in beams which are slightly transsonic and are less dense than the external medium. A simple ballistic precession model (Icke 1982) cannot account for the energetic requirements of the radio tails. It is unlikely that variations in momentum flux are responsible for the wiggles.

6.8. The data are consistent with the jets (except for knot W1) being in pressure balance with the external pressure. This suggests that the conditions in the jets are close to those of minimum pressure. This also suggests that the contribution of the thermal particles is negligible.

6.9. Both in situ particle acceleration and amplification of the magnetic field are required all along the jets in order to explain the very flat variation of surface brightness with radius.

6.10. The observed variation of pressure and bending scale length with beam radius are in conflict with the simple assumptions of the BRB model. A non-adiabatic equation of state is consistent with the data with $P_b \propto n_b^{0.6}$. This may be a result of the dissipation of kinetic energy along the beam.

6.11. The flat spectrum of knot W1 between 6 and 2 cm is roughly consistent with an electron population with a flat energy spectrum and low energy cutoff produced by in situ particle acceleration (Eilek and Henriksen 1984). If the flat spectrum extends much above 15 GHz, the knot cannot be confined by the available external pressure. Other possibilities (which also require the knot to be out of pressure balance) include a self-absorbed synchrotron component associated with a compact, massive object; and a hot, dense HII region.

CHAPTER VII

LIFE, THE UNIVERSE, AND EVERYTHING

In this chapter the physics which may be applicable to the bending of quasi-continuous beams in Narrow Angle Tailed sources (NATs) is discussed in detail. Constraints are placed on the velocity, particle density, and efficiency of continuous beams and plasmons in a channel. The general results of the thesis are summarized and directions for future research are discussed.

7.1 The Physics of Bent Beams

The constraints on the energy and momentum flux in bent radio beams in NATs may provide important insight into the physical conditions within the beams. For this reason, the physics of bent radio luminous beams is discussed here in great detail. The constraints are combined to derive limits on the bulk velocity, Mach number, particle density, and efficiency of conversion of bulk kinetic energy into radio luminosity of quasi-continuous beams and plasmons in a channel. The basic equations are derived, and their inherent assumptions and limitations are examined. The three basic models are reviewed and the allowed parameter space is examined. A detailed comparison of the models is made.

Following Baan (1980), the term jet will refer to the observed radio structure, and the term beam will refer to the postulated flow.

The beam energy flow

The total energy density, U_{tot}, (in ergs cm^{-3}) of a unit volume of fluid in a beam of mass density, ρ_b, and nonrelativistic bulk velocity, v_b, consists of three components, the kinetic energy density, the internal energy density, U_{int}, and the rest mass energy, i.e.,

$$U_{tot} = (1/2)\rho_b v_b^2 + U_{int} + \rho_b c^2. \qquad (7.1)$$

For a radio luminous beam, the internal energy density is given by

$$U_{int} = B^2/8\pi + E_{rel}/V + (3/2)\, nkT, \qquad (7.2)$$

where B is the magnetic field, E_{rel} is the energy in relativistic particles (see Chap. VI), V is the volume, n and T are the thermal particle density and temperature, and k is the Boltzmann constant. The change of U_{tot} with time from conservation of energy (but ignoring minor sinks and sources such as radiative cooling) is given by:

$$\partial(U_{tot})/\partial t = -\nabla \cdot [v_b\, ((1/2)\, \rho_b v_b^2 + U_{int} + P_{int} + \rho_b c^2)], \qquad (7.3)$$

(Landau and Lifshitz 1959), where

$$P_{int} = B^2/8\pi + (1/3)E_{rel}/V + nkT \qquad (7.4)$$

is the internal pressure. Thus,

$$F = v_b\, ((1/2)\, \rho_b v_b^2 + U_{int} + P_{int} + \rho_b c^2) \qquad (7.5)$$

is the energy flowing through a unit area of the fluid element per unit time. The net rate of energy flow, L_E, (in ergs sec^{-1}) down a beam of radius r_b is then

$$L_E = (F - v_b\rho_b c^2)\pi r_b^2 = \pi r_b^2\, v_b \left[(1/2)\rho_b v_b^2 + U_{int} + P_{int}\right], \quad (7.6)$$

where the rest mass flux has been subtracted (assuming mass is conserved).

It can be easily shown that the relative importance of the kinetic and internal energy density terms in equation 7.6 depends on the beam Mach number, M ($M = v_b/c_s$), where $c_s = (\gamma P_{int}/\rho_b)^{1/2}$ is the sound speed, and γ is the adiabatic index). If magnetic fields are ignored, $U_{int} = P_{int}/(\gamma - 1)$, and equation 7.6 can be written,

$$L_E = (1/2)\pi r_b^2 \rho_b v_b^3 \left[1. + 2\gamma P_{int}/\{(\gamma - 1)\rho_b v_b^2\}\right]. \quad (7.7)$$

Using $\gamma = 5/3$ for a beam dominated by nonrelativistic particles, and substituting for c_s and M as given above, results in

$$L_E = (1/2)\pi r_b^2 \rho_b v_b^3 \left[1. + 3/M^2\right]. \quad (7.8)$$

Thus, the pressure term can be neglected only for supersonic ($M > 1$) beams. This is expected since the internal energy is small compared to the kinetic energy if the random motions of the gas are small compared to the bulk velocity of the flow. This will be true if the beam is moving with a velocity much higher than its sound speed.

The relativistic generalization of equation 7.6 is derived using the usual relativistic transformations between quantities in the proper frame (i.e., co-moving with the fluid) and those in a stationary frame in which the observer is located. The total energy density observed in a stationary frame $U_{tot}' = U_{tot}\Gamma^2$, where U_{tot} is now measured in the

co-moving frame, $\Gamma = (1. - \beta_b^2)^{-1/2}$, and $\beta_b = v_b/c$. The total energy density is given by

$$U_{tot}' = \Gamma^2 \left[c^2\rho_b + U_{int}\right]. \tag{7.9}$$

Then, the net energy flow down the beam (subtracting off the rest mass flux, $c^2\Gamma\rho_b\pi r_b^2 v_b$), is given by

$$L_E = \pi r_b^2 v_b \Gamma\left[(\Gamma - 1)c^2\rho_b + \Gamma(U_{int} + P_{int})\right]. \tag{7.10}$$

For a nonrelativistic beam $\Gamma \simeq 1$ and $\Gamma - 1 \simeq (1/2)\beta_b^2$ and equation 7.6 is recovered. If magnetic fields are ignored, equation 7.10 becomes

$$L_E = \pi r_b^2 v_b \Gamma\left[(\Gamma - 1)c^2\rho_b + \gamma\Gamma P_{int}/(\gamma - 1)\right] \tag{7.11}$$

which is the form used by Eilek et al. (1984).

The first constraint on the properties of the beams comes from the assumption that the beam energy flow is tapped with an efficiency, ε, to provide the observed radio luminosity, L_{rad}. (At this point it is not important how this is done.) In addition, if the beams expand, adiabatic losses will reduce the energy of the radiating particles ($E \propto r_b^{-2/3}\ v_b^{-1/3}$). Taking this into account, and assuming a constant velocity beam, gives

$$L_{rad} = \varepsilon L_E (r_{bi}/r_{bf})^{2/3} \tag{7.12}$$

where r_{bi} and r_{bf} are the initial and final beam radii (cf. Jones and Owen 1979). The assumption that the jet luminosity is powered by the beam kinetic energy requires in situ particle acceleration all along the beam. How good is this assumption? Since the jets in NATs tend to be

relatively short, the usual synchrotron lifetime arguments do not suffice. In the case of NGC 1265, for example, relativistic particles which are created in or near the core can travel the entire ~20 kpc length of the jets within their estimated synchrotron and inverse Compton lifetime of $\sim 3 \times 10^6$ yrs (in a 15 μG field) for a beam velocity of ~0.02 c, which is plausible.

However, the surface brightness of jets tends to decrease much slower with increasing radius than expected, given magnetic flux conservation and adiabatic expansion losses (e.g., Burch 1979; Fomalont et al. 1980; Bridle 1982; Bridle and Perley 1984; Perley, Bridle, and Willis 1984; and Chap. VI). Unless the conditions in the beams are very different from the current ideas, the slow dependence of the intensity on radius strongly suggests that in situ particle acceleration is taking place all along the beams. However, the changes in both surface brightness and spectral index along jets suggest that the amount and possibly the form of the particle acceleration varies along the beams. Thus, the amount of success attained in applying this constraint on the kinetic energy of the beams to radio jets will depend to a large extent on how realistic it is to assume that ε is roughly constant along the beams.

The beam momentum flux

The second constraint on the jets is based on the assumption that the bending of the beams can be described by simple hydrodynamics. Following Landau and Lifshitz (1959), the derivation of Euler's equation for an ideal fluid (i.e., no viscosity) will be given. The

equation of motion for a volume element of fluid is simply given by Newton's second law, i.e.,

$$\rho_b \, dv(x,y,z,t)/dt = - \nabla P, \tag{7.13}$$

where the force on the fluid element is taken to be the gradient of an externally applied pressure, P. The velocity derivative consists of two separate parts, the change in velocity in time at one fixed point in space and the change in velocity between two nearby points at one instant in time, so

$$dv(x,y,z,t)/dt = \partial v/\partial t + (v \cdot \nabla)v. \tag{7.14}$$

Then, substituting equation 7.14 into 7.13 and making the assumption of steady flow ($\partial v/\partial t = 0$), the time-independent Euler's equation is obtained:

$$(v \cdot \nabla)v = - (1/\rho_b)\nabla P \tag{7.15}$$

For a beam whose change in velocity over a bending scale length R is comparable to its velocity, $(v \cdot \nabla)v \simeq v_b^2/R$, giving

$$\rho_b v_b^2/R \simeq - \nabla P. \tag{7.16}$$

A NAT source moving with velocity v_g through an intracluster medium (ICM) of mass density ρ_{icm} experiences a ram pressure $\rho_{icm} v_g^2$. This pressure is exerted over a scale length, h, which depends on the extent of the ISM in the galaxy (see Sec. 7.5). Equation 7.16 then becomes

$$\rho_b v_b^2/R \simeq \rho_{icm} v_g^2/h. \tag{7.17}$$

The relativistic generalization of equation 7.16 is obtained by replacing $\rho_b v_b^2$ by $w_b \Gamma^2 \beta_b^2$, where

$$w_b = \rho_b c^2 + U_{int} + P_{int} \tag{7.18}$$

is the proper relativistic enthalpy (Landau and Lifshitz 1959). This gives (see also Jones and Owen 1979):

$$w_b \Gamma^2 \beta_b^2 / R = -\nabla P = \rho_{icm} v_g^2 / h. \tag{7.19}$$

For a fluid with a nonrelativistic equation of state (i.e., dominated by thermal particles), $w_b \simeq \rho_b c^2$; while for a fluid with a relativistic equation of state (dominated by relativistic particles in rough equipartition with the magnetic fields), $w_b \simeq B^2/4\pi + (4/3)E_{rel}/V$. Note that if $(U_{int} + P_{int}) \simeq 10^{-11}$ erg cm^{-3} (as is the case in the NATs; see Chap. III), then $\rho_b c^2 > (U_{int} + P_{int})$ if the beam particle density is larger than $n_b = \rho_b / m_H > 9 \times 10^{-9}$ cm^{-3}, where m_H is the mass of the hydrogen atom.

The assumption of negligible viscosity has been made in order to obtain the simplest form of Euler's equation (7.15). If viscosity is included, then the simple form of Euler's equation may be replaced with (see Landau and Lifshitz 1959):

$$\rho_b (v_b \cdot \nabla) v_b = -\nabla P + \eta \nabla^2 v_b + (\zeta + (1/3)\eta) \nabla (\nabla \cdot v_b), \tag{7.20}$$

where η and ζ are coefficients of viscosity. This makes things sufficiently complex that the simple analytical results presented here are no longer possible.

Baan (1980) has considered various sources of viscosity in radio jets. The actual numerical value of the viscosity coefficient is expected to be small, and, thus, the viscosity terms in equation 7.20 will be negligible (Baan 1983, private communication).

In any event, the basic result of the existence of viscosity is that kinetic energy is dissipated along the beam (e.g., Landau and Lifshitz 1959). Such energy dissipation is required by the slow dependence of the intensity and the pressure on the jet radius (Chap. VI) and is assumed here as a constraint on the beam kinetic energy flow (eq. 7.12). The neglect of viscosity in Euler's equation is equivalent to neglecting the effects of energy dissipation on the bending of the beam. This is a good assumption only if a very small fraction of the beam kinetic energy is dissipated. The results obtained below suggest that in general relatively low efficiencies ($\varepsilon \ll 1\%$) are required to produce the observed radio luminosities in the jets. An additional (possibly larger) fraction of the beam kinetic energy may be dissipated in heating of the thermal particles in the beam (e.g., Eilek 1979). This amount is harder to estimate, but even if it is a factor of ~10 larger than that needed to power the radio luminosity, the total fraction of the energy dissipated would only be a few percent or less. The very gradual bending of the radio jets (Chap. III) is also consistent with this estimate, since the effect of a substantial energy dissipation would be to bend the beam very quickly. Thus, the assumption of negligible viscosity is probably adequate for these order of magnitude calculations.

The first case to be considered here is that of "cold" beams.

7.2 Cold Beams

Beams in which $M \gg 1$, i.e., $(\Gamma - 1)c^2 \rho_b \gg \Gamma(U_{int} + P_{int})$, have internal energies which are small compared to their bulk kinetic energies and are called "cold." This is the most commonly made assumption. Combining equations 7.10 and 7.12 and ignoring the pressure term gives:

$$L_{rad} = \varepsilon \pi r_b^2 (\Gamma - 1) c^2 \Gamma \rho_b v_b (r_{bi}/r_{bf})^{2/3}. \tag{7.21}$$

Since $\beta_b^2 = 1. - 1/\Gamma^2 = (\Gamma + 1)(\Gamma - 1)/\Gamma^2$, equation 7.21 becomes

$$L_E \simeq \pi r_b^2 \rho_b v_b^3 \, (\Gamma^3/(\Gamma + 1))(r_{bi}/r_{bf})^{2/3}, \tag{7.22}$$

which is the form used by Rees (1978) in his model for the jet in M87.

In this limit, $\rho_b c^2 \gg U_{int} + P_{int}$, hence $w_b \simeq \rho_b c^2$ and equation 7.19 becomes:

$$\rho_b v_b^2 \Gamma^2 / R = \rho_{icm} v_g^2 / h. \tag{7.23}$$

Beam velocity

Using equation 7.23 to substitute for $\rho_b v_b$ in equation 7.21 gives:

$$\frac{\beta_b \Gamma^2}{T(\Gamma - 1)} = \frac{\rho_{icm} v_g^2 \varepsilon \pi r_b^2 c R (r_{bi}/r_{bf})^{2/3}}{L_{rad}\, h} \equiv k, \tag{7.24}$$

where the constant, k, is composed of quantities which in principle can be observed or estimated. This gives a quadratic equation in Γ which has only one non-trivial root, i.e., $\Gamma = (k^2 + 1)/(k^2 - 1)$, where $k > 1$.

In the nonrelativistic limit $\Gamma \simeq 1$, hence $k >> 1$, while in the ultra-relativistic limit, $\Gamma >> 1$ and $k \geq 1$. Since $\beta_b = (1-1/\Gamma^2)^{1/2}$,

$$v_b = 2ck/(k^2 + 1). \tag{7.25}$$

The other (trivial) solution requires $\Gamma = 1$, i.e., $v_b = 0$. The important things to note here are that equations 7.24 and 7.25 are correct for any velocity, and that the dependence on the beam density, ρ_b, has been eliminated. This latter point is especially interesting due to the current controversy over the interpretation of polarization measurements of jets (e.g., Laing 1981). The relationships between the different physical parameters can be seen more clearly in the nonrelativistic limit, $k >> 1$, $v_b \simeq 2c/k$, i.e.,

$$v_b = \frac{2hL_{rad}(r_{bf}/r_{bi})^{2/3}}{\rho_{icm}v_g{}^2\varepsilon\pi r_b{}^2R} \tag{7.26}$$

Beam density

The particle number density, $n_b = \rho_b/m_H$, where m_H is the mass of the hydrogen atom, can be obtained from equation 7.23 by using the substitution $v_b{}^2\Gamma^2 = c^2(\Gamma^2 - 1)$, from the definition of Γ. Then, the most general form for the number density is

$$n_b = \frac{\rho_{icm}v_g{}^2R}{hm_Hc^2[\{(k^2 + 1)/(k^2 - 1)\}^2 - 1]} \tag{7.27}$$

and in the nonrelativistic limit, $k >> 1$,

$$n_b = \frac{\rho_{icm}^3 v_g^6 \varepsilon^2 \pi^2 r_b^4 R^3}{4h^3 L_{rad}^2 (r_{bf}/r_{bi})^{4/3} m_H} . \qquad (7.28)$$

Note that the beam particle density depends on higher powers of the observables than does the beam velocity and is thus more sensitive to the uncertainties in those parameters.

Efficiency

Upper and lower limits to the efficiency of conversion of bulk kinetic energy to radio luminosity can be obtained if upper limits to the beam velocity and particle density can be estimated. If an upper limit to the beam velocity, v_{bmax}, can be obtained (e.g., through limits on the amount of relativistic beaming allowed in the jets), then equation 7.24 can be arranged to give a lower limit to the particle acceleration efficiency, ε, i.e.,

$$\varepsilon > \frac{\beta_{bmax} \Gamma_{max}^2 h L_{rad} (r_{bf}/r_{bi})^{2/3}}{\Gamma_{max}(\Gamma_{max} - 1)\rho_{icm} v_g^2 \pi r_b^2 cR} . \qquad (7.29)$$

If the upper limit to the velocity, v_{bmax}, is nonrelativistic, as is the case for the NATs studied in this thesis (see Sec. 7.7), then

$$\varepsilon > \frac{2h L_{rad} (r_{bf}/r_{bi})^{2/3}}{\rho_{icm} v_g^2 \pi r_b^2 R v_{bmax}} . \qquad (7.30)$$

An upper limit to ε can be obtained from equation 7.28; i.e., if an upper limit to the beam number density, n_{bmax}, can be obtained (e.g., from multifrequency polarization measurements), then

$$\varepsilon < \frac{2n_{bmax}{}^{1/2}h^{3/2}L_{rad}(r_{bf}/r_{bi})^{2/3}m_H{}^{1/2}}{\rho_{icm}{}^{3/2}v_g{}^3\pi r_b{}^2R^{3/2}} . \qquad (7.31)$$

7.3 Warm Jets

In some cases, the equations for highly supersonic beams may not be appropriate. In fact, in the Jones and Owen (1979) model, the beam must have a Mach number ~1. For this reason the more general case of a warm beam ($M \geq 1$) will be considered. Thus, equations 7.10 and 7.12 are combined without further assumptions at this point to give the kinetic energy constraint. The case of a beam with a nonrelativistic equation of state (i.e., dominated by thermal particles) will be considered first and equation 7.23 for the momentum flow constraint will be used. Together these constraints give

$$L_{rad} = \varepsilon\pi r_b{}^2c\Gamma\beta_b[(\Gamma - 1)\rho_{icm}v_g{}^2R/(h\Gamma^2\beta_b{}^2) + \Gamma(U_{int} + P_{int})](r_{bi}/r_{bf})^{2/3} \qquad (7.32)$$

Unfortunately, this results in a sixth order polynomial in Γ, or a similar one for β_b. Thus, simplifying assumptions are needed. The case of the nonrelativistic limit will be taken first.

Beam velocity

In the nonrelativistic limit, equation 7.32 becomes

$$L_{rad} = \varepsilon\pi r_b{}^2v_b[\rho_{icm}v_g{}^2R/(2h) + (U_{int} + P_{int})](r_{bi}/r_{bf})^{2/3} \qquad (7.33)$$

and, solving for v_b,

$$v_b = \frac{L_{rad}(r_{bf}/r_{bi})^{2/3}/(\varepsilon\pi r_b^2)}{\rho_{icm}v_g^2R/(2h) + U_{int} + P_{int}} . \qquad (7.34)$$

Beam density

For a beam with $M \geq 1$, $(\Gamma - 1)c^2\rho_b \geq \Gamma(U_{int} + P_{int})$. If the beam is also nonrelativistic, then $\rho_b c^2 >> (U_{int} + P_{int})$ and the version of Euler's equation, given by equation 7.17, is appropriate. If the equation of state of the beam fluid is relativistic, but the beam bulk velocity is nonrelativistic, then the beam must also be subsonic. The beam particle number density is $n_b = \rho_{icm}v_g^2R/(hm_Hv_b^2)$ which leads, after substitution, into equation 7.34, to

$$n_b = \frac{\rho_{icm}v_g^2R/(hm_H)[\rho_{icm}v_g^2R/(2h) + (U_{int} + P_{int})]^2}{[\{L_{rad}/(\varepsilon\pi r_b^2)\}\ \{r_{bf}/r_{bi})^{2/3}\}]^2} . \qquad (7.35)$$

Note that if an upper limit to the beam number density can be set using multifrequency polarization measurements, an upper limit to $(U_{int} + P_{int})$ can be derived. This upper limit will be lower for a warm beam ($M \sim 1$) than for a cold beam ($M >> 1$).

If an upper limit to the beam particle density, n_{bmax}, and a lower limit to $(U_{int} + P_{int})$ can be obtained through the minimum pressure arguments, then equation 7.35 can be used to constrain other, perhaps less well known, parameters. An upper limit to the intracluster medium density, ρ_{icm}, and the galaxy velocity, v_g, can be obtained in this

manner; though in most cases these quantities will be better known than n_b.

Efficiency

If an upper limit to the beam velocity, v_{bmax}, can be obtained, then equation 7.34 can be arranged to give a lower limit to the efficiency, ε, i.e.,

$$\varepsilon > \frac{L_{rad}/(v_{bmax}\pi r_b^2)(r_{bf}/r_{bi})^{2/3}}{\rho_{icm}v_g^2R/(2h) + U_{int} + P_{int}} . \qquad (7.36)$$

An upper limit to ε can be set if an upper limit to the beam particle density and a lower limit to $(U_{int} + P_{int})$ can be determined, i.e., from equation 7.35,

$$\varepsilon < \frac{[hn_{bmax}m_H/(\rho_{icm}v_g^2R)]^{1/2}L_{rad}/(\pi r_b^2)(r_{bf}/r_{bi})^{2/3}}{[\rho_{icm}v_g^2R/(2h) + U_{min} + P_{min}]} . \qquad (7.37)$$

At this point, the respective equations for v_b, n_b, and ε can be compared for both the warm and cold beams in the nonrelativistic limit. All other properties being equal, the warm beam will be about a factor of 2 lower in velocity and less efficient and a factor of 4 denser than the cold beam.

Mach number

The beam Mach number, M, was defined earlier as $M = [v_b^2P_{int}/(\gamma\rho_b)]^{1/2}$, ignoring magnetic fields. Substituting for the beam

density, ρ_b, using equation 7.23 for a beam with nonrelativistic equation of state, gives

$$M = [\rho_{icm} v_g^2 R/(h\gamma P_{int}\Gamma^2)]^{1/2}. \tag{7.38}$$

Taking $\rho_{icm} v_g^2 \simeq P_{int}$, which must be the case if the beam is to be bent, gives

$$M \simeq [R/(h\gamma\Gamma^2)]^{1/2}\ , \tag{7.39}$$

which is the general relation for the Mach number of a bent beam (cf. Rudnick and Burns 1981). For a beam with nonrelativistic bulk motion, $\Gamma \sim 1$, and $M \simeq [R/(h\gamma)]^{1/2}$ (eq. 2 of Begelman, Rees, and Blandford 1979). Thus, the Mach number is roughly the square root of the ratio of bending scale length, R, to the pressure gradient scale length, h.

Warm relativistic beams

For a warm beam with relativistic bulk motion $(\Gamma - 1)\rho_b c^2 \simeq \Gamma(U_{int} + P_{int})$. But if $\Gamma >> 1$, then $\Gamma - 1 \sim \Gamma$, and $\rho_b c^2 \simeq (U_{int} + P_{int})$. Thus the assumption that the equation of state is nonrelativistic (i.e., $w_b \simeq c^2\rho_b$), is no longer viable. This rules out the substitutions used earlier, and prevents a satisfactory solution for this regime of parameter space. The best thing to do when faced with a bent and possibly relativistic beam is to assume that it is cold and use the relativistically correct relationships for a cold beam derived earlier. In this case, the cold beam approximation is probably adequate (see Sec. 7.4).

7.4 Can NATs Be Hot Beams?

For very subsonic ($M \ll 1$) beams, $(\Gamma - 1)c^2\rho_b \ll \Gamma(U_{int} + P_{int})$. In this class of beam, the internal energy of the beam is large compared to the bulk kinetic energy of the beam, and this type of beam is called "hot." In this limit, equation 7.32 becomes

$$L_{rad} \simeq \varepsilon\pi r_b^2 \left[U_{int} + P_{int}\right] c\Gamma^2\beta_b (r_{bi}/r_{bf})^{2/3}. \tag{7.40}$$

If the equation of state is nonrelativistic, then Euler's equation becomes equation 7.23. (In this limit the bulk velocity must also be nonrelativistic.) Note that the two constraints on the beams can no longer be coupled. However, equation 7.40 can be solved for the velocity giving, in the nonrelativistic limit,

$$v_b = \frac{L_{rad}(r_{bf}/r_{bi})^{2/3}}{\varepsilon\pi r_b^2 \left[U_{int} + P_{int}\right]}, \tag{7.41}$$

which is the appropriate limit of equation 7.34 for a warm beam. However, the constraint that the beam is bent has not yet been used. The bending constraint can be examined in terms of the Mach number, i.e., from equation 7.39, $M \simeq \left[R/(h\gamma)\right]^{1/2} \ll 1$. This means that the beam bends on a scale much smaller than the pressure gradient. For a "naked" jet this requires $R \ll r_b$, and for a jet within an ISM of radius, r_s, this requires $R \ll r_s$ (and probably $R < r_b$). The beam would be bent before it had traveled a distance equal to its radius. Thus,

the thin, well collimated jets ($R >> r_b$) seen in NATs (Chap. III) cannot be hot beams with a nonrelativistic equation of state.

Now, the same result is also true for the case of a hot beam with a relativistic equation of state, since regardless of its equation of state, a hot beam will respond to transverse pressure gradients on a time scale shorter than that required to traverse a distance equal to its own radius. The beam will be sheared off in an ICM, or will move buoyantly (like a bubble) in an ISM. These considerations suggest the following:

(1) The thin, well collimated jets ($R >> r_b$) in NATs cannot be hot beams ($M < 1$).

(2) These jets can be warm beams only if they are shielded by a significant ISM (then $R \sim h \sim r_s >> r_b$, and $M \sim 1$), otherwise they must be cold, $M >> 1$.

7.5 The Effects of an ISM

The two basic models for the energetics of NATs differ to the extent to which the ISM of the parent galaxy is important.

In the naked jet model of Begelman, Rees, and Blandford (1979), the ISM is insignificant and the beam interacts directly with the ICM gas which streams freely through the galaxy. For a galaxy velocity which is supersonic in the ICM, there will be a bow shock in front of the beams and the scale height of the pressure gradient is simply the beam radius, $h \simeq r_b$. In this case the beam must carry enough bulk kinetic energy to power the luminosity of the tails.

In the Jones and Owen (1979) model, a significant ISM exists in the galaxy. This appears to be consistent with the results of numerical hydrodynamic calculations of ram pressure stripping of the ISM from galaxies moving at supersonic velocity ($M \geq 1$) through the cluster gas (e.g., Gisler 1976; Lea and De Young 1976; Shaviv and Salpeter 1982). In this case, a bow shock will form in front of the galaxy, and there will be a turbulent wake behind the galaxy. The ram pressure from the ICM is then distributed across the ISM ($h \simeq r_s$, the radius of the ISM). The pressure gradient across the beam is weaker by a factor of r_b/r_s than in the case of the BRB model. Thus, for a given bending scale length, a beam embedded in an ISM will have a momentum flux ($\rho_b v_b^2$) which is weaker by r_b/r_s than a beam exposed to the ICM. Although the weaker JO jet may be unable to power the radio luminosity of the tails, the energy in the turbulent galactic wake is available to reaccelerate the particles if the beam can be bent on the scale r_s. The luminosity of the tail is then given by (Jones and Owen 1979)

$$L_{rad} \simeq \varepsilon \pi \rho_{icm} r_s^2 v_g^3 \ . \qquad (7.42)$$

If the beam is only barely supersonic, $M \simeq 1$ and $R \simeq h \simeq r_s$ (eq. 7.39) and the beam is bent back into the galactic wake; hence these warm beams need only power their own radio emission.

7.6 Multiple Plasmons in a Channel

Christiansen, Pacholczyk, and Scott 1981, CPS, suggested that the multiple plasmon in a channel model (Christiansen 1973, Christiansen, Pacholczyk and Scott 1977) would work for the case of NGC 1265 if there were a significant ISM. CPS only consider the case of cold, $M \gg 1$, nonrelativistic plasmons. In this model, the time scale between plasmon ejections is given by

$$t_p \simeq d/v_p \ , \tag{7.43}$$

where d is the distance between plasmons and v_p is the plasmon velocity. The relaxation time scale of the channel, t_c, is the sound crossing time of the channel

$$t_c \simeq r_p/c_{ism} \ , \tag{7.44}$$

where r_p is the plasmon radius or channel radius and c_{ism} is the sound speed in the ISM (CPS). The channel will remain open if $t_p < t_c$. The plasmons traveling through the channel would have smaller energetic requirements than those in the independent multiple plasmon model (Wellington et al. 1973; Jaffe and Perola 1973; Pacholczyk and Scott 1976). The energetics of this model are then similar to those of the JO model in that for a given transverse pressure gradient across the beam and bending scale length, the time-averaged momentum flux in the two models must be the same. Each plasmon must have a momentum flux which is higher by the factor d/r_p than a similar volume of fluid in a JO beam. In addition, CPS assume that the pressure gradient scale length

is the channel/plasmon radius (CPS eq. 4) instead of the ISM radius. This requires the plasmons to be supersonic (eq. 7.39) and increases the estimated plasmon momentum flux by an additional factor of r_s/r_p over that of the JO beam. As in the JO model, the turbulent galactic wake is assumed to provide the energy for the radio luminosity in the tail.

The radio luminosity in the jets, or "inner trails," is

$$L_{rad} \simeq E_p \varepsilon / t_p \ , \tag{7.45}$$

(CPS eq. 17) where the energy of a cold plasmon, E_p, is simply its kinetic energy,

$$E_p \simeq (1/2)\pi r_p^3 \rho_p v_p^2 \ , \tag{7.46}$$

(CPS eq. 21) where ρ_p is the mass density in the plasmon. The constraint on the plasmon kinetic energy flux is then:

$$L_{rad} \simeq (1/2)\varepsilon \pi r_p^3 \rho_p v_p^3 d^{-1}. \tag{7.47}$$

The constraint on the momentum flux of a cold, nonrelativistic plasmon is given by Euler's equation:

$$\rho_{icm} v_g^2 / h \simeq \rho_p v_p^2 r_p / (Rd) \tag{7.48}$$

(CPS eq. 8) and CPS take $h \simeq r_p$ (CPS eq. 4). Combining these two conditions, 7.47 and 7.48, gives the plasmon velocity and density, $n_p = \rho_p / m_H$:

$$v_p \simeq 2hL_{rad} / [\pi \varepsilon r_p^2 \rho_{icm} v_g^2 R] \tag{7.49}$$

and

$$n_p \simeq (\varepsilon\pi/2)^2 \, (R\rho_{icm}r_p/h)^3 v_g{}^6 d L_{rad}{}^{-2} m_H{}^{-1}. \qquad (7.50)$$

If an upper limit to the plasmon particle density can be obtained (and the other parameters can be estimated), an upper limit to the distance between plasmons, d, can be derived. The condition $d > r_p$ must be met for this model to be distinguished from the continuous beam models.

If an upper limit to the plasmon velocity, v_{pmax} is obtained, a lower limit to the particle acceleration efficiency in the plasmon, ε, can be obtained from 7.49.

$$\varepsilon > 2hL_{rad}/[v_{pmax}\pi r_p{}^2 \rho_{icm} v_g{}^2 R]. \qquad (7.51)$$

If an upper limit to the plasmon particle density, n_{pmax}, can be obtained, an upper limit to the efficiency can be obtained from 7.50,

$$\varepsilon < \frac{2[h^3 n_{pmax} m_H]^{1/2} L_{rad}}{\pi v_g{}^3 [R\rho_{icm} r_p]^{3/2} d^{1/2}}. \qquad (7.52)$$

7.7 Upper Limits to the Beam Velocity

The observed limits to the intensity ratios of two oppositely directed jets can be used to set limits to the beam velocities. The intensity ratio due to relativistic Doppler enhancement of two beams with velocity $\beta = v_b/c$ and inclination angle to the line of sight θ is given by

$$\frac{S_1}{S_2} = \frac{[1- \beta_2 \cos(\theta_2)]^{2-\alpha}}{[1- \beta_1 \cos(\theta_1)]^{2-\alpha}} , \qquad (7.53)$$

where α is the spectral index ($S \propto \nu^{\alpha}$) (e.g., Blandford and Konigl 1979; Scheuer and Readhead 1979; Van Groningen, Miley, and Norman 1980). Using data from Chapter III and from the references in Chapter IV, average intensity ratios of the two jets in 26 twin jet NATs were estimated (shown in Fig. 7.1). These ratios are upper limits to the amount of intensity enhancement due to Doppler enhancement, since there are also intrinsic variations in jet intensity. For the purposes of this calculation it is assumed that $\beta_1 = \beta_2$, $\theta_2 = \theta_1 - 180°$, and $\alpha = -0.65$. The distribution of intensity ratios expected for given values of β and a random distribution of angles was determined for an artificial Monte-Carlo generated sample of 10^4 sources. The median of the observed intensity ratio distribution (1.6) was compared to the median of the artificial distribution using a chi-square test (Conover 1980). Even moderately low values of β predict larger ratios of intensities between the opposing jets than are observed. The median of the observed distribution is less than that expected for $\beta = 0.15$ with a 94% confidence and is less than that expected for $\beta = 0.20$ with a 99.7% confidence. (The expected distribution for $\beta > 0.2$ is also shown in Fig. 7.1.) Thus, values of $B > 0.2$ are unlikely for these sources. One possible problem is that the choice of twin jet sources for this statistical comparison may discriminate against sources whose jets are at a small angle to the line-of-sight. Such sources might appear to be single tail sources because of the much smaller projected distance

Figure 7.1

The observed distribution of intensity ratios between opposing jets in the twin jet sources, and the predicted distribution due to relativistic beaming effects for $\beta = 0.2c$, and assuming a random distribution of angles to the line-of-sight.

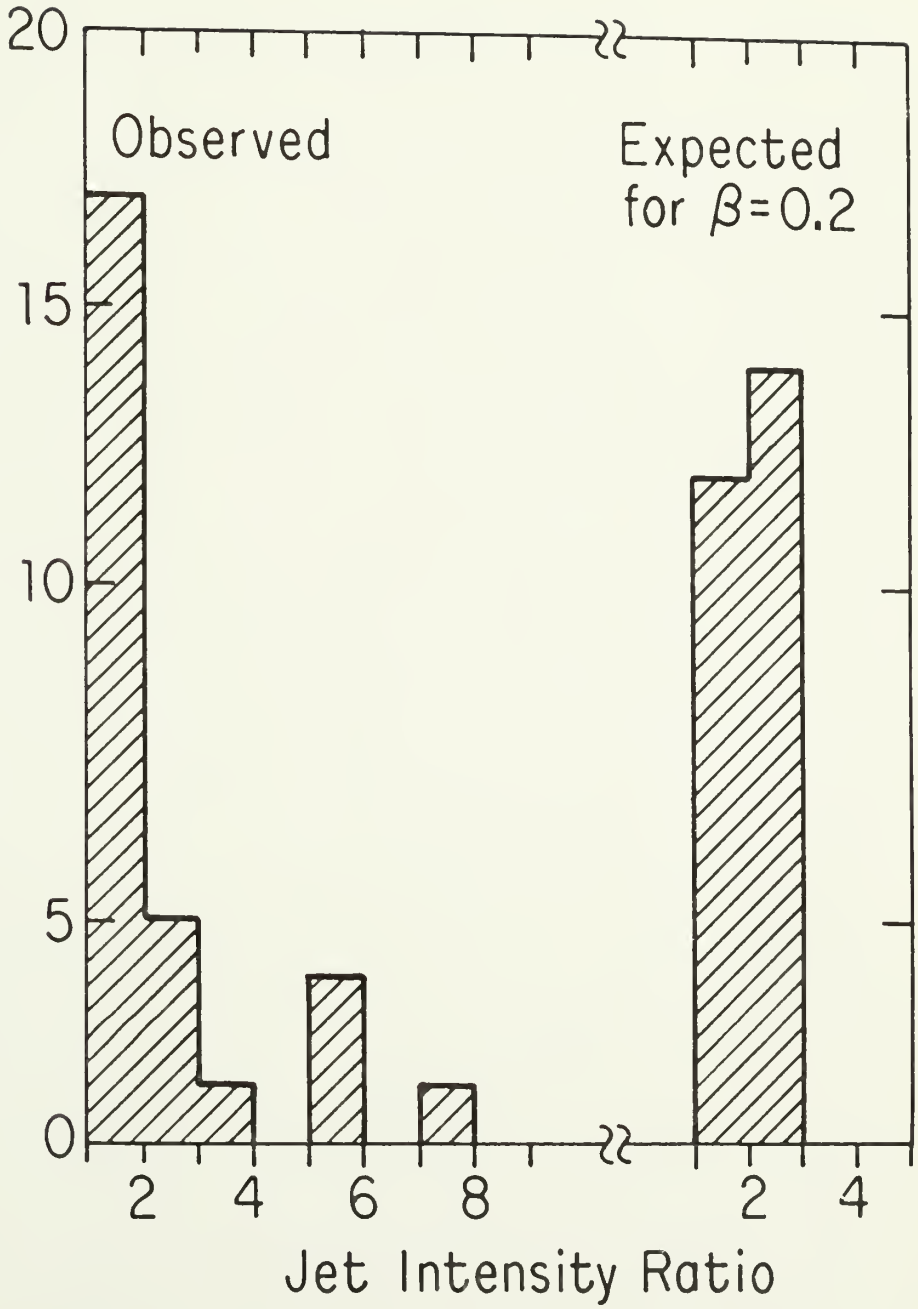
20
15
10
5
0
Observed
Expected
for β=0.2
2
4
6
8
2
4
Jet Intensity Ratio

between the jets, and so would not have been included in the sample of twin jet NATs. However, these results are unchanged if angles less than 40° to the line-of-sight are omitted.

7.8 A Comparison of the Models

It has been shown that the beams are probably nonrelativistic and at least mildly transsonic, and now the parameter space available to the models will be explored. It is of interest to compare the velocities, densities, and efficiencies for the three models, BRB, JO, and CPS. All three models input different values for radio luminosity, pressure gradient scale height, and beam expansion which result in significantly different model parameters. The radio luminosity which the beams/plasmons must supply is $L_{rad} \simeq L_{tail}$ in the BRB model, while in the JO and CPS models $L_{rad} \simeq L_{jet}$. The scale height of the pressure gradient is $h \simeq r_b$ in the BRB and CPS models and $h \simeq r_s$, the ISM radius, in the JO model. In the JO and CPS models $r_{bi}/r_{bf} \sim 1$ since the jets do not expand by very much over the region in which they bend, and in any event only the global parameters of the beams/plasmons are estimated. In the BRB model $r_{bf}/r_{bi} \sim 10$ since the diffuse tails are typically a factor of ~10 wider than the jets (though there is a great deal of variation). In this case the beams experience significant adiabatic losses before they can convert their energy into the radio luminosity of the tails. This results in a higher required efficiency for the BRB model.

To illustrate the effects of these differing constraints on the models, the cold, nonrelativistic BRB beam will be compared with the cold, nonrelativistic CPS plasmons. The ratio of the velocities in the BRB (eq. 7.26) and CPS (eq. 7.49) models is

$$v_p/v_b \simeq L_{jet}(r_{bi}/r_{bf})^{2/3}L_{tail}^{-1}. \tag{7.54}$$

Since $L_{tail} \simeq 10L_{jet}$ and $r_{bf}/r_{bi} \sim 10$, the plasmon velocity is much lower than that of the BRB beam ($v_b \sim 40v_p$). The ratio of the densities (eqs. 7.28 and 7.50) is

$$n_p/n_b \simeq (d/r_b)[L_{tail}/L_{jet}]^2(r_{bf}/r_{bi})^{4/3}. \tag{7.55}$$

Since $d \sim 3r_b$, $L_{tail} \sim 10L_{jet}$, and $r_{bf}/r_{bi} \sim 10$, the plasmon particle density is much higher than that of the BRB beam ($n_p \sim 3\times10^3 n_b$). The ratio of the lower limits to the efficiencies (eqs. 7.30 and 7.51) is

$$\varepsilon_p/\varepsilon_b \simeq L_{jet}/[L_{tail}(r_{bf}/r_{bi})^{2/3}] \tag{7.56}$$

and the required BRB efficiency is much higher than the CPS efficiency ($\varepsilon_b \sim 40\varepsilon_p$).

The warm beam version of the JO model (presented in this thesis) tends to be somewhere in between the other two models (depending on the exact values for the internal pressure (or Mach number) and the radius of the ISM).

The range of parameter space required by the nonrelativistic warm beam and plasmon models can be explored using the data from Chapters III and IV. For completeness, all of the input parameters to the models are

given in Table 7.1. The source name is given in column 1. The $\log_{10}$ of the average radio luminosity (in ergs sec^{-1}) of the tails and jets is given in columns 2 and 3, respectively. The quantity $U_{int} + P_{int}$ (in units of 10^{-11} dynes cm^{-2}), calculated assuming minimum pressure conditions and neglecting the thermal particles (see Chap. VI), is given in column 4. The observed bending scale length, R_{obs}, and the deconvolved jet radius, r_b, (in kiloparsecs) are given in columns 5 and 6, respectively. The bending scale length is foreshortened by projection, i.e., $R \simeq R_{obs}/\sin(\theta)$, where R_{obs} is the observed scale length and θ is the inclination angle to the line-of-sight of the plane in which the jets lie. A value of $\theta = 60°$ is assumed for all galaxies. It is assumed that $r_s = R$ in the JO model, and that the distance between plasmons is $d = 3r_p$, which is the value used by CPS for NGC 1265. The choice of d effects only the estimated value for the density and not the value for the velocity. The beam Mach number, $M = [3R/(5r_b)]^{1/2}$, is given in column 7. The galaxy velocity (in units of 10^3 km sec^{-1}; column 8) is taken to be ($v_g = 3^{1/2}v_r$), where v_r is either the measured radial velocity of the NAT with respect to the cluster mean or the radial velocity dispersion of the cluster (given in Chap. IV). For sources where neither of these measurements is available, a value for v_r of 473 km sec^{-1} and 808 km sec^{-1} was assumed for clusters of Abell Richness Classes 0 and 1, respectively (Danese, De Zotti, and Di Tullio 1980). The ICM particle density was estimated by assuming that the gas is in hydrostatic equilibrium with a cluster gravitational potential given by an isothermal sphere (e.g., Lea 1975; see also Chap. I). A core radius for the cluster mass distribution of 170 kpc (Bahcall 1975;

Table 7.1

Input Parameters of the Models

Name	Log_{10} L_{tail}	Log_{10} L_{jet}	$(U_{int}+P_{int})$ (dynes cm^{-2})	R_{obs} (kpc)	r_b (kpc)	M	$v_g(x10^3)$ (cm sec^{-1})	$n_{icm}(x10^{-4})$ (cm^{-3})
0039+211	41.7	40.5	$9(x10^{-11})$	12	1.0	2.9	1.4	7
0039-097	40.4	39.9	1	13	2.1	2.1	1.4	7
0053-016	41.2	39.7	0.9	9	1.9	1.8	1.4	8
0256+132	40.9	40.3	5	21	0.8	4.2	2.2	3
0314+416	41.3	40.0	10	10	0.35	4.4	3.8	5
0335+096	40.5	39.6	16	2	0.3	2.1	0.82	100*
0431-134	40.6	39.9	6	8	1.2	2.1	1.4	6
0457+054	40.5	40.1	1	20	2.0	2.7	1.4	5
0907-091	40.9	40.0	0.9	19	2.2	2.5	3.1	3
1108+411	41.6	41.0	12	8	0.7	2.8	1.8	8
1132+492	40.6	39.2	1	7	1.0	2.1	0.76	8
1244+699	41.7	40.4	0.4	52	5.7	2.5	1.4	6
1256+282	39.7	39.1	12	2.5	0.2	2.9	1.5	8
1619+428	41.3	40.2	2	5	1.6	1.4	1.4	6
1705+786	40.2	39.5	1	15	1.9	2.3	2.7	8
1712+638	40.9	40.2	1	25	2.8	2.5	1.2	2
1753+580	41.7	40.8	6	16	2.0	2.4	1.4	9
1850+702	41.2	40.2	2	14	1.5	2.6	1.4	7
2316+184	40.7	40.3	15	8	0.4	3.8	0.82	8

Notes to Table 7.1

*The density is calculated using an isothermal model for the X-ray emission (in the direction of the small group of which 0335+096 is a number) with a central density of $n_c = 0.03$ cm^{-3} and a core radius of $r_c = 65$ kpc (Schwartz, Schwarz, and Tucker 1980). A projected distance of 98 kpc from the X-ray centroid is used.

assuming H_o = 75 km sec^{-1}) and a central gas density and temperature of $n_c = 10^{-3}$ cm^{-3} and $T_c = 10^8$ K (Forman and Jones 1982) were assumed. Since the NATs may be further from the cluster center than their projected distance, this estimate of the ICM density is an upper limit. The value of n_{icm} (in units of 10^{-4} cm^{-3}) for each NAT is given in column 9.

Efficiencies for the conversion of the beam energy into radio luminosity of 1% were assumed for the calculations of the velocities and densities. This is the value most often used in models of extragalactic radio sources (e.g., Pacholczyk and Scott 1976; Christiansen, Pacholczyk, and Scott 1977; Eilek 1979; Christiansen, Rolison, and Scott 1979). The value for $\varepsilon \sim 1\%$ is required by the various theoretical models for extended sources in order to explain the observed radio luminosity. It is not clear that these models can provide such an efficiency since very little work has been done in predicting the efficiencies of the various particle acceleration mechanisms (cf. Eilek 1979). An upper limit to the beam velocity of $v_b < 0.20c$ (based on the upper limits to the relativistic beaming enhancements) was assumed for the calculation of the lower limit to the efficiency. For unresolved jets, the velocities and efficiencies will be lower limits and the densities will be upper limits.

The results are given in Tables 7.2 and 7.3. These numbers are meant only to be ballpark estimates which illustrate the requirements of the three models. The velocities are given in units of 10^3 km sec^{-1}, densities are in cm^{-3}, and exponents are given in parentheses. The particle densities in the BRB model for 0039+211, and 1108+411 were

Table 7.2

Limits on the Parameters of the Models

	Min. Velocity (10^3 km sec^{-1})				Max. Density (cm^{-3})			Min. Efficiency		
Name	Galaxy	BRB	JO	CPS	BRB	JO	CPS	BRB	JO	CPS
0039+211	2.5	300*	10	7	5(-9)	1(-5)	1(-3)	6(-2)	2(-3)	1(-3)
0039-097	0.8	9	3	0.8	1(-4)	2(-4)	5(-2)	2(-3)	5(-4)	1(-4)
0053-016	2.0	90	2	0.7	1(-6)	3(-4)	5(-2)	1(-2)	4(-4)	1(-4)
0256+132	1.2	50	20	3	2(-5)	5(-6)	1(-2)	8(-3)	3(-3)	5(-4)
0314+416	2.2	100	20	2	2(-5)	2(-5)	3(-1)	2(-2)	3(-3)	3(-4)
0335+096	1.3	100	7	4	5(-6)	1(-4)	1(-2)	2(-2)	1(-3)	6(-4)
0431-134	1.4	30	3	3	9(-6)	1(-4)	3(-3)	5(-3)	5(-4)	5(-4)
0457+054	0.8	10	5	1	7(-5)	4(-5)	3(-2)	2(-3)	9(-4)	2(-4)
0907-091	1.3	10	2	0.3	3(-4)	6(-4)	1(0)	2(-3)	4(-4)	5(-5)
1108+411	2.7	300*	50	30	3(-8)	9(-7)	1(-4)	5(-2)	9(-3)	5(-3)
1132+492	1.5	100	3	2	1(-7)	4(-5)	3(-3)	3(-2)	6(-4)	3(-4)
1244+699	1.0	20	2	0.3	3(-5)	4(-4)	6(-1)	4(-3)	3(-4)	4(-5)
1256+282	1.4	60	8	5	8(-6)	3(-5)	3(-3)	1(-2)	1(-3)	8(-4)
1619+428	3.4	200	7	6	5(-8)	3(-5)	3(-4)	3(-2)	1(-3)	1(-3)
1705+786	0.6	2	0.5	0.1	2(-2)	2(-2)	3(+1)	3(-3)	9(-5)	1(-5)
1712+638	1.1	40	5	1	2(-6)	1(-5)	2(-3)	6(-3)	8(-4)	4(-4)
1753+580	1.7	90	6	3	2(-6)	4(-5)	4(-3)	2(-2)	1(-3)	6(-4)
1850+702	1.4	70	9	2	3(-6)	2(-5)	1(-2)	1(-2)	2(-3)	3(-4)
2316+184	1.3	200	30	40	3(-7)	7(-7)	3(-5)	3(-2)	5(-3)	7(-3)

Notes to Table 7.2

*The cold, relativistic model (eq. 7.27) was used to calculate the density.

calculated using the relativistically correct cold beam equation (7.27) since for an efficiency of ~1% these sources are in the regime ($v_b \sim c$) where the nonrelativistic warm beam equation breaks down and seriously underestimates the particle density. The contents of Table 7.2 are as follows. The source name is given in column 1. The galaxy velocity required to provide the radio luminosity of the tails through turbulence in a galactic wake (eq. 7.42) assuming an efficiency of 1% is given in column 2. The beam/plasmon velocity in the BRB, JO, and CPS models is given in columns 3, 4, and 5. The beam/plasmon particle density in the BRB, JO and CPS models are given in columns 6, 7, and 8. The lower limit to the efficiency for the BRB, JO, and CPS models is given in columns 9, 10, and 11.

The contents of Table 7.3 are as follows. The source name is given in column 1. The upper limit to the efficiency, assuming an upper limit to the particle density of $n_b < 2\text{x}10^{-3}$ (from NGC 1265, Chap. VI), is given in columns 2, 3, and 4, respectively, for the BRB, JO, and CPS models. The mass loss rates through the beams/channels (in units of $M_\odot\ yr^{-1}$; i.e., solar masses per year) are given in columns 5, 6, and 7, respectively, for the BRB, JO, and CPS models. The mass loss rate through a continuous beam, m'_b, is given by $m'_b = \pi r_b^2 \rho_b v_b$, and for a stream of plasmons in a channel, $m'_p \simeq m'_b(r_p/d)$. Note that $m' \propto \varepsilon$, so that these results can be scaled using different values of ε.

For an efficiency of 1%, both JO and CPS models require lower limits to the velocities in the range ~1-10(x10^3) km s^{-1}. The BRB model requires beam velocities which are systematically higher by a factor of ~10. In general, these nonrelativistic beam velocities are consistent

Table 7.3

Limits on the Parameters of the Model

Name	Max. Efficiency			Mass Loss Rate ($M_\odot$ yr^{-1})		
	BRB	JO	CPS	BRB	JO	CPS
0039+211	4(0)	5(-1)	1(-2)	1(-4)	9(-3)	2(-1)
0039-097	2(-1)	1(-1)	2(-3)	4(-1)	2(-1)	4(0)
0053-016	1(0)	8(-2)	2(-3)	2(-2)	2(-1)	3(0)
0256+132	5(-1)	1(0)	4(-3)	5(-2)	4(-3)	7(-1)
0314+416	4(-1)	3(-1)	8(-4)	2(-2)	4(-3)	1(0)
0335+096	3(-1)	6(-2)	4(-3)	3(-3)	6(-3)	1(-1)
0431-134	4(-1)	1(-1)	8(-3)	3(-2)	4(-2)	3(-1)
0457+054	3(-1)	4(-1)	2(-3)	3(-1)	6(-2)	3(0)
0907-091	1(-1)	9(-2)	5(-4)	1(0)	5(-1)	4(+1)
1108+411	2(0)	1(0)	4(-2)	3(-4)	2(-3)	4(-2)
1132+492	3(0)	2(-1)	8(-3)	1(-3)	1(-2)	1(-1)
1244+699	7(-1)	2(-1)	6(-4)	1(0)	2(0)	1(+2)
1256+282	3(-1)	1(-1)	8(-3)	1(-3)	7(-4)	2(-2)
1619+428	3(0)	2(-1)	3(-2)	2(-3)	3(-2)	1(-1)
1705+786	1(-2)	1(-2)	8(-5)	9(0)	3(0)	2(+2)
1712+638	2(0)	7(-1)	1(-2)	5(-2)	4(-2)	7(-1)
1753+580	1(0)	3(-1)	7(-3)	5(-2)	8(-2)	1(0)
1850+702	1(0)	4(-1)	4(-3)	4(-2)	3(-2)	1(0)
2316+184	2(0)	2(0)	9(-2)	6(-4)	2(-4)	4(-3)

with the upper limit of $\beta < 0.2c$ (60×10^3 km s^{-1}) from the limits on relativistic beaming (Sec. 7.7). This provides evidence that the beams in these low-luminosity sources have nonrelativistic bulk velocities, as suggested by Burns, Owen, and Rudnick (1979). There are a few exceptions, however (i.e., in the BRB model, 0039+211 and 1108+411 are required to have beam velocities $v_b \sim c$, unless $\epsilon > 1\%$).

Assuming an upper limit to the beam velocity of 0.2c, fairly low lower limits to the efficiency (10^{-2} -10^{-4}) are required for the JO and CPS models. The BRB model requires lower limits to the efficiencies which are a factor of ~10 higher. Ten sources (including NGC 1265) are

required for the BRB model to have lower limits to the efficiency $\geq$ 1%. It remains to be seen whether such high efficiencies can be produced by reacceleration models.

The galaxy velocities required to power the tails through a turbulent wake (at 1% efficiency) are less than, or are comparable to, the assumed galaxy velocities for nearly all of the sources. The required galaxy velocities for four sources with relatively high radio luminosities, 0039+211, 1108+411, 1132+492, and 1619+428, are a factor of ~2 higher than the assumed velocities. However, velocities this high (i.e., ~2-3x10^3 km sec^{-1}) are not ruled out for these sources, and requiring the jets themselves to provide the tail luminosity also has problems with these sources. All four of these sources require either relativistic velocities (v_b ~0.5c-1c) or efficiencies > 1% in the BRB model. Thus, a turbulent galactic wake, as suggested by Jones and Owen, is capable of providing the radio luminosity in the tails of these sources if a 1% efficiency can be achieved.

The Mach numbers required by the BRB and CPS models are only mildly transsonic (M ~ 2-4), though these numbers would be increased for smaller jet radii.

The upper limits to the particle density for the BRB and JO models are generally in the range ~10^{-4}-10^{-6} cm^{-3}. The densities in the CPS model are typically higher by a factor of ~10^3-10^4. For the current parameters, the CPS model requires densities $\geq$ 0.1 cm^{-3} for NGC 1265, 0907-091, 1244+699, and 1705+786. This difficulty could be relieved by using an efficiency much less than 1% or by using a much smaller plasmon radius. No more than a factor of 3 can be gained by reducing the value

of the distance between plasmons. Higher resolution observations of some of these sources would be interesting.

The predicted density for NGC 1265 is $\sim 2 \times 10^{-5}$ cm^{-3} in both the BRB and JO models. This density is well below the current upper limit from the lack of depolarization at 21 cm of $n_b < 2 \times 10^{-3}$ cm^{-3}. However, the estimated density of ~ 0.3 cm^{-3} in the CPS model is grossly inconsistent with this limit. Since the jets are resolved, the only way to reduce the estimated density below the upper limit is to reduce the efficiency to $\varepsilon < 8 \times 10^{-4}$. This is not inconsistent with the lower limit on ε from the upper limit on the plasmon velocity of 0.2c; however, it is much lower than previous estimates of the efficiency of plasmons (e.g., Christiansen, Rolison, and Scott 1979; CPS) which suggest that efficiencies of at least 10^{-2} are required to account for the luminosity of double radio sources. If the density in NGC 1265, $n_b < 2 \times 10^{-3}$ cm^{-3}, is typical of other NATs, then the same situation would be encountered by the CPS model in nearly all the other NATs.

The upper limits to the efficiencies (estimated by requiring the density to be less than 2×10^{-3} cm^{-3}) in the BRB and JO models are fairly high, typically $\varepsilon_{max} \sim 0.1$-1, and are not very useful. Lower upper limits to the particle densities are needed in order to more tightly constrain the efficiencies. The JO model requires $1 < \varepsilon < 10^{-4}$, but is also consistent with the narrower range $10^{-2} < \varepsilon < 10^{-4}$. The BRB model requires $1 < \varepsilon < 10^{-2}$. In the CPS model, much lower upper limits to the efficiencies are required, with typical values $\varepsilon < 10^{-2}$-10^{-3}. All of the upper limits are consistent with the lower limits and define a parameter space for the efficiency in the CPS model of $10^{-2} < \varepsilon < 10^{-4}$.

In the calculations presented here, the CPS model gives an upper limit to the efficiency in NGC 1265 of $\varepsilon < 8\times10^{-4}$; while Christiansen et al. (1980) obtain a much higher estimate of $\varepsilon \sim 10^{-2}$. The reason appears to be that there is a numerical error in one of their calculations. Combining equation 7.46 for the plasmon kinetic energy with Euler's equation (7.48) gives the plasmon kinetic energy in terms of the observable quantities,

$$E_p = (1/2)\pi\rho_{icm}v_g^2 dRr_p \qquad (7.57)$$

(CPS eq. 22). Taking $v_g = 3\times10^8$ cm sec^{-1}, $\rho_{icm} = 10^{-27}$ g cm^{-3}, $r_p = 1$ kpc, $d = 3$ kpc, and $R = 10$ kpc, which are the input values used by CPS, gives $E_p \simeq 1.2\times10^{56}$ ergs and not 5×10^{54} ergs as given by CPS. Using the constraint on the jet luminosity (CPS eq. 20) gives $\varepsilon\beta_p \simeq 2.4\times10^{-5}$ and not 6×10^{-4} as given by CPS. If $\varepsilon = 1\%$, then $v_p \simeq 7.2\times10^7$ cm sec^{-1} which is a factor of two lower than the value given here ($v_p \simeq 1.6\times10^8$ cm sec^{-1}) which is good agreement considering that slightly different input parameters have been used. The plasmon density is then given by inverting equation 7.46, which gives $n_p \simeq 0.3$ cm^{-3} which is the same as the result given in Table 7.2.

CPS obtain an estimate for the plasmon velocity of $v_p \sim 4.5\times10^9$ cm sec^{-1} by requiring the plasmons to provide the "seed" relativistic electrons in the tails. The much higher value of v_p results in a much lower value for the plasmon density, $n_p \sim 7\times10^{-5}$ cm^{-3}. However, a much lower value of the efficiency, $\varepsilon \sim 2\times10^{-4}$ is also required, which is consistent with the limits given here.

Thus, once the numerical error of CPS is corrected, the same parameters for the plasmons are obtained. This is expected, since the same physics and roughly the same input parameters are used in both cases. The same conclusion must also be reached (i.e., the required plasmon efficiency is much lower than 1%).

The mass loss rates, assuming an efficiency of 1% ($m' \propto \varepsilon$), are typically $\sim 10^{-1}$-10^{-3} $M_\odot$ yr^{-1} for the JO and BRB models and $\sim 10^{1}$-10^{-1} $M_\odot$ yr^{-1} for the CPS model (i.e., the mass loss rate in the CPS model is much higher than in the BRB and JO models). The large dispersion in the estimates may at least partially be due to the uncertainties in the input parameters. These numbers can be compared with estimates for sources of mass in the ISM and the mass loss rate due to ram pressure stripping. The mass input rate from stars (stellar winds, etc.) into the ISM is estimated to be roughly ~ 0.1-1 $M_\odot$ yr^{-1} for a typical elliptical galaxy (e.g., Faber and Gallagher 1976, Gisler 1976). The mass loss rate from a galaxy due to ram pressure stripping is given by $m' \sim \pi r_s^2 f c_{ism} \rho_{ism}$, where r_s, ρ_{ism}, and c_{ism} are the radius, density, and sound speed of the ISM, and f is a factor which takes into account the radial decrease in density (f ~ 0.1; JO). Using r_s = 10 kpc, ρ_{ism} = 10^{-25} g cm^{-3}, and c_{ism} = 2x107 cm sec^{-1} (for a pressure of 3×10^{-11} dynes cm^{-2}) gives $m' \sim 10$ $M_\odot$ yr^{-1}. This suggests that the mass loss due to the beams/channels is small compared to both the mass input into the ISM from stars and the mass loss from the galaxy due to ram pressure stripping.

At this point, all three models for the jets in NATs can be made consistent with the observations with the appropriate value for the

efficiency. A choice between the models or even better estimates for the beam/plasmon velocity and density cannot be made until better constraints on the efficiency can be obtained.

7.9 Overview

In this section the broad implications of the results of this thesis are discussed. The impact of the data on our understanding of the nature of Narrow Angle Tail sources in Abell clusters, the conditions in the ISM of the galaxies, the parameters of the beams, and the models for jets and extragalactic sources in general are discussed.

The nature of NATs

The parent galaxies of NATs appear to be otherwise ordinary cluster members. Their distribution of velocities is consistent with the observed gaussian distribution of velocities for cluster members (Ulrich 1978, Baggio, Perola, and Tarenghi 1978). Also, the observed distribution of projected distance from the cluster center is consistent with that of an isothermal King model (which describes very well the galaxy and gas distribution in clusters [e.g., Bahcall 1977]). The problem of *why* these galaxies are radio sources is still unsolved since there seems to be nothing special about them.

The properties of NATs as radio sources are similar to those of other morphological groups, in the sense that there is a correlation between core and integrated power (e.g., Burns and Gregory 1982;

Fabbiano et al. 1984) and that brighter optical galaxies tend to be stronger radio sources (e.g., Auriemma et al. 1977).

Within the context of the bending models for quasi-continuous beams, the observed galaxy velocities and ICM densities are sufficient to account for both the morphology and energetic requirements of NATs. These results are entirely consistent with the idea, first proposed by Miley et al. (1972), that the tailed morphology is due to the interaction of the moving radio source with the ICM.

Thoughts about an ISM

The statistical results provide inconclusive answers to the question of the existence of an ISM and/or a turbulent galactic wake; i.e., there is no correlation of integrated power with velocity. However, the dispersion in the values of the other important parameters could wash this out. There is a correlation between the width and the integrated radio power; however, this is expected in both models. The existence of the subgroup of sources with a very abrupt jet/tail transition and a narrow range of bending scale lengths is suggestive of the existence of an ISM. The more gentle jet/tail transition seen in the other twin tail sources do not rule out the existence of an ISM in these sources, however.

On the other hand, the detailed data for NGC 1265 (the differential rotation measure structure, the existence of the cocoon, and the expansion of the jets) favor the existence of an ISM. The X-ray, optical, and radio data on NGC 1265 are consistent with an ISM of density $n < 0.3\ cm^{-3}$ and temperature $T > 8 \times 10^5$ K. This confirms the need

for a mechanism of gas removal from ellipticals (Faber and Gallagher 1976) and is roughly consistent with the predictions of the ram pressure stripping models (e.g., Gisler 1976; Lea and De Young 1976; Jones and Owen 1979; Shaviv and Salpeter 1982). The generally smooth intensity distribution of the tails argues against very drastic changes in the ISM over the $\sim 10^8$ yr lifetime of these NATs. Thus, a steady mass removal mechanism (e.g., ram pressure stripping) is favored for these sources over a more abrupt and episodic mechanism (e.g., sporadic winds driven by supernovae; Sanders 1981). In addition, the existence of an ISM at the level predicted by Jones and Owen (1979) supports their choice of relatively high stellar mass loss rates ($\sim$1-10 $M_\odot$ yr^{-1}) rather than the smaller values of $\sim$0.1 $\sim$1 $M_\odot$ yr^{-1} which are typically used (e.g., Faber and Gallagher 1976, Gisler 1976).

Jets, beams, and one-sided ejection

This thesis presents evidence which suggests that the beams in these NATs have nonrelativistic bulk velocities, $v_b \sim 10^3$-10^4 km sec^{-1}, and relatively low densities, $n_b \sim 10^{-4}$-10^{-6} cm^{-3}. How do these beams compare to those in the more powerful sources? The kinetic energy flow in a beam of radius $r_b \sim 1$ kpc, velocity $v_b \sim 10^4$ km sec^{-1}, and density $n_b \sim 10^{-4}$ cm^{-3} is $L_{KE} \sim 2.5 \times 10^{42}$ ergs sec^{-1}. This is sufficient to power the radio luminosity in a NAT jet ($L_{rad} \sim 10^{40}$ erg sec^{-1}) with an efficiency of 1%. However, the beams in very high luminosity sources ($L_{rad} > 10^{42}$ erg sec^{-1}) cannot simply be more efficient versions of this beam and must carry a higher kinetic energy flow by increasing the beam radius, density, or velocity. Beam radii, in general, are not much

larger than 1 kpc, and densities much larger than 10^{-4} cm^{-3} would probably be ruled out by polarization measurements (e.g., Perley et al. 1984). The easiest way to increase the kinetic energy flow is to increase the beam velocity since $L_{rad} \propto v_b^3$. Thus, one of the main differences between low- and high-luminosity sources could be that the brighter sources have higher beam velocities. The one-sidedness seen in powerful sources (e.g., quasars) could be due to Doppler beaming at moderately relativistic velocities in the beams. However, the existence of NATs with large, side-to-side asymmetries (e.g., 0039+211 and 1753+580) suggests that environmental effects or intrinsic variations in the beam properties can also be very important.

In general, the very continuous and symmetric structure of the twin jet NATs argues against alternating one-sided ejection in these sources except on very fast time scales. The switching time scale would have to be shorter than the lifetime of the channel in the external medium left by the last ejection, otherwise the beam/plasmon would essentially have to start over and re-establish a path through the external medium (e.g., CPS). The beam would essentially behave as an independent plasmon. Even if the energetic requirements could be satisfied by such a stream of independent plasmons, the variations in the jet intensity structure and bending scale length would be much larger than are observed. The upper limit to the channel lifetime is given by the sound crossing time of the channel if it is embedded in an ISM. Using r_b ~1 kpc and $c_s \sim 2 \times 10^7$ cm sec^{-1}, which are appropriate to NGC 1265, gives a channel lifetime of $\sim 5 \times 10^6$ yrs. Thus, the time between ejections on a given side would have to be less than 5×10^6 yrs.

7.10 Directions for Future Research

The NAT sample

The results of the statistical analysis are consistent with the idea that NATs (other than being radio sources) are ordinary members of rich clusters, and that their morphology is due to their motion through the intracluster medium. There are several important comparisons between NAT and non-NAT sources in clusters which can be used to further test this hypothesis. Do non-NAT radio sources have the same distribution of velocities as do NATs? If they do, then this would argue against the galaxy velocity being important in determining the morphology.

In rich clusters, the interaction between the radio source and the ICM is stronger because of the denser ICM and higher galaxy velocities and tends to produce more NATs (as opposed to other radio structures). It would be interesting to compare the fractional contributions of the various radio source morphologies found in clusters as a function of cluster richness or other cluster properties (i.e., BM and RS type). If this picture is correct, in richer clusters a higher fraction of the cluster radio sources should be NATs.

The more dominant (and presumably the brighter) optical galaxies tend to have stronger radio cores and integrated radio powers than the less dominant optical galaxies. In addition, the apparent low-power cutoff to the distribution of core and total radio powers is intriguing, although it may only be due to a selection effect. These results should be tested with a larger sample of NATs (and perhaps cluster sources in

general) by making radio observations to a lower limiting radio luminosity and obtaining absolute optical magnitudes. The construction of an optical-radio luminosity function for NATs would be interesting. Do non-NAT radio sources of comparable optical magnitude have similar radio luminosities? If the NATs are stronger radio sources than the non-NATs, this would argue that the processes which are responsible for the morphology also influence the radio luminosity. A galactic wake would occur only in NATs and would boost the radio luminosity of the sources above what it would be if the galaxies were relatively stationary.

NGC 1265 (3C 83.1B)

Both the existence of the jet cocoon, the collimation structure of the jets, and the differential foreground rotation measure structure are consistent with the existence of an ISM in the galaxy NGC 1265. The results obtained by combining the radio, optical, and X-ray data suggest that $r_s \sim 10$ kpc, $n \leq 3\times10^{-1}$ cm^{-3}, and $T \geq 8\times10^5$ K. A more sensitive search for optical line emission, as well as a better limit on the X-ray luminosity, would be useful in order to place stronger constraints on the properties of the ISM.

The lack of depolarization between 6 and 21 cm allows an upper limit to $n_b < 1\times10^{-3}$ cm^{-3} to be placed on the internal particle density. This is sufficient to rule out the CPS plasmons (unless $\varepsilon \ll 1\%$) for NGC 1265, but is not sufficient to allow a choice to be made between the JO and BRB beams. Polarization observations at much lower frequency (e.g., the 327 MHz system to be installed at the VLA) will improve the

constraints on n_b by a factor of ~10. This may still not allow a choice, since the expected densities are $\sim 10^{-5}$ cm^{-3}, but it will constrain the models more tightly.

The very flat dependence of the intensity on the jet radius suggests that there is particle reacceleration and magnetic field amplification all along the jets. In particular, knot W1 has a flat spectrum ($\alpha \simeq -0.05$) between 6 and 2 cm which could be due to a burst of particle acceleration. Since this knot is so unusual, and because of the implications for models for particle acceleration in radio jets, it is important to confirm this result and to determine the spectrum of the knot above 2 cm.

Parameters of bent beams

Based on the analysis in Chapter VII, most beams/plasmons appear to have nonrelativistic bulk velocities and are at least mildly transsonic ($M \sim 1$-4).

The CPS model tends to predict much higher thermal particle densities than the BRB and JO models. Unless the efficiency is much less than 1%, in many sources these predicted particle densities are much higher than the upper limits derived for NGC 1265. Multifrequency polarization observations may be able to tightly constrain (or perhaps rule out) the CPS model in these sources since an upper limit to the particle density gives an upper limit to the efficiency. If upper limits to the efficiency (from the polarization) can be obtained which are lower than the lower limits (from the velocity), it would make the CPS model rather implausible. Upper limits to the particle density of

$n < 10^{-5}$ cm^{-3} ($n < 10^{-4}$ cm^{-3} in the case of NGC 1265) would be sufficient to definitively test the CPS model.

The BRB model requires higher efficiencies than the other two models because the beam energy flux must power the radio luminosity of the entire source, and also because adiabatic losses are more important due to the large expansion of the jets to form the diffuse tails. The current lower limits to the efficiencies can be raised by obtaining higher resolution observations of the jets. In some sources this will push the efficiencies considerably above 1%. It is not yet clear at what level these efficiencies become unrealistic. Other constraints on the efficiency (both theoretical and observational) need to be established. Upper limits to the particle density in the relatively low range $\sim 10^{-6} - 10^{-7}$ cm^{-3} would be required to test the BRB model in most of the NATs.

The JO model tends to require more moderate values of velocity, density, and efficiency than the other two models and so is harder to constrain (e.g., thermal particle densities much lower than those in the CPS model, but comparable to those in the BRB model, are needed). The most effective way to test the JO model is to search for evidence of an ISM. Useful future experiments include X-ray observations as well as a sensitive search for optical-line emission.

More accurate cluster velocity dispersions and radial velocities for NATs are important since ε and $v_b \propto v_g^{-2}$ and $n_b \propto v_g^{6}$. Obtaining these observations, as well as better estimates for the ICM density, would firm up the current limits on the beam/plasmon parameters.

Eventually, if choices can be made between the models and reasonable estimates of the beam parameters can be obtained, then other problems could be addressed (e.g., does the beam velocity correlate with other radio source properties [see Bridle and Perley 1984] such as magnetic field structure, core power, or one-sidedness?). How important is the existence of an ISM in the formation of NAT sources? Can observations of NATs be used to constrain models for ram pressure stripping of galaxies?

REFERENCES

Abell, G. O. 1958, Ap. J. Suppl., 3, 211.

___. 1965, Ann. Rev. Astr. Ap., 3, 1.

___. 1975, in "Galaxies and the Universe," eds. A. Sandage, M. Sandage, J. Kristian, (Chicago: Univ. of Chicago Press), p. 601.

Andernach, H., Waldthausen, H., and Wielebinski, R. 1980, Astr. Ap. Suppl., 41, 339.

Auriemma, C., Perola, G. C., Ekers, R., Fanti, R., Lari, C., Jaffe, W. J., and Ulrich, M.-H. 1977, Astr. Ap., 57, 41.

Austin, T. B. and Peach, J. V. 1974, M.N.R.A.S., 167, 437.

Baan, W. A. 1980, Ap.J., 239, 433.

Baan, W. A. and McKee, M. R. 1983, Astr. Ap., submitted.

Baars, J. W. M., Genzel, R., Pauliny-Toth, I. I. K., and Witzel, A. 1977, Astr. Ap., 61, 99.

Baggio, R., Perola, G. C., and Tarenghi, M. 1978, Astr. Ap., 70, 303.

Bahcall, N. A. 1975, Ap. J., 198, 249.

___. 1977, Ann. Rev. Astr. Ap., 15, 505.

___. 1981, Ap. J., 247, 787.

Bahcall, J. N. and Sarazin, C. L. 1977, Ap. J. (Letters), 213, L99.

Bautz, L. P. and Morgan, W. W. 1970, Ap. J. (Letters), 162, L149.

Begelman, M. C. Blandford, R. D., and Rees, M. J. 1980, Nature, 287, 307.

Begelman, M. C., Rees, M. J., and Blandford, R. D. 1979, Nature, 279, 770. (BRB)

Benford, G. 1981, Ap. J., 247, 792.

Benford, G., Ferrari, A., and Trussoni, E. 1980, Ap. J., 241, 98.

Bicknell, G. V. and Henriksen, R. N. 1980, Ap. Lett., 21, 29.

Bignell, R. C. 1982a, Notes From The NRAO Aperture Synthesis Workshop, Chap. 4.

___. 1982b, NRAO VLA Cookbook.

Bijleveld, W. and Valentijn, E. A. 1982, Astr. Ap., 111, 50.

Birkinshaw, M. 1978, M.N.R.A.S., 184, 387.

Blandford, R. D. and Konigl, A. 1979, Ap. J., 232, 34.

Blandford, R. D. and Rees, M. J. 1974, M.N.R.A.S., 169, 395.

Bracewell, R. N. and Roberts, J. A. 1954, Aust. J. Phys., 7, 615.

Bracewell, R. N. 1978, "The Fourier Transform and its Applications" (New York: McGraw-Hill), Chap. 6.

Bridle, A. H. 1982, in "Extragalactic Radio Sources," Proc. I.A.U. Symposium No. 97, ed. D. S. Heeschen and C. M. Wade (Dordrecht: Reidel), p. 121.

___. 1984, A. J., 89, 979.

Bridle, A. H. and Fomalont, E. B. 1976, Astr. Ap., 52, 107.

___. 1978, A. J., 83, 704.

Bridle, A. H., Fomalont, E. B., Miley, G. K., and Valentijn, E. A. 1979, Astr. Ap., 80, 201.

Bridle, A. H. and Perley, R. A., 1984 Ann. Rev. Astr. Ap., 22, in press.

Bridle, A. H. and Vallee, J. P. 1981, A. J., 86, 1165.

Burch, S. F. 1979, M.N.R.A.S., 187, 187.

Burn, B. J. 1966, M.N.R.A.S., 133, 67.

Burns, J. O. 1979, Ph.D. thesis, Univ. of Indiana.

Burns, J. O. 1981, M.N.R.A.S., 195, 523.

Burns, J. O. and Balonek, T. J. 1982, Ap. J., 263, 546.

Burns, J. O. and Gregory, S. A. 1982, A. J., 87, 1245.

Burns, J. O. and Owen, F. N. 1980, A. J., 85, 204.

Burns, J. O., Owen, F. N., and Rudnick, L. 1979, A. J., 84, 1683.

Burns, J. O., and Ulmer, M. P. 1980, A. J., 85, 773.

Cavaliere, A. and Fusco-Femiano, R. 1976, Astr. Ap., 49, 137.

Chan, K. L. and Henriksen, R. N. 1980, Ap. J., 241, 534.

Chincarini, G. and Rood, H. J. 1971, Ap. J., 168, 321.

___. 1977, Ap.J., 214, 351.

Chincarini, G., Rood, H. J., Sastry, G. N. and Welch, G. A. 1971, Ap. J., 168, 11.

Christiansen, W. A. 1973, M.N.R.A.S., 164, 211.

Christiansen, W. A., Pacholczyk, A. G., and Scott, J. S. 1977, Nature, 266, 593.

___. 1981, Ap. J., 251, 518. (CPS)

Christiansen, W. A., Rolison, G. G., and Scott, J. C. 1979, Ap. J., 234, 456.

Cioffi, D. F. and Jones, T. W. 1980, A. J., 85, 368.

Clark, B. G. 1980, Astr. Ap., 89, 399.

___. 1981, VLA Scientific Memo No. 137.

___. 1982, Notes From The NRAO Aperture Synthesis Workshop, Chap. 10.

Cohn, H. 1983, Ap. J., 269, 500.

Coleman, G. D., Hintzen, P., Scott, J. S., and Tarenghi, M. 1976, Nature, 262, 476.

Conover, W. J. 1980, "Practical Nonparametric Statistics," (New York: John Wiley and Sons).

Cornwell, T. J. 1982a, Notes From The NRAO Aperture Synthesis Workshop, Chap. 9.

___. 1982b, ibid. Chap. 13.

___. 1983a, Astr. Ap., 121, 281.

___. 1983b, VLA Scientific Memorandum No. 149.

Cowie, L. L. and Binney, J. 1977, Ap. J., 215, 723.

Cowie, L. L. and McKee, C. F. 1975, Astr. Ap., 43, 337. (CM)

Danese, L., De Zotti, G., and di Tullio, G. 1980, Astr. Ap., 82, 322.

De Young, D. S. 1976, Ann. Rev. Astr. Ap., 14, 447.

Dickens, R. J. and Moss, C. 1976, M.N.R.A.S., 174, 47.

Downes, A. 1980, M.N.R.A.S., 190, 261.

Dressler, A. 1978, Ap. J., 226, 55.

Eilek, J. A. 1979, Ap.J., 230, 373.

Eilek, J. A. 1982, Ap.J., 254, 472.

Eilek, J. A., Burns, J. O., O'Dea, C. P., and Owen, F. N. 1984, Ap. J., 278, 37.

Eilek, J. A. and Henriksen, R. N. 1984, Ap. J., 277, 820.

Ekers, R. D. 1982, Notes From The NRAO Aperture Synthesis Workshop, Chap. 12.

Ekers, R. D., Fanti, R., Lari, C., and Parma, P. 1981, Astr. Ap., 101, 194.

Ekers, R. D., Fanti, R., Lari, C., Ulrich, M.-H. 1978, Astr. Ap. 69, 253.

Fabbiano, G., Miller, L., Trinchieri, G., Longair, M., and Elvis, M. 1984, Ap. J., 277, 115.

Fabian, A. C., Hu, E. M., Cowie, L. L., and Grindlay, J. 1981, Ap. J., 249, 47.

Fabian, A. C. and Nulsen, P. E. J. 1977, M.N.R.A.S., 180, 479.

Faber, S. M. and Dressler, A. 1976, Ap. J., 210, 65.

___. 1977, A. J., 82, 187.

Faber, S. M. and Gallagher, J. S. 1976, Ap. J., 204, 365.

Fabricant, D., Branduardi, G., Gorenstein, P., and Zamorani, G. 1979, Bull. A.A.S., 11, No. 4, 784.

Fanti, C., Fanti, R., Feretti, L., Gioia, I. M., Giovannini, G., Gregorini, L., Padrelli, L., Parma, P., Tomasi, P., Marano, B., and Zitelli, V. 1983, Astr. Ap. Suppl., 51, 179.

Fanti, R., Lari, C., Parma, P., and Ekers, R. D. 1981, Astr. Ap., 94, 61.

Fanti, R., Lari, C., Parma, P., Bridle, A. H., Ekers, R. D., and Fomalont, E. B. 1982, Astr. Ap., 110, 169.

Fanti, R. and Perola, G. C. 1977, in "Radio Astronomy and Cosmology," Proc. I.A.U. Symposium No. 74., ed. D. L. Jauncey (Dordrecht: Reidel), p. 171.

Feigelson, E. D. and Berg, C. J. 1983, Ap. J., 269, 400.

Felton, J. E., and Morrison, P. 1966, Ap. J., 146, 686.

Ferland, G. J. 1980, Pub.A.S.P., 92, 596.

Ferrari, A., Massaglia, S., and Trussoni, E. 1982, M.N.R.A.S., 198, 1065.

Ferrari, A., Trussoni, E., and Zaninetti, L. 1978, Astr. Ap., 64, 43.

___. 1981, M.N.R.A.S., 196, 1051.

Fiedler, R. and Jones, T. W. 1983, preprint.

Fomalont, E. B. 1982, Notes From The NRAO Aperture Synthesis Workshop, Chap. 11.

Fomalont, E. B., Bridle, A. H., Willis, A. G., and Perley, R. A. 1980, Ap. J., 237, 418.

Fomalont, E. B. and Rogstad, D. H. 1966, Ap. J., 146, 528.

Fomalont, E. B. and Wright, M. C. H. 1974, Interferometry and Aperture Synthesis, in "Galactic and Extragalactic Astronomy," eds. G. L. Verschuur and K. I. Kellermann (New York: Springer-Verlag), pp. 256-290.

Forman, W., Bechtold, J., Blair, W., Giacconi, R., Van Speybroeck, L., and Jones, C. 1981, Ap. J. (Letters), 243, L133.

Forman, W. and Jones, C. 1982, Ann. Rev. Astr. Ap., 20, 547.

Forman, W., Kellogg, E., Gursky, H., Tananbaum, H., and Giacconi, R. 1972, Ap. J., 178, 309.

Gavazzi, G. and Perola, G. C. 1980, Astr. Ap., 84, 228.

Giacconi, R., Kellogg, E., Gorenstein, P., Gursky, H., and Tananbaum, H. 1971, Ap. J. (Letters), 167, L81.

Giaconni, R., Branduardi, G., Briel, U., Epstein, A., Fabricant, D. Feigelson, E., Forman, W., Gorenstein, P. Grindlay, J., Gursky, H., Harnden, F. R., Henry, J. P., Jones, C., Kellogg, E., Koch, D., Murray, S., Schreier, E., Seward, F., Tananbaum, H., Topka, K., van Speybroek, L., Holt, S. S., Becker, R. H., Boldt, E. A., Serlemitisos, P. J., Clark, G., Canizares, C., Markert, T., Novick, R., Helfand, D., and Long, K. 1979, Ap. J., 230, 540.

Gisler, G. R. 1976, Astr. Ap., 51, 137.

Gisler, G. R. and Miley, G. K. 1979, Astr. Ap., 76, 109.

Gould, R. J. 1971, Ap. Letters, 8, 129.

Grandi, S. A. 1983, M.N.R.A.S., 204, 691.

Guindon, B. 1978, M.N.R.A.S., 183, 195.

Guindon, B. and Bridle, A. H. 1978, M.N.R.A.S., 184, 221.

Gull, S. F. and Northover, K. J. E. 1975, M.N.R.A.S., 173, 585.

Gunn, J. E. and Gott, J. R. 1972, Ap. J., 176, 1.

Gursky, H., Kellogg, E., Murray, S., Leong, C., Tananbaum, H., and Giacconi, R. 1971, Ap.J. (Letters), 167, L81.

Gursky, H., Solinger, A., Kellogg, E., Murray, S., Tananbaum, H., Giacconi, R., and Cavaliere, A. 1972, Ap. J. (Letters), 173, L99.

Hardee, P. E. 1979, Ap. J., 234, 47.

___. 1982, Ap. J., 257, 509.

___. 1984, Ap. J., 277, 106.

Hardee, P. E., Eilek, J. A., and Owen, F. N. 1980, Ap. J., 242, 502.

Harris, D. E. 1982, in "Extragalactic Radio Sources," Proc. I.A.U. Symposium No. 97, ed. D. S. Heeschen and C. M. Wade (Dordrecht: Reidel), p. 77.

Harris, D. E., Bachall, N. A., and Strom, R. G. 1977, Astr. Ap., 60, 27.

Harris, D. E., Costain, C. H., and Dewdney, P. E. 1984, Ap. J., 280, 532.

Harris, D. E., Costain, C. H., Strom, R. G., Pineda, F. J., Delvaille, J. P., and Shnopper, H. W. 1980b, Astr. Ap., 90, 283.

Harris, D. E., Kapahi, V. K., and Ekers, R. D. 1980, Astr. Ap. Suppl., 39, 215.

Harris, D. E., Lari, C., Vallee, J. P., and Wilson, A. S. 1980a, Astr. Ap. Suppl., 42, 319.

Harris, D. E. and Miley, G. K. 1978, Astr. Ap., 34, 117.

Harrison, E. R. 1974, Ap.J. (Letters), 191, L51.

Henriksen, R. N., Bridle, A. H., and Chan, K. L. 1982, Ap.J., 257, 63.

Hill, J. M. and Longair, M. S. 1971, M.N.R.A.S., 154, 125.

Hintzen, P., Scott, J. S., and Tarenghi, M. 1977, Ap. J., 212, 8.

Hintzen, P. and Scott, J. S. 1979, Ap. J. (Letters), 232, L145.

___. 1980, Ap. J., 239, 765.

Hintzen, P. 1979, Pub. A.S.P., 91, 426.

Hjellming, R. M. 1982, Notes From The NRAO Aperture Synthesis Workshop, Chap. 4.

Hjellming, R. M., Basart, J. P., Bridle, A. H., Fomalont, E. B., Rots, A. H., and Torson, J. 1982, An Introduction to The NRAO Very Large Array, ed. R. M. Hjellming (NRAO).

Hogbom, J. 1974, Astr. Ap. Suppl., 15, 417.

Hogbom, J. A. and Carlsson, I. 1974, Astr. Ap., 34, 341.

Hoglund, B. 1967, Ap. J. Suppl., 15, 61.

Holman, G. D., Ionson, J. A., and Scott, J. S. 1979, Ap. J., 228, 576.

Hubble, E. 1934, Ap. J., 79, 8.

Icke, V. 1981, Ap. J. (Letters), 246, L65.

Jaffe, W. 1980, Ap. J., 241, 925.

Jaffe, W. J. and Perola, G. C. 1973, Astr. Ap., 26, 423. (JP)

Jaffe, W. J. and Perola, G. C. 1974, Astr. Ap., 31, 223.

Jaffe, W. J., Perola, G. C., and Valentijn, E. A. 1976, Astr. Ap., 49, 179.

Jokippi, J. R. 1966, Ap. J., 146, 480.

Jones, T. W. and Owen, F. N. 1979, Ap. J., 234, 818. (JO)

Kapahi, V. K., Joshi, M. N., Subrahmanya, C. R., and Krishna, G. 1973, A. J., 78, 673.

Kellermann, K. I. and Pauliny-Toth, I. I. K. 1981, Ann. Rev. Astr. Ap., 19, 373.

King, I. 1972, Ap. J. (Letters), 174, L123.

Kraichnan, R. H. 1965, Phys. Fluids, 8, 1385.

Krupp, E. C. 1972, Ph.D. dissertation, U.C.L.A.

Laing, R. A. 1980, M.N.R.A.S., 193, 439.

___. 1981, Ap. J., 248, 87.

Laing, R. A. and Bridle, A. H. 1983, in preparation.

Laing, R. A., Riley, J. M., and Longair, M. S. 1983, M.N.R.A.S., 204, 151.

Landau, L. D. and Lifshitz, E. M. 1959, "Fluid Mechanics" (New York: Pergamon).

Lea, S. M. 1975, Ap. Letters, 16, 141.

Lea, S. M. and De Young, D. S. 1976, Ap. J., 210, 647.

Lea, S., Silk, J., Kellogg, E., and Murray, S. 1973, Ap. J. (Letters), 184, L105.

Leir, A. A. and van den Bergh, S. 1977, Ap. J. Suppl., 34, 381.

Longair, M. S. 1981, "High Energy Astrophysics" (Cambridge: Cambridge University Press).

Mcdonald, G. H., Kenderdine, S. and Neville, A. C. 1968, M.N.R.A.S., 139, 259.

McHardy, I. M. 1978, M.N.R.A.S., 185, 927.

McHardy, I. M. 1979, M.N.R.A.S., 188, 495.

McKee, J. D., Mushotzky, R. F., Boldt, E. A., Holt, S. S., Marshall, F. E., Pravdo, S. H., and Serlemitsos, P. J. 1980, Ap. J., 242, 843.

Melnick, J. and Quintana, H. 1981a, Astr. Ap. Suppl., 44 ,87.

___. 1981b, A. J., 86, 1567.

Melrose, D. B. 1980, "Plasma Astrophysics," vol. 2, (New York: Gordon and Breach).

Menon, T. K. 1980, A. J., 85, 1577.

Miley, G. K. 1973, Astr. Ap., 26, 413.

___. 1980, Ann. Rev. Astr. Ap., 18, 165.

Miley, G. K. and Harris, D. E. 1977, Astr. Ap., 61, L23.

Miley, G. K., Perola, G. C., Van der Kruit, P. C. and van der Laan, H. 1972, Nature, 237, 269.

Miley, G. K., Wellington, K. J. and van der Laan, H. 1975, Astr. Ap., 38, 381.

Mills, B. Y. and Hoskins, D. G. 1977, Aust. J. Phys., 30, 509.

Mills, B. Y., Hunstead, R. W., and Skellern, D. J. 1978, M.N.R.A.S., 185, 51p.

Mitton, S. 1972, M.N.R.A.S., 155, 373.

Mushotzky, R. and Smith, B. 1980, "Highlights of Astronomy," ed. P. A. Wayman, (Dordrecht: D. Reidel), p. 735.

Mushotzky, R. F., Holt, S. S., Smith, B., Boldt, E. A., and Serlemitsos, P. J. 1981, Ap. J. (Letters), 244, L47.

Mushotzky, R. F., Serlimitsos, P. J., Smith, B. W., Boldt, E. A., and Holdt, S. S. 1978, Ap. J., 225, 21.

Noonan, T. W. 1981, Ap. J. Suppl., 45, 613.

Nulsen, P. E. J. and Fabian, A. C. 1980, M.N.R.A.S., 191, 887.

O'Dea, C. P., Dent, W. A., and Balonek, T. J. 1984, Ap.J., 278, 89.

O'Dell, S. L. and Sartori, L. 1970, Ap. J. (Letters), 162, L37.

Oemler, A. 1974, Ap. J., 194, 1.

Oort, J. H. 1983, Ann. Rev. Astr. Ap., 21, 373.

Owen, F. N. 1974, A. J., 79, 427.

___. 1975, A. J., 80, 263.

Owen, F. N., Burns, J. O. and Rudnick, L. 1978, Ap. J. (Letters), 226, L119. (OBR)

Owen, F. N., Burns, J. O., Rudnick, L. and Greisen, E. W. 1979, Ap. J. (Letters), 229, L59.

Owen, F. N., Burns, J. O., and White, R. A. 1984, in "Groups and Clusters of Galaxies," ed. M. Mardirossian, G. Giuricin, and M. Mezetti (Dordrecht: Reidel).

Owen, F. N., Inoue, M., and O'Dea, C. P. 1982, in preparation.

Owen, F. N. and Rudnick, L. 1976, Ap. J. (Letters), 205, L1.

Owen, F. N., Rudnick, L., and Peterson, B. M. 1977, A. J., 82, 677.

Owen, F. N., White, R. A., and Burns, J. O. 1982b, in preparation.

Owen, F. N., White, R. A., Hilldrup, K. C. and Hanisch, R. J. 1982a, A. J., 87, 1083.

Pacholczyk, A. G. 1970, "Radio Astrophysics" (San Francisco: Freeman).

___. 1977, "Radio Galaxies" (New York: Pergamon).

Pacholczyk, A. G. and Scott, J. S. 1976, Ap. J., 203, 313. (PS)

Peebles, P. J. E. 1980, "The Large Scale Structure of The Universe," Princeton, NJ: Princeton Univ. Press).

Perley, R. A. 1981, VLA Scientific Memo No. 138.

Perley, R. A. 1982, A. J., 87, 859.

Perley, R. A., Bridle, A. H., and Willis, A. G. 1984, Ap. J. Suppl., 54, 291.

Perley, R. A., Bridle, A. H., Willis, A. G., and Fomalont, E. B. 1980, A. J., 85, 499.

Primini, F. A., Basinska, E., Howe, S. K., Lang, F., Levine, A. M., Lewin, W. H. G., Rothschild, R., Baity, W. A., Gruber, D. E., Knight, F. K., Matteson, J. L., Lea, S. M., and Reichert, G. A. 1981, Ap. J. (Letters), 243, L13.

Quintana, H. 1979, A. J., 84, 15.

Ray, T. P. 1981, M.N.R.A.S., 196, 195.

___. 1982, M.N.R.A.S., 198, 617.

Rees, M. J. 1978, M.N.R.A.S., 184, 61P.

Reynolds, J. E. 1980, Proc. Astron. Soc. Austral., 4, 74.

Riley, J. M. 1973, M.N.R.A.S., 161, 167.

___. 1975, M.N.R.A.S., 170, 53.

Riley, J. M. and Pooley, G. C. 1975, Mem. R.A.S., 80, 105.

Rogstad, D. H. and Ekers, R. D. 1969, Ap. J., 157, 481.

Roland, J. 1982, Astr. Ap., 107, 267.

Rood, H. J., Page, T. L., Kintner, E. C., and King, I. R. 1972, Ap. J., 175, 627.

Rood, H. J. and Sastry, G. N. 1971, Pub. A.S.P., 83, 313.

Rothschild, R. E., Baity, W. A., Marscher, A. P., and Wheaton, W. A. 1981, Ap. J. (Letters), 243, L9.

Rudnick, L. 1982, in "Extragalactic Radio Sources," Proc. I.A.U. Symposium No. 97, ed. D. S. Heeschen and C. M. Wade (Dordrecht: Reidel), 47.

Rudnick, L. and Burns, J. O. 1981, Ap. J. (Letters), 246, L69.

Rudnick, L. and Edgar, B. K. 1984, Ap. J., 279, 74.

Rudnick, L. and Owen, F. N. 1976, Ap. J. (Letters), 203, L107.

___. 1977, A. J., 82, 1.

Ryle, M. and Windram, M. D. 1968, M.N.R.A.S., 138, 1.

Sandage, A., Kristian, J., and Westphal, J. A. 1976, Ap. J., 205, 688.

Sanders, R. H. 1981, Ap. J., 224, 820.

Sarazin, C. L., Rood, H. J. and Struble, M. F. 1982, Astr. Ap., 108, L7.

Sastry, G. A. and Rood, H. J. 1971, Ap. J. Suppl., 23, 371.

Scheuer, P. A. G. and Readhead, A. C. S. 1979, Nature, 277, 182.

Schilizzi, R. T., Lockhart, I. A., and Wall, J. V. 1972, Austr. J. Phys., 25, 545.

Schilizzi, R. T. and McAdam, W. B. 1975, Mem. R.A.S., 79, 1.

Schilizzi, R. T. 1975, Mem. R.A.S., 79, 75.

Schneider, D. P. and Gunn, J. E. 1982, Ap. J., 263, 14.

Schwab, F. 1980, Proc. S.P.I.E., 231, 18.

Schwartz, D. A., Schwarz, J., and Tucker, W. 1980, Ap. J. (Letters), 238, L59.

Schwarz, U. J. 1978, Astr. Ap., 65, 345.

Shane, C. D. 1975, in "Galaxies and the Universe," eds. A. Sandage, M. Sandage, and J. Kristian (Chicago: Univ. of Chicago Press), p. 647.

Shapley, H. 1933, Proc. Natl. Acad. Sci., 19, 591.

___. 1957, "The Inner Metagalaxy," (New Haven: Yale Univ. Press), Chap. 9.

Shaviv, G. and Salpeter, E. E. 1982, Astr. Ap., 110, 300.

Simard-Normandin, M., Kronberg, P. P., and Button, S. 1981, Ap. J. Suppl., 45, 97.

Simon, A. J. B. 1978, M.N.R.A.S., 184, 537.

___. 1979, M.N.R.A.S., 188, 637.

Slee, O. B., Wilson, I. R. G., and Siegman, B. C. 1983, Aust. J. Phys., 36, 101.

Slingo, A. 1974a, M.N.R.A.S., 166, 101.

___. 1974b, M.N.R.A.S., 168, 307.

Sparke, L. S. 1983, Ap. Letters, 23, 113.

Spinrad, H. and Bahcall, N. A. 1976, Pub. A.S.P., 88, 660.

Spitzer, L. 1978, "Physical Processes in the Interstellar Medium" (New York: Wiley).

Sramek, R. A. 1982, Notes from the NRAO Aperture Synthesis Workshop, Chap. 2.

Stauffer, J., Spinrad, H., and Sargent, W. L. W. 1979, Ap. J., 228, 379.

Struble, M. F. and Rood, H. J. 1982, A. J., 87, 7.

___. 1983, preprint.

Sunyaev, R. A. 1970, Ap. Lett., 7, 19.

___. 1971, Soviet A. J., 15, 190.

Thompson, A. R. 1982, Notes from the NRAO Aperture Synthesis Workshop, Chap. 5.

Thompson, A. R., Clark, B. G., Wade, C. M., and Napier, P. J. 1980, Ap. J. Suppl., 44, 151.

Tifft, W. G. 1978, Ap. J., 222, 54.

Tovmassian, H. M. and Moiseev, I. G. 1967, Austral. J. Phys., 20, 715.

Ulrich, M.-H. 1978, Ap. J., 221, 422.

Valentijn, E. A. 1979a, Astr. Ap., 78, 367.

___. 1979b, Astr. Ap. Suppl., 38, 319.

___. 1981, Astr. Ap., 102, 53.

Vallee, J. P., Bridle, A. H., and Wilson, A. S. 1981, Ap. J., 250, 66.

Vallee, J. P. and Wilson, A. S. 1976, Nature, 259, 451.

Vallee, J. P., Wilson, A. S., and van der Laan, H. 1979, Astr. Ap., 77, 183.

Valtonen, M. J. and Byrd, G. G. 1980, Ap. J., 240, 442.

van Breugel, W. 1982, Astr. Ap., 110, 225.

van der Laan, H. and Perola, G. C. 1969, Astr. Ap., 3, 468.

van Groningen, E., Miley, G. K., and Norman, C. A. 1980, Astr. Ap., 90, L7.

Wardle, J. F. C. and Kronberg, P. P. 1974, Ap. J., 194, 249.

Webber, J. C. 1974, Pub. A. S. P., 86, 223.

Wellington, K. J., Miley, G. K. and van der Laan, H. 1973, Nature, 244, 502.

Wentzel, D. G. 1974, Ann. Rev. Astr. Ap., 12, 71.

White, S. D. M. 1976, M.N.R.A.S., 177, 717.

White, R. A., Owen, F. N., and Hanisch, R. J. 1982, in "Extragalactic Radio Sources," Proc. of I.A.U. Symposium No. 97, ed. D. S. Heeschen and C. M. Wade (Dordrecht: Reidel), p. 87.

Willson, M. A. G. 1970, M.N.R.A.S., 151, 1.

Wilson, A. S. and Vallee, J. P. 1977, Astr. Ap., 58, 79.

Wirth, A., Smarr, L., and Gallagher, J. S. 1982, A. J., 87, 602.

Yahil, A. and Ostriker, J. P. 1973, Ap. J., 185, 787.

Yahil, A. and Vidal, N. V. 1977, Ap. J., 214, 347.

Zwicky, F. 1938, Pub. A.S.P., 50, 218.

Zwicky, F., Herzog, E., and Wild, R. 1961, Catalog of Galaxies and Clusters of Galaxies. (Pasadena: California Institute of Technology).

Zwicky, F., Karpowicz, M., and Kowal, C. T. 1965, ibid., vol. 5.